Graduate School for Cellular and Biomedical Sciences
University of Bern

Integration of dynamic table translations into dynamic trajectory radiotherapy and mixed photon-electron beam radiotherapy

PhD Thesis submitted by

Gian Mauro Carlo Guyer

for the degree of

PhD in Biomedical Engineering

Supervisors

Prof. Dr. Michael K. Fix and Prof. Dr. Peter Manser
Division of Medical Radiation Physics and Department of Radiation Oncology
of the Inselspital, Bern University Hospital and University of Bern

Co-advisor

Prof. Dr. Mauricio A. Reyes Aguirre
ARTORG Center for Biomedical Engineering Research
Center for AI in Medicine of the University of Bern

Accepted by the Faculty of Medicine, the Faculty of Science and the Vetsuisse Faculty of the University of Bern at the request of the Graduate School for Cellular and Biomedical Sciences

Bern, Dean of the Faculty of Medicine

Bern, Dean of the Faculty of Science

Bern, Dean of the Vetsuisse Faculty Bern

“*A difficulty ceases to be as soon as you laugh at it and get down to work.*”

Lord Robert Baden-Powell (BiPi)

Inselspital, Bern University Hospital and University of Bern - Department of
Radiation Oncology - Division of Medical Radiation Physics

Abstract

Integration of dynamic table translations into dynamic trajectory radiotherapy and mixed photon-electron beam radiotherapy

by Gian Mauro Carlo Guyer

Radiotherapy aims at delivering a lethal dose of radiation to tumor cells while sparing the surrounding healthy tissue and organs. Highly specialized devices, such as C-arm linear accelerators (linacs), have been developed for external beam radiotherapy, which deliver high-energy photon and electron beams. Over the last decades, several improvements in photon beam radiotherapy, such as introducing the photon multileaf collimator (pMLC), enabled intensity-modulated radiotherapy (IMRT), resulting in improved target conformality compared to 3D conformal techniques. Volumetric modulated arc therapy (VMAT) improves the delivery efficiency while maintaining the dosimetric plan quality of IMRT by using dynamic gantry rotation during beam on.

Next to the dynamic gantry rotation, also the table and the collimator can rotate dynamically during beam on. This is used in a technique called dynamic trajectory radiotherapy (DTRT). Furthermore, the table can also translate dynamically in three directions, enabling non-isocentric DTRT. However, the potential of dynamic table translations for radiotherapy on a C-arm linac is unexplored. Thus, in this thesis, treatment techniques including dynamic table translations are developed, and potential use cases are shown.

A treatment planning process (TPP) for non-isocentric DTRT is developed to create treatment plans with photon beams including dynamic gantry, collimator, and table rotation and dynamic table translation. The intensity modulation optimization of the TPP is based on a hybrid column generation and simulated annealing direct aperture optimization algorithm. The TPP is used to create non-isocentric DTRT plans and several potential use cases for non-isocentric DTRT are demonstrated: While maintaining treatment plan quality, the delivery efficiency is improved by using non-isocentric DTRT instead of multi-isocentric IMRT for craniospinal irradiation. Extending the source-to-target distance in DTRT plans reduces the risk of collision between the gantry and the patient or table and enables additional beam directions, which could be exploited to improve the dosimetric treatment plan quality compared to isocentric DTRT.

Contrary to photon beam radiotherapy, electron treatments are still applied using patient-specific cut-outs placed in an applicator. By using the pMLC for electron beam collimation instead of the cut-outs, efficient electron beam treatments are possible. Further, the use of the pMLC facilitates mixed photon-electron beam radiotherapy (MBRT). An MBRT technique using pMLC-collimated electron arcs instead of electron beams with a static gantry angle is developed, resulting in improved delivery efficiency while maintaining the dosimetric plan quality of MBRT plans using electron beams with a static gantry angle.

One of the challenges of DTRT on C-arm linacs is accurately predicting potential collisions between the gantry, the patient, and the table during treatment planning. Thus, a collision prediction tool is developed, which is able to predict possible collision interlocks. The tool was successfully validated against measurements.

The created treatment plans for non-isocentric DTRT and MBRT were shown to be accurately deliverable on a C-arm linac. For several treatment plans, the dosimetric accuracy was successfully validated using film measurements.

In conclusion, this thesis demonstrates the benefits of dynamic table translations in photon and electron beam radiotherapy. With the demonstrated benefits of improved dosimetric treatment plan quality, delivery efficiency, and collision risk, dynamic table translations further facilitate the use of MBRT and DTRT treatment techniques in clinics in the future.

Acknowledgements

First and foremost, I want to thank Prof. Dr. Michael K. Fix and Prof. Dr. Peter Manser. Thank you for the opportunity to do my PhD thesis under your supervision. Thank you for supporting, advising, challenging, and guiding me during the last four years. Thank you for always having an open door and taking time for me in your busy schedules. Thank you for all the great discussions across the board of medical physics. Thank you for supporting me in pursuing further studies and enabling me to learn so much during this time. Thank you for all your trust in me to conduct my own measurements, to supervise master students, and many other tasks I was able to carry out. Thank you for enabling me to attend many conferences and pushing me to present my own research. It was a great pleasure working with you.

Furthermore, I thank Prof. Dr. Hendrik von Tengg-Kobligk for mentoring this PhD project. I would like to thank Dr. Wilko F. A. R. Verbakel for agreeing to be the external co-referee for this thesis.

I thank my co-advisor, Prof. Dr. Mauricio Reyes, for the interesting discussions and his great inputs from an outside perspective. My thanks also go out to the team from the Graduate School for Cellular and Biomedical Sciences for all their help with administrative things.

My sincere gratitude goes to Dr. Silvan Müller. I thank you for your great support for measurements, scientific writing, code quality, presentations, and treatment planning you provided without hesitation during the entire four years. I enjoyed it greatly to work together with you. A very heartfelt thank you goes to Dr. Jenny Bertholet, who supported me greatly, especially in the last year. I profited greatly from your vast knowledge and your proficient writing, and your enthusiasm for medical physics research is very contagious.

My warmest thanks go to Dr. Paul-Henry Mackeprang for his great medical insights and feedback, regardless of how late the hour was. I thank Hannes A. Löbner for all his support; it was great having someone who went through the same struggles during this time. Thanks to Dr. Werner Volken and Dr. Daniel Frei for their indispensable knowledge of Monte Carlo and programming in general. Finally, thanks to the rest of the research group, Dr. Florian Amstutz, Chengchen Zhu, and Dr. Reto Küng, for all their support. The coffee meetings with the research group were always a great source of new ideas and solutions.

I thank all the master's students who contributed to this project: Carole Köchli, Yanick Wyss, Stefan Velja, and Kyriakos Rossis. It was a great pleasure to supervise the master thesis projects.

Thanks to all the clinical medical physicists, technicians, IT specialists, and secretaries at the Division of Medical Radiation Physics. I profited greatly from all your clinical knowledge. Thank you for all your support and trust in me not to break the machine during measurements. Furthermore, thanks to all the radiation oncologists and radiation therapy technologists in the Department of Radiation Oncology at Inselspital in Bern.

Last but certainly not least, I want to thank my family and friends for all their support. Thank you to my parents, Christiane and Walo, who always believed in me and supported me on my path since I was born. Without your guidance and support throughout my studies, I would not be at the point I am today. Thank you to my siblings, Flurin, Dominique, Olivia, and Annette, for always being there for me regardless of the situation. Thank you to my grandparents, Marianne and Pio, for their financial and emotional support during my studies. Finally, thank you to my partner, Johanna, for always encouraging me, supporting me, listening to me, and enduring my busy schedule during these four years.

Contents

List of Figures

List of Tables

List of Abbreviations

3D-CRT	3D **C**onformal **R**adio**T**herapy
AAA	**A**nisotropic **A**nalytical **A**lgorithm
API	**A**plication **P**rogramming **I**nterface
ART	**A**lderson **R**adiation **P**hantom
ASO	**A**perture **S**hape **O**ptimization
BECT	**B**olus **E**lectron **C**onformal **T**herapy
BVH	**B**ounding **V**olume **H**ierarchy
CBCT	**C**one-Beam **C**omputed **T**omography
CG	**C**olumn **G**eneration
CP	**C**ontrol **P**oint
CSI	**C**ranio**S**pinal **I**rradiation
CT	**C**omputed **T**omography
CTV	**C**linical **T**arget **V**olume
DAO	**D**irect **A**perture **O**ptimization
DMPO	**D**irect **M**achine **P**arameter **O**ptimization
DoF	**D**egree **o**f **F**reedom
DPE	**D**ose **P**rediction **E**rror
DTRT	**D**ynamic **T**trajectory **R**adio**T**herapy
DVH	**D**ose **V**olume **H**istogram
EAT	**E**lectron **A**rc **T**herapy
EBRT	**E**xternal **B**eam **R**adio**T**herapy
gEUD	**g**eneralized **E**quivalent **U**niform **D**ose
FF	**F**lattening **F**ilter
FFF	**F**lattening **F**ilter **F**ree
FLEC	**F**ew **L**eaf **E**lectron **C**ollimator
GTV	**G**ross **T**arget **V**olume
GUI	**G**raphical **U**ser **I**nterface
H-DAO	**H**ybrid **D**irect **A**perture **O**ptimization
HI	**H**omogeneity **I**ndex

H&N	**H**ead and **N**eck
IMRT	**I**ntensity **M**odulated **R**adio**T**herapy
IGRT	**I**mage **G**uided **R**adio**T**herapy
ITV	**I**nternal **T**arget **V**olume
L-BFGS	**L**imited-memory **B**royden-**F**letcher-**G**oldfarb-**S**hanno
LNI	**L**ymph **N**ode **I**rradiation
MBRT	**M**ixed **B**eam **R**adio**T**herapy
MC	**M**onte **C**arlo
eMLC	**e**lectron **M**ulti**L**eaf **C**ollimator
pMLC	**p**hoton **M**ulti**L**eaf **C**ollimator
MMC	**M**acro **M**onte **C**arlo
MRI	**M**agnetic **R**esonance **I**maging
MU	**M**onitor **U**nit
NT	**N**ormal **T**issue
OAR	**O**rgan-**A**t-**R**isk
OCE	**O**ptimization **C**onvergence **E**rror
PET	**P**ositron **E**mission **T**omography
PSQA	**P**atient **S**pecific **Q**uality **A**ssurance
PTV	**P**lanning **T**arget **V**olume
QA	**Q**uality **A**ssurance
SA	**S**imulated **A**nnealing
SBRT	**S**tereotactic **B**ody **R**adio**T**herapy
SMCP	**S**wiss **M**onte **C**arlo **P**lan
SRS	**S**tereotactic **R**adio**S**urgery
SSD	**S**ource-to-**S**urface **D**istance
STD	**S**ource-to-**T**arget **D**istance
TNR	**T**rue **N**egative **R**ate
TPP	**T**reatment **P**lanning **P**rocess
TPR	**T**rue **P**ositive **R**ate
TPS	**T**reatment **P**lanning **S**ystem
VMAT	**V**olumetric **M**odulated **A**arc **T**herapy
VMC++	**V**oxel **M**onte **C**arlo
WBI	**W**hole **B**reast **I**rradiation

1

Introduction

Cancer is a generic term for a large group of diseases characterized by the rapid creation of abnormal cells leading to malignant tumors with the ability to spread throughout the body, which can cause organ failure and ultimately death (Hanahan and Weinberg, 2011). Cancer is a leading cause of death worldwide, accounting for nearly 10 million deaths annualy (Ferlay et al., 2020). In Switzerland, cancer is the second highest cause of death (Cirillo et al., 2021), with 48’000 new cancer diagnoses and 19’000 cancer-related deaths in 2021. However, the chance of survival has increased over the last few years due to constantly improving treatments against cancer (Cirillo et al., 2021).

Multiple treatment modalities against cancer are available either as single treatments or in combination (Debela et al., 2021). The intent of the treatments may be curative or palliative. In curative treatments, the aim is to eradicate the disease, while the aim in palliative treatments is to improve quality of life, such as relieving pain. The three main treatment modalities are surgery, chemotherapy, and radiotherapy, but other approaches such as targeted therapy, stem cell therapy, ablation therapy, and immunotherapy (Debela et al., 2021) are also available. The treatment intent and the choice of single or combined treatment modalities depend on many factors, such as type of cancer, disease progression, and patient condition. On average, around half of all cancer patients receive radiotherapy as part of their treatment (Borras et al., 2015; Atun et al., 2015).

1.1 Basics of radiotherapy

In radiotherapy, ionizing radiation is used to eradicate cancer cells. Ionizing radiation is radiation with sufficient energy to ionize atoms or molecules by detaching electrons from them and consequently depositing energy within the medium. In tissue, the deposited energy can cause single or double-strand breaks in the deoxyribonucleic acid (DNA) in cells, which ultimately can kill the cell. The deposited energy per mass is quantified by the dose with the unit Gray (1 Gy = 1 J / kg). There are two types of ionizing radiation: directly ionizing radiation and indirectly ionizing radiation. In directly ionizing radiation, charged particles such as electrons or protons deposit energy directly within the medium through multiple Coulomb interactions. In indirectly ionizing radiation, uncharged particles such as photons deposit energy by interacting with the medium and releasing charged particles, which in turn deposit energy.

Radiotherapy aims to eradicate cancer cells while sparing the surrounding healthy tissue and organs. Fortunately, there are different radiobiological principles between healthy tissue and cancer tissue. These principles are summarized in the 5 Rs of Radiobiology: Radiosensitivity, Repair, Reoxygenation, Redistribution, and Repopulation (Steel, Mcmillan, and Peacock, 1989). For example, healthy tissue has a superior repair capacity compared to tumor cells (Hubenak et al., 2014). These principles allow fractionation, where the total dose is given over multiple fractions, each with the same fraction dose typically five times a week (Ghaderi et al., 2022). Additionally, fractionation allows for reoxygenation and cell cycle redistribution, increasing tumor radiosensitivity (Pawlik and Keyomarsi, 2004) but also allows for repopulation of the tumor cells between fractions (Kim and Tannock, 2005). Thus, a balance between these different factors needs to be determined for each cancer type.

The ionizing radiation used in radiotherapy treatments is provided in two ways: by placing a radioactive source inside the patient or directing a beam of ionizing radiation at the patient. A sealed radioactive source placed inside the patient is used in brachytherapy (Chargari et al., 2019), and an unsealed radioactive source attached to a targeting molecule is used in radiopharmaceutical therapy (Sgouros et al., 2020). Using a beam of ionizing radiation coming from a source outside the patient is called external beam radiotherapy (EBRT). The beam for EBRT is created either by a radioactive isotope, for example, in Cobalt-60 machines (Dyk and Battista, 1996; Healy et al., 2017), or by a particle accelerator (Bryant, 1994). Synchrotron and cyclotron accelerators are used to create proton and Carbon ion beams (Bonnett, 1993; Hiramoto et al., 2007; Mohan, 2022) or even neutrons, for example, for Boron neutron capture therapy (Jin et al., 2022). However, linear accelerators producing photon and electron beams are the most common machines (IAEA, 2023).

1.2 Linear accelerators

In typical medical linear accelerators (linacs), electrons are accelerated to relativistic speeds using microwave radiation and then directed onto a high-Z material to produce a photon beam, illustrated in fig. 1.1. The electrons are initially released by heating a filament. The electrons then enter a waveguide in which they accelerate by microwave radiation produced by a radiofrequency power generator. If the waveguide is not parallel to the direction of the treatment beam, a bending magnet guides the electron beam in the right direction. The electron beam then hits a target, which produces high-energy photons due to bremsstrahlung. Monitor chambers are placed in the beam to control the delivered radiation. The monitor chambers measure the delivered radiation in monitor units (MUs). They are calibrated for each beam quality, such that a specified amount of MUs (for example 100) correspond to a specific dose in a reference condition, such as 1 Gy in the dose maximum of a 10 x10 cm^2 jaw collimated beam in water with a source-to-surface distance (SSD) of 100 cm.

Finally, a collimation system shapes the beam. Typically, the collimation system consists of a fixed primary collimator, a set of movable secondary collimators, and a photon multileaf collimator (pMLC), which allows the collimation of the photon beams into complex shapes. A flattening filter (FF) can be placed inside the beam to flatten the photon beam dose profile.

The linac is mounted either inside a ring-based system, on a robotic arm, or on a C-arm gantry. Ring-based systems typically have a straight-through beam design with a 6 MV photon beam, such as the Halcyon system (Varian, a Siemens Healthineers Company, Germany). Another design of a ring-based linac is the tomotherapy system (Mackie, 2006). In tomotherapy, a fan-like photon beam is produced, which rotates around the patient in a helical pattern similar to that of a CT machine. Another unique ring-based system was the Vero system (Hiraoka et al., 2020). The Vero system stands out because the collimator system was mounted on a gimbal, and the entire ring could rotate ±60° allowing for non-coplanar treatments.

In robotic systems, a linear accelerator is mounted on top of a robotic arm (Masterson-McGary, 2013), such as in the CyberKnife system (Accuray Incorporated, USA). The robotic arm allows precise, non-coplanar beams and tumor

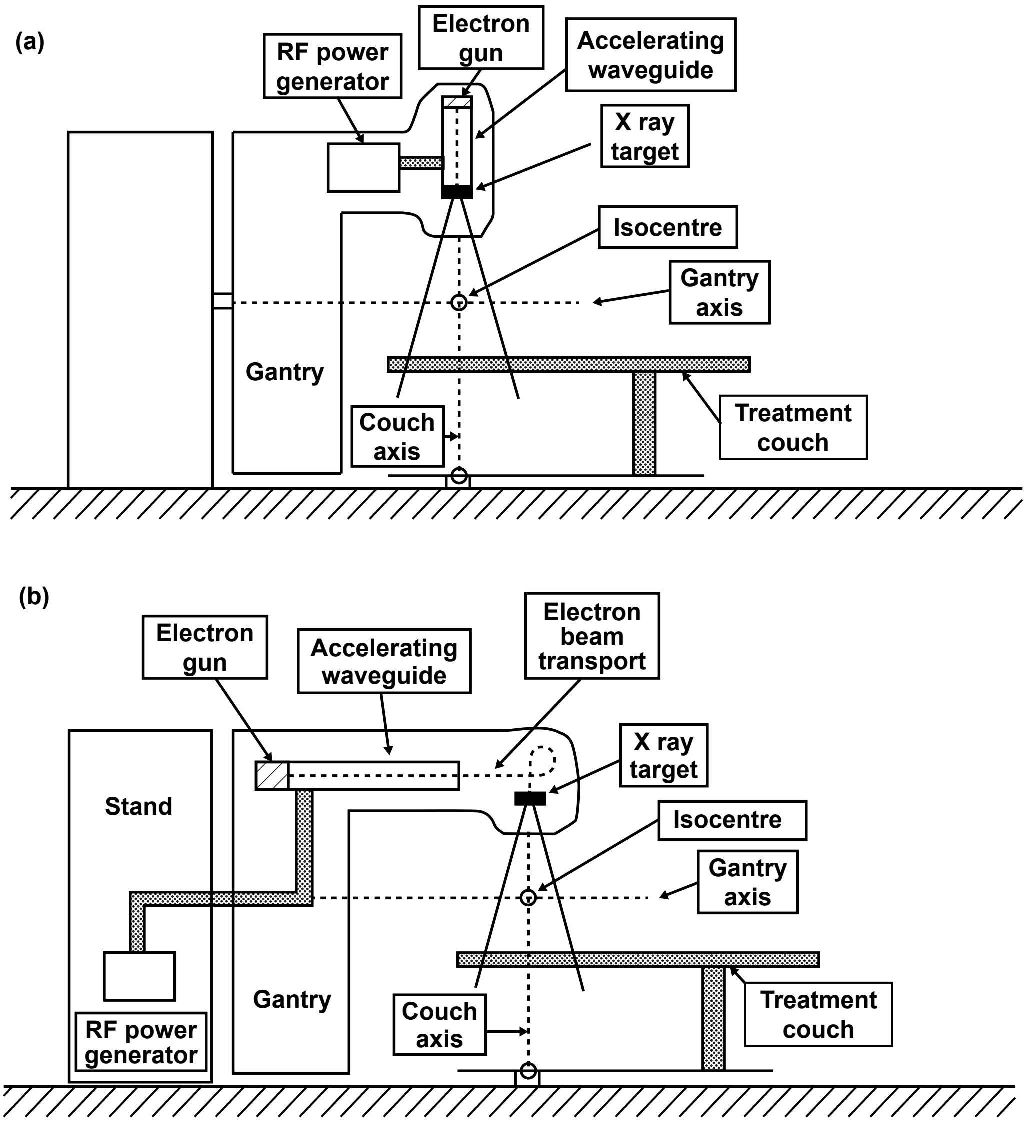

FIGURE 1.1: Schematics of medical linacs, reproduced from IAEA, 2005. a) A straight-through beam design. This design does not have a bending magnet, typically has a smaller linear accelerator, and can produce photon beams with energies of 4-6 MV. b) C-arm gantry design. This design has a linear accelerator perpendicular to the direction of the treatment beam and a bending magnet. The machine can produce photon as well as electron beams.

tracking during treatments. The system was developed for stereotactic radiosurgery (SRS), in which small tumors in the brain are treated very precisely in only one or a few fractions with a high dose per fraction (Lippitz et al., 2014). However, it is also used to treat body tumors, called stereotactic body radiotherapy (SBRT) (Timmerman and Kavanagh, 2005).

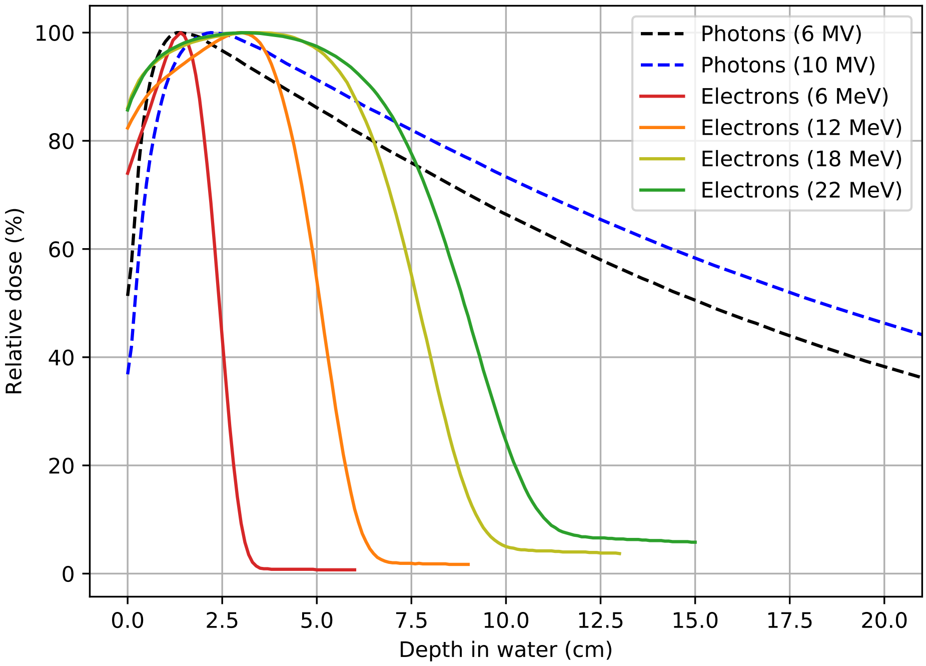

FIGURE 1.2: Depth dose curves in water of 6 and 10 MV photon beams and 6, 15, 22 MeV electron beams.

The most common systems are C-arm linacs mounted on a gantry, such as the TrueBeam system (Varian, a Siemens Healthineers Company, Germany) and the Elekta Infinity system (Elekta, Sweden). On a C-arm linac, the linear accelerator is usually not in line with the beam direction, and hence, a bending magnet is used. Because the linear accelerator is longer than in a straight-through design, photon beams from 4 MV to 16 MV are available. Next to photon beams, electron beams with energies from 6 MeV to 22 MeV are available on the C-arm linacs. For this, the target is retracted, and scattering foils are inserted instead to achieve a broad electron beam. In fig. 1.2, the depth dose curves of three electron and two photon beams available on a C-arm linac are shown. Because the electrons are charged particles, the electron beams have a finite range and are thus used to treat superficial tumors. The electron beams also scatter more in air compared to photon beams. To reduce the lateral beam penumbra, typically an applicator is mounted onto the treatment head, and a patient-specific cut-out is placed inside the applicator. Standard electron applicator apertures range from 6 x 6 cm^2 to 25 x25 cm^2.

Usually, the system is equipped with a 6 degree-of-freedom patient couch, allowing for translational movement in the vertical, longitudinal, and lateral direction and rotational movement in the pitch, roll, and yaw direction. The yaw rotation range is ±90°, which enables non-coplanar treatments. The yaw rotation is commonly called just table rotation. Pitch and roll have a range of ±3° and are mostly used for corrections of patient setup. Finally, a kV system is mounted either directly onto the gantry or in the room for taking X-ray images or cone-beam computed tomography (CBCT) scans before treatment to help setting up the patient correctly.

1.3 Radiotherapy process

Because the anatomy and the location and shape of the tumor vary from patient to patient, the patient must be imaged, and a specific treatment plan must be created for the patient before the delivery of ionizing radiation and a quality assurance (QA) is made to reduce the risk of potential errors. This process is illustrated in fig. 1.3 and explained in detail in the following subchapters.

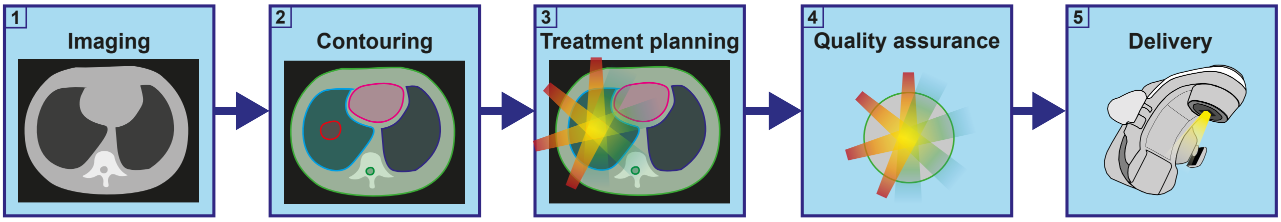

FIGURE 1.3: Overview of the radiotherapy process.

1.3.1 Imaging

In the first step, a computed tomography (CT) scan of the treated area is done, called the planning CT. The patient is set up in the exact position required for the treatment for this scan. The position is then the same for every treatment. Immobilization devices such as masks, headrests, and vacuum fixes are used to ensure the patient's position every day.

The planning CT provides anatomical information as well as information about the energy absorption properties of the tissue. Optionally, other imaging modalities, such as magnetic resonance imaging (MRI) or positron emission tomography (PET), are added to obtain functional information about the tissue.

The additional imaging data is then registered to the CT dataset to correlate the different image information spatially.

1.3.2 Contouring

In the next step, regions of interest are contoured on the planning CT. For EBRT photon treatments, report 83 from the International Commission on Radiation Units (ICRU) defines a standardized hierarchy for contouring target volumes (Hodapp, 2012). The gross target volume (GTV) is the tumor volume clearly distinguishable from normal tissue. The clinical target volume (CTV) consists of the GTV plus a margin encompassing tissue with microscopic disease extending beyond the tumor's boundaries. To consider uncertainties related to internal movement of the patient's anatomy, such as breathing, sometimes an internal target volume (ITV) is drawn. Finally, the planning target volume (PTV) adds a margin to the CTV (or ITV) to consider patient setup uncertainties, patient and tumor motion during the treatment, and machine tolerances. In addition to the target, all relevant organs-at-risk (OARs) are contoured. The contours allow the evaluation of dosimetric endpoints to the OARs during the treatment planning. Similar to the PTV, planning organ-at-risk volumes (PRVs) are drawn for specific organs by adding a margin around the OAR to consider the internal and external uncertainties.

1.3.3 Treatment planning

After contouring, the treatment planning is performed, in which the dose distribution to be delivered to the patient is optimized (Webb, 1997). In this step, the directions from which the beams irradiate, as well as the intensity of the beams defined by the beam shape and the number of MUs are determined, which is done in two different approaches:

- Forward planning: In the forward planning approach, a planner manually chooses the beam directions and beam intensities. This approach is generally only feasible when there are only a few degrees of freedom for the planner to tune, such as the beam energy, gantry angles, collimator angles, and MUs of 2-4 beams.
- Inverse planning: In the inverse planning approach, the planner does not set the beam intensities directly. Instead, the planner defines a set of planning goals and the beam directions. The beam intensities are then

determined using an optimization algorithm that tries to fulfill the planning goals.

Different optimization algorithms are used to optimize the intensity modulation in the inverse planning approach, which can be categorized into two broad categories: fluence map optimization (FMO) and direct aperture optimization (DAO). In FMO, the beam is discretized into small segments, called beamlets, and the non-negative weights of the beamlets are optimized, resulting in the fluences of the beams. The optimized fluences must then be converted into pMLC shapes using leaf-sequencing. DAO directly optimizes the pMLC shapes and MU weights, thus eliminating the need for the leaf-sequencing step but leading to a large non-convex optimization problem. Several algorithms have been developed for DAO, such as stochastic search methods (Webb, 1989; Shepard et al., 2002; Otto, 2008), which randomly change the pMLC shape and MU weights, and column generation (CG) algorithms (Desaulniers, Desrosiers, and Solomon, 2005; Carlsson and Forsgren, 2014), which iteratively generate pMLC shapes with corresponding MU weights. Finally, local gradient-based methods use an initial optimization, such as FMO plus leaf-sequencing, to define a good starting position and then refine the pMLC shapes and MU weights to a local optimum (Bzdusek et al., 2009).

An essential aspect of the forward and inverse planning approach is the dose distribution simulation inside the patient. The resulting simulated dose distribution allows the evaluation of dosimetric endpoints to the target and OARs, which is an integral part of the treatment plan quality. Multiple algorithms exist for the calculation of dose distributions. One set of algorithms is convolution/superposition algorithms such as the collapsed cone convolution algorithm (Anders, 1989) or the Anisotropic Analytical Algorithm (AAA) (Ulmer, Pyyry, and Kaissl, 2005). Another method consists of solving the linear Boltzmann transport equation where the open-form transport equation is discretized and typically solved in an iterative manner (Vassiliev et al., 2010). Finally, there are Monte Carlo (MC) dose calculation algorithms, where tracks of particles are simulated by statistically sampling the interactions, and the deposited dose along the tracks is averaged for many particles (Rogers, 2006).

1.3.4 Quality assurance

To ensure a safe fulfillment of the medical prescription, quality assurance (QA) procedures are put in place (Thwaites, 2013). QA includes daily, weekly, monthly, and yearly checks, in which the machine components, beam characteristics, and beam output are tested to be in specified tolerances (Klein et al., 2009). Furthermore, a patient-specific QA (PSQA) is performed for every treatment plan. Typically, this consists of a measurement-based QA, in which machine QA specific to each treatment plan is performed using a measurement device (Miften et al., 2018), and an independent dose calculation, which ensures an accurate dose calculation inside the patient geometry.

1.3.5 Delivery

After successful PSQA, the treatment plan is delivered to the patient. The patient is set up in the exact same position as for the planning CT, using the same immobilization devices. The table is moved such that the desired position inside the patient lies in the linac's isocenter with the help of a laser guidance system or a surface guidance system (Freislederer et al., 2020). Furthermore, image guidance in the form of X-rays and CTBT is used to position the patient accurately (Verellen, Ridder, and Storme, 2008; Oelfke, 2009). MRI has recently been used for patient positioning as well (Chin et al., 2020). During the delivery, techniques such as gating and tracking may be used to manage the tumor's motion for specific treatments (Keall et al., 2006).

1.4 External beam radiotherapy techniques

One of several EBRT techniques can be chosen for treatment during the treatment planning process. The following subchapters give an overview of the different EBRT techniques available on a C-arm linac, illustrated in fig. 1.4.

1.4.1 3D conformal radiotherapy

Over the last few decades, enormous technological advances have revolutionized the field of photon radiotherapy. The replacement of patient-specific blocks with the pMLC substantially improved treatment efficiency and safety (Kallman et al., 1988), and improvements in imaging enabled CT-based planning (Battista, Rider, and Van Dyk, 1980). These innovations led to the introduction of 3D conformal radiotherapy (3D-CRT) (Brewster et al., 1995), in which the target is irradiated from multiple beam directions with the pMLC set conformal to the shape of the tumor from the beam's eye view. Typically, 3D-CRT plans are created using a forward planning approach.

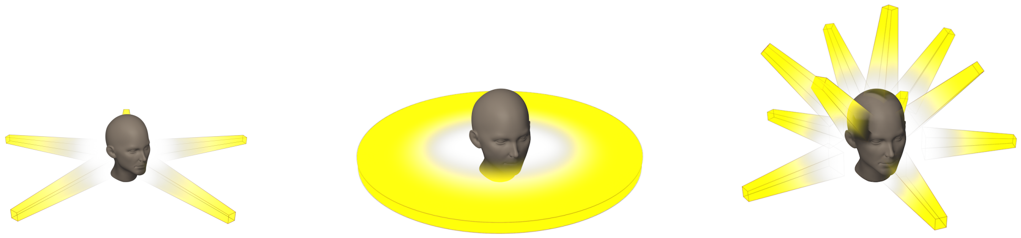

(a) 3D-CRT / IMRT (b) VMAT (c) Non-coplanar IMRT

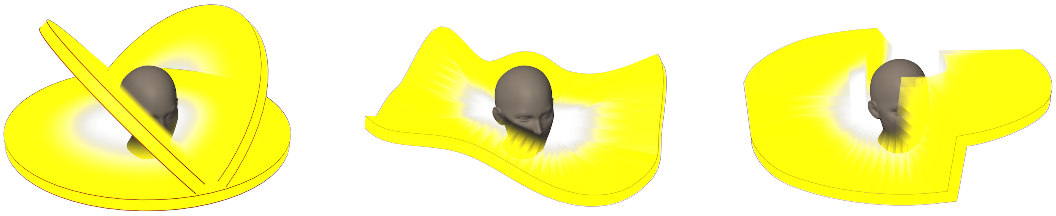

(d) Non-coplanar VMAT (e) DTRT (f) Non-isocentric DTRT

FIGURE 1.4: Overview over photon treatment techniques. 3D-CRT: 3D conformal radiotherapy. IMRT: Intensity-modulated radiotherapy. DTRT: Dynamic trajectory radiotherapy. The techniques are described in detail in the following subchapters.

1.4.2 Intensity-modulated radiotherapy

Next to efficient shaping of beams for 3D-CRT, the pMLC enabled intensity-modulated radiotherapy (IMRT), in which non-uniform intensities of photon beams are delivered from multiple beam directions (Convery and Rosenbloom, 1992). Due to the non-uniform intensities, IMRT has improved conformity of the dose distribution to the target compared to 3D-CRT (Bortfeld, 2006). The intensity modulation is achieved using either a step-and-shoot or a sliding-window method. In step-and-shoot, multiple segments are delivered one after the other, with the beam turned off when the pMLC moves between segments (step) and the pMLC fixed to a specific pattern while the beam is on (shoot). In sliding-window, the pMLC leaves move while the beam is on, and the intensity modulation is achieved by moving the pMLC leaves at different speeds at different time points.

Volumetric modulated arc therapy (VMAT) uses photon arcs instead of photon beams with a static gantry angle. In VMAT, the gantry is rotated continuously during beam-on, and the intensity modulation is achieved by controlling the gantry speed, MU rate, and pMLC leaves (Otto, 2008). VMAT achieves a similar treatment plan quality while improving the delivery efficiency compared to IMRT (Verbakel et al., 2009; Teoh et al., 2011). IMRT and VMAT plans are usually created using an inverse planning technique.

1.4.3 Non-coplanar radiotherapy

While IMRT and VMAT are coplanar techniques, photon radiotherapy is not limited to one plane, and non-coplanar photon radiotherapy techniques also exist. Historically, non-coplanar radiotherapy is primarily used for SRS treatments and pioneered by Leksell, 1951. In this technique, multiple photon or proton beams are cross-fired from many directions to treat malignant diseases in the brain (Leksell, 1983). Podgorsak et al., 1988 introduced dynamic SRS in which the photon beam follows a trajectory. While dedicated systems for SRS such as gamma knife (Wu, 1992) or CyberKnife system (Accuray Incorporated, USA) exist, more recently, C-arm linacs are also used for SRS treatments (Ohira et al., 2018; Ho et al., 2020; Ikawa et al., 2023). One commercially available non-coplanar technique on C-arm linacs is the Hyperarc system (Varian, a Siemens Healthineers Company, Germany), which delivers multiple VMAT arcs with different table angles. However, non-coplanar radiotherapy does not need to be limited to stereotactic treatments and there is a research interest into general non-coplanar radiotherapy on C-arm linacs (Dong et al., 2013; Rwigema et al., 2015; Yu et al., 2018; Smyth et al., 2013; MacDonald and Thomas, 2015; Papp, Bortfeld, and Unkelbach, 2015; Wild et al., 2015; Lyu et al., 2018a; Mullins et al., 2020a; Yang et al., 2011; Fix et al., 2018; Langhans et al., 2018; Dong, Liu, and Xing, 2018; MacDonald et al., 2020; Bertholet et al., 2022).

Non-coplanar radiotherapy is categorized into different techniques, visualized in fig. 1.4. In non-coplanar IMRT, intensity-modulated beams are applied from multiple non-coplanar static beam directions (Dong et al., 2013; Rwigema et al., 2015; Yu et al., 2018). In non-coplanar VMAT, multiple VMAT arcs are delivered using different table angles (Audet et al., 2011; Clark et al., 2012; Wild et al., 2015; Ohira et al., 2018; Reis et al., 2021). The table is fixed during beam on in both non-coplanar IMRT and non-coplanar VMAT. Dynamic trajectory radiotherapy (DTRT) utilizes synchronous dynamic gantry and table rotation during beam on, either without (Smyth et al., 2013; MacDonald and Thomas, 2015; Papp, Bortfeld, and Unkelbach, 2015; Wild et al., 2015; Lyu et al., 2018a; Mullins et al., 2020a) or with (Yang et al., 2011; Fix et al., 2018; Langhans et al., 2018; Dong, Liu, and Xing, 2018; MacDonald et al., 2020) additional dynamic collimator rotation. While in these studies the table is only rotated dynamically, the table could also be translated dynamically during beam on, resulting in non-isocentric DTRT. For example, the table could be translated dynamically to irradiate large targets, potentially reducing the delivery time.

One of the main challenges of non-coplanar radiotherapy on C-arm linacs is the risk of collisions between the gantry and the table or patient (Smyth et al., 2019b). One possible way to decrease the collision risk is by moving the table away from the gantry along the central beam axis (Liang et al., 2015; Yu et al., 2015). For DTRT, this could also be enabled by dynamic table translations during beam on.

1.4.4 Electron radiotherapy

While the pMLC has enabled efficient planning and delivery of photon beams and allowed clinical implementation of intensity modulation for photon beams, the same advancements were not made for electron radiotherapy. Electron treatments are still applied using patient-specific cut-outs placed in an applicator, which is mounted onto the gantry head (Hogstrom and Almond, 2006). This method makes electron treatments inefficient and cumbersome because a cut-out must be molded for every treatment plan, and the cut-out and applicator must be manually installed for every treatment fraction. Furthermore, only limited treatment planning features are available for electron treatments (Klein et al., 2008). Due to this, electron radiotherapy has only limited use in the clinic (Hogstrom and Almond, 2006), although the distal dose fall-off of electron beams provides advantageous dose characteristics for treatments of superficial targets compared to photon beams.

Another disadvantage of cut-outs and applicators is that intensity modulation is practically infeasible, which limits the usage of electron beams in inhomogeneous media or for large targets (Hogstrom and Almond, 2006). Several methods have been investigated to overcome this issue. Electron arc therapy (EAT) is a technique already proposed many decades ago, in which an electron beam is applied with a dynamic gantry rotation (Khan et al., 1977; Leavitt et al., 1985; McNeely et al., 1988; Leavitt and Stewart, 1993; Gaffney et al., 2001; Sharma et al., 2011). EAT was primarily used for chest wall treatments. Bolus electron conformal therapy (BECT) makes use of custom-made boli to modulate the intensities of electron beams, with the boli being either milled (Low et al., 1992; Low et al., 1995; Perkins et al., 2001) or 3D printed (Su, Moran, and Robar, 2014; Zou et al., 2015). However, both EAT and BECT suffer from complex and resource-intensive treatment setup and logistics burdens and have limited use in clinics today.

Several institutions investigated the potential of modulated electron radiotherapy (MERT), and several different collimation devices were presented for enabling the intensity modulation for electron beams, such as a few leaf electron collimator (FLEC) (Al-Yahya et al., 2005a; Al-Yahya et al., 2005b; Al-Yahya, Verhaegen, and Seuntjens, 2007; Alexander, DeBlois, and Seuntjens, 2010; Alexander et al., 2011; Eldib et al., 2013), a custom electron multileaf collimator (eMLC) (Ma et al., 2000; Gauer et al., 2008; Engel and Gauer, 2009; Vatanen, Traneus, and Lahtinen, 2009; O'Shea et al., 2011; Eldib et al., 2013; Jin et al., 2014) and the already installed pMLC (du Plessis et al., 2006; Jin et al., 2008; Klein, Mamalui-Hunter, and Low, 2008; Klein et al., 2008; Klein et al., 2009; Salguero et al., 2010; Surucu et al., 2010; Mihaljevic et al., 2011; Henzen et al., 2014a; Henzen et al., 2014b; Mueller et al., 2018a; Kaluarachchi et al., 2020; Fix et al., 2023; Brost, Wan Chan Tseung, and Antolak, 2023). Using the pMLC for modulating the intensities of electron beams has the advantage that no additional hardware needs to be mounted onto the gantry head. One limiting factor of pMLC-collimated electron treatments is the increased lateral penumbra of electron beams due to in-air scatter (Mueller et al., 2018a). One possible solution is to reduce the SSD by moving the patient closer to the gantry with the table for electron treatments to reduce the air volume between the gantry and the patient, thus reducing the amount of in-air scatter. These collimation devices have yet to find widespread clinical implementation for electron beams.

1.4.5 Mixed photon-electron beam radiotherapy

Mixed photon-electron radiotherapy (MBRT) makes use of the dose characteristics of both photon and electron beams in one single treatment plan (Xiong et al., 2004; Mu et al., 2004). Thus, MBRT takes advantage of both the sharp distal dose fall-off of electron beams and the deeper penetration depth and sharper lateral penumbra of photon beams. Today, MBRT has only limited use in clinics, possibly due to MBRT using cut-outs and applicators for the electron beams suffering from the interruption to mount and dismount the applicators for the electron beams during the treatment (Henzen et al., 2014b).

To overcome this issue, several institutions investigated pMLC-collimated MBRT (Karlsson and Zackrisson, 1993; Jansson et al., 1998; Li et al., 2000; Palma et al., 2012; Míguez et al., 2017; Mueller et al., 2017; Mueller et al., 2018b; Renaud, Serban, and Seuntjens, 2019; Heath et al., 2021; Heng et al., 2021; Heng et al., 2023a). The more recent studies take advantage of using multiple electron energies and intensity-modulated electron beams collimated by the pMLC (Palma et al., 2012; Míguez et al., 2017; Mueller et al., 2017; Mueller et al., 2018a; Renaud, Serban, and Seuntjens, 2019; Heath et al., 2021; Heng et al., 2021; Heng et al., 2023a). This approach has the advantage of having a single collimation device for both modalities. It thus eliminates the need to mount and dismount any equipment onto the gantry when switching between photon and electron beams.

One limiting factor of pMLC-collimated MBRT is that the electron beams are always delivered from static gantry angles, increasing the delivery time compared to photon-only treatments. Hypothetically, the delivery time of MBRT can be reduced by delivering the electron beams as arcs, similar to the increased delivery efficiency of VMAT over IMRT. A shortened SSD for pMLC-collimated electron arcs could be maintained by translating the table dynamically during beam on.

1.5 Hypothesis and Aim

The aim of this thesis is to integrate dynamic table translations into EBRT treatment techniques on a C-arm linac, to develop treatment planning processes (TPPs) that can generate accurate and deliverable treatment plans including dynamic table translations, and to investigate the potential benefit of the dynamic table translations. It is hypothesized that integrating dynamic table translations into photon and electron radiotherapy treatments improves the dosimetric treatment plan quality, delivery efficiency, and collision risk for several treatment techniques and treatment sites.

1.5.1 Part 1

To integrate dynamic table translations into EBRT treatment techniques, first, a TPP for IMRT and pMLC-based MBRT based on a step-and-shoot technique is developed. The TPP is based on an MC dose calculation and an inverse planning approach using a hybrid column generation and simulated annealing direct aperture optimization (H-DAO), which can optimize the intensity of photon and electron beams simultaneously. IMRT and MBRT plans are created using the developed TPP to demonstrate the effectiveness of the H-DAO in generating high-quality treatment plans.

1.5.2 Part 2

In the second part, the TPP of the first part is extended to create treatment plans with photon beams including dynamic gantry, collimator, and table rotation and dynamic table translation. The developed TPP is used to create non-isocentric DTRT plans, and the potential of non-isocentric DTRT is investigated for three use cases: efficient delivery for craniospinal irradiation, improved dosimetric treatment plan quality for bilateral whole breast irradiation and reduced collision risk by extending the source-to-target distance.

1.5.3 Part3

The developed TPP is further extended in the third part to include electron arcs, that is, pMLC-collimated electron beams with a dynamic gantry rotation. The SSD of the electron arcs is shortened utilizing dynamic table translations. The TPP is used to create MBRT plans including electron arcs (Arc-MBRT), which are compared to photon-only plans and MBRT plans with static electron beams (Static-MBRT) to assess the dosimetric suitability and delivery efficiency of the Arc-MBRT plans compared to the other treatments.

1.5.4 Part4

One of the challenges of the treatment planning of non-coplanar techniques is the prediction of infeasible beam directions due to collision between the gantry and patient or table. In the fourth part, a collision prediction tool for a C-arm linac is developed using Blender, a free and open-source computer graphics software. The collision prediction tool is validated by comparing collision predictions to manual checks for collision interlocks.

1.5.5 Part 5

In the fifth part, the TPP is further advanced with an H-DAO-based path determination strategy for non-isocentric DTRT plans. The TPP is used to create non-isocentric DTRT plans for two purposes: first, to automate the path creation of non-isocentric DTRT plans for craniospinal irradiation, and second, to exploit the additional collision-free space of an extended source-to-target distance for dosimetric improvement of DTRT plans.

2

A hybrid column generation and simulated annealing algorithm for direct aperture optimization

Silvan Mueller[1], Guyer Guyer[1], Terence Risse[1], Sefan Tessarini[1], Daniel M. Aebersold[1],
Marco F. M. Stampanoni[2], Michael K. Fix[1] and Peter Manser[1]

[1] Division of Medical Radiation Physics and Department of Radiation Oncology, Inselspital, Bern University Hospital, and University of Bern, Switzerland
[2] Institute for Biomedical Engineering, ETH Zürich and PSI, Villigen, Switzerland

Published in
Physics in Medicine and Biology
2022, Vol. 67, No. 7, 075003
DOI: 10.1088/1361-6560/ac58db

2.1 Preface

In this first part, a treatment planning process for intensity modulated radiotherapy and mixed beam radiotherapy with static gantry angles using a step-and-shoot technique is developed. A hybrid column generation and simulated annealing direct aperture optimization is used to simultaneously optimize the intensity of photon and electron beams.

Contribution: While S. Müller did most of the work for this study, G. Guyer wrote part of the code for the beamlet dose calculation and transmission calculation and did extensive code review. G. Guyer provided feedback during the preparation of the manuscript several times.

2.2 Abstract

The purpose of this work was to develop a hybrid column generation (CG) and simulated annealing (SA) algorithm for direct aperture optimization (H-DAO) and to show its effectiveness in generating high quality treatment plans for intensity modulated radiation therapy (IMRT) and mixed photon-electron beam radiotherapy (MBRT).

The H-DAO overcomes limitations of the CG-DAO with two features improving aperture selection (branch-feature) and enabling aperture shape changes during optimization (SA feature). The H-DAO algorithm iteratively adds apertures to the plan. At each iteration, a branch is created for each field provided. First, each branch determines the most promising aperture of its assigned field and adds it to a copy of the current apertures. Afterwards, the apertures of each branch undergo an MU-weight optimization followed by an SA-based simultaneous shape and MU-weight optimization and a second MU-weight optimization. The next H-DAO iteration continues the branch with the lowest objective function value. IMRT and MBRT treatment plans for an academic, a brain and a head and neck case generated using the CG-DAO and H-DAO were compared.

For every investigated case and both IMRT and MBRT, the H-DAO leads to a faster convergence of the objective function value with number of apertures compared to the CG-DAO. In particular, the H-DAO needs on average half the apertures to reach the same objective function value as the CG-DAO for a specifically selected number of apertures. The average aperture areas are 27% smaller for H-DAO than for CG-DAO leading to a slightly larger discrepancy between optimized and final dose. However, a dosimetric benefit remains.

The H-DAO was successfully developed and applied to IMRT and MBRT. The faster convergence with number of apertures of the H-DAO compared to the CG-DAO allows to select a better compromise between plan quality and number of apertures.

2.3 Introduction

Treatment plans are generated and delivered in photon intensity modulated radiation therapy (IMRT) (Bortfeld, 2006) to achieve a highly conformal dose distribution to the target volume. This was enabled through the introduction of the multileaf collimator (MLC) (Convery and Rosenbloom, 1992), which collimates photon beams delivered from static beam directions in a step-and-shoot or dynamic movement manner such as sliding-window. Optimization algorithms were introduced to determine a suitable intensity modulation of the photon fields, which are discretized into beamlets (Webb, 1989; Bortfeld, 2006). These algorithms are classified in two categories: fluence map optimization (FMO) and direct aperture optimization (DAO). FMO optimizes the non-negative and independent weights of the beamlets in terms of monitor units (MUs) of each provided treatment field simultaneously. FMO is a large-scale convex optimization problem that can be efficiently solved using deterministic algorithms such as gradient descent. However, FMO results only in a non-deliverable fluence map for each field. Thus, a post-processing leaf-sequencing step is added translating the fluence maps to deliverable plans, resulting in a degraded plan quality (Mohan et al., 2000). In contrast, DAO directly considers the machine constraints of the MLC such as leaf movement constraints or minimal gaps. Thus, DAO deals with MU weighted mechanically deliverable apertures that describe which beamlets are covered by the MLC leaves. However, this leads to a difficult large-scale non-convex optimization problem which cannot be solved efficiently. Several algorithms were developed for DAO:

- Column generation based DAO (CG-DAO) (Romeijn et al., 2005; Preciado-Walters et al., 2006; Men et al., 2007; Carlsson, 2008; Renaud, Serban, and Seuntjens, 2017) iteratively adds the most promising aperture shape to the aperture pool of the plan using a pricing mechanism. The most promising aperture shape of all the provided fields is the one with the steepest gradient on the objective function, called price. After each aperture addition, the aperture MU weights are optimized (restricted master problem) using a deterministic algorithm. This approach is computationally efficient and has full freedom in the number of apertures per field. On the other side, the aperture shapes stay fixed as soon as appended to the aperture pool. Moreover, the selection of the most promising aperture is only based on the objective function gradient, i.e. it is unknown by how much the objective function value can be decreased by increasing its MU weight and re-adjusting the MU weights of the already added apertures. Thus, a suboptimal aperture selection is given, especially if many fields are provided like this is the case for 4Pi (Dong et al., 2013) or mixed beam radiotherapy (MBRT) (Palma et al., 2012; Renaud, Serban, and Seuntjens, 2017; Mueller et al., 2017).

- Stochastic DAO approaches such as simulated annealing (SA-DAO) (Sheppard et al., 2002), quantum tunnel annealing (Pakela et al., 2020) and genetic algorithms (Li, Yao, and Yao, 2003) randomly change the shapes and MU weights of apertures according to a scheme. In contrast to the CG-DAO algorithm, the number of apertures per field is pre-defined. Moreover, these approaches start with arbitrary aperture shapes such as conformal to the target or closed. Hence, numerous optimization steps are needed leading to a long computation time. On the other side, these algorithms have basically the ability to overcome local minima, because they also accept changes on the apertures leading to a worse objective function value with a certain probability. In comparison to the CG-DAO, another benefit is the ability to simultaneously optimize the shapes and MU weights of the apertures.

- Local gradient-based leaf refinement approaches such as the direct machine parameter optimization (DMPO) (Hardemark et al., 2003) and aperture shape optimization (ASO) (Cassioli and Unkelbach, 2012) typically start with an initial aperture set generated through CG-DAO (Carlsson, 2008; Cassioli and Unkelbach, 2012) or FMO and leaf-sequencing. Subsequently, they refine the leaf positions locally within the current beamlet using a linear function of the leaf positions approximating the dose distribution. They are able to simultaneously optimize shapes and MU weights of the apertures. However, they can end up in a local minimum making them dependent on the starting conditions.

- Segmentation of fluence maps can also be directly integrated into FMO as shown by Nguyen et al., 2017 using a multiphase piecewise constant Mumford-Shah formulation. Thus, the MLC constraints are directly included in the FMO formulation making it a DAO. Potential limitations of the published approach are that it is designed to generate only non-overlapping apertures and that the maximal number of allowed apertures per field is pre-defined.

In this work, a novel algorithm called hybrid DAO (H-DAO) is developed to solve the DAO problem. The H-DAO follows the basic idea of the CG-DAO of adding apertures iteratively, but the H-DAO overcomes limitations of the CG-DAO with the following newly implemented features:

- The branch-feature exploring the most promising aperture of each field in a separate branch to identify the aperture improving the objective function value the most.
- The SA-feature applying the simulated annealing algorithm to enable continuous optimization of the aperture shapes and to enable continuous leaf positions not limited by the discrete beamlet grid resolution.

The H-DAO is applied to IMRT and MBRT. We demonstrate the effectiveness of the H-DAO in generating treatment plans of high quality compared to the baseline of a CG-DAO.

2.4 Methods

2.4.1 Treatment planning process

An implementation of the H-DAO is embedded in the treatment planning process (TPP) as illustrated in fig. 2.1 (top). The TPP considered here is used to create treatment plans for IMRT (photon apertures only) and MBRT (photon and electron apertures) deliverable in a step-and-shoot manner on a TrueBeam (Varian, a Siemens Healthineers Company, Germany) treatment unit equipped with a Millennium MLC 120 (Varian, a Siemens Healthineers Company, Germany) to collimate photon and electron beams. However, the whole TPP could also be conceptually applied to other MLC based and photon-electron beam supporting treatment units. In the first subprocess, the CT image set is imported into a research version of the Eclipse treatment planning system (TPS) 15.6 (Varian, a Siemens Healthineers Company, Germany) and the contouring of the PTV, organs at risk (OARs) and normal tissue (body without PTV) is done using Eclipse.

The second subprocess consists of the manual setup of photon and optionally electron radiation fields within Eclipse. The definition of a field consists of the gantry, table and collimator angles, isocenter location, particle type, beam energy, secondary collimator jaw positions and the beamlet grid size. For photon beams, the secondary collimator jaw positions are equivalent to the maximum rectangular beamlet grid size, while for the electron beams, the secondary collimator jaws are always set to 15 x 35 cm^2 due to the electron beam model utilized (Henzen et al., 2014a). These field definitions stay fixed, but one can setup as many fields as wanted with different field aspects (e.g. for each electron beam direction, all possible beam energies can be setup to give the H-DAO more freedom in selecting the energy of apertures to be added).

To perform Monte Carlo (MC) beamlet dose calculations of the photon and electron fields, the Eclipse interfaced Swiss Monte Carlo Plan (SMCP) (Fix et al., 2007) is used. The source of the beamlet dose calculations are pre-simulated phase-spaces located at the treatment head exit plane. The dose distributions of photon and electron beamlets are calculated using Voxel Monte Carlo (VMC++) (Kawrakow and Fippel, 2000) and Macro Monte Carlo (MMC) (Neuenschwander and Born, 1992; Neuenschwander, Mackie, and Reckwerdt, 1995; Fix et al., 2013), respectively. Both MC algorithms are embedded within the SMCP framework. The beamlet size is 0.5 x 0.5 cm^2 or 0.5 x 1.0 cm^2 depending whether the beamlet belongs to an inner 0.5 cm wide leaf pair or outer thicker 1 cm wide leaf pair. After beamlet dose calculation, the plan optimization is performed using the H-DAO as described in detail in the next section 2.4.2.

Next, a final dose calculation of the optimized apertures considering the impact of the MLC is performed within the SMCP framework. Source of the dose calculation for photon beams is a pre-simulated phase-space located on a plane above the secondary collimator jaws. For photon beams, VMC++ is used to simulate the patient-specific part of the treatment head including secondary collimator jaws and MLC as well as the dose calculation in the patient. For electron beams, the source is a multiple source beam model, called ebm70 (Henzen et al., 2014a), consisting of a foil and a jaw source. The dose calculation in the patient is performed using the MMC. All the utilized beam sources and dose calculation algorithms are validated against measurements of photon (Magaddino et al., 2011; Mueller et al., 2017) and electron beams (Henzen et al., 2014a; Mueller et al., 2018a; Mueller et al., 2017).

After final dose calculation, the MU weights of the apertures are re-optimized using a limited-memory Broyden-Fletcher-Goldfarb-Shanno (L-BFGS) algorithm to reduce the degradation from optimized to final dose distribution, called optimization convergence error (OCE) (Jeraj, Keall, and Siebers, 2002).

2.4.2 Plan optimization

The goal of the optimization is to minimize the objective function F, which quadratically penalizes deviations of the plan's dose distribution to N_{DV} upper and lower dose-volume objectives (Wu and Mohan, 2000) $f_{r,DV}$ weighted by $p_{r,DV}$, N_{gEUD} generalized equivalent uniform dose (gEUD) objectives (Niemierko, 1997) $f_{s,gEUD}$ weighted by $p_{s,gEUD}$ and N_{NT} normal tissue objectives (Varian Medical Systems, 2017) $f_{q,NT}$ weighted by $p_{q,NT}$:

$$F(D_i) = \sum_{r=1}^{N_{DV}} p_{r,DV} \cdot f_{r,DV}(D_i) + \sum_{s=1}^{N_{gEUD}} p_{s,gEUD} \cdot f_{s,gEUD}(D_i) + \sum_{q=1}^{N_{NT}} p_{q,NT} \cdot f_{q,NT}(D_i) \tag{2.1}$$

$$f_{r,DV}(D_i) = \frac{1}{V_{str,r}} \sum_{i=1}^{M_r} v_{i,r} \cdot \Theta(a_r \cdot (D_i - D_r)) \cdot \Theta(a_r \cdot (D(V_r) - D_i)) \cdot (D_i - D_r)^2 \tag{2.2}$$

$$f_{s,gEUD}(D_i) = \Theta(gEUD(t,s) - gEUD_s) \cdot (gEUD(t,s) - gEUD_s)^2 \tag{2.3}$$

$$f_{q,NT}(D_i) = \frac{1}{V_{str,q}} \sum_{i=1}^{M_q} v_{i,q} \cdot \Theta(D_i - D_{i,q}) \cdot (D_i - D_{i,q})^2 \tag{2.4}$$

$$gEUD(t,s) = \left(\frac{1}{V_{str,s}} \cdot \sum_{i=1}^{M_s} v_{i,s} \cdot (D_i)^t \right)^{1/t} \tag{2.5}$$

$$D_{i,q} = \begin{cases} d_0 e^{-b(x_i - x_{start})} + d_\infty (1 - e^{-b(x_i - x_{start})}) & \text{, if } x_i \geq x_{start} \\ d_0 & \text{, otherwise} \end{cases} \tag{2.6}$$

where D_i is the dose of the plan to voxel i, $v_{i,r}$, $v_{i,s}$ and $v_{i,q} \in [0,1]$ are the fraction of voxel i overlapping with the considered structure, $V_{str,r}$, $V_{str,s}$ and $V_{str,q}$ are the summed voxel fractions of the voxels overlapping with the considered structure, M_r, M_s and M_q are the number of voxels of the considered structure, Θ is the Heaviside function, a_r is equal to 1 and -1 for upper and lower dose-volume objectives, respectively, D_r is the objected dose and $D(V_r)$ is the dose received by at least the tolerated volume V_r of the considered structure for dose-volume objective r, $gEUD(t,s)$ is the $gEUD$ value with tissue-specific factor t, $gEUD_s$ is the objected $gEUD$ value, $D_{i,q}$ is the objected normal tissue dose to voxel i which is a function of the nearest distance x_i of voxel i to the target, d_0 and d_∞ are the start and end dose parameters, respectively, x_{start} is the start distance of the fall-off and b is the fall-off factor.

Plan dose D_i can be formulated as

$$D_i = \sum_{k \in K} A_{ki} \cdot w_k \tag{2.7}$$

where A_{ki} is the dose delivered to voxel i with unit MU and w_k is the MU weight of aperture k. K is the set of all deliverable apertures of the provided fields. For clarification, deliverable does not make any statement about the accuracy of the delivered dose. In this work, deliverable just means mechanically deliverable by the MLC. A_{ki} can be further defined as

$$A_{ki} = \sum_{j \in F_k} B_{ji} \cdot t_j(G_{j,L}, G_{j,R}) \tag{2.8}$$

where F_k is the set of all beamlets belonging to the field of aperture k and B_{ji} is the delivered dose to voxel i per unit MU of beamlet j. B_{ji} is calculated by the subprocess 3 of the TPP as described in the previous section 2.4.1. $t_j(G_{j,L}, G_{j,R}) \in [0\%, 100\%]$ is the transmission factor for beamlet j given by

$$\begin{aligned} & t_j(G_{j,L}, G_{j,R}) \\ = & \begin{cases} t_{Open} & \text{, if } G_{j,L} \geq 1 \text{ and } G_{j,R} \geq 1 \\ t_{Open}(G_{j,L} + G_{j,R} - 1) + t_{Tip}(2 - G_{j,L} - G_{j,R}) & \text{, if } 0 < G_{j,L} < 1 \text{ and } 0 < G_{j,R} < 1 \\ t_{Open} G_{j,L} + t_{Tip}(1 - G_{j,L}) & \text{, if } 0 \leq G_{j,L} < 1 \text{ and } G_{j,R} > 1 \\ t_{Open} G_{j,R} + t_{Tip}(1 - G_{j,R}) & \text{, if } 0 \leq G_{j,R} < 1 \text{ and } G_{j,L} > 1 \\ t_{Tip}(G_{j,L} + 1) - t_{MLC} G_{j,L} & \text{, if } -1 < G_{j,L} < 0 \\ t_{Tip}(G_{j,R} + 1) - t_{MLC} G_{j,R} & \text{, if } -1 < G_{j,R} < 0 \\ t_{MLC} & \text{, else} \end{cases} \end{aligned} \tag{2.9}$$

where $G_{j,L} = C_{j,L} - P_{k,j,L}$ and $G_{j,L} = C_{j,R} - P_{k,j,R}$. $C_{j,L}$ and $C_{j,R}$ are the position of beamlet j counted from the left and right beamlet grid border, respectively, and $P_{k,j,L}$ and $P_{k,j,R}$ are the left and right leaf position of the leaf pair in aperture k in the line of beamlet j. t_{Open} is 100%, t_{Tip} is 12.9% (photon beam) and 0% (electron beam) and t_{MLC} is 1.3% (photon beam) and 0% (electron beam). These transmission factors of photon beams are an empirically determined model to approximate the transmission through the MLC (t_{MLC}) and increased transmission through the leaf tip (t_{Tip}). This model aims to reduce the dose prediction error (DPE) and therefore, the OCE (Jeraj, Keall, and Siebers, 2002; Bergman et al., 2006; Men et al., 2007; Mueller et al., 2017). In other words, the discrepancy between optimized and final dose distribution is reduced, because the transmission of photon beams through the MLC is already considered during optimization. Beside of that, the transmission model defined above also allows for leaf positions between beamlet borders. The calculation of $t_j(G_{j,L}, G_{j,R})$ is illustrated in section 2.4.2.

Note that eq. (2.7) must be understood as a sum over all possible deliverable apertures. Apertures which are part of the aperture pool have a weight $w_k > 0$ and all other apertures have a weight of 0. The H-DAO algorithm starts with an empty aperture pool, iteratively adds apertures to the pool and optimizes the shapes and MU weights of the apertures at each iteration to minimize F given in eq. (2.1). Figure 2.1 (middle) illustrates the workflow of the H-DAO algorithm. In the following the details of one iteration are described. One iteration creates as many branches as there are fields provided (branch-feature). The subprocess of these branches are performed in parallel in multiple computer threads. For the current work we used an AMD Epyc2 CPU featuring 2x64 CPU cores to have enough cores such that no thread needs to share a CPU core with another thread. A specific optimization example of the H-DAO algorithm workflow illustrating the concept of parallel branches is shown in fig. 2.1 (bottom). As visible there, a branch consists of four sequential subprocesses. First, the pricing is performed to find the most promising aperture shape of the field considered in this branch. This determination of the most promising aperture per field is the same as for the CG-DAO (Romeijn et al., 2005; Men et al., 2007). The most promising aperture is a set of beamlets that can be translated to a deliverable aperture and for which the summed gradient components of the beamlets not covered by the MLC on the objective function, called price, is minimal. The optimization problem to find the most promising aperture of a field can be formulated by

$$\min_{k \in K} \left(\frac{\partial F(D_i)}{\partial w_k} \right) \tag{2.10}$$

For derivation and description of strategies to solve this problem, the work of Romeijn et al., 2005 and Men et al., 2007 is referenced here.

After determination of the most promising aperture, it is added to a copy of the current aperture pool. It follows an MU weight optimization of the apertures using a projected L-BFGS two loop recursion (Nocedal and Wright, 1999; Bangert, 2011), which is a quasi-Newton algorithm approximating the product of the inverse Hessian and the gradient. The length of the L-BFGS history to store objective function values and gradient values is set to 4. The algorithm is combined with a line search to find an appropriate step length satisfying Armijo's Rule. If any aperture MU weight is below 0 during line search, the MU weight is projected to 0. The L-BFGS terminates if the objective function value is not lowered more than 0.01% in three consecutive iterations.

The next subprocess is the SA-feature, which simultaneously optimizes shapes and weights of the apertures in the pool including the recently added aperture according to an SA cooling schedule. The SA-feature runs maximally for a total of 5000 iterations. It stops earlier, if the objective function value did not decrease more than 0.1% for 250 consecutive iterations. At every iteration, an aperture of the pool is selected randomly for which its shape or MU weight is changed with a probability of P_S or $(1 - P_S)$, respectively. The change is accepted if the objective function value is decreased or otherwise with a probability of

$$P = 2 \cdot P_0 \cdot \frac{1}{1 + e^{\frac{\log\left(\frac{n_S + n_W}{N_A} + 1\right)}{T_P}}}, \tag{2.11}$$

where T_P is the cooling rate, P_0 is the initial value of P, N_A is the number of apertures and n_S and n_W are the number of previous total accepted shape and MU weight changes, respectively. If the shape of the aperture is aimed to be changed, a leaf is randomly selected, and its position is randomly changed according to a normal distribution around the current leaf position and a width of

$$\sigma_S = 1 + (\sigma_{S0} - 1) \cdot e^{-\frac{\log\left(\frac{n_S}{N_L} + 1\right)}{T_S}} \tag{2.12}$$

in units of number of beamlets. T_S is the cooling rate and σ_{S0} is the initial width of the normal distribution and N_L is the total number of leaf pairs of all apertures in the pool. In case of a weight change, the weight is changed according to a normal distribution around the current aperture weight w_k and a width of

$$\sigma_W = 0.01 + (\sigma_{W0} - 0.01) \cdot e^{-\frac{\log\left(\frac{n_W}{N_A} + 1\right)}{T_W}} \tag{2.13}$$

in relative units of w_k. T_W is the cooling rate and σ_{W0} is the initial width of the normal distribution. Following parameter values are used in this work: $P_S = 90\%$, $T_P = 1$, $P_0 = 3.5\%$, $T_S = 2$, $\sigma_{S0} = 0.3$, $T_W = 1$, $\sigma_{W0} = 0.1$. Note that σ_{S0} is only 0.3 beamlets wide. Thus, most of the shape changes are small such that the SA-feature follows its purpose of a leaf refinement.

When the SA-feature terminates, the MU weights of the apertures are again optimized using the same L-BFGS implementation. Due to performing an MU weight optimization before and after performing the SA-feature, the SA-feature starts with a better initial solution and the need for more iterations of the SA is also smaller. Note that the MU optimization is convex and involves many optimization variables less (i.e. leaf positions) than the whole DAO optimization problem. Thus, it can be solved very efficiently with the L-BFGS.

When all branches are performed, the objective function value is evaluated for each branch and the aperture pool for the next iteration of the H-DAO is the one with the lowest objective function value among all branches. These H-DAO iterations are repeated until the desired number of apertures in the aperture pool is reached.

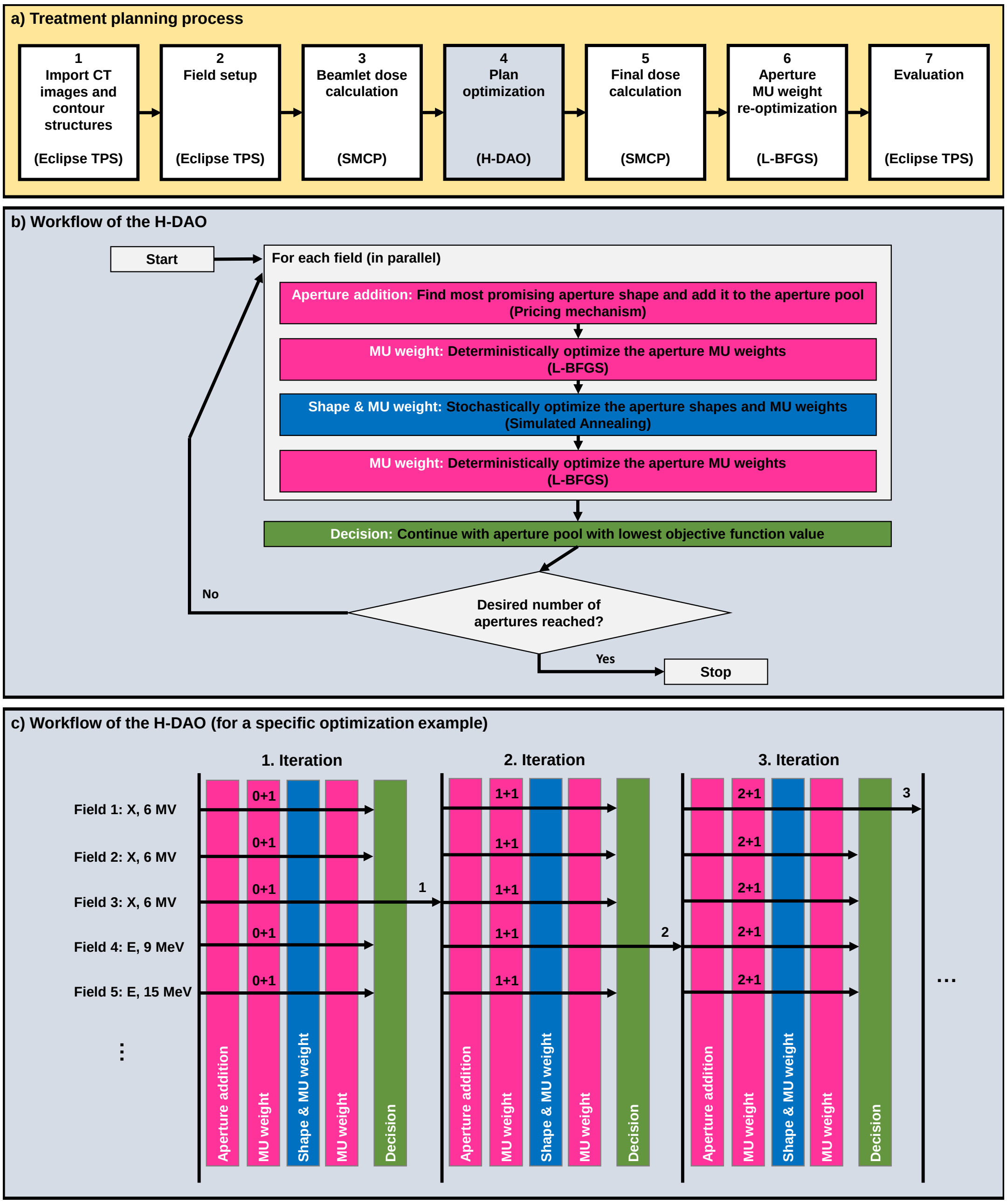

FIGURE 2.1: a): TPP in which the H-DAO is embedded. b): General workflow of the H-DAO. While the processes with magenta color are part of the CG-DAO algorithm, the processes with blue and green color are extensions described in this work. c): Again, the workflow of the H-DAO though presented for a specific optimization example to better illustrate the parallel execution. Each arrow represents a branch run in a separate computer thread. The numbers stand for the number of apertures currently present in the aperture pool.

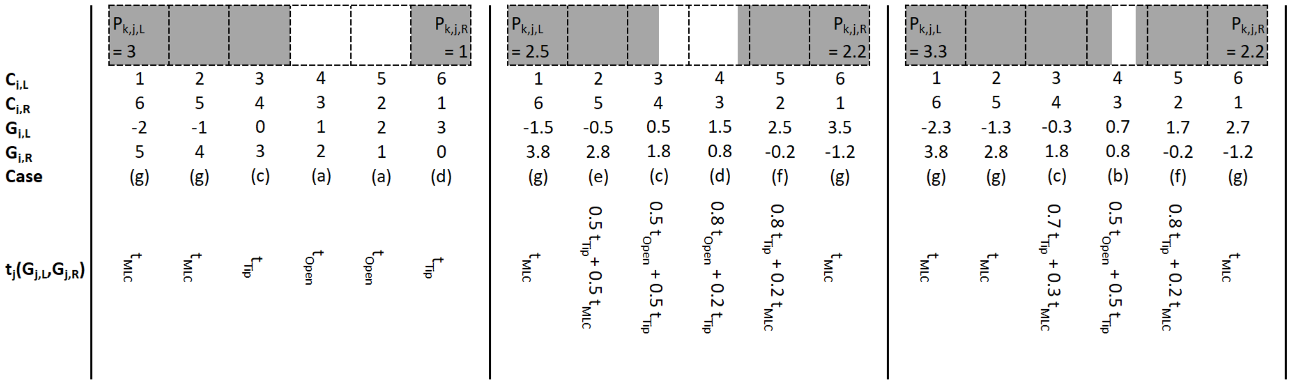

$C_{i,L}$	1	2	3	4	5	6	1	2	3	4	5	6	1	2	3	4	5	6
$C_{i,R}$	6	5	4	3	2	1	6	5	4	3	2	1	6	5	4	3	2	1
$G_{i,L}$	-2	-1	0	1	2	3	-1.5	-0.5	0.5	1.5	2.5	3.5	-2.3	-1.3	-0.3	0.7	1.7	2.7
$G_{i,R}$	5	4	3	2	1	0	3.8	2.8	1.8	0.8	-0.2	-1.2	3.8	2.8	1.8	0.8	-0.2	-1.2
Case	(g)	(g)	(c)	(a)	(a)	(d)	(g)	(e)	(c)	(d)	(f)	(g)	(g)	(g)	(c)	(b)	(f)	(g)
$t_j(G_{j,L},G_{j,R})$	t_{MLC}	t_{MLC}	t_{Tip}	t_{Open}	t_{Open}	t_{Tip}	t_{MLC}	$0.5t_{Tip}+0.5t_{MLC}$	$0.5t_{Open}+0.5t_{Tip}$	$0.8t_{Open}+0.2t_{Tip}$	$0.8t_{Tip}+0.2t_{MLC}$	t_{MLC}	t_{MLC}	t_{MLC}	$0.7t_{Tip}+0.3t_{MLC}$	$0.5t_{Open}+0.5t_{Tip}$	$0.8t_{Tip}+0.2t_{MLC}$	t_{MLC}

FIGURE 2.2: Illustration of the transmission calculation for three example leaf pairs (left, center and right). The gray areas are the areas blocked by the leaves and the dashed grid represents the beamlet grid seen from beams eye view. The cases (a) (g) are related to eq. (2.9).

2.4.3 Academic and clinical cases

In the computational study of this work, treatment plans of the treatment techniques IMRT and MBRT are generated for an academic case (Mueller et al., 2017), a brain case and a head and neck case. Motivation behind the selection of these three cases and the corresponding field setup illustrated in fig. 2.3 is to have an increasing complexity in the geometrical treatment situation and number of fields. The collimator rotation of all the fields is 0°, except the photon fields for the two clinical cases, which have a collimator rotation such that the maximal field width parallel to leaf movement direction is minimized. Reason for this is to get a field width smaller than 15 cm, which is the maximal leaf separation distance between leaves of the same MLC bank.

The academic case is a cylindric homogeneous water phantom with a radius of 10 cm to be treated with a prescribed median dose of 50 Gy to the PTV in 25 fractions. A superficially located PTV including a deep-seated part and two OARs, OAR-lateral and OAR-distal, are contoured. These three structures are extended perpendicular to the transversal plane by 7.4 cm. The first clinical case is a glioblastoma brain case to be treated with a prescribed median dose of 60 Gy to the PTV in 30 fractions. The second clinical case is an oropharynx head and neck case to be treated with a prescribed D95% of 50 Gy to the PTV in 25 fractions. For each case, every optimization used the same dose objectives listed in table 2.1.

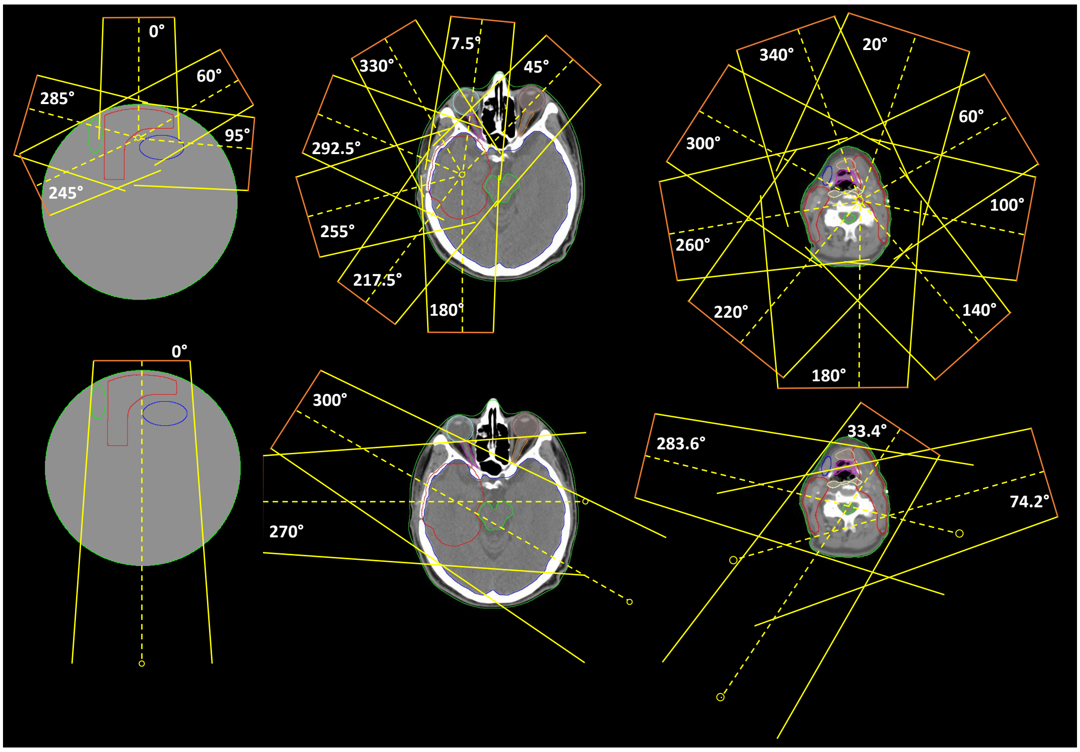

Figure 2.3: Photon (top row) and electron (bottom row) field setup for an academic case (left column), a brain case (center column) and a head and neck case (right column) used to create IMRT and MBRT treatment plans. Following structures are visible on the transversal views: PTV (red), OAR-distal (blue) and OAR-lateral (green) for the academic case, PTV (red), brainstem (green), brain (blue), left (cyan) and right (brown) eyes and left (magenta) and right (orange) optic nerves for the brain case, PTV (red), spinal cord (green), right submandibular gland (blue), oral cavity (light brown), larynx (magenta) and pharyngeal constrictors (light yellow) for the head and neck case.

Table 2.1: Objectives used for all the optimizations performed in the computational study. The parameters for the normal-tissue objective have the same values for every case: Start dose d_0 is 95%, end dose d_∞ is 10%, start distance x_{start} of the fall-off is 0.5 cm and fall-off factor b is 0.15. Note that $gEUD(t = 1)$ is equivalent to the mean dose.

Case	Structure	Objective type	Priority factor	Dose (%)	Volume (%)
Academic	PTV	Upper dose-volume	700	101	0
		Lower dose-volume	700	99	100
	OAR-distal	gEUD(t=1)	20	15	-
	OAR-lateral	gEUD(t=1)	20	15	-
	Normal tissue	Upper dose-volume	700	100	0
		Normal-tissue objective	50	See caption	-
Brain	PTV	Upper dose-volume	700	101	0
		Lower dose-volume	700	99	100
	Ipsilateral eye	Upper dose-volume	20	5	0
	Contralateral eye	Upper dose-volume	20	0	0
	Ipsilateral lens	Upper dose-volume	20	0	0
	Contralateral lens	Upper dose-volume	20	0	0
	Ipsilateral optical nerve	Upper dose-volume	20	40	0
	Contralateral optical nerve	Upper dose-volume	20	0	0
	Chiasma	Upper dose-volume	20	35	0
	Brainstem	Upper dose-volume	100	65	0
	Brain	gEUD(t=1)	20	18	-
	Normal tissue	Upper dose-volume	40 000	98	0
		Normal-tissue objective	20	See caption	-
Head and neck	PTV	Upper dose-volume	5000	105	0
		Lower dose-volume	5000	100	100
		Lower dose-volume	5000	95	100
		Lower dose-volume	5000	100	95
	Brainstem	Upper dose-volume	20	20	0
	Spinal cord	Upper dose-volume	20	35	0
	Mandibula	Upper dose-volume	20	100	0
	Oral cavity	gEUD(t=1)	20	55	-
	Pharyngeal constrictors	gEUD(t=1)	20	35	-
	Larynx	gEUD(t=1)	20	45	-
	Esophagus	gEUD(t=1)	20	25	-
	Left Parotid gland	gEUD(t=1)	20	55	-
	Right Parotid gland	gEUD(t=1)	20	0	-
	Right submandibular gland	gEUD(t=1)	20	7	-
	Lips	gEUD(t=1)	20	17	-
	Normal tissue	Upper dose-volume	50 000	98	0
		Normal-tissue objective	30	See caption	-

2.4.4 Computational study

A computational study is performed to analyze the influence of the two features added to the CG-DAO algorithm, i.e. the branch- and SA-features, on the following optimization results and properties.

1. Convergence behavior with number of apertures

2. Final dose distribution
3. Convergence error (OCE)
4. Plan complexity
5. Field contributions
6. Computational performance
7. Statistical uncertainty

In this computational study, treatment plans of the treatment techniques IMRT and MBRT are generated for the introduced academic and clinical cases using the optimization algorithms listed in Table 2. We investigated both IMRT and MBRT to find out if the complexity of the field setup plays any role in the algorithm performance. Due to the choice of two particle types and multiple beam energies, the complexity of the field setup for MBRT can be judged substantially higher. In particular, the fields provided to IMRT are a subset of the fields provided to MBRT, because the same photon fields are provided to both IMRT and MBRT.

Table 2.2: The DAO algorithms compared in the computational study. The columns “Branch-feature” and “SA-feature” indicate whether the listed algorithms utilize these features.

Name	Branch-feature	SA-feature
CG-DAO	No	No
CG-DAO_Branch	Yes	No
CG-DAO_SA	No	Yes
H-DAO	Yes	Yes

To study the convergence with number of apertures of the investigated DAO algorithms, the objective function value after plan optimization (subprocess 4 in the TPP) is collected as a function of the apertures for up to 200 apertures assuming that more than 200 apertures would only lead to marginal improvements in plan quality. Furthermore, an FMO is performed with the L-BFGS using the same beamlets without any constraints on smoothness of the fluence map. This FMO optimized plan is used as an ideal benchmark. This is done for IMRT and MBRT for all three cases.

To also see the differences between the different DAO algorithms in the dosimetric space for a specific number of apertures, the TPP is further performed to the end utilizing 50 (academic case), 100 (brain case) and 150 (head and neck case) apertures for all DAO algorithms investigated and the final dose distribution is evaluated by dose-volume-histograms (DVHs) and following dosimetric quantities: PTV dose homogeneity index, mean dose to normal tissue D_{mean}^{NT}, average mean dose to parallel OARs $\hat{D}_{mean}$ and average $D_{2\%}$ to serial OARs $\hat{D}_{2\%}$. The OARs with a gEUD(t=1) objective are considered as parallel and the others as serial for the scope of this study. The PTV dose homogeneity index HI is defined as

$$HI = \frac{D_{2\%} - D_{98\%}}{D_p} \tag{2.14}$$

where D_p is the prescribed dose and $D_{2\%}$ and $D_{98\%}$ the dose receiving at least 2% and 98% of the PTV volume.

Using the results of these final re-optimized plans, OCE, plan complexity described in numbers of MU and average aperture area $\hat{A}$, field contributions (only academic case) and the computation time are also evaluated. The OCE is calculated as

$$OCE(\%) = \frac{F_F - F_O}{F_O} \times 100\% \tag{2.15}$$

where F_O is the objective function value after optimization (subprocess 4 of the TPP) and F_F is the objective function value after aperture MU weight re-optimization of the final dose distributions (subprocess 6 of the TPP). Connected to the investigation of the OCE, it is evaluated how a potential improvement in terms of objective function value after optimization of the extended DAO algorithms over the CG-DAO evolves after the aperture MU weight re-optimization. Therefore, the improvement after optimization is calculated by

$$\Delta F_o = \frac{F_O - F_O^{CG-DAO}}{F_O^{CG-DAO}} \cdot 100\% \tag{2.16}$$

and after aperture MU weight re-optimization by

$$\Delta F_F = \frac{F_F - F_F^{CG-DAO}}{F_F^{CG-DAO}} \cdot 100\% \tag{2.17}$$

where F_O^{CG-DAO} and F_F^{CG-DAO} are the objective function value of the reference CG-DAO after optimization and after aperture MU weight re-optimization, respectively. F_O and F_F are the analogous values for the DAO algorithm for which ΔF_O and ΔF_F are calculated for.

A field contribution is defined as the fraction of the PTV mean dose delivered by all the apertures belonging to the corresponding field. In case of MBRT, also photon and electron contributions are analyzed, which is the sum of all photon and electron field contributions, respectively.

To study the statistical uncertainty on the objective function value and the DVH of the DAO algorithms utilizing the SA-feature, the optimizations for the academic case utilizing 50 apertures are repeated 100 times using different seeds to initialize the random number generator.

2.5 Results

2.5.1 Convergence behavior with number of apertures

fig. 2.4 shows the convergence behavior of the objective function value as a function of the number of apertures for all the investigated DAO algorithms. It is visible that for each combination of case and treatment technique (IMRT or MBRT), the fastest convergence is always given by H-DAO, followed by CG-DAO_SA, CG-DAO_Branch and CG-DAO. All the DAO algorithms do not converge to the value given by the FMO, because all the DAO algorithms consider transmission through the MLC in case of photon apertures in contrast to FMO.

As the fields provided to IMRT is a subset of the fields provided to MBRT, it is reasonable to hypothesize that the objective function value for MBRT is at least as good as for IMRT. This is true for all the DAO algorithms for at least 10 apertures with the following two exceptions given for the head and neck case: CG-DAO and CG-DAO_SA.

It is noteworthy how many apertures the H-DAO could use less than the CG-DAO to reach the same objective function value, e.g. when the number of apertures of 50, 100 and 150 are selected for the CG-DAO for the academic, brain and head and neck case, respectively, the H-DAO needs on average 44.3% (IMRT) and 55.3% (MBRT) less apertures to reach the same objective function value as the CG-DAO.

2.5.2 Specific number of apertures

fig. 2.5 compares DVHs and table 2.3 dosimetric quantities of the IMRT and MBRT plans optimized with the different DAO algorithms after performing the whole TPP, i.e. including final dose calculation and MU weight re-optimization. For these plans with a specific number of apertures of 50 (academic case), 100 (brain case) and 150 (head and neck case), the DVHs confirm the finding of the convergence behavior analysis that H-DAO performed best followed by CG-DAO_SA, CG-DAO_Branch and CG-DAO. Only the PTV and selected OARs are shown in the DVH comparison for better visibility, but the mentioned finding

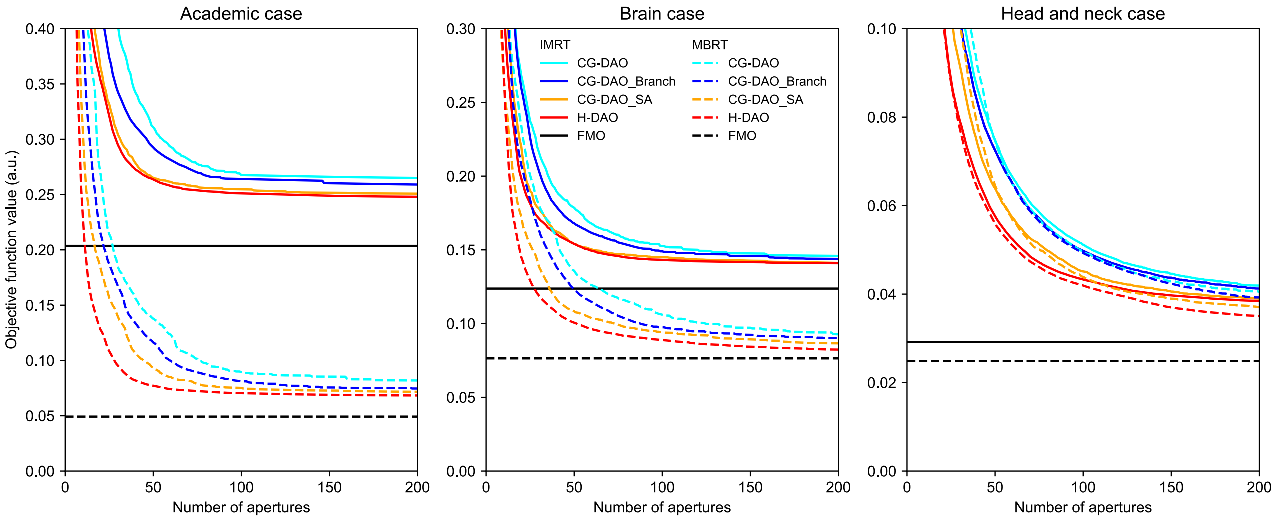

FIGURE 2.4: Convergence behavior of the objective function value as a function of the number of apertures created for all the investigated DAO algorithms applied to an academic case (left), a brain case (center) and a head and neck case (right). As the FMO does not generate apertures, its resulting objective function value is indicated as a constant line.

is in general also confirmed by the DVHs of other structures considered during optimization.

table 2.3 also shows that the OCE is higher for the DAO algorithms using the introduced branch- and SA-feature compared to the CG-DAO. However, the OCE is typically small enough such that the improvement after optimization ΔF_O over the CG-DAO is not vanished after aperture weight re-optimization. In case of H-DAO, the improvement ΔF_F is reduced by 15.4% (IMRT) and 14.5% (MBRT) compared to ΔF_O averaged over the three investigated academic and clinical cases.

Regarding plan complexity, table 2.3 shows that the branch- and SA-features lead to smaller apertures and connected to it, also to higher number of MUs. This is true for every investigated case and both IMRT and MBRT. In case of H-DAO, the aperture areas are 21.8% (IMRT) and 31.2% (MBRT) smaller and the MUs are 11.3% (IMRT) and 30.1% (MBRT) higher compared to CG-DAO averaged over the three investigated academic and clinical cases. Averaged over the three investigated academic and clinical cases, the CG-DAO_Branch required 19.3% (IMRT) and 27.4% (MBRT) longer computation time than the CG-DAO. Thus, the computation time is not substantially increased due to the use of a multi-core CPU being able to perform the branches in parallel. Again, averaged over the three cases and compared to the CG-DAO, CG-DAO_SA required 146.8% (IMRT) and 110.9% (MBRT) longer computation time and the H-DAO required 179.2% (IMRT) and 201.8% (MBRT) longer computation time.

fig. 2.6 compares the field contributions and photon and electron contribution for the plans generated by the different DAO algorithms utilizing 50 apertures for the academic case. In case of IMRT, the variations between the different DAO algorithms in field contributions are only a few percent. The field contributions also match well with those received by the FMO algorithm. For MBRT, the field contributions vary more between the different DAO algorithms, but they are still within 11% of the FMO field contributions. Overall, the field contributions of the H-DAO match closest with those of the FMO. The same is true for the photon and electron contribution.

The statistical uncertainty of the CG-DAO_SA and H-DAO due to the seed to initialize the random number generator for the SA-feature is demonstrated in fig. 2.7. The standard deviations of the objective function value distributions are 0.0045 (IMRT) and 0.0079 (MBRT) for CG-DAO_SA and 0.0033 (IMRT) and 0.0028 (MBRT) for H-DAO. Thus, the branch-feature included in the H-DAO seems to lead to a lower statistical uncertainty. The dosimetric differences between the worst and best optimization run out of 100 runs are demonstrated in fig. 2.7 for the H-DAO applied to IMRT.

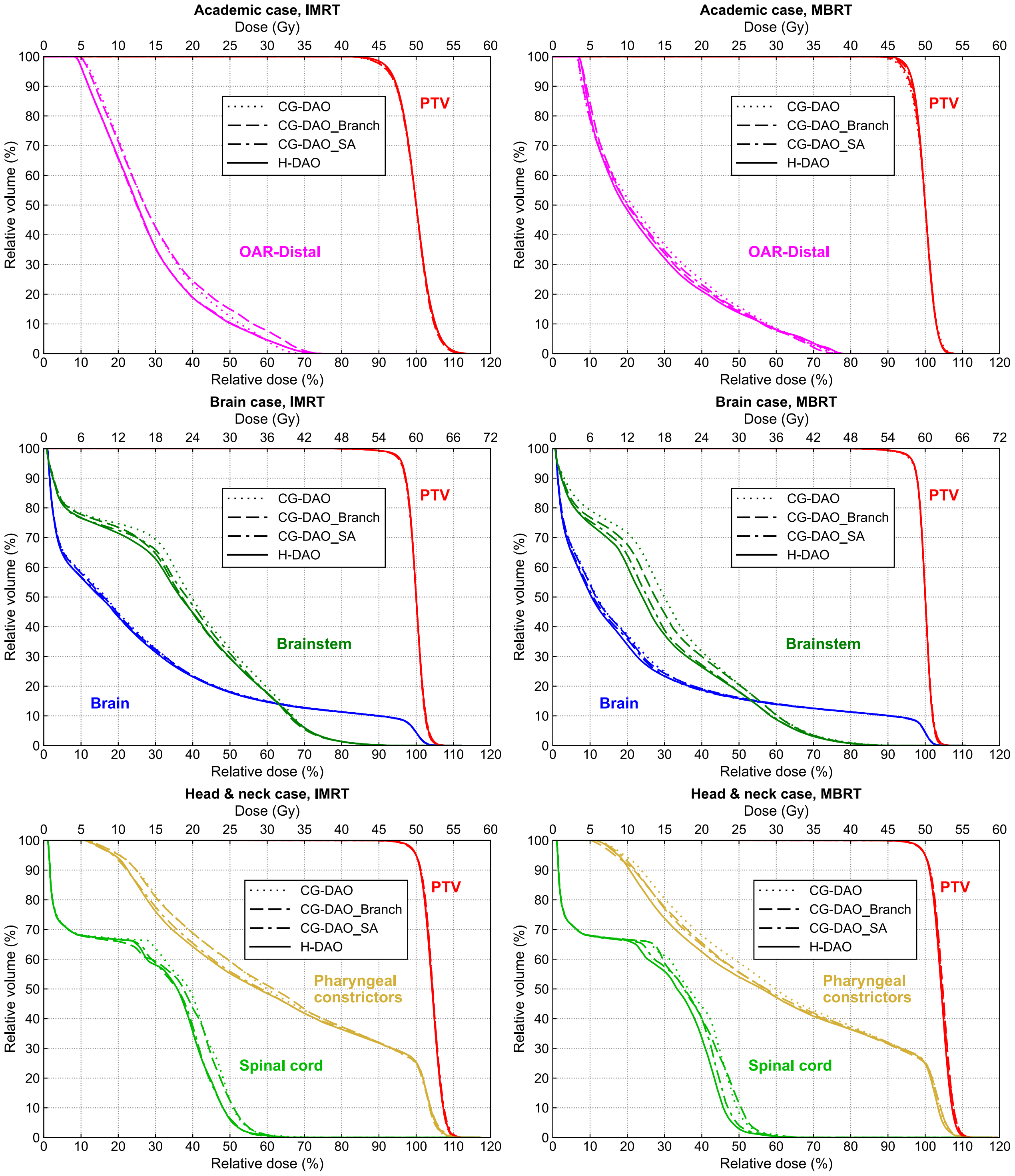

FIGURE 2.5: DVHs for the PTV and selected OARs of the IMRT (left column) and MBRT (right column) plans for the academic case with 50 apertures (top row), the brain case with 100 apertures (middle row) and the head and neck case with 150 apertures (bottom row) optimized by the different DAO algorithms.

Table 2.3: Dosimetric quantities and several plan characteristics are compared between the different DAO algorithms applied to IMRT and MBRT for the academic, brain and head and neck cases.

	IMRT				MBRT			
	H-DAO	CG-DAO_SA	CG-DAO_Branch	CG-DAO	H-DAO	CG-DAO_SA	CG-DAO_Branch	CG-DAO
Academic case								
HI	0.179	0.182	0.197	0.192	0.106	0.111	0.118	0.129
D^{NT}_{mean} (Gy)	3.0	3.0	3.1	3.0	2.7	2.6	2.9	2.7
$\hat{D}_{mean}$ (Gy)	14.1	14.1	15.0	15.1	12.0	12.8	13.0	13.7
Electron contr. (%)	-	-	-	-	55.5	60.9	48.1	61.1
OCE (%)	11.6	12.3	10.5	9.2	41.8	37.6	29.3	27.5
ΔF_O (%)	15.2	14.7	5.9	-	43.9	32.3	15.6	-
ΔF_F (%)	13.3	12.3	4.8	-	37.6	26.9	14.4	-
MUs	884.4	859.3	809.2	785.5	925.9	838.5	799.6	751.3
$\hat{A}$ (cm^2)	17.6	19.1	21.0	23.9	22.9	31.9	29.8	38.8
Computation time (s)	94.9	81.3	62.4	60.6	107.2	92.5	76.9	77.1
Brain case								
HI	0.119	0.126	0.122	0.123	0.102	0.105	0.102	0.109
D^{NT}_{mean} (Gy)	5.3	5.3	5.5	5.5	4.9	4.9	5.1	5.1
$\hat{D}_{mean}$ (Gy)	16.0	16.1	16.3	16.4	23.7	23.9	24.4	24.6
$\hat{D}_{2\%}$ (Gy)	16.9	16.9	17.2	17.4	16.1	15.8	16.1	16.4
Electron contr. (%)	-	-	-	-	53.8	50.3	48.9	45.9
OCE (%)	23.1	25.1	21.3	20.6	21.5	17.0	18.2	16.1
ΔF_O (%)	6.1	4.9	2.3	-	16.1	11.1	8.0	-
ΔF_F (%)	4.2	1.4	1.7	-	12.2	10.4	6.3	-
MUs	623.7	582.4	583.6	569.7	672.0	578.1	591.4	509.4
$\hat{A}$ (cm^2)	13.9	15.4	16.0	16.8	14.8	16.3	18.0	19.1
Computation time (s)	187.0	146.9	79.1	61.5	196.8	154.4	80.0	71.7
Head and neck case								
HI	0.107	0.111	0.109	0.112	0.107	0.113	0.115	0.113
D^{NT}_{mean} (Gy)	9.6	9.6	9.8	9.8	9.4	9.5	9.4	9.6
$\hat{D}_{mean}$ (Gy)	22.8	23.0	23.4	23.6	22.7	22.9	22.8	23.5
$\hat{D}_{2\%}$ (Gy)	33.2	33.2	33.6	33.7	31.7	32.3	32.8	33.2
Electron contr. (%)	-	-	-	-	14.7	12.0	6.9	11.0
OCE (%)	22.3	23.0	20.6	20.7	21.4	23.3	21.7	20.8
ΔF_O (%)	11.0	9.0	2.0	-	13.8	9.1	1.3	-
ΔF_F (%)	9.8	7.3	2.1	-	13.3	7.2	0.5	-
MUs	682.2	676.0	643.4	609.3	669.0	572.5	548.1	495.0
$\hat{A}$ (cm^2)	40.8	44.9	49.6	52.1	44.9	55.0	50.6	64.2
Computation time (s)	1264.7	1233.1	424.0	335.8	2333.8	1410.8	810.7	474.6

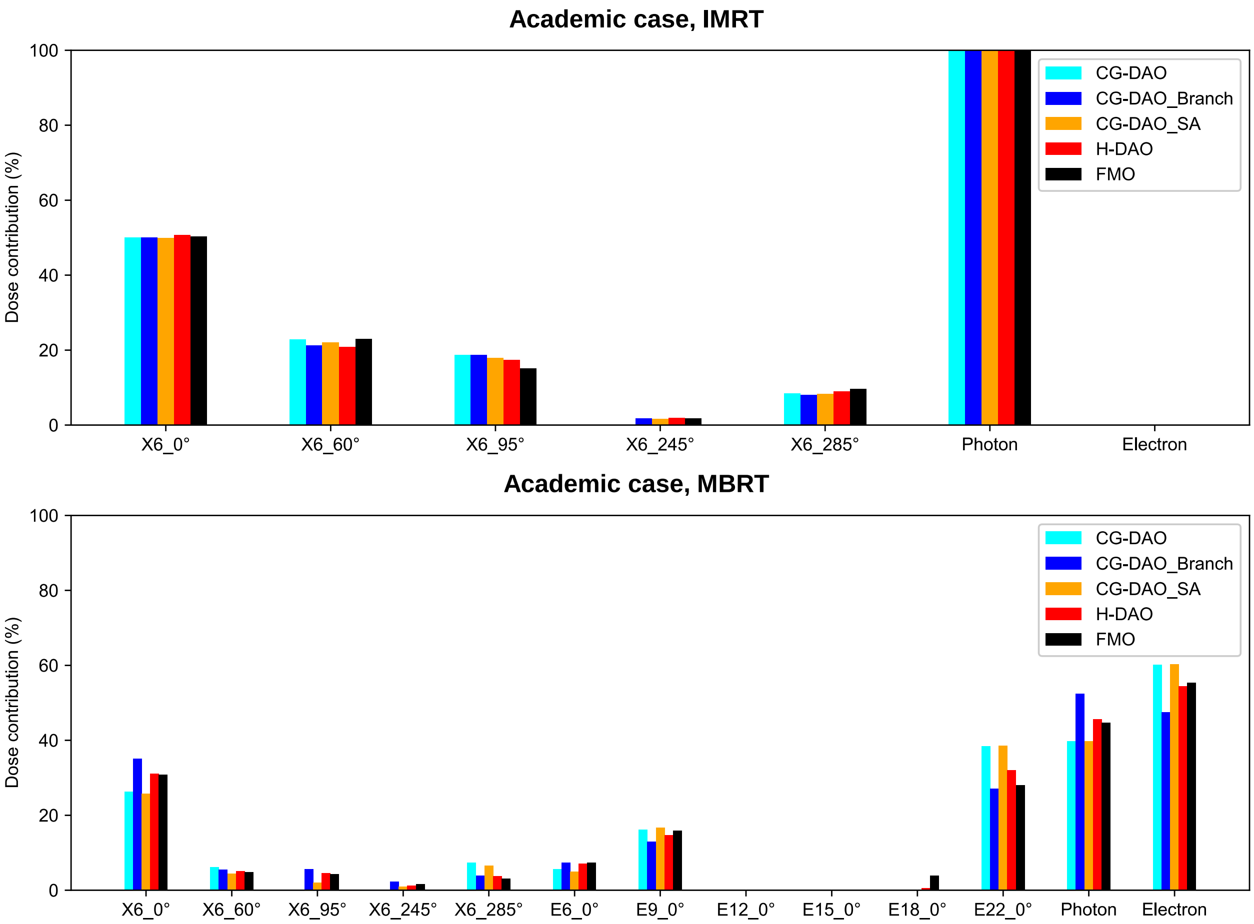

FIGURE 2.6: Dose contributions of the single fields and photon and electron dose contributions for the DAO plans determined for the academic case utilizing 50 apertures and the corresponding FMO plan.

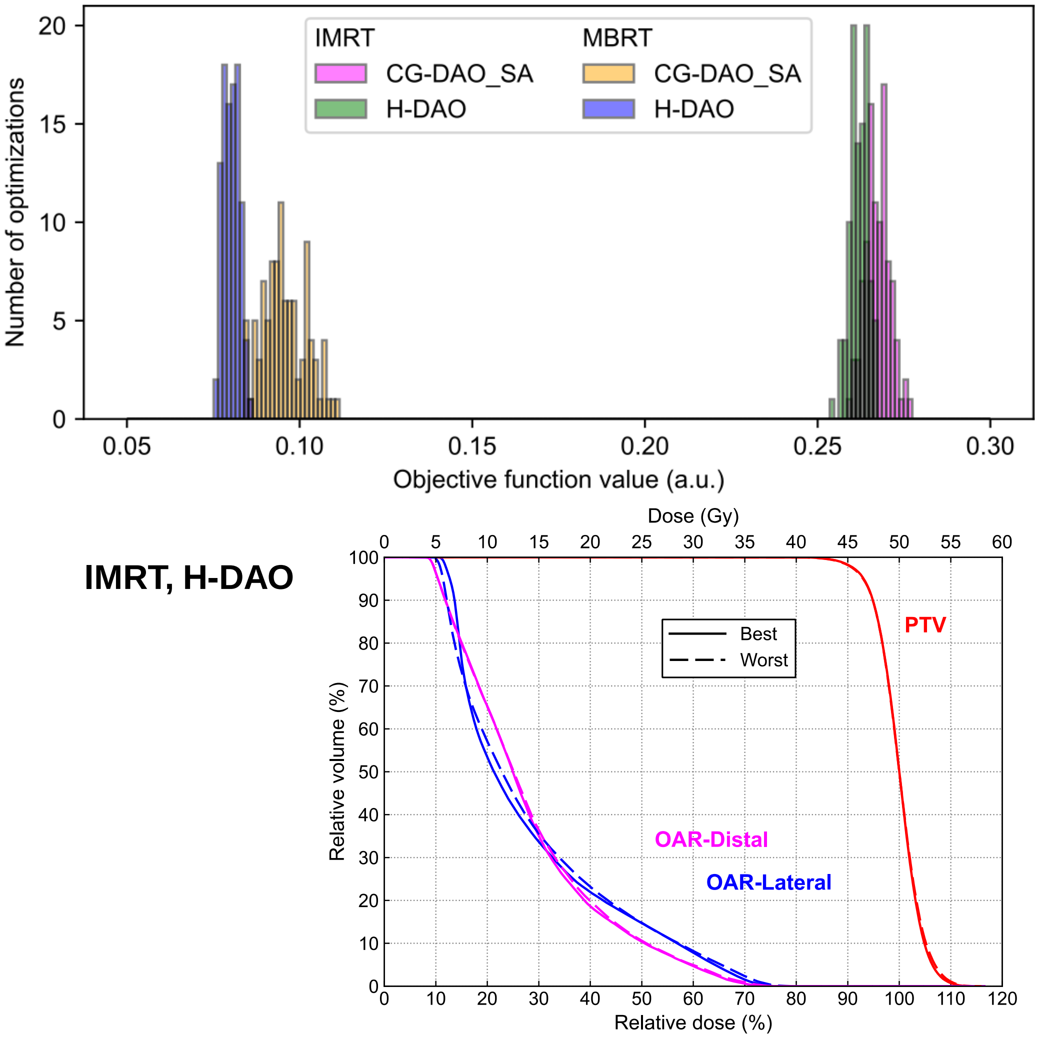

Figure 2.7: Top: Histograms of the objective function values received for the IMRT and MBRT plans generated with the CG-DAO_SA and H-DAO utilizing different seeds for the academic case. Bottom: DVH comparison of the two optimizations leading to the best and the worst result in terms of objective function value of the distribution shown for IMRT, H-DAO shown at the top (green histogram).

2.6 Discussion

The H-DAO algorithm extending the CG-DAO with the branch- and SA-features is successfully implemented and investigated. Each feature alone leads to a faster convergence with number of apertures than the CG-DAO and the combination of the two features also lead to an additional benefit in fast convergence. These statements are generally true for both IMRT and MBRT and for all three investigated cases. The faster convergence with number of apertures can be exploited to create treatment plans with higher dosimetric plan quality or with reduced number of apertures leading to shorter plan delivery time.

Interestingly, CG-DAO and CG-DAO_SA showed a slower convergence with number of apertures for IMRT than for MBRT for the head and neck case up to about 50 apertures, even though the fields provided to IMRT are a subset to those provided to MBRT. This was not observed for CG-DAO_Branch and H-DAO, which both use the branch-feature. Thus, utilizing the branch-feature fulfills better that the provided fields are exploited and not overburdening the DAO algorithm. Therefore, the branch-feature is promising to be also used as a beam angle optimization feature for any CG based DAO algorithm, similarly as it was used for FMO algorithms (Papp, Bortfeld, and Unkelbach, 2015). Other treatment techniques than MBRT that also handle many fields such as 4Pi radiotherapy or treatment techniques including path-finding such as dynamic trajectory radiotherapy (DTRT) (Smyth et al., 2019b; Papp, Bortfeld, and Unkelbach, 2015; Fix et al., 2018) could benefit from this feature.

Both branch- and SA-feature lead to smaller apertures. Thus, the finding by Cassioli and Unkelbach, 2012 that the CG-DAO leads to large apertures, whose MU weight can only be reduced by generating more other apertures, is confirmed. At least for the SA-feature this was expected as it has the purpose of a leaf refinement similar to the aperture shape optimization (ASO) (Cassioli and Unkelbach, 2012). Through the evaluation of the OCE, ΔF_O and ΔF_F, it was shown that the smaller apertures can be handled successfully through the whole TPP without substantial deterioration of the objective function value. Main reason for this is a feature considering transmission through the leaves and increased transmission through the leaf ends during optimization. The plans are also deemed to be accurately deliverable by the treatment unit with high accuracy in the delivered dose as this was shown by a recent work of Heath et al. about robust optimized MBRT utilizing the H-DAO algorithm for plan generation (Heath et al., 2021). There, the delivery of MBRT plans was validated by dose measurements using gafchromic film placed in an anthropomorphic phantom. However, any uncertainties in the modeling of the MLC would be amplified by smaller apertures making an accurate consideration of the treatment head necessary. Furthermore, smaller apertures are usually connected to an increase in MUs and therefore to an increase in delivery time. However, only a minor increase in delivery time is expected when switching from CG-DAO to H-DAO, e.g. for the plans with equal number of apertures shown in this work, the additional delivery time for H-DAO compared to CG-DAO is expected to be about 12 s with 600 MU/min due to the additional 120 MUs on average.

The additional computational effort to perform the SA-feature is substantial and even enormous in case of the branch-feature. However, the branch-feature can be easily parallelized by running each branch in a separate thread like this is done in this computational study. Utilizing state-of-the-art CPUs with high number of CPU-cores are of high value for this task. The results of this computational study show, that in the worst case the computation time to perform the optimization using H-DAO instead of CG-DAO was not more than 3.9 times increased. Multiple techniques were recently investigated to enhance computational efficiency for DAO that could be combined with the H-DAO.

- Yang et al., 2018 replaced the original pricing mechanism with a combination of noise cancellation of the prices using a fuzzy controller followed by aperture generation using threshold segmentation. This allowed to reduce optimization time by 58.61%. This technique could be also used in combination with the H-DAO to determine the most promising aperture per field.

- Men et al., 2009 developed a GPU based implementation of the column generation leading to optimization times below 3.8 s. A GPU implementation would be compliant with the branch-feature and the SA-feature could also be implemented to be performed on the GPU.

- MacFarlane et al., 2019 reformulated the objective function using a second order Taylor series expansion allowing to find the global minimum by a fast matrix inversion. They applied it to a gradient-based optimization algorithm with at least 70-200 times faster execution and noted that it could be also applied to SA.

- Renaud, Serban, and Seuntjens, 2017 applied the CG-DAO to MBRT and investigated different aperture addition-schemes adding multiple apertures per iteration. These aperture addition-schemes could be combined with the SA-feature but not directly with the branch-feature presented in this work.

A limitation of this work is the small number of test cases, which does not allow to state any treatment site specific benefits. The H-DAO algorithm could be tuned scenario specific leading potentially to further improvements, e.g. using different parameter values for the SA-feature depending on the treatment site or by adapting the parameter values according to characteristics of the clinical case such as the target size.

2.7 Conclusions

The H-DAO algorithm is successfully developed. It extends the CG-DAO algorithm by the branch-feature acting as a more founded decision on the aperture to be added to the aperture pool and by the SA-feature acting as a leaf refinement. This computational study shows that both features lead to a faster convergence of the objective function value with number of apertures. This allows to select a better compromise between dosimetric plan quality and number of apertures.

2.8 Acknowledgments

This work was supported by grant 200021_185366 of the Swiss National Science Foundation and by Varian, a Siemens Healthineers company. Calculations were performed on UBELIX (http://www.id.unibe.ch/hpc), the HPC cluster at the University of Bern.

3

Enabling non-isocentric dynamic trajectory radiotherapy by integration of dynamic table translations

Gian Guyer, Silvan Mueller, Carole Koechli, Daniel Frei, Werner Volken, Jenny Bertholet, Paul-Henry Mackeprang, Hannes A. Loebner, Daniel M. Aebersold, Peter Manser and Michael K. Fix

Division of Medical Radiation Physics and Department of Radiation Oncology, Inselspital, Bern University Hospital, and University of Bern, 3010 Bern, Switzerland

Published in
Physics in Medicine and Biology
2022, Vol. 67, No. 17, 175003
DOI: 10.1088/1361-6560/ac840d

3.1 Preface

A treatment planning process for non-isocentric dynamic trajectory radiotherapy is created in this project. The treatment planning process developed in the last chapter is extended to include photon beams with dynamic gantry rotation, collimator rotation, table rotation and/or table translations. The developed treatment planning process is then used to test the potential of dynamic table translations for several different use cases.

Contribution: G. Guyer wrote a majority of the code and did extensive code review of the entire treatment planning process. G. Guyer did the treatment planning, performed the analysis of the treatment plans and created all figures with the exception of the illustration of the PMMA cube. G. Guyer did the measurements including the development of the measurement protocoll with the help of S. Müller. G. Guyer wrote the manuscript with critical feedback from all co-authors.

3.2 Abstract

Objective: The purpose of this study is to develop a treatment planning process (TPP) for non-isocentric dynamic trajectory radiotherapy (DTRT) using dynamic gantry rotation, collimator rotation, table rotation, longitudinal, vertical and lateral table translations and intensity modulation and to validate the dosimetric accuracy.

Approach: The TPP consists of two steps. First, a path describing the dynamic gantry rotation, collimator rotation and dynamic table rotation and translations is determined. Second, an optimization of the intensity modulation along the path is performed. We demonstrate the TPP for three use cases. First, a non-isocentric DTRT plan for a brain case is compared to an isocentric DTRT plan in terms of dosimetric plan quality and delivery time. Second, a non-isocentric DTRT plan for a craniospinal irradiation (CSI) case is compared to a multi-isocentric intensity modulated radiotherapy (IMRT) plan. Third, a non-isocentric DTRT plan for a bilateral breast case is compared to a multi-isocentric volumetric modulated arc therapy (VMAT) plan. The non-isocentric DTRT plans are delivered on a TrueBeam in developer mode and their dosimetric accuracy is validated using radiochromic films.

Main results: The non-isocentric DTRT plan for the brain case is similar in dosimetric plan quality and delivery time to the isocentric DTRT plan but is expected to reduce the risk of collisions. The DTRT plan for the CSI case

shows similar dosimetric plan quality while reducing the delivery time by 45% in comparison with the IMRT plan. The DTRT plan for the breast case showed better treatment plan quality in comparison with the VMAT plan. The gamma passing rates between the measured and calculated dose distributions are higher than 95% for all three plans.

Significance: The versatile benefits of non-isocentric DTRT are demonstrated with three use cases, namely reduction of collision risk, reduced setup and delivery time and improved dosimetric plan quality.

3.3 Introduction

Modern radiotherapy aims at delivering highly conformal dose distributions to the tumor while sparing the surrounding normal tissue. The introduction of intensity modulated radiotherapy (IMRT) utilizing the multileaf collimator (MLC) improved target conformality in comparison with 3D conformal radiotherapy (Bortfeld, 2006). Volumetric modulated arc therapy (VMAT) improved upon the delivery efficiency of IMRT while maintaining the dosimetric treatment plan quality by rotating the gantry continuously during beam on (Otto, 2008). Both VMAT and IMRT are established treatment techniques in radiotherapy for more than a decade.

Next to the MLC, current linear accelerators offer additional degrees of freedom (DoFs) applicable to improve upon VMAT and IMRT in terms of dosimetric treatment plan quality, delivery efficiency or patient safety. By rotating the patient table between the delivery of different beams, non-coplanar beam directions can be achieved to further improve organ-at-risk (OAR) sparing either for IMRT (Dong et al., 2013; Rwigema et al., 2015; Yu et al., 2018) or for VMAT (Audet et al., 2011; Clark et al., 2012). In a more advanced technique, the table is rotated simultaneously with the gantry during beam on (Smyth et al., 2013; MacDonald and Thomas, 2015; Papp, Bortfeld, and Unkelbach, 2015; Wild et al., 2015; Lyu et al., 2018a; Mullins et al., 2020a). In dynamic trajectory radiotherapy (DTRT), the collimator is rotated additionally to the gantry and table, yielding a further DoF (Yang et al., 2011; Fix et al., 2018; Langhans et al., 2018; Dong, Liu, and Xing, 2018; MacDonald et al., 2020). Dynamic collimator rotations enable connectedness improvements between MLC apertures (Locke and Bush, 2017). In addition, the whitespace inside the open MLC area is reduced, which is especially relevant for treating multiple targets (MacDonald, Thomas, and Syme, 2018; Battinelli, Fredriksson, and Eriksson, 2021). High dosimetric accuracy of DTRT has been shown in the past (Smyth et al., 2019a; Manser et al., 2019). A review of non-coplanar radiotherapy techniques is given by Smyth et al., 2019b.

Currently, DTRT is limited to fixed isocenter positions. This could be extended to a non-isocentric technique utilizing the translational DoFs offered by modern patient tables in longitudinal, vertical and lateral direction (Schmidhalter et al., 2014), resulting in an even more general trajectory for DTRT (Manser et al., 2020). One potential use case of non-isocentric DTRT, i.e. DTRT including dynamic table translations, is to extend the source-target distance (STD) for VMAT and DTRT plans. This is achieved by defining a virtual isocenter (Humm, 1994) given by the position of the machine isocenter in the isocentric VMAT or DTRT plan inside the patient. The STD can thus be extended by moving the table such that the virtual isocenter is moved further away from the source in beam direction in comparison to the actual machine isocenter. With extended STD, the risk of collision between gantry and patient is reduced, e.g. for targets positioned laterally in the body, and at the same time the solution space could be expanded by avoiding collisions between gantry and table (Yu et al., 2015; Liang et al., 2015; Yu et al., 2018). Another possible use case is the dynamic translation similar to helical VMAT (Bedford et al., 2012) to irradiate large targets such as craniospinal irradiation (CSI) for pediatric brain tumors (Laprie et al., 2015; Massimino et al., 2016) or leptomeningeal disease (Maillie, Salgado, and Lazarev, 2021), which is commonly performed with a multi-isocenter proton or photon technique (Seravalli et al., 2018), with e.g. 2-3 isocenters. A third possible use case is to exploit dynamic table translation for concave targets such as whole breast irradiation (WBI) in order to use more tangential beam directions in comparison with a single isocenter technique (Li et al., 2014).

Non-isocentric DTRT requires a treatment planning process (TPP) which is able to handle all the dynamic axes appropriately. To the best of our knowledge, no optimization algorithm has been described in literature, which can perform intensity modulation optimization along any predefined path including dynamic table translation. Mullins et al., 2020a proposed a TPP for DTRT plans with a predefined, non-isocentric trajectory for cranial targets at a shortened STD. However, the proposed TPP is not able to handle arbitrary non-isocentric dynamic trajectories.

A possibility is to extend an existing isocentric DTRT intensity modulation optimization algorithm to non-isocentic DTRT. In our group, a two-step planning technique for isocentric DTRT was developed in previous work, where in a first step the path describing the dynamic gantry, collimator and table rotation is determined and in a second step, intensity modulation is performed (Fix et al., 2018). However, the intensity modulation optimization is done within a commercial treatment planning system, which is not able to handle dynamic table translations.

The purpose of this work is to develop a TPP for DTRT using dynamic axes, that is rotating gantry and rotating collimator, rotating and translating table and intensity modulation during beam on. For this, intensity modulation optimization of DTRT plans is enabled in an in-house DAO algorithm. Three clinically motivated cases are used to investigate potential use cases for non-isocentric DTRT. Furthermore, the deliverability of non-isocentric DTRT plans is shown on a TrueBeam linear accelerator (Varian, a Siemens Healthineers Company, Germany) in developer mode and dosimetric accuracy is demonstrated using radiochromic film measurements.

3.4 Methods

3.4.1 Treatment planning process

In the following section, the TPP for non-isocentric DTRT is described in detail. The TPP consists of two main parts. First, determination of the dynamic path, which is given by a set of control points (CPs) defining the dynamic axes, that is gantry rotation, collimator rotation, table rotation and longitudinal, lateral and vertical table translation. If an axis has a constant value for all CPs, it is called a static axis in the following. Second, optimization of the intensity modulation is performed by setting the MLC sequence and corresponding MU weights for each CP. The TPP is described for DTRT plans, but also works for VMAT as VMAT is a special case of DTRT with static table and collimator.

Path determination

Planning CTs and structure sets were taken from cases previously treated at our institution and imported into a research version of the Eclipse treatment planning system (TPS) 15.6 (Varian, a Siemens Healthineers Company, Germany). A normal tissue structure was created, defined as the body contour excluding the planning target volume (PTV). The paths are determined by using one of two different Eclipse TPS interfaced scripts. In the following, the two different scripts for path determination are described:

1. Manual path generation. For this, anchor points are defined in a list by the user by setting values for gantry angle, collimator angle, table angle and lateral, vertical and longitudinal table position. Using these anchor points, the CPs are obtained by linearly interpolating between two consecutive anchor points in the list with a given spacing in each axis, resulting in the definition of the path. This can be used for VMAT and DTRT. In the case of VMAT, two anchor points are used for start and end point of the arc with a static table position and collimator angle. Multiple paths are obtained by starting the script multiple times.
2. Path determination as described in Fix et al., 2018 for isocentric DTRT. In brief, in this approach, the gantry, collimator and table angles are optimized using mainly a geometrical approach. A map based on volumetric target/OAR overlap in beam's eye view is created. On this map, the gantry-table path is determined using an A* algorithm (Hart, Nilsson, and Raphael, 1968). For the collimator rotation along the gantry-table path, a map is created scoring different gantry-collimator combinations by the distance between the outer most MLC leaf positions when the MLC is set conformal. Then, the gantry-collimator path is determined by finding the collimator rotation for which this distance is minimal.

For both options, the STD can be changed from the conventional 100 cm to a value d in a post-processing step by moving the virtual isocenter further away in beam direction using the following trigonometric calculations:

$$\Delta_{lateral} = (d - 100\ cm) \cdot \sin(-\alpha_{gantry}) \cdot \cos(\alpha_{table}) \tag{3.1}$$

$$\Delta_{vertical} = (d - 100\ cm) \cdot \cos(\alpha_{gantry}) \tag{3.2}$$

$$\Delta_{longitudinal} = (d - 100\ cm) \cdot \sin(-\alpha_{gantry}) \cdot \sin(\alpha_{table}), \tag{3.3}$$

where α_{gantry} and α_{table} are the gantry and table angles, respectively, and $\Delta_{lateral}$, $\Delta_{vertical}$ and $\Delta_{longitudinal}$ are the lateral, vertical and longitudinal table positions relative to the table position in the isocentric DTRT.

Next, the field size defined by the secondary collimator jaws is set to the smallest possible opening such that the PTV with an additional 5 mm margin is not blocked by the jaws for any CPs from the beam's-eye-view or set to the largest possible size in the case where the PTV is larger than the largest possible field size, e.g. in CSI.

Intensity modulation optimization

To provide the necessary dosimetric information for the intensity modulation optimization, a beamlet dose calculation is performed using the Eclipse TPS interfaced Swiss Monte Carlo Plan (SMCP) (Fix et al., 2007) for each CP after the path generation. The beamlet grid is set up for each CP with the grid spacing given by the width of the MLC leaves in transverse direction and 5 mm in direction of MLC leaf movement and the grid size equivalent to the field size rounded to the next beamlet border. A precalculated phase space at the exit of the treatment head, used as an input the VMC++ dose calculation algorithm (Kawrakow and Fippel, 2000) are used to calculate the beamlet dose distributions for each CP.

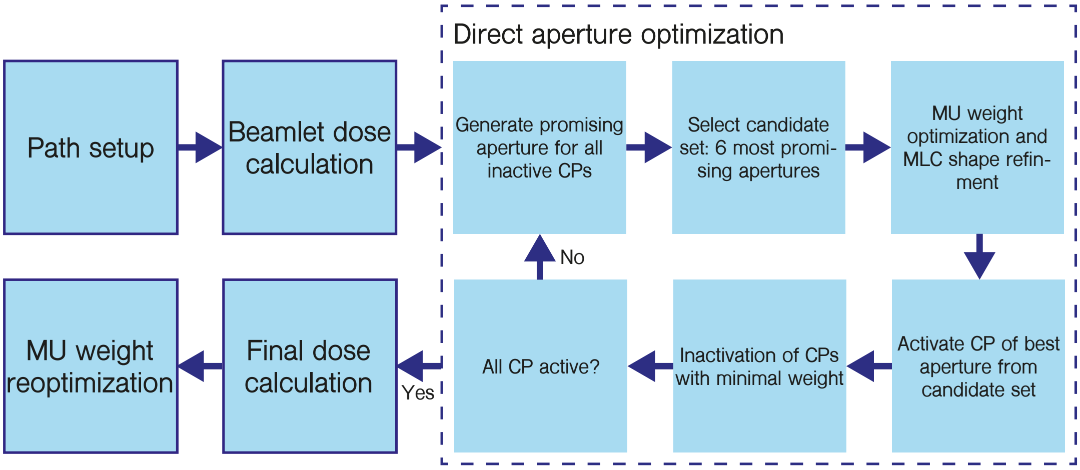

Figure 3.1: Overview of the intensity modulation optimization steps. After the path setup, a beamlet dose calculation is performed for all CPs. Next, an aperture is determined for all CPs using a direct aperture optimization by iteratively adding apertures to CPs, i.e. activating the CPs. For this, a promising aperture is determined for all inactive CPs. Out of these, the six most promising apertures are selected, i.e. those with the steepest gradient on the objective function value. Each CP of these six apertures is activated individually and a MU weight optimization and MLC shape refinement is performed together with all active CPs. Next, the best aperture out of the six most promising ones is identified based on the objective function value. Afterwards, some active CPs are allowed to be inactivated if their MU weight is below a minimal value and if the total number of inactivated CPs in the optimization is not higher than a selected threshold. When all CPs are activated, a final dose calculation and a MU weight reoptimization are performed.

Using the beamlet dose distributions, the intensity modulation is optimized with inverse planning by determining exactly one aperture, i.e. the MLC shape and the corresponding MU weight, at each CP. The intensity modulation optimization algorithm is an extension of the hybrid DAO algorithm and based on column generation (CG) and simulated annealing (SA) described by Mueller et al., 2022. The objective function is evaluated on a plan dose D_{plan}, which is given by the following equation:

$$D_{plan} = \sum_{n=1}^{\#CPs} \sum_{j=1}^{\#leafpairs} \sum_{b=1}^{\#beamlets} D_n(b,j) \cdot w_n \cdot \phi_n(b,j), \tag{3.4}$$

where $D_n(b,j)$ is the dose of beamlet b and leaf pair j at the nth CP, w_n is the MU weight of the aperture at the nth CP and $\phi_n(b,j)$ is the fluence of the beamlet b and leaf pair j of the aperture at the nth CP. An overview of the optimization is given in fig. 3.1. The optimization starts with each CP having an undetermined aperture and w_n set to 0, called an inactive CP. In every iteration, one CP is set to active by determining the corresponding aperture, i.e. the MLC leaf pattern and MU weight w_n. For this, a promising aperture, i.e. the aperture with the lowest price on the gradient objective function value of each beamlet belonging to the aperture summed together, is determined for each inactive CP.

In the determination of these promising apertures, the maximum distance the MLC is allowed to travel between neighboring CPs is steered with Δx ranges for each leaf. For a new promising aperture at the nth CP, the MLC range is determined with the next preceding and succeeding active CPs, as illustrated in fig. 4.2(a). For an already preceding active CP at $(n-q)$, the MLC $\Delta x_{pre}(n)$ range is given by

$$\Delta x_{pre}(n) = \lambda_{MLC} \cdot v_{MLC} \cdot \sum_{i=n-q}^{n-1} t(i), \tag{3.5}$$

where v_{MLC} is the maximal mechanical MLC leaf speed, $t(i)$ is the time needed to move all the dynamic axes from the ith CP to the $(i+1)$th CP and λ_{MLC} is the so-called MLC freedom factor, which is a parameter defining how much the MLC is allowed to slow down the delivery. If λ_{MLC} is equal to 1, the MLC range is limited such that the time needed for the MLC leaves to move is not longer than the time needed to move the dynamic axes between CPs. If λ_{MLC} is equal to 2, the time needed for moving the MLC leaves can be at most two times longer than the maximal time needed to move all the dynamic axes and consequently delivery time can be up to doubled. If λ_{MLC} is smaller than 1, the range is restricted further but without an impact on the delivery time because

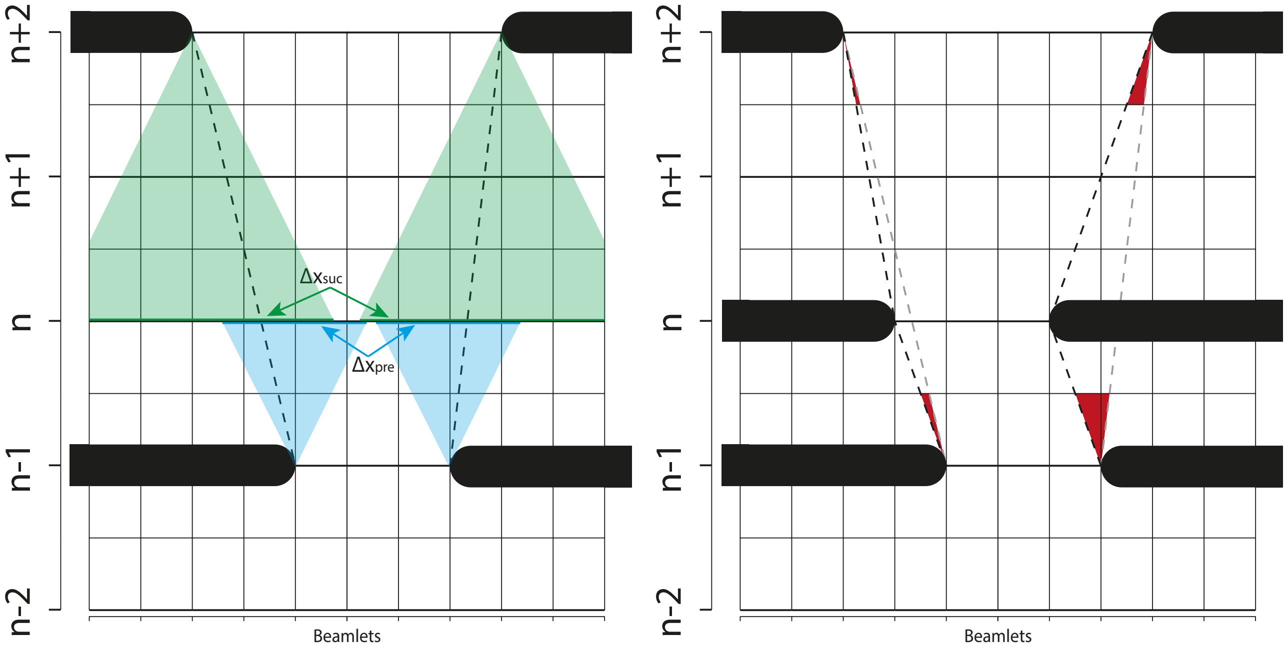

(a) Before (b) After

Figure 3.2: Illustration of the fluence interpolation for one MLC leaf pair. (a) Situation before the leaf pair at the nth CP is inserted. The leaf motion is interpolated between the next active CPs $n-1$ and $n+2$. The MLC preceding $\Delta x_{pre}(n)$ and succeeding $\Delta x_{suc}(n)$ ranges are illustrated in blue and green. The position of the leaf pair at the nth CP is restricted to the intersection of these ranges. (b) Situation after the leaf pair at n is inserted. The black dashed lines represent the interpolated leaf motion and the red areas correspond to the change in fluence of the neighboring apertures due to the insertion of a new leaf pair.

the MLC leaf travel is not the limiting motion. The allowed $\Delta x_{suc}(n)$ range is calculated similarly if there is a succeeding active CP.

The time $t(i)$ in eq. (3.5) is calculated by

$$t(i) = \max_a \Big(\big(x_a(i+1) - x_a(i) \big) / v_a \Big), \tag{3.6}$$

where $x_a(i)$ is the position of the axis a at the ith CP and v_a is the maximal mechanical speed limit of axis a with $a \in$ {gantry rotation, collimator rotation, table rotation, longitudinal table translation, vertical table translation, lateral table translation}. The values used for v_a are given in table 3.1.

Among all the promising apertures, the one which leads to the largest decrease of the objective function is determined. For this, the six most promising apertures with the lowest price are identified. This is done for the six most promising instead of all promising apertures to keep computational efficiency reasonable for dynamic plans which have typically over 100 CPs and the number of six has proven to be an adequate number in preliminary investigations. Each CP of the six promising apertures is set separately to active and a suboptimization is performed with all active CPs including one CP of the six promising apertures. The suboptimization consists of an MU weight optimization of the active CPs using an L-BFGS quasi newton method (Nocedal and Wright, 1999). Subsequently, the aperture shapes and weights of the active CPs are refined using a stochastic SA algorithm, where either an MLC leaf or the MU weight of a CP is selected and tested for potential improvement in each iteration. The MLC leaf positions are restricted by the maximal MLC range given by eq. (3.5). The SA algorithm is followed by a second MU weight optimization of the CPs. The MU weights of the active CPs are limited to a maximal value given by

$$w_{max} = \lambda_{MU} \cdot r_{max} \cdot t_n, \tag{3.7}$$

where r_{max} is the maximal MU rate of the beam, λ_{MU} is the so-called MU freedom factor and t_n is the time associated with CP n, which is calculated by

$$t_n = \frac{1}{2} \cdot t(n-1) + \frac{1}{2} \cdot t(n), \tag{3.8}$$

where $t(i)$ is given by eq. (3.6). Like the MLC freedom factor, the maximal time needed for delivering the MUs is equal or lower than the time needed to move all dynamic axes if λ_{MU} is set to 1. To prevent a beam hold due to a too low MU rate during the delivery, the MU weights are also limited by a minimal value

$$w_{min} = r_{min} \cdot t_n, \tag{3.9}$$

where r_{min} is the minimal MU rate such that no beam hold occurs. During dose delivery of trajectories with dynamic axes, the MLC leaves move continuously from the aperture of one CP to the next CP simultaneously with the dynamic axes. Thus, when a promising aperture at a CP is determined or the aperture shape at an active CP is changed, the fluence associated with this aperture is dependent on the shape of the neighboring apertures. This is taken into account by interpolating the fluence to the neighboring apertures. The fluence of the neighboring apertures is recalculated using the same formalism to respect the influence of changes on the neighboring apertures, as illustrated in fig. 3.2(b). Note that due to the influence of changes on the neighboring apertures, the optimization problem is considerably more complicated when considering fluence interpolation in comparison to optimization without fluence interpolation. The fluence interpolation is considered both in the pricing of promising apertures as well as calculating the objective function value and gradient of the active CPs. The full formalism of fluence interpolation is described in section 3.9.

After the suboptimization, the aperture among the six most promising apertures is identified, for which the suboptimization together with all apertures of active CPs yielded the lowest objective function value. The CP of this promising aperture is set to active, while all other promising apertures are removed. If the MU weight of an active CP is set to the minimal weight in one iteration, the CP is inactivated to allow for a better aperture shape at this CP at a later iteration. The total number of active CPs which can be inactivated in all iterations summed together is limited to 33% of the number of CPs to guarantee that the optimization reaches an end and for computational efficiency reasons. This threshold was determined in preliminary investigations showing that higher percentages only increase the computational time without having an impact on the optimization result. If this number is reached, no further CPs are inactivated. The optimization is terminated when every CP is active.

As mentioned, the beamlet dose calculations are performed for the discrete set of CPs. However, the delivery of the beam is not done from the discrete set of CPs, but by simultaneous continuous movement of the MLC and dynamic axes between CPs. Thus, the summed beamlet dose after the optimization and the actual dose delivered to the patient differ. Additionally, the transmission through the MLC leaves and contributions from scatter considered during optimization are only an approximation. Hence, a final dose calculation taking the continuous movement and the exact MLC geometry into account is performed.

A Monte Carlo (MC) dose calculation algorithm is favorable over other calculation algorithms for this task, because the simulated particles can be continuously sampled from all positions of the continuously moving and changing aperture (Manser et al., 2019). The MC dose calculation is performed using the SMCP integrated beam model (Magaddino et al., 2011) and VMC++ dose calculation algorithm (Kawrakow and Fippel, 2000). A voxel size of $2.5 \times 2.5 \times 2.5$ mm^3 is used for all MC dose calculations and the actual mean statistical uncertainty of the voxels with dose values higher than 50% of the maximum dose calculated is below 0.5% for all presented dose distributions.

To mitigate the difference between the optimized beamlet dose and final dose calculation, a reoptimization of the MU weights of the CPs is performed after the final dose calculation. The MU weight reoptimization is done with an L-BFGS algorithm while considering the limitations on the MU weights from the optimization. After the reoptimization, the dose distribution of each aperture is weighted with the reoptimized MUs and summed to obtain the reoptimized final dose distribution of the plan. Some investigations of the optimization efficacy are given in section 3.10.

3.4.2 Use cases

As a first use case, non-isocentric DTRT with an extended STD is considered. For this, a DTRT plan with extended STD of 110 cm for a brain case with a prescribed dose of 60 Gy to the median dose of the PTV in 30 fractions is compared in terms of dosimetric quantities and estimated delivery time to a plan with the same DTRT path but with normal STD of 100 cm, i.e. an isocentric plan. The gantry-table and gantry-collimator path is determined by the method described by Fix et al., 2018. The resulting path is duplicated into two paths. The spacing between CPs is 5° based on the gantry angle value. In fig. 3.3(a), the path of the DTRT plan with extended STD is illustrated. The parameters used for the optimization are $\lambda_{MU} = 2$, $\lambda_{MLC} = 1$ and with fluence interpolation applied.

The dosimetric quantities used are $D_{2\%}$ for serial OARs, D_{mean} for parallel OARs, $V_{10\%}$ for normal tissue and homogeneity index (HI) for the PTV

$$\mathrm{HI} = (D_{2\%} - D_{98\%})/D_p, \tag{3.10}$$

where D_p is the prescribed dose. The estimated delivery time is calculated by summing the time per CPs of all trajectories, as well as the time to move axes between fields, if necessary. The time per CP is estimated using eq. (3.6)

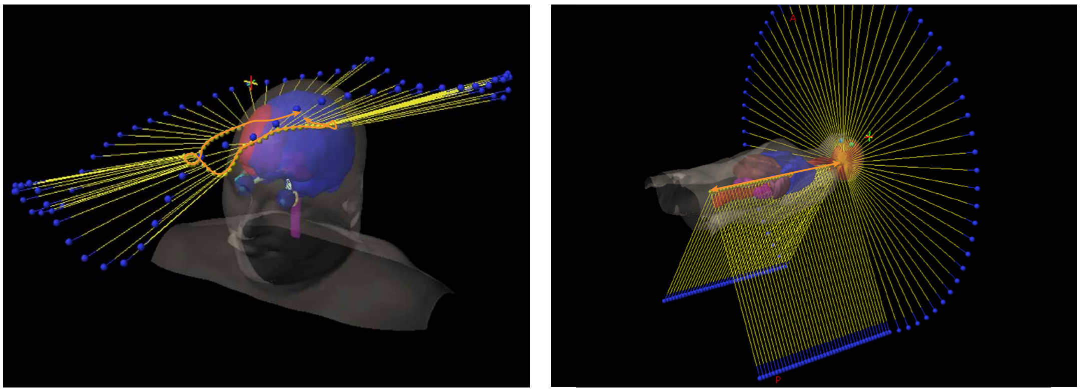

(a) brain case (b) CSI case

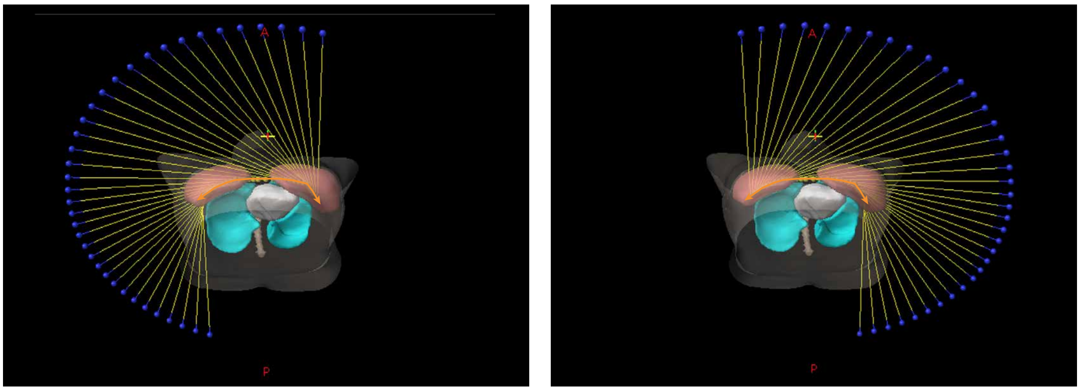

(c) WBI case A (d) WBI case B

FIGURE 3.3: Illustrations of the paths in Eclipse TPS for the DTRT plan with extended STD for the brain case (top left), the DTRT plan for the CSI case (top right) and the DTRT plan for the WBI case (bottom). The paths are given by a set of CPs defining the gantry rotation, collimator rotation and table rotation and translation. For better visibility, only the central axis of the beam at each CPs is shown as yellow lines. The position of the machine isocenter in the patient coordinate system is illustrated in orange.

TABLE 3.1: Values used for time calculation.

Axis a	Speed limit v_a
Gantry rotation	6°/s
Collimator rotation	15°/s
Table rotation	3°/s
Longitudinal table translation	8 cm/s
Vertical table translation	2 cm/s
Lateral table translation	4 cm/s
Max. dose rate	600 MU/min
Min. dose rate	5 MU/min
MLC leaf movement	2.5 cm/s

with the MLC leaf travel and the MU weight as additional components. In this formula, the acceleration of the mechanical axes as well as the beam ramp up are neglected. The mechanical speed limits v_a used for the calculation are shown in table 3.1.

As a second use case, a CSI case with a prescribed median dose of 23.4 Gy to the PTV in 13 fractions is considered. A DTRT plan is created consisting of a 70 cm longitudinal table translation along the spinal axis with a static gantry angle of $-150°$, a gantry rotation around the head and another 70 cm longitudinal table translation with a gantry angle of 150°. The spacing of CPs is set to 2 cm along the longitudinal table axis and 5° along the gantry rotation. The path of the DTRT plan is illustrated in fig. 3.3(b). The path is duplicated and the intensity optimization is performed using $\lambda_{MU} = 2$, $\lambda_{MLC} = 1$ and with fluence interpolation applied. The resulting DTRT plan is compared to an IMRT plan consisting of six fields, four dorsal angulated fields for the spinal axis and two lateral fields for the brain, separated in three isocenters, which corresponds to the field setup used in the original clinical plan. The number of total apertures of the IMRT plan is set to 30, because investigations for this field setup showed that additional apertures improve the dosimetric plan quality only marginally. The plans are compared in terms of estimated delivery time and dosimetric quantities.

As a third use case, a non-isocentric DTRT plan for a bilateral WBI case with a prescribed median dose of 50 Gy to the PTV in 25 fractions is compared to a VMAT plan in terms of dosimetric treatment plan quality and delivery time. The non-isocentric DTRT setup consists of half arcs with dynamic vertical and lateral table translation such that the central beam axis stays tangential to the body contour. In fig. 3.3(c) and fig. 3.3(d) the DTRT paths are illustrated. Each of the two paths is duplicated for a total of four half arcs. The VMAT setup consists of 12 partial arcs in two isocenters, which corresponds to the clinical field setup. For the right breast, two arcs range from $-180°$ to $-115°$ in gantry angle, two arcs range from $-180°$ to $45°$ and two range from $-20°$ to $60°$. For the left breast, the gantry angles range from $-60°$ to $20°$, from $-45°$ to $180°$ and from $115°$ to $180°$ for two arcs each. For both the DTRT and the VMAT setup, the spacing between CPs is $5°$ based on the gantry angle value and the parameters used for the optimization are $\lambda_{MU} = 2$, $\lambda_{MLC} = 1$ and with fluence interpolation applied. All optimizations are calculated on an AMD Epyc2 processor using six CPU cores.

3.4.3 Validation

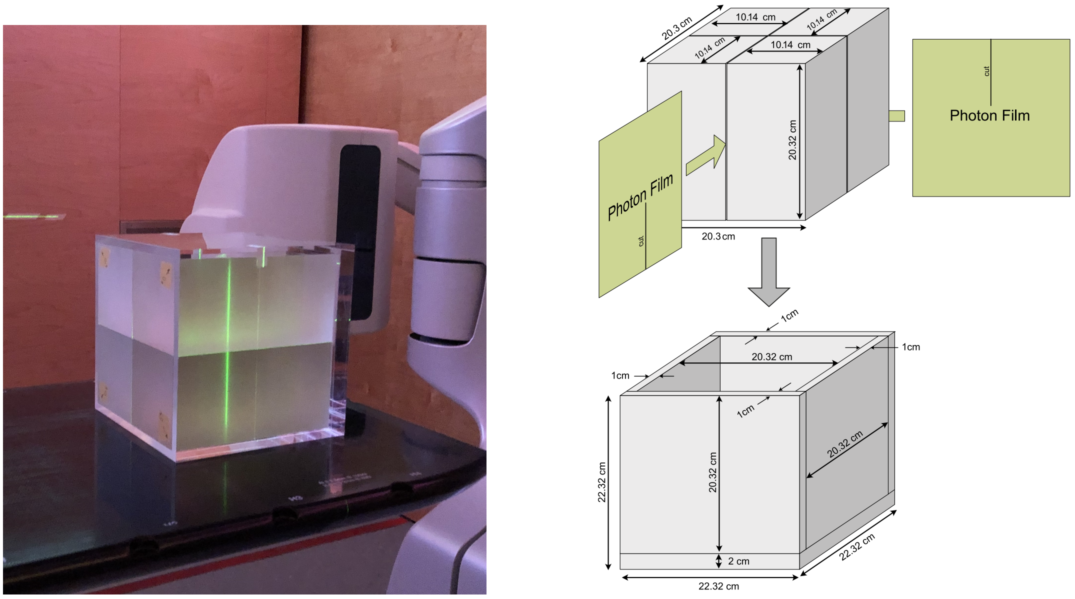

(a) (b)

FIGURE 3.4: Photo and illustration of the PMMA cube used for the validation measurements. Two EBT3 films, one in the sagittal and one in the coronal plane are placed inside the cube.

To validate the TPP for non-isocentric DTRT, the plan with extended STD of the brain case, the DTRT plan of the CSI case and the DTRT plan of the WBI case are delivered on a TrueBeam linear accelerator in developer mode. The dose is measured using two interleaved radiochromic EBT3 films (Ashland Advanced Materials, Bridgewater, NJ) placed inside a PMMA cube. The PMMA cube is made of an outer case with four blocks inside. This phantom allows to put the EBT3 films in the middle of the blocks and between the blocks and the outer case of the cube in the axial, sagittal and coronal plane of a patient lying on the treatment table. An image of the measurement setup as well as an illustration of the PMMA cube including proportions is shown in fig. 3.4. For the plans of the brain and CSI case, the films are placed in the middle of the cube in the sagittal and coronal plane while for the plan of the WBI case one film is placed in the middle in the axial plane and one film is placed on a coronal plane in a depth of 2 cm, i.e. between the outer case and the inner blocks. Because the target of the CSI case is too long to fit into the PMMA cube, the neck region is chosen for measurement to incorporate both the longitudinal table translation and the gantry arc into the measurement. The films are scanned using an Epson XL 10000 flatbed scanner (Seiko Epson Co., Tokyo, Japan) 18h after irradiation. The scanned films are corrected for the lateral response artifact of the scanner using a one-dimensional linear correction function (Lewis and Chan, 2015). The color values on the films are converted to absolute dose using a triple channel calibration (Micke, Lewis, and Yu, 2011) and rescaled according to the one-scan protocol by using two additional film strips (Lewis et al., 2012). The resulting dose of the red channel is compared to the corresponding 2D plane of the dose recalculated for the PMMA cube using a gamma evaluation with a 3% (global) / 2 mm and a 2% (global) / 2 mm criterion and a 10% low-dose threshold of the maximum dose.

3.5 Results

3.5.1 Treatment quality of use cases

In fig. 3.5 the values of the dynamic axes are shown for the first trajectory of the DTRT plan with extended STD for the brain case. As can be seen, the gantry, collimator and table dynamically rotate and the table dynamically translates in all three directions during the trajectory. In fig. 3.6 the DVH comparison of the brain case DTRT plans with extended vs. normal STD is shown. The DVHs of the PTV, OARs and normal tissue of the two plans are similar. The estimated delivery time is 3.4 min for the plan with normal STD and 3.5 min for extended STD. The total number of MUs are 550 and 610 for normal and extended STD plans, respectively.

fig. 3.7 shows the DVH comparison between the DTRT plan and the IMRT plan for the CSI case. The dosimetric quantities are compared in table 3.2. The plan quality is similar between the two plans. The estimated delivery time is 4.6 min for the DTRT plan and 8.3 min for the IMRT plan. The total number of MUs are 1145 for the DTRT plan and 764 for the IMRT plan.

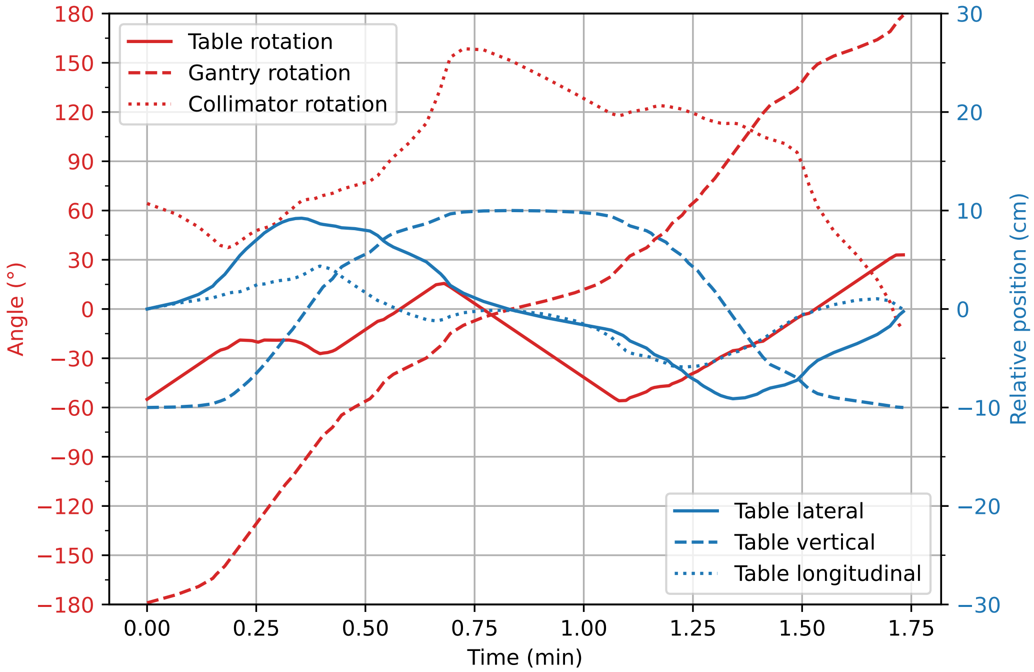

FIGURE 3.5: Gantry, collimator and table values for first trajectory of the DTRT plan with extended STD for the brain case.

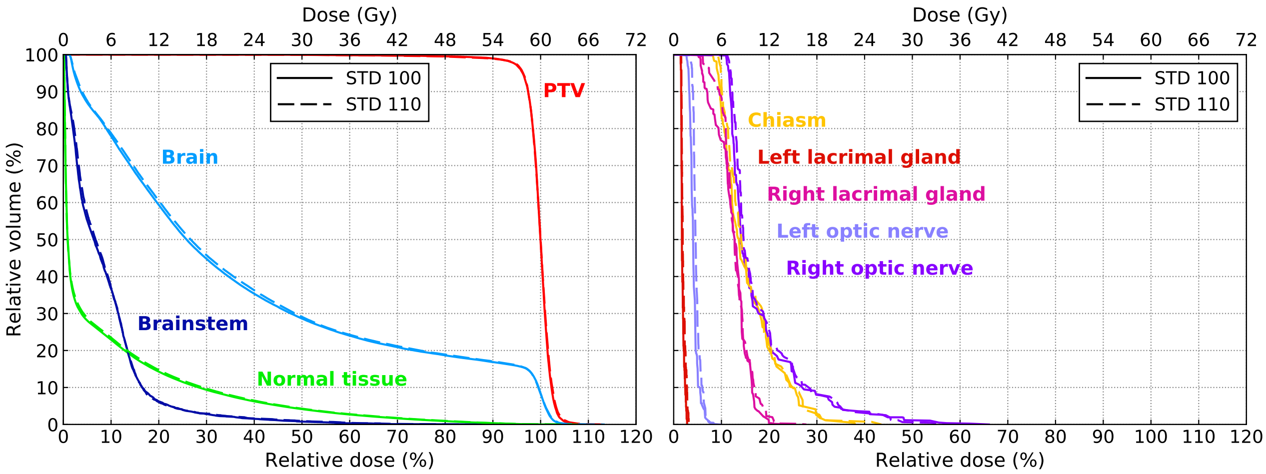

FIGURE 3.6: DVH comparison of the DTRT plan with extended STD (110 cm) and isocentric DTRT plan (100 cm) for the brain case.

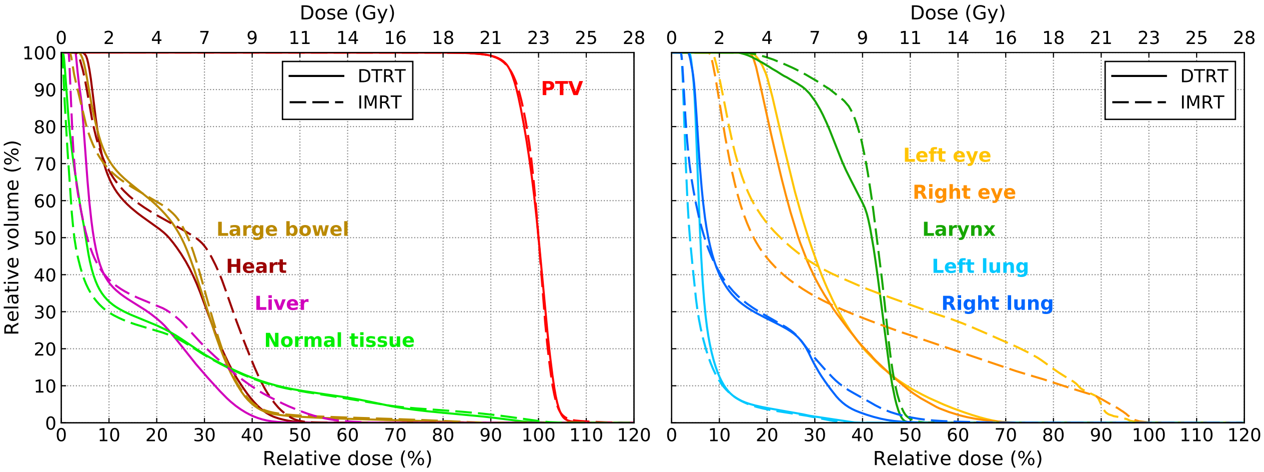

FIGURE 3.7: DVH comparison of the IMRT and the DTRT plan for the CSI case.

TABLE 3.2: Comparison of the dosimetric quantities of the IMRT and DTRT plan for the CSI case. The lower value of each quantity is highlighted in bold.

	IMRT plan	DTRT plan
PTV HI	13.8	**13.3**
Heart D_{mean} (Gy)	5.7	**5.0**
Left eye $D_{2\%}$ (Gy)	21.8	**15.2**
Right eye $D_{2\%}$ (Gy)	22.4	**15.6**
Left lung D_{mean} (Gy)	**1.3**	1.8
Right lung D_{mean} (Gy)	3.3	3.3
Left Kidney D_{mean} (Gy)	**1.3**	1.9
Right kidney D_{mean} (Gy)	**1.4**	2.0
Liver D_{mean} (Gy)	3.4	**3.1**
Large bowel D_{mean} (Gy)	**5.2**	5.3
Thyroid D_{mean} (Gy)	9.7	**9.5**
Larynx D_{mean} (Gy)	9.6	**9.1**
Normal tissue $V_{10\%}$ (%)	**29.3**	32.3

In fig. 3.8(a) and fig. 3.8(b) the doses of the DTRT and IMRT plans for the CSI case are visualized in a sagittal plane and in fig. 3.8(c) dose profiles are shown for the fields of the IMRT and DTRT plans. Due to the longitudinal table translation, there are no field junctions as in the multi-isocentric IMRT plan.

The results for the WBI case are shown in Figures fig. 3.9 and fig. 3.10. As can be seen in the DVHs in fig. 3.9, the HI is similar between the VMAT and the DTRT plan. However, the mean heart dose is 6.6 Gy in the VMAT plan and 3.9 Gy in the DTRT plan, which corresponds to a 40% reduction. In

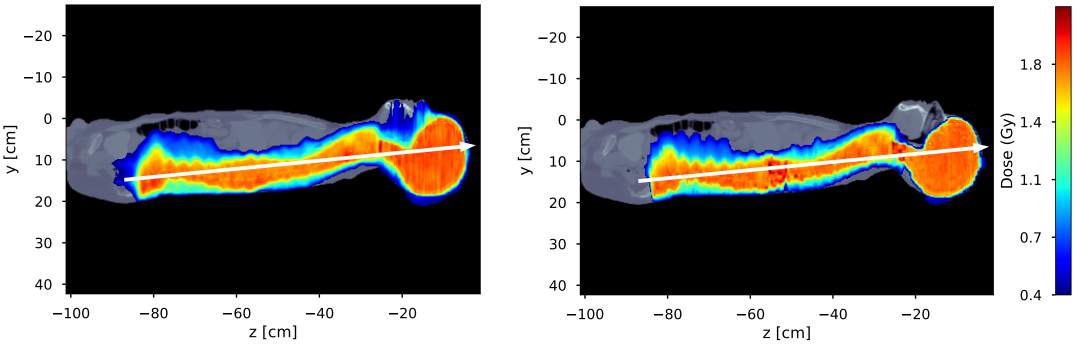

(a) DTRT (b) IMRT

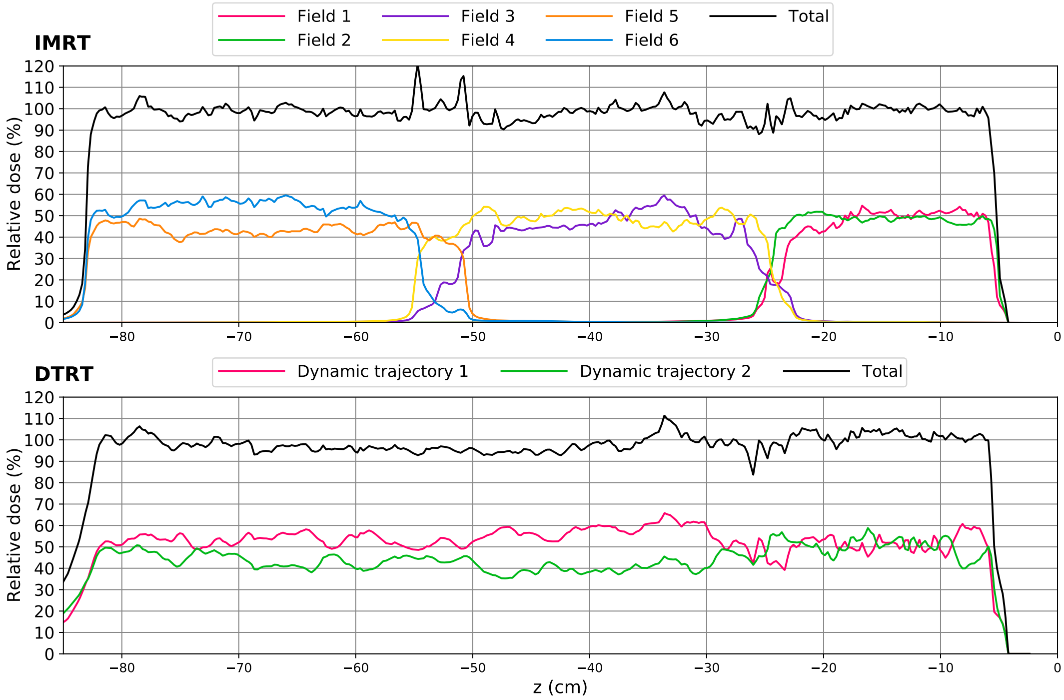

(c)

FIGURE 3.8: Dose visualization (top) of the IMRT and DTRT plans for the CSI case in a sagittal plane. Dose profiles of the IMRT plan and the DTRT plan along the white arrow are shown on the bottom.

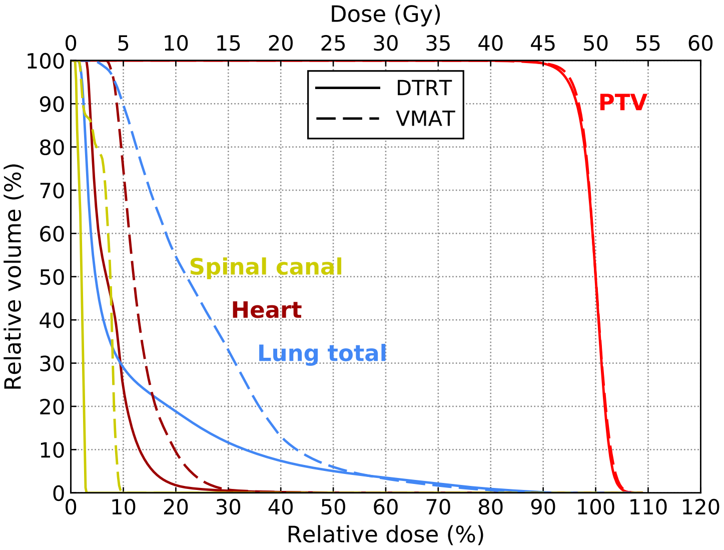

Figure 3.9: DVH comparison of the VMAT and DTRT plans for the WBI case.

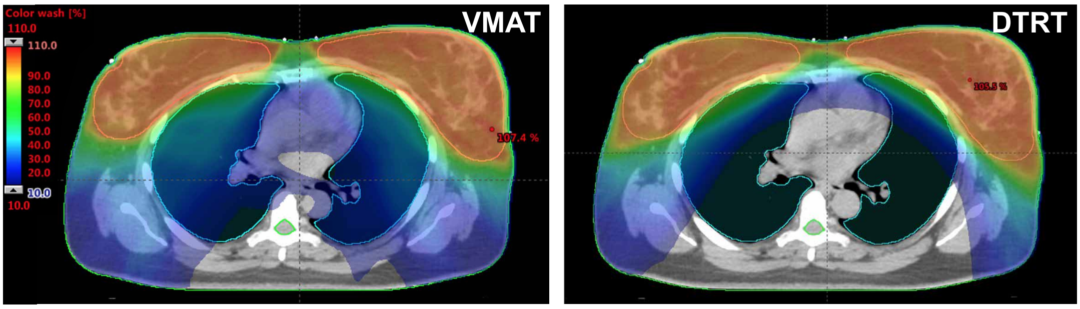

Figure 3.10: Dose distributions of an axial plane shown in color wash of the VMAT plan (left) and of the DTRT plan (right).

addition, the total lung volume receiving at least 5 Gy is 90% in the VMAT plan and 29% in the DTRT plan, which corresponds to a reduction of 67%. In fig. 3.10, the dose distributions of the VMAT and DTRT plans of an axial plane are shown. The total MUs are 1204 for the VMAT plan and 728 for the DTRT plan. The estimated delivery times are 4.5 min for the VMAT plan and 2.4 min for the DTRT plan.

3.5.2 Deliverability and dosimetric validation

The DTRT plan with extended STD for the brain case and the DTRT plan for the CSI case were successfully delivered on a TrueBeam linear accelerator in developer mode without any interlocks. Videos of the deliveries are presented in the supplementary material. The passing rates of the gamma evaluation between the calculated and the measured doses on the EBT3 films are shown in table 3.3.

TABLE 3.3: Passing rates of gamma evaluation between measured and calculated dose distributions.

Plan	film orientation	passing rate 3%/2 mm	passing rate 2%/ 2 mm
DTRT with extended STD	sagittal	99.8%	99.1%
for brain case	coronal	99.2%	96.5%
DTRT for CSI case	sagittal	98.2%	95.6%
	coronal	97.9%	92.1%
DTRT for WBI case	axial	99.1%	97.1%
	coronal	99.2%	95.8%

3.6 Discussion

A TPP for creating non-isocentric DTRT plans was successfully developed and a DAO algorithm for intensity modulation optimization was extended for optimizations of DTRT plans. To demonstrate a possible use case of non-isocentric DTRT, a DTRT plan with an extended STD of 110 cm is compared to the same DTRT plan with normal STD of 110 cm, i.e. an isocentric DTRT plan, for a brain case. The two plans show similar dose distributions and delivery times, but extended STD is expected to reduce the risk of collision. Mullins et al., 2020a demonstrated optimization of non-isocentric DTRT plans using a CG DAO algorithm presented by Renaud, Serban, and Seuntjens, 2017. In their study, DTRT plans at a shortened STD of 80 cm are compared to DTRT plans with normal STD and similar dose distributions are observed. This is consistent with our findings, even though in our case extended instead of shortened STD is investigated.

A second use case of non-isocentric DTRT is demonstrated by creating a DTRT plan for a CSI case including dynamic longitudinal table translations. Compared to the IMRT plan, the DTRT plan shows similar homogeneity in the PTV while improving the dose sparing to the heart, liver and eyes but worsening the dose to the lungs. The low dose bath is slightly higher for the DTRT plan, possibly due to the leakage through the MLC leaves inside the opened secondary collimator jaw area. A possible solution to reduce the low dose bath is enabling dynamic jaw tracking in the optimization or as a post-processing step. In the IMRT plan the jaw area is different for every field and thus less leakage through the MLC leaves occurs. Compared to the IMRT plan, the DTRT plan reduces the estimated delivery time by 45%. Another advantage of the DTRT plan is that the fields do not have field junctions as in the IMRT plan. At the field junctions, there is potential of under- or overdosage if the distance between the isocenters is not consistent (Myers et al. 2013), which makes the setup challenging. Total session time for CSI can thus take up to 20-30 min. In the DTRT plan, there are no field junctions and the plan is potentially more robust against patient setup uncertainties. Thus, the DTRT plan benefits from a simpler patient setup which reduces overall session time.

As a third use case of non-isocentric DTRT, a DTRT plan for a concave target in a bilateral WBI case is created and compared to a multi-isocentric VMAT plan. While the target coverage is maintained in the DTRT plan in comparison with the VMAT plan, the mean dose to the heart is reduced by 40% in the DTRT plan due to the more tangential beam directions in the DTRT plan, which correlates with the risk of heart disease (Darby et al., 2013). Additionally, the mean lung volume receiving 5 Gy is reduced by 67% in the DTRT plan. The delivery time is reduced by 46% in the DTRT plan in comparison with the the VMAT plan. Furthermore, the VMAT plan is a multi-isocentric setup. Because the DTRT plan covers the whole target at once, the DTRT plan might benefit from a simplified setup and thus reduced overall session time in comparison with the VMAT plan similar to the CSI case.

The three non-isocentric DTRT plans were successfully delivered in developer mode on a TrueBeam linear accelerator and the gamma passing rates of the evaluation between measured and calculated dose distributions are above 92% with 2%/2 mm criteria and above 97.9% with 3%/2 mm criteria. Thus, all passing rates are within tolerance recommended by the AAPM TG 218 (Miften et al., 2018) and validation can be judged successful. However, the topic of patient motion when the table is moved should be investigated, similar to the study of Joehl et al., 2018 for the purpose of couch tracking.

A fluence interpolation was introduced in the intensity modulation optimization to consider the dynamic movement of the MLC leaves between CPs. The effect of plan parameters on dosimetric accuracy on calculated dose distributions for VMAT plans has been studied extensively in the past (Bedford, 2009; Masi et al., 2013; Park et al., 2017). For the dose calculation of VMAT plans without fluence interpolation, a fine CP spacing has been recommended by Otto, 2008 and Masi et al., 2013. However, a finer CP spacing increases the optimization computation time and beamlet dose calculation time as well as the necessary computer memory. A dose calculation for VMAT including interpolation of the MLC leaves between CPs has been proposed by Alahmad et al., 2020. However, our results show that consideration of interpolation of the MLC leaves between CPs only in the final dose calculation still leads to a large optimization convergence error. Bedford, 2009, Park et al., 2017 and Christiansen, Heath, and Xu, 2018 implemented a continuous aperture optimization for VMAT similarly to the fluence interpolation in this work. Christiansen, Heath, and Xu, 2018 concluded that the dose prediction error due to omission of fluence interpolation is higher than the dose prediction error due to the static approximation of the CP axes in the beamlet dose calculation. Bedford et al., 2019 implemented an optimization algorithm for dynamic trajectories for Cyberknife and confirmed the findings also for dynamic trajectories. This is consistent with our results for DTRT since the DPE for optimizations with fluence interpolation is an order of magnitude lower in comparison with optimizations without fluence interpolation.

The presented two-step approach of path determination and intensity modulation optimization is beneficial in that it is straight forward to define the table translations for applications following a specific purpose or strategy such as collision avoidance. On the other side, only limited dosimetric information is considered when the paths are set up, which means the paths are potentially suboptimal. For isocentric DTRT also a one-step approach was suggested, where the gantry-table-collimator path is determined simultaneously with the intensity modulation (Dong, Liu, and Xing, 2018; Lyu et al., 2018a; Mullins et al., 2020b; MacDonald et al., 2020). However, finding an optimized path in up to six axes for non-isocentric DTRT is a difficult optimization problem and the number of CPs to be considered and consequently the number of beamlet dose calculations would rise enormously.

The beamlet dose calculations make up the bulk of the calculation time to generate a treatment plan. Including beamlet dose calculation, optimization and final dose calculation, a plan creation can take several hours. However, our beamlet dose calculation framework is currently not outlaid for high computational performance. A more sophisticated approach to reduce computation time for beamlet dose calculation is to implement a GPU-based MC dose calculation algorithm (Jia et al., 2011). More recently, deep neural networks have been used for denoising MC dose calculations (Fu et al., 2020; Bai et al., 2021; Kontaxis et al., 2020). Due to this denoising, the number of simulated particles in the MC algorithm and consequently the calculation time can be greatly reduced.

3.7 Conclusion

In this work, non-isocentric DTRT is enabled by integration of dynamic table translations during beam on. Three different use cases for novel non-isocentric DTRT are presented including validation of delivery and dosimetric accuracy. The demonstrated benefits of non-isocentric DTRT are versatile: reduced risk of collisions for the brain case, reduced setup and delivery time for the CSI case and improved dosimetric plan quality for the bilateral breast case.

3.8 Acknowledgements

This work was supported by grant 200021_185366 of the Swiss National Science Foundation and by Varian, a Siemens Healthineers company. Calculations are performed on UBELIX (http://www.id.unibe.ch/hpc), the high performance computing cluster at the University of Bern.

3.9 Appendix A: Calculation of fluence considering neighbor interpolation

In the following, the formalism of calculating the fluence considering interpolation to the neighboring apertures for one MLC leaf pair j is described.

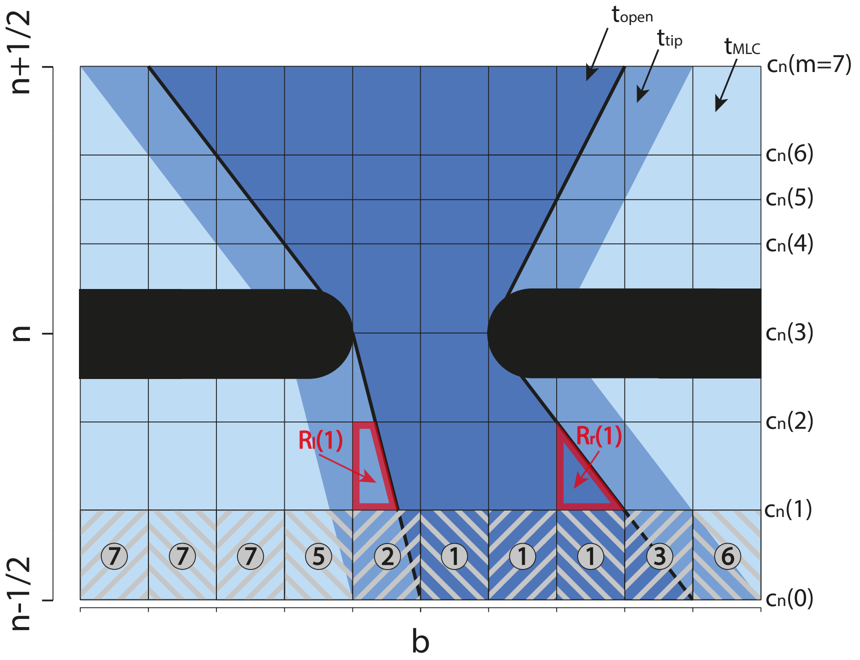

FIGURE 3.11: Illustration of the fluence calculation for one leaf pair at the nth CP. The interpolated leaves move from $n-1/2$ to $n+1/2$. The tips of either the left or the right leaf cross beamlet boundaries in the leaf direction at the positions $c_n(0), \ldots, c_n(7)$ along the CP direction including start and endpoint. Between positions $c_n(0)$ and $c_n(1)$ the case which each beamlet occupies in eq. (3.13) is visualized with the number in each section corresponding to the case number in eq. (3.13). Between positions $c_n(1)$ and $c_n(2)$ the area of the trapezoids $R_l(1)$ and $R_r(1)$ are highlighted, which are used for the fluence calculation in eq. (3.13). The transmission factors t_{open}, t_{tip} and t_{MLC} are used in the fluence calculation to approximate the leakage through the MLC leaves and ar illustrated in different colors.

Let $l_j(n)$ be the position of the left leaf and $r_j(n)$ be the position of the right leaf of the MLC leaf pair j at the nth CP. The fluence of the aperture at the nth CP takes the interpolated leaf positions between $n-1/2$ to $n+1/2$ into account. The leaf positions at $n-1/2$ are calculated using linear interpolation to the next preceding active CP

$$l_j(n-1/2) = \Big(1/(2\cdot q)\Big)\cdot l_j(n-q) + \Big(1-1/(2\cdot q)\Big)\cdot l_j(n) \tag{3.11}$$

$$r_j(n-1/2) = \Big(1/(2\cdot q)\Big)\cdot r_j(n-q) + \Big(1-1/(2\cdot q)\Big)\cdot r_j(n), \tag{3.12}$$

with q CPs between the two apertures. The leaf positions at $n+1/2$ are calculated analogously using linear interpolation to the next succeeding active CP. To calculate the fluence $\phi_n(b,j)$ per beamlet b of the leaf pair j, let $l_j(y)$ and $r_j(y)$ be the linearly interpolated functions of leaf positions with continuous CP position y between $n-1/2$, n and $n+1/2$. Let $c_n\colon [0,1,\dots,m] \to [n-1/2, n+1/2]$ be the function of positions in the CP direction where either $l_j(y)$ or $r_j(y)$ crosses a beamlet border in the leaf direction with $c_n(0) = n-1/2$ and $c_n(m) = n+1/2$ where m is the number of crossings. Start and end point are included as a crossing regardless of position. With this formalism, the fluence can be split up into $k = 0,\dots,m-1$ fluence sections and calculated in the following way:

$$\phi_n(b,j,k) = \begin{cases} t_{open}\cdot(c_n(k+1)-c_n(k)) & \text{1) if } b_l(k) < b < b_r(k) \\ t_{open}\cdot(1-R_l(k)) + t_{tip}\cdot R_l(k) & \text{2) if } b_l(k) = b \text{ and } b < b_r(k) \\ t_{open}\cdot R_r(k) + t_{tip}\cdot\Big(1-R_r(k)\Big) & \text{3) if } b_l(k) < b \text{ and } b = b_r(k) \\ t_{open}\cdot(R_r(k)-R_l(k)) + t_{tip}\cdot(1-R_r(k)+R_l(k)) & \text{4) if } b_l(k) = b \text{ and } b = b_r(k) \\ t_{tip}\cdot(1-R_l(k)) + t_{MLC}\cdot R_l(k) & \text{5) if } b_l(k)-1 = b \\ t_{tip}\cdot R_r(k) + t_{MLC}\cdot(1-R_r(k)) & \text{6) if } b = 1+b_r(k) \\ t_{MLC}\cdot(c_n(k+1)-c_n(k)) & \text{7) else} \end{cases} \tag{3.13}$$

This is illustrated in fig. 3.11. $R_l(k)$ and $R_r(k)$ correspond to the area of the trapezoid shown in the figure and are calculated as follows.

$$R_l(k) = \Big(\tfrac{1}{2}l_j(c_n(k+1)) + \tfrac{1}{2}l_j(c_n(k)) - b_l(k)\Big)\cdot\Big(c_n(k+1)-c_n(k)\Big) \tag{3.14}$$

$$R_r(k) = \Big(\tfrac{1}{2}r_j(c_n(k+1)) + \tfrac{1}{2}r_j(c_n(k)) - b_r(k)\Big)\cdot\Big(c_n(k+1)-c_n(k)\Big) \tag{3.15}$$

$b_l(k)$ and $b_r(k)$ refers to the beamlet, where the left and right leaf tip lies within k and $k+1$, respectively. To consider the leakage through the MLC leaves, three transmission factors ($t_{open}, t_{tip}, t_{MLC}$) are defined, corresponding to no cover with an MLC leaf, cover with the MLC tip and cover with the rest of the MLC leaf. The values for the transmission factors were determined for a specific TrueBeam linear accelerator equipped with a Millennium 120 MLC (Varian, a Siemens Healthineers Company, Germany) and are $1, 0.129, 0.013$ for

TABLE 3.4: Results of the VMAT plans for the H&N case with and without interpolation used during optimization.

	with fluence interpolation				without fluence interpolation				IMRT
$\lambda_{MU} \mid \lambda_{MLC}$	$1 \mid 1$	$1 \mid \infty$	$\infty \mid 1$	$\infty \mid \infty$	$1 \mid 1$	$1 \mid \infty$	$\infty \mid 1$	$\infty \mid \infty$	
Optimization time (min)	31.1	26.6	31.9	28.5	21.0	22.1	25.8	18.3	23.7
Total MUs	579.5	640.6	756.7	824.8	610.7	700.9	772.3	850.9	839.8
Obj. fct. after optim. f_O	1.7	1.2	1.1	0.9	1.2	0.7	0.8	0.6	0.5
Obj. fct. after final dose calc. f_F	13.3	6.0	3.5	2.7	18.7	146.2	10.9	176.0	1.9
Obj. fct. after reoptim. f_R	2.6	2.0	2.0	1.8	3.2	8.9	4.5	11.4	1.4
PTV HI	14.9	14.3	14.5	14.3	17.5	25.6	21.3	28.2	14.1
Estimated delivery time (min)	2.0	6.8	2.4	6.9	2.0	6.6	2.4	6.7	9.2

$t_{open}, t_{tip}, t_{MLC}$, respectively. The fluence $\phi_n(b, j)$ is now calculated by summing over k

$$\phi_n(b, j) = \sum_{k=0}^{m-1} \phi_n(b, j, k). \tag{3.16}$$

3.10 Appendix B: Optimization efficacy

To evaluate the efficacy of the optimization algorithm, a VMAT setup for a unilateral head and neck (H&N) case and the non-isocentric DTRT setup for the CSI case are considered.

The VMAT field setup consists of two arcs for the H&N case with a prescribed dose of 50 Gy to D_{95} of the PTV in 25 fractions. The spacing between CPs is 5° in gantry angle. Treatment plans for the H&N case are created using the following parameters for the optimization of the intensity modulation:

1. Fluence interpolation: yes, no
2. MLC freedom factor λ_{MLC}: 1, ∞
3. MU freedom factor λ_{MU}: 1, ∞

Additionally, an IMRT plan is created with the fields given by the CPs of the paths, where the maximal number of apertures is the same as the number of CPs. Thus, the number of apertures in the IMRT plan are the same as the number of apertures in the VMAT plans with the possibility of multiple apertures at one CP.

In table 3.4 the objective function values after the optimization f_O, after the final dose calculation f_F and after the reoptimization f_R of the VMAT plans for the H&N case are shown. As can be seen, there is a much greater difference between f_O, f_F and f_R without fluence interpolation than with fluence interpolation. Figure 3.12 shows the dosimetric differences between optimizations

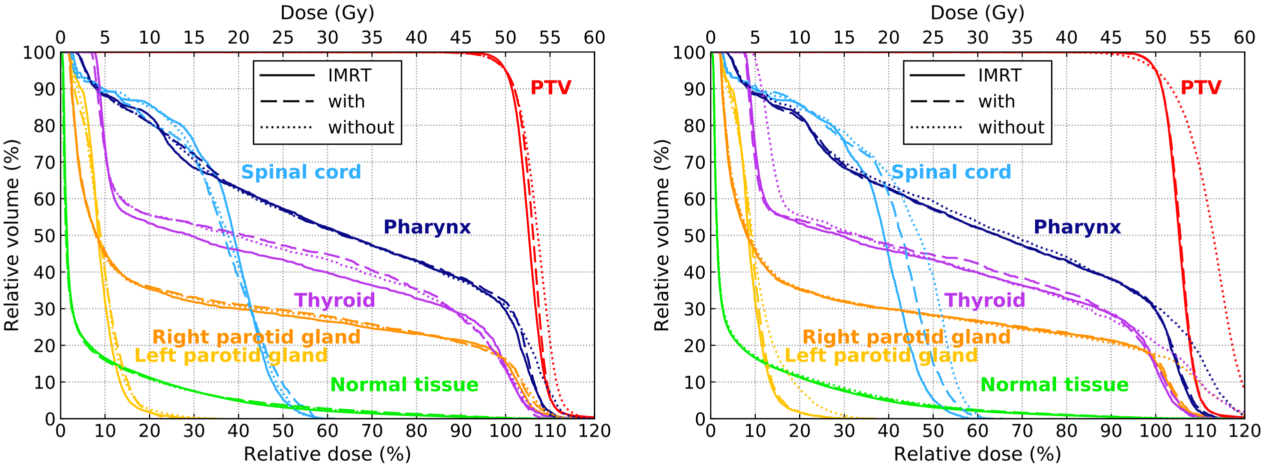

(a) $\lambda_{MU} = 1$ and $\lambda_{MLC} = 1$ (b) $\lambda_{MU} = \infty$ and $\lambda_{MLC} = \infty$

FIGURE 3.12: DVH comparison of plans with and without consideration of fluence interpolation and the benchmark IMRT plan for the H&N case after the final dose calculation and MU weight reoptimization.

performed with and without fluence interpolation for the two extreme settings of $\lambda_{MU} = 1$, $\lambda_{MLC} = 1$ and $\lambda_{MU} = \infty$, $\lambda_{MLC} = \infty$ of the VMAT plan and the benchmark IMRT plan. It is visible that while the PTV homogeneity and doses to OARs decrease with increasing freedom for the plans with fluence interpolation, the PTV homogeneity and maximum doses to OARs increase with increasing freedom for the plans without fluence interpolation. Thus, optimizations without fluence interpolation show inaccuracies in dose prediction, which cannot be accounted for with the MU weight reoptimization. The plans with fluence interpolation are similar to the benchmark IMRT plan.

The DTRT setup for the CSI case is the same as in section 3.4.2 with the spacing of CPs set to 5° along the gantry direction, $\lambda_{MU} = 2$ and $\lambda_{MLC} = 1$. For the spacing along the longitudinal table axis and fluence interpolation, following parameters are used:

1. Fluence interpolation: yes, no
2. CP spacing in longitudinal direction: 1 cm, 2 cm and 4 cm

In figure B2(a) the objective function values after the optimization f_O, after the final dose calculation f_F and after the reoptimization f_R of the DTRT plans for the CSI case are shown. The values are similar for a spacing of 1 cm with and without fluence interpolation but diverge increasingly for 2 cm and 4 cm without fluence interpolation. In figure B2(b), the DVHs of the final DTRT

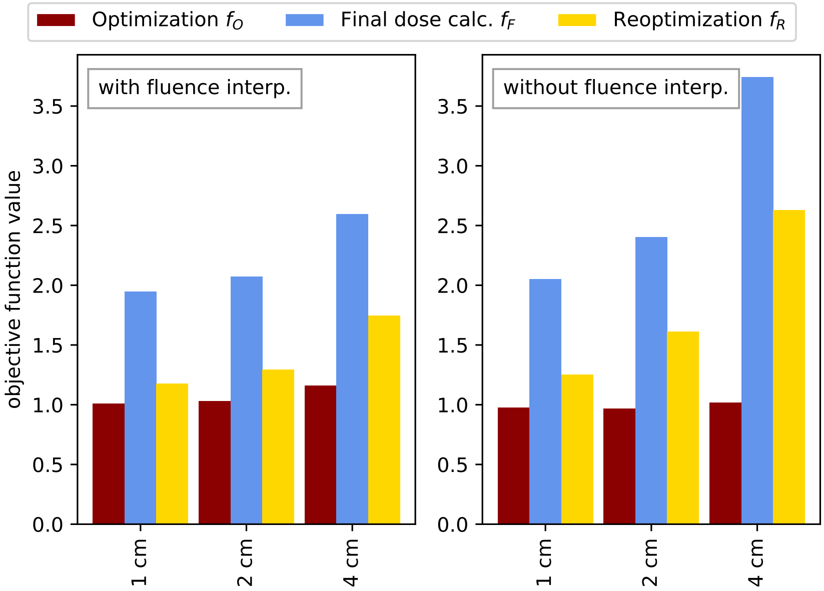

(a) Objective function values

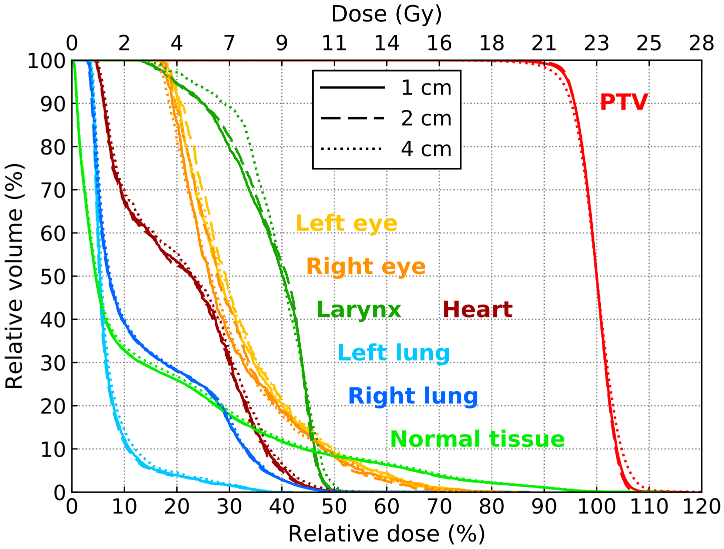

(b) DVH

FIGURE 3.13: a) Objective function values after the optimization f_O, after the final dose calculation f_F and after the reoptimization f_R of the DTRT plans for the CSI case with CP spacing along the longitudinal axis set to 1 cm, 2 cm and 4 cm and with and without fluence interpolation applied. b) DVHs of the final DTRT plans with fluence interpolation for CP spacing of 1 cm, 2 cm and 4 cm.

plans with fluence interpolation for 1, 2 and 4 cm spacing are shown. As can be seen, the DVHs of the plans with 1 cm and 2 cm are similar, while for 4 cm the dose homogeneity in the PTV is lower and the dose to the larynx is higher. Thus, a spacing of 2 cm in table translation provides similar results to a 1 cm spacing for optimizations with fluence interpolation, but optimizations with a coarser spacing are not able to accurately predict the dose for the investigated CSI case.

4

Delivery time reduction for mixed photon-electron radiotherapy by using photon MLC collimated electron arcs

Gian Guyer[1], Silvan Mueller[1], Paul-Henry Mackeprang[1], Daniel Frei[1], Werner Volken[1], Daniel M. Aebersold[1], Kristina Loessl[1], Peter Manser[1], Michael K. Fix[1]

[1] Division of Medical Radiation Physics and Department of Radiation Oncology, Inselspital, Bern University Hospital, and University of Bern, Bern, Switzerland

Published in
Physics in Medicine and Biology
2023, Vol. 68 No. 21, 215009
DOI: 10.1088/1361-6560/ad021a

4.1 Preface

In the last chapter, the treatment planning process was extended to create treatment plans with photon arcs and trajectories. In this next project, the developed treatment planning process is further extended to include also electron arcs. The treatment planning process is used to create mixed photon-electron radiotherapy plans including electron arcs, which are compared to photon-only techniques and mixed photon-electron radiotherapy plans with electron beams with a static gantry angle.

Contribution: G. Guyer developed the methodology and wrote the code for this study, performed the validation measurements, performed the treatment planning, analysis and interpretation of the data and created all figures. G. Guyer wrote the manuscript with critical feedback from all co-authors.

4.2 Abstract

Objective: Electron arcs in mixed-beam radiotherapy (Arc-MBRT) consisting of intensity-modulated electron arcs with dynamic gantry rotation potentially reduce the delivery time compared to mixed-beam radiotherapy containing electron beams with static gantry angle (Static-MBRT). This study aims to develop and investigate a treatment planning process (TPP) for photon multileaf collimator (pMLC) based Arc-MBRT.

Approach: An existing TPP for Static-MBRT plans is extended to integrate electron arcs with a dynamic gantry rotation and intensity modulation using a sliding window technique. The TPP consists of a manual setup of electron arcs, and either static photon beams or photon arcs, shortening of the source-to-surface distance for the electron arcs, initial intensity modulation optimization, selection of a user-defined number of electron beam energies based on dose contribution to the target volume and finally, simultaneous photon and electron intensity modulation optimization followed by full Monte Carlo dose calculation. Arc-MBRT plans, Static-MBRT plans, and photon-only plans were created and compared for four breast cases. Dosimetric validation of two Arc-MBRT plans was performed using film measurements.

Main results: The generated Arc-MBRT plans are dosimetrically similar to the Static-MBRT plans while outperforming the photon-only plans. The mean heart dose is reduced by 32% on average in the MBRT plans compared to the photon-only plans. The estimated delivery times of the Arc-MBRT plans are similar to the photon-only plans but less than half the time of the Static-MBRT plans. Measured and calculated dose distributions agree with a gamma passing rate of over 98% (3% global, 2 mm) for both delivered Arc-MBRT plans.

Significance: A TPP for Arc-MBRT is successfully developed and Arc-MBRT plans showed the potential to improve the dosimetric plan quality similar as Static-MBRT while maintaining short delivery times of photon-only treatments. This further facilitates integration of pMLC-based MBRT into clinical practice.

4.3 Introduction

In external beam radiotherapy, photon treatments performed in clinical routine are typically applied using the photon multileaf collimator (pMLC) integrated into the treatment head of a linear accelerator. The introduction of the pMLC facilitated intensity-modulated radiotherapy (IMRT), which improved target dose conformality compared to 3D conformal radiotherapy (Bortfeld, 2006). Volumetric modulated arc therapy (VMAT) has improved upon the delivery efficiency of IMRT while maintaining the dosimetric plan quality by combining synchronized intensity modulation and dynamic gantry rotation (Otto, 2008; Teoh et al., 2011).

Meanwhile, standard electron treatments are still applied using patient-specifically fabricated cerrobend cut-outs placed in dedicated electron applicators mounted onto the linear accelerator head for every field and treatment fraction. This makes electron treatments inefficient and cumbersome. Furthermore, using cut-outs for energy modulation or intensity modulation of electron beams is practically infeasible (Hogstrom and Almond, 2006). This infeasibility makes electron treatments in inhomogeneous media challenging, where energy modulation is necessary (Åsell et al., 1997). Likewise, electron treatments of large targets such as chest wall irradiation are challenging, because multiple conformal electron beams from different directions create hot or cold spots (Khan et al., 1977). To avoid such hot and cold spots, techniques such as electron arc therapy (EAT) have been developed (Khan et al., 1977; Leavitt et al., 1985; McNeely et al., 1988; Leavitt and Stewart, 1993; Gaffney et al., 2001; Sharma et al., 2011). In EAT, a narrow electron field is rotated around the patient. Custom secondary collimators are mounted onto the gantry and tertiary collimators, and boli are placed on the patient (Leavitt et al., 1985). The main disadvantage of EAT is that the treatment planning and fabrication and mounting of the custom collimators is very labour and time intensive. More recently, Rodrigues, Yin, and Wu, 2014 proposed an EAT technique called dynamic electron arc radiotherapy (DEAR) with a mounted standard applicator and cut-out, reducing the time needed to manufacture custom collimators. To avoid collisions between the applicator and the patient, the table translates synchronously with the gantry rotation. However, an applicator still has to be mounted onto the gantry for every treatment fraction, and dynamic collimation of the beam is not possible. Furthermore, the short distance between the end of the applicator and the patient may increase the collision risk.

To overcome these limitations, some research groups investigated different motorized collimators for electron treatments aiming at replacing the cut-outs and applicators. The investigated collimators were a few leaf electron collimator (FLEC) (Al-Yahya et al., 2005a; Al-Yahya et al., 2005b; Al-Yahya, Verhaegen, and Seuntjens, 2007; Alexander, DeBlois, and Seuntjens, 2010; Alexander et al., 2011), a custom electron multileaf collimator (eMLC) (Ma et al., 2000; Gauer et al., 2008; Engel and Gauer, 2009; Vatanen, Traneus, and Lahtinen, 2009; O'Shea et al., 2011; Eldib et al., 2013; Jin et al., 2014), and the existing pMLC (du Plessis et al., 2006; Jin et al., 2008; Klein, Mamalui-Hunter, and Low, 2008; Klein et al., 2008; Salguero et al., 2010; Surucu et al., 2010; Mihaljevic et al., 2011; Henzen et al., 2014a; Henzen et al., 2014b; Mueller et al., 2018a; Fix et al., 2023). Additionally, these motorized collimators make intensity and energy modulation of electron beams feasible in modulated electron radiotherapy (MERT). The pMLC has the additional advantage that no additional hardware needs to be mounted onto the gantry head for every fraction.

However, pMLC collimated electron beams have a larger beam penumbra due to increased scatter within the larger volume of air between the end of the pMLC and the patient (Mueller et al., 2018a). Reducing the source-to-surface distance (SSD) by moving the patient closer to the gantry reduces the beam penumbra. Although, a very short SSD poses a collision risk between the gantry and the patient. It has been shown that electron-only plans do not achieve the same dose homogeneity in the target as photon-only plans (Surucu et al., 2010; Alexander et al., 2011; Henzen et al., 2014b; Mueller et al., 2017; Renaud, Serban, and Seuntjens, 2017). A possible solution to overcome these dosimetric limitations of electron beams is to combine electron and photon beams in mixed beam radiotherapy (MBRT) (Li et al., 2000; Korevaar et al., 2002; Mu et al., 2004; Xiong et al., 2004; Palma et al., 2012; Rosca, 2012; Renaud, Serban, and Seuntjens, 2017; Míguez et al., 2017; Mueller et al., 2017; Mueller et al., 2018a; Renaud, Serban, and Seuntjens, 2019; Heath et al., 2021; Heng et al., 2021). Mueller et al., 2017 showed that pMLC-based intensity-modulated electron beams combined with static photon beams or photon beams with dynamic trajectories (Mueller et al., 2018b) improved dosimetric plan quality compared to photon-only treatments. However, until now MBRT only contains electron beams delivered from a static gantry angle (Static-MBRT), which results in substantially longer delivery times for Static-MBRT plans compared to VMAT. Besides less patient throughput, longer delivery times might also increase the intrafraction motion and impact patient comfort negatively. We hypothesize that using electron beams with a dynamic gantry rotation during beam-on combined with photon beams (Arc-MBRT) improves the delivery efficiency and thus further facilitates clinical implementation of mixed photon-electron beam treatments.

The aim of this work is to develop a treatment planning process (TPP) to create Arc-MBRT plans consisting of both photon and electron beams with dynamic gantry rotation and pMLC sliding window-based intensity modulation. Several breast cases are investigated retrospectively to demonstrate the delivery efficiency, dosimetric accuracy, and dosimetric plan quality of Arc-MBRT.

4.4 Methods

An existing TPP used for creating Static-MBRT plans (Mueller et al., 2017; Mueller et al., 2022) was extended to accommodate electron beams with a dynamic gantry rotation and sliding window-based intensity modulation, called electron arcs henceforth. The TPP is described in the following subsection. The second subsection describes the investigations of the TPP for Arc-MBRT and describes the dosimetric validation of Arc-MBRT plans.

4.4.1 Treatment planning process

Beam setup

The first part in the TPP illustrated in fig. 4.1 consists of the manual setup of electron arcs and setup of photon beams within a research version of Eclipse. This research version is embedded in the Aria framework v15.6 (Varian, a Siemens Healthineers Company, Germany). The user needs to define the gantry range, collimator and table rotation angle for electron arcs. Due to the finite range of electron beams, the gantry range for the electron arcs is suggested to be set to the area where the planning target volume (PTV) is close to the patient's surface. For the defined gantry range, electron arcs are set up for

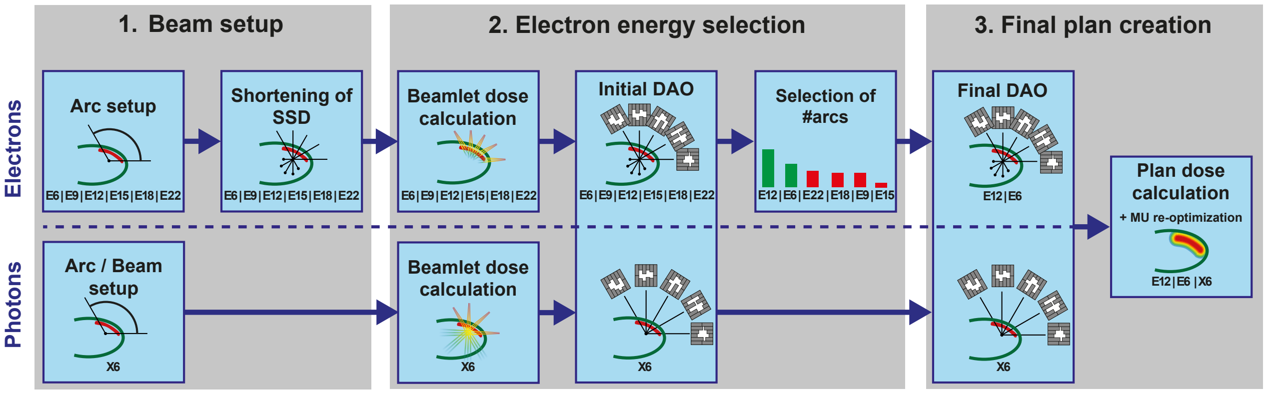

FIGURE 4.1: Illustration of the treatment planning process to create Arc-MBRT plans. The upper half describes the steps for the electron beams, while the steps for the photon beams are described in the lower half. SSD: source-surface distance. DAO: direct aperture optimization. Eβ: Electron arc with an energy of β MeV. X6: 6 MV photon arc / beam. MU: Monitor unit.

all available electron beam energies with control points (CPs) every 5°. Additionally, the user defines photon beams, consisting either of 3D conformal or intensity-modulated photon beams with a static gantry angle or photon arcs with dynamic gantry rotation (with CPs every 5°). The beams with static gantry angle are called static beams from now on.

Next, the position of the isocenter is shifted for every CP of the electron arcs along the central axis such that the SSD matches a user defined setting $\text{SSD}_{desired}$. This allows to shorten the distance between the gantry head and the patients' surface, which influences the amount of in-air scatter of the electron beams. A shorter SSD hence means a smaller beam penumbra for the electron beams. For this, the current SSD along the central axis $\text{SSD}_{current}$ is calculated and the position of the isocenter is shifted $\Delta_{lateral}$, $\Delta_{vertical}$, and $\Delta_{longitudinal}$ cm along the central beam direction for every CP to match $\text{SSD}_{desired}$. The central beam direction is defined by the the gantry rotation angle α_{gantry} and table rotation angle α_{table} of the CP. The isocenter shift is calculated using the following equations:

$$\Delta_{lateral} = (\text{SSD}_{desired} - \text{SSD}_{current}) \cdot \sin(-\alpha_{gantry}) \cdot \cos(\alpha_{table}) \tag{4.1}$$

$$\Delta_{vertical} = (\text{SSD}_{desired} - \text{SSD}_{current}) \cdot \cos(\alpha_{gantry}) \tag{4.2}$$

$$\Delta_{longitudinal} = (\text{SSD}_{desired} - \text{SSD}_{current}) \cdot \sin(-\alpha_{gantry}) \cdot \sin(\alpha_{table}) \tag{4.3}$$

This results in a dynamic table translation synchronous with the gantry rotation to keep the fixed SSD along the central axis for the electron arcs.

Electron energy selection

In the second part of the TPP, the number of electron arcs is reduced to a user-defined number to control the number of total electron arcs in the plan. Because an electron arc was set up for each available beam energy, the delivery time would be unnecessarily long if all electron arcs are used. Thus, the most important electron beam energies are selected based on an initial intensity modulation optimization of all electron arcs and photon beams. For this, a beamlet dose calculation is performed for every CP of electron and photon arcs and static beam using the Eclipse research version interfaced Swiss Monte Carlo Plan (SMCP) (Fix et al., 2007). In SMCP, pre-simulated beamlet phase spaces and the Macro Monte Carlo (MMC) (Neuenschwander, Mackie, and Reckwerdt, 1995; Fix et al., 2013) and Voxel Monte Carlo (VMC++) (Kawrakow and Fippel, 2000) dose calculation algorithms are used for electron and photon beams, respectively. The beamlet size is 0.5 cm × 0.5 cm or 0.5 cm × 1 cm in the isocenter plane, depending on the width of the pMLC leaf. For static conformal photon beams, a dose calculation of the whole beam is performed using VMC++. The beamlet dose distributions are then used for the intensity modulation optimization based on a hybrid direct aperture optimization (H-DAO) (Mueller et al., 2022). In H-DAO, apertures describing the pMLC shapes and monitor unit (MU) weights are determined using a hybrid column generation and simulated annealing approach. With column generation, apertures are iteratively generated and with simulated annealing, the shapes and MU weights of the apertures are refined after each aperture addition. For each CP of electron and photon arcs, exactly one aperture is determined, while for static beams a user defined number of apertures is generated. For static conformal photon beams, no apertures are generated, but the MU weight of the static conformal photon beam is simultaneously optimized with the MU weights of the apertures of the electron arcs. The optimization is finished when every CP has exactly one aperture and the static beams have their total number of apertures assigned. For all arcs, the movement range of the pMLC leaves is restricted such that the gantry rotation is not slowed down by the leaf movement and the MU weight is restricted such that the gantry rotation is maximally slowed down to half the full speed. During the optimization, the fluence belonging to an electron or photon aperture is interpolated between consequent CPs as described by Guyer et al., 2022 to account for the continuous movement of the pMLC leaves. For photons, the transmission through the pMLC is considered during the optimization, while for the electrons it is assumed that the transmission through the pMLC is zero due to the thickness of the pMLC.

After the initial DAO, the dose contribution of each electron arc to the PTV is calculated. The electron arcs are then ranked according to their PTV dose contribution from highest to lowest. Only the highest-ranking electron arcs, up to the user-defined number, are kept while the others are discarded.

Final plan creation

In the third part, a final DAO is performed with the remaining electron arcs and the photon beams. After all apertures are determined, a dose calculation is performed for each aperture using the SMCP framework (Fix et al., 2007; Manser et al., 2019) considering the exact geometry of the pMLC and the full dynamic movement of the pMLC, table and gantry between consecutive CPs for photon and electron arcs. The source for the electron beams is a validated multiple source model (Henzen et al., 2014a; Fix et al., 2023), consisting of a primary and a jaw source and the dose is calculated using the MMC algorithm. The source of the photon beams is a pre-simulated phase-space located on a plane above the secondary collimator jaws and the dose is calculated using the VMC++ algorithm. After the dose calculation, a MU weight reoptimization is performed to mitigate the differences between the beamlet-based and final dose distributions. Finally, the dose from all apertures is summed to get the plan dose. All dose distributions in this work use a voxel size of $2.5 \times 2.5 \times 2.5\ mm^3$ and the mean statistical uncertainty of the dose in voxels receiving at least 50% of the maximum dose is less than 0.5%.

TABLE 4.1: Beam setup for the Arc-MBRT plans used for investigation of the influence of the number of electron arcs on the resulting treatment plan. The table rotation angle is 0° for all beams. Split beam refers to splitting the beam size using the x-jaws.

	Beam	Gantry angle (°)	Collimator angle (°)
Case 1: Right WBI	2 static conformal photon beams	-123 and 60	102 and 75
	1 − 6 electron arcs	-100 – 30	0
Case 2: Left WBI	2 photon arcs (split beam)	-60 – 155	355
	2 photon arcs (split beam)	-60 – 155	95
	1 − 6 electron arcs	-40 – 80	0
Case 3: Right WBI+LNI	2 photon arcs (split beam)	-155 – 50	355
	2 photon arcs (split beam)	-155 – 50	95
	1 − 6 electron arcs	-100 – 40	0
Case 4: Left WBI+LNI	2 photon arcs (split beam)	-60 –180	355
	2 photon arcs (split beam)	-60 –180	95
	1 − 6 electron arcs	-40 – 110	0

4.4.2 Treatment plan investigations

Four breast cases were selected for retrospective investigation, each with a prescribed total dose of 42.4 Gy to the median dose in the planning target volume (PTV) in 16 fractions. One case is a right-sided whole breast irradiation (WBI) case without axillary lymph node irradiation (LNI), which was clinically treated with 3D conformal radiotherapy (CRT) using two tangential photon beams (case 1). One case is a left-sided WBI case without axillary LNI (case 2), one case is a right-sided WBI case including axillary LNI (case 3) and one case is a left-sided WBI case including axillary LNI (case 4). The cases were selected for the following purposes:

1. To investigate the influence of the number of electron arcs on the resulting plan.
2. To evaluate the dosimetric plan quality and delivery time of Arc-MBRT for breast treatments compared to Static-MBRT and photon-only treatments.
3. To validate the deliverability of Arc-MBRT plans in terms of dosimetric accuracy.

For the first purpose, six Arc-MBRT plans are created for each of the four cases. The six Arc-MBRT plans have a varying number of electron arcs, ranging from 1 to 6 arcs. A plan with 1 electron arc means, that only one electron beam energy is used while a plan with 6 electron arcs means, that all electron beam energies are used, and no arcs were discarded in the electron arcs selection step. The available electron beam energies are 6, 9, 12, 15, 18, and 22 MeV. For all electron arcs, the SSD is shortened to 80 cm as a compromise between reducing the in-air scatter and ensuring collision-free delivery (Mueller et al., 2018a; Ma et al., 2019). The photon beam setup for case 1 (right WBI) consists of two static conformal tangential beams and of four partial VMAT arcs for the other three cases. The beam setups are illustrated in fig. 4.2 and described in detail in table 4.1. For all plans, the dose contribution to the PTV of the electron and photon beams is investigated and the dosimetric plan quality of the plans with 2 and 6 electron arcs are analyzed in detail.

For the second purpose, Arc-MBRT plans, Static-MBRT plans, and photon-only plans are created and the dosimetric plan quality and the estimated delivery time is compared for all plans of the four cases. The different plans are described in detail in table 4.2. All electron arcs and static electron beams have an SSD of 80 cm. Comparisons between the dosimetric plan quality of the resulting plans is performed by analyzing dose-volume histogram (DVH) parameters for

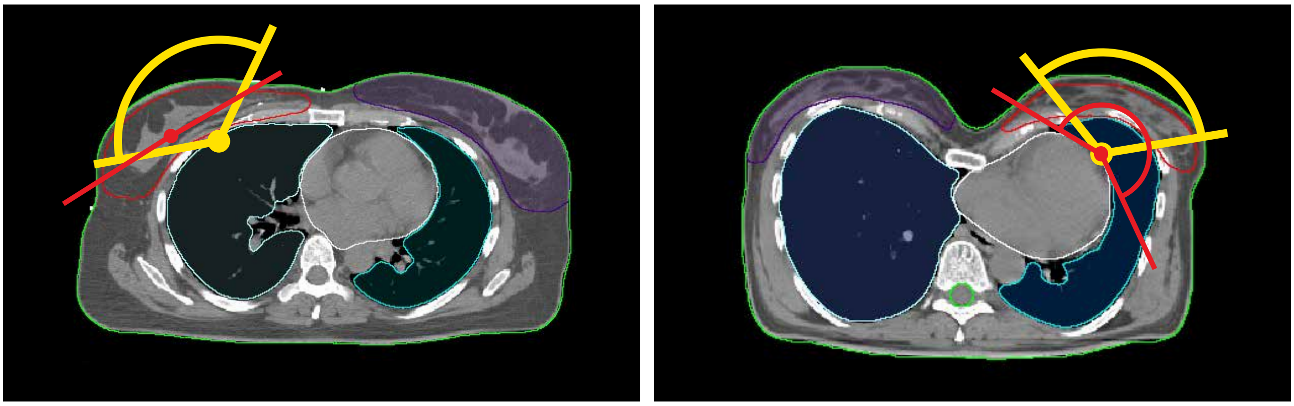

(a) Case 1: Right WBI

(b) Case 2: Left WBI

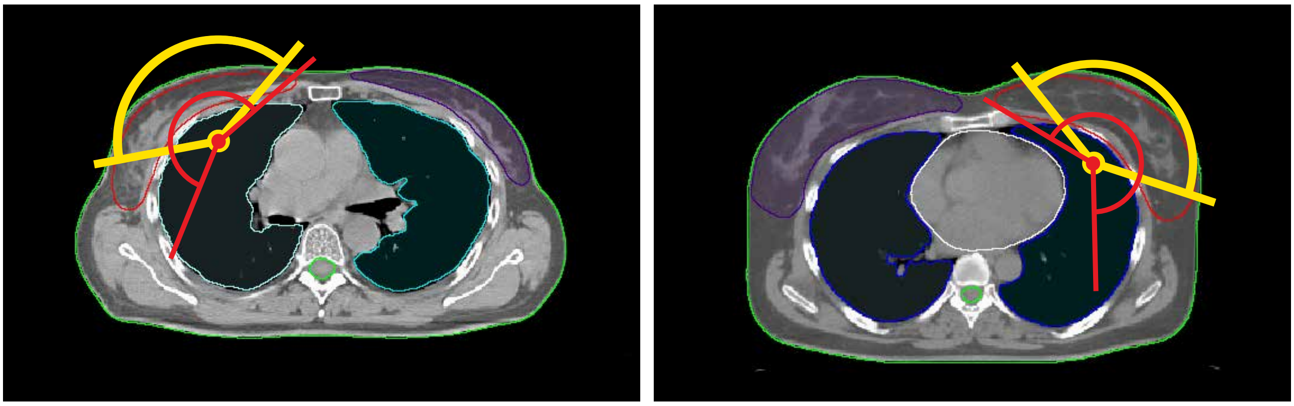

(c) Case 3: Right WBI+LNI

(d) Case 4: Left WBI+LNI

Figure 4.2: Illustration of the beam setup of the Arc-MBRT plans for the four cases. The gantry angle range of the electron arcs is indicated in yellow and the static gantry angles (a) and gantry angle ranges (b, c, d) of the photon beams are indicated in red. WBI: whole breast irradiation. LNI: lymph node irradiation

Table 4.2: Beam setup for the plans used for investigating the dosimetric plan quality of Arc-MBRT. In brackets, the gantry ranges and gantry angles of the photon and electron beams are indicated. The table angle is 0° for all beams. The photon arcs are always split beams using the x-jaws.

	Plan (electrons | photons)	Electron beams	Photon beams
Case 1: Right WBI	Arc-MBRT (2 arcs | 2 static conf)	2 arcs (-100° – 30°)	2 static conformal (-123° & 60°)
	Static-MBRT (3 static | 2 static conf)	3 static (-80°, -35° and 0°)	2 static conformal (-123° & 60°)
	CRT (0 | 2 static conf)	–	2 static conformal (-123° & 60°)
	Arc-MBRT (2 arcs | 2 static)	2 arcs (-100° – 30°)	2 static (-123° & 60°)
	Static-MBRT (3 static | 2 static)	3 static (-80°, -35° and 0°)	2 static (-123° & 60°)
	IMRT (0 | 2 static)	–	2 static (-123° & 60°)
	Arc-MBRT (2 arcs | 2 arcs)	2 arcs (-100° – 30°)	2 arcs (-160° – 60°)
	Static-MBRT (3 static | 2 arcs)	3 static (-80°, -35° and 0°)	2 arcs (-160° – 60°)
	VMAT (0 | 4 arcs)	–	4 arcs (-160° – 60°)
Case 2: Left WBI	Arc-MBRT (2 arcs | 4 arcs)	2 arcs (-40° – 80°)	4 arcs (-60° – 155°)
	Static-MBRT (3 static | 4 arcs)	3 static (-30°, 28° and 63°)	4 arcs (-60° – 155°)
	VMAT (0 | 6 arcs)	–	6 arcs (-60° – 155°)
Case 3: Right WBI+LNI	Arc-MBRT (2 arcs | 4 arcs)	2 arcs (-100° – 40°)	4 arcs (-155° – 50°)
	Static-MBRT (3 static | 4 arcs)	3 static (-76° - 46° and 0°)	4 arcs (-155° – 50°)
	VMAT (0 | 6 arcs)	–	6 arcs (-155° – 50°)
Case 4: Left WBI+LNI	Arc-MBRT (2 arcs | 4 arcs)	2 arcs (-40° – 110°)	4 arcs (-60° – 180°)
	Static-MBRT (3 static | 4 arcs)	3 static (-25°, 33° and 79°)	4 arcs (-60° – 180°)
	VMAT (0 | 6 arcs)	–	6 arcs (-60° – 180°)

the PTV, heart, lung, contralateral breast and spinal canal. For the PTV, the Paddick conformity index (CI) (Paddick, 2000) and homogeneity index (HI $= (D_{2\%} - D_{98\%})/D_{50\%}$) are calculated and compared, where $D_{X\%}$ represents the minimum dose in $X\%$ of the PTV volume. The estimated delivery times are calculated by summing the time per CPs of all arcs and beams of one plan, while the accelerations of the mechanical axes are neglected. Additionally, the time to move all axes to the starting position of the next arc / beam is taken into account with a minimum time of 20 s for switching between photon and electron beams and between different electron energies.

For the third purpose, the Arc-MBRT plans for the left WBI and right WBI+LNI cases (cases 2 & 3) are delivered on a TrueBeam linear accelerator (Varian, a Siemens Healthineers Company, Germany) equipped with a Millennium 120 pMLC (Varian, a Siemens Healthineers Company, Germany) in developer mode. The dose is measured using radiochromic EBT3 film sheets (Ashland Advanced Materials, Bridgewater, NJ) placed in 1 cm depth inside a PMMA cube. Film measurements are taken for each plan for the following deliveries:

1. The total plan (each consisting of two electron and four photon arcs).
2. Only the electron arcs of each plan.
3. The electron arcs with a collapsed gantry angle to 0°.

The reason for these different deliveries is to measure individually the dosimetric accuracy of the whole plan, of the electron arcs and the sliding window technique for electrons. The film sheets are scanned using an Epson XL 10000 flatbed scanner (Seiko Epson Co., Tokyo, Japan) 18h after irradiation. The scanned films are corrected for the lateral response artifact of the scanner using a one-dimensional linear correction function (Lewis and Chan, 2015), converted to absolute dose using a triple channel calibration (Micke, Lewis, and Yu, 2011) and rescaled according to the one-scan protocol by using two additional film strips (Lewis et al., 2012). The resulting dose distribution of the red channel is compared to the corresponding 2D plane of the dose recalculated for the PMMA cube using a gamma evaluation with a 3% (global) / 2 mm criterion and a 10% low-dose threshold of the maximum dose.

4.5 Results

4.5.1 Number of electron arcs

The dose contributions to the PTV of the different electron and photon beams in Arc-MBRT plans varying in the number of electron arcs are shown in fig. 4.3 for the four cases. For case 1 (right WBI), the electron dose contribution increases from 31% to 51% with increasing number of electron arcs. For case 2 (left WBI), the electron dose contribution is between 13% and 19% for all six plans. The electron dose contribution for case 3 (right WBI+LNI) increases from 11% to 29% from one to six electron arcs. Similarly, the electron dose contribution for the Left WBI+LNI case increases from 16% to 28% from one to six electron arcs. The electron dose contribution is almost twice as high in case 1 (right WBI) compared to all other cases. Overall, the lower three electron energies contribute more than half of the electron dose contribution for all four cases.

In fig. 4.4, the DVHs of Arc-MBRT plans with 2 and 6 electron arcs are shown. For case 1 (right WBI), the maximum dose to the ipsilateral lung slightly decreases while the low-dose bath to the lung slightly increases from 2 to 6 electron arcs. The PTV coverage and dose to the OARs are similar for case 2 (left WBI). The two-electron arc plan of case 3 (right WBI+LNI) has a higher maximum dose to the spinal canal and a slightly increased mean dose to the contralateral lung while maintaining the same PTV coverage as the six-electron arc plan. For case 4 (left WBI+LNI), the PTV coverage and dose to OARs is similar between the 2 and 6 electron arc plans. Overall, the dosimetric plan quality is similar between the two plans for each of the four cases.

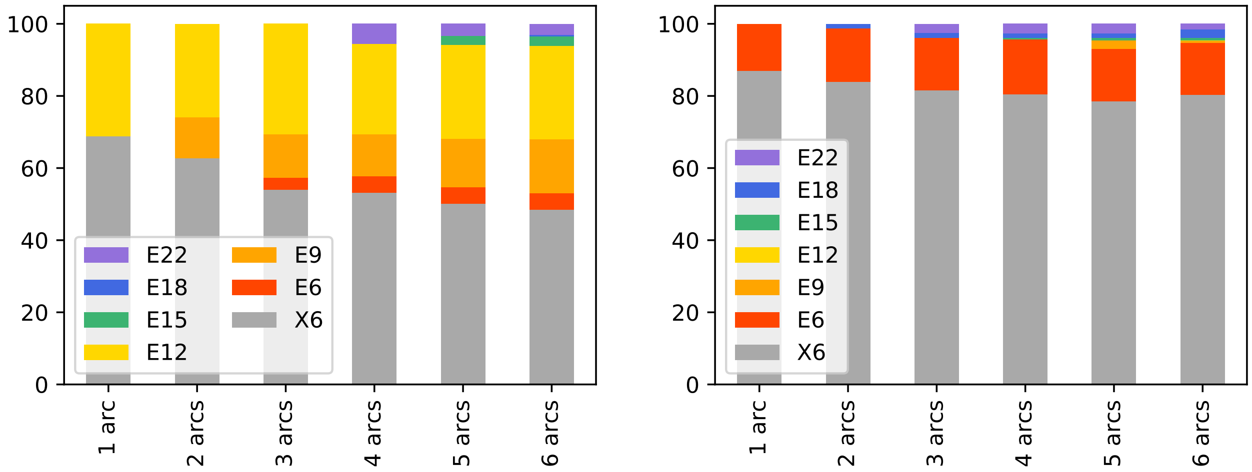

(a) Case 1: Right WBI (b) Case 2: Left WBI

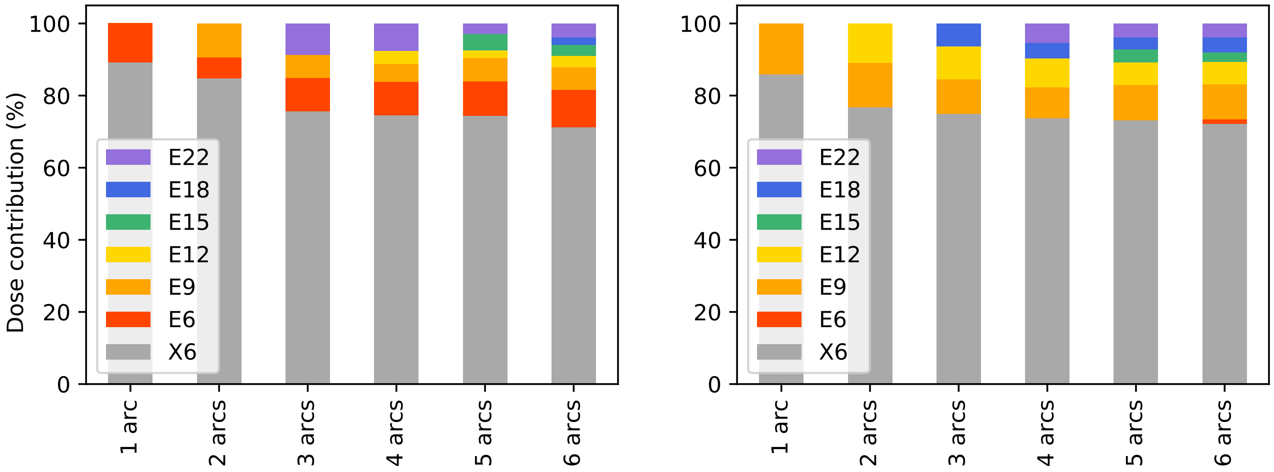

(c) Case 3: Right WBI+LNI (d) Case 4: Left WBI + LNI

FIGURE 4.3: Dose contribution to the PTV of electron and photon beams in Arc-MBRT plans with the number of electron arcs ranging from 1 to 6 arcs for all four cases. Eβ: Electron arc with an energy of β MeV. X6: VMAT arc with 6 MV photons.

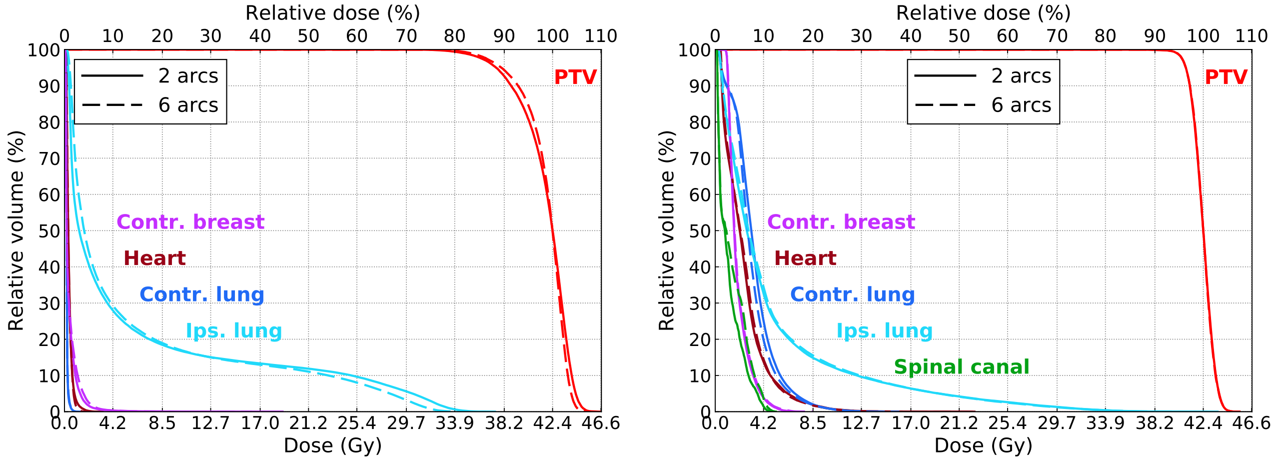

(a) Case 1: Right WBI

(b) Case 2: Left WBI

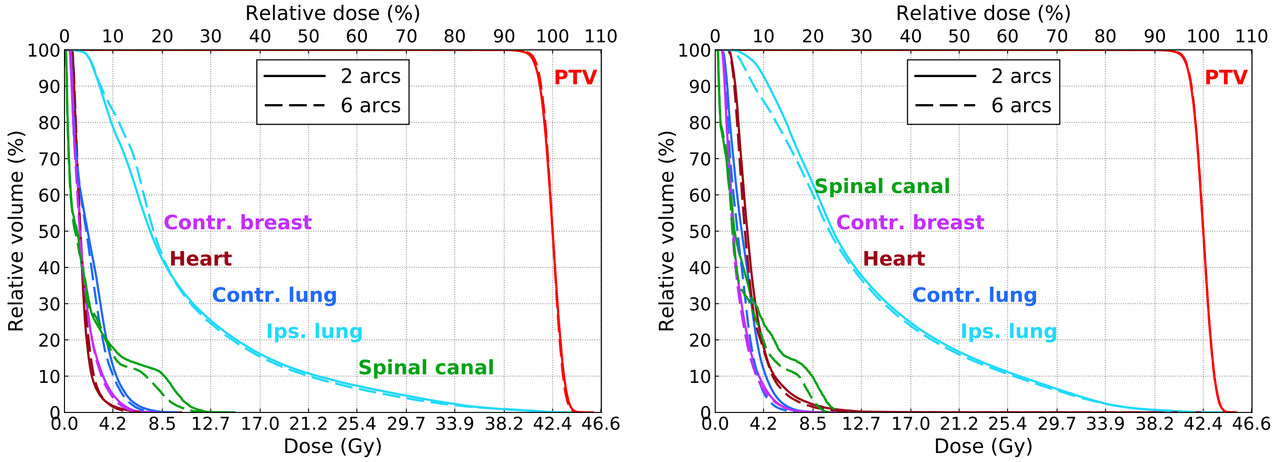

(c) Case 3: Right WBI+LNI

(d) Case 4: Left WBI + LNI

FIGURE 4.4: DVH comparisons of Arc-MBRT plans with 2 and 6 electron arcs for each of the four cases.

4.5.2 Dosimetric investigations

Case 1: Right WBI

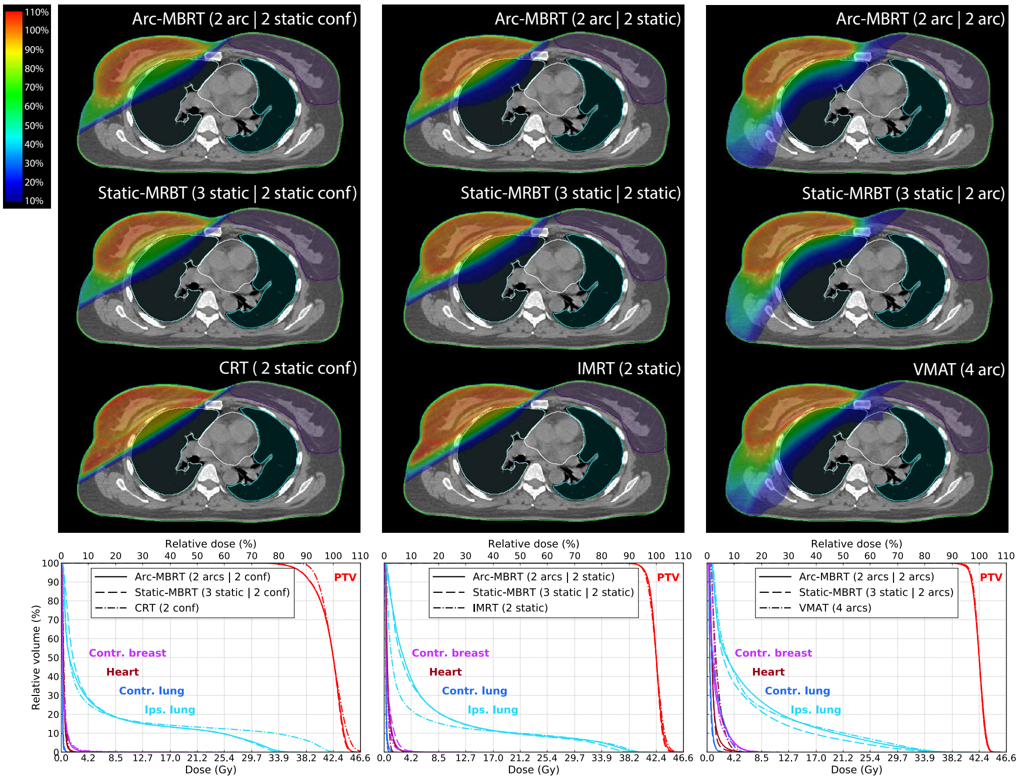

FIGURE 4.5: Dose color wash comparison (top) on a representative transversal plane and DVH comparison (bottom) of the Arc-MBRT, Static-MBRT and photon-only plans for case 1 (right WBI). To distinguish between the different photon beam setups, the electron and photon beams are indicated in brackets.

The results of the dosimetric comparison for case 1 (right WBI) are shown in fig. 4.5. The dosimetric values and estimated delivery times are presented in table 4.3. The MBRT plans with static conformal photon beams have a reduced PTV coverage in comparison with the CRT plan. On the other hand, the volume of normal tissue receiving 100% of the prescribed dose is reduced in the MBRT plans compared with the CRT plan. For the MBRT plans with static photon beams and MBRT plans with photon arcs, the PTV coverage is similar to the IMRT plan and VMAT plan, respectively, while the dose to the normal tissue is reduced in the MBRT plans.

Comparing Arc-MBRT plans versus Static-MBRT plans, the delivery time is reduced by at least 55%. The estimated delivery time of the photon-only plans is 35% and 16% shorter for the CRT and IMRT plans and 37% longer for the VMAT plan compared to the respective Arc-MBRT plans.

TABLE 4.3: Comparison of the dosimetric quantities of the Arc-MBRT, Static-MBRT and photon-only plans for case 1 (right WBI). The best value of each quantity whithin the group is highlighted in bold.

	Arc-MBRT	Static-MBRT	photon-only RT
	(2 arcs | 2 static conf)	(3 static | 2 static conf)	(2 static conf)
HI (%)	21	20	**17**
CI	**0.50**	0.49	0.33
Normal tissue $V_{42.4Gy}$ (cm^3)	**2**	**2**	136
Heart D_{mean} (Gy)	**0.4**	**0.4**	**0.4**
Contr. breast D_{mean} (Gy)	**0.4**	**0.4**	**0.4**
Ips. lung V_{17Gy} (%)	**13.3**	**13.3**	14.2
Ips. lung $D_{2\%}$ (Gy)	32.5	**31.8**	40.7
Estimated delivery time (min)	2.3	8.5	**1.5**
Electron dose contribution (%)	37	40	–
	(2 arcs | 2 static)	(3 static | 2 static)	(2 static)
HI (%)	10	**9**	11
CI	**0.50**	0.49	0.40
Normal tissue $V_{42.4Gy}$ (cm^3)	5	**1**	78
Heart D_{mean} (Gy)	0.6	0.6	**0.5**
Contr. breast D_{mean} (Gy)	0.6	0.6	**0.5**
Ips. lung V_{17Gy} (%)	11.4	11.2	**11.1**
Estimated delivery time (min)	5.7	12.6	**4.8**
Electron dose contribution (%)	35	50	–
	(2 arcs | 2 arcs)	(3 static | 2 arcs)	(4 arcs)
HI (%)	8	8	**7**
CI	**0.50**	**0.50**	0.49
Normal tissue $V_{42.4Gy}$ (cm^3)	**2**	3	21
Heart D_{mean} (Gy)	**0.8**	**0.8**	1.6
Contr. breast D_{mean} (Gy)	**1.3**	1.4	1.5
Ips. lung V_{17Gy} (%)	12.8	**9.4**	13.4
Estimated delivery time (min)	**3.0**	7.8	4.1
Electron dose contribution (%)	41	37	–

Case 2: Left WBI

The Arc-MBRT, Static-MBRT and VMAT plans for case 2 (left WBI) are compared in fig. 4.6 (dose distributions and DVHs) and in table 4.4 (dosimetric values & delivery time). As can be seen in the top of fig. 4.6, the electron dose contributes mostly to the superficial part of the PTV and to the part where the heart is close to the PTV in the distal direction. The photon dose covers the more distal parts of the PTV, especially near the ribs where the ipsilateral lung is only a few millimeters apart from the PTV.

While the PTV coverage and the dose to OARs are similar in the Arc-MBRT and Static-MBRT plans, the dose to the OARs is substantially higher in the photon-only VMAT plan. Compared to the VMAT plan, the mean dose to the heart is reduced by 32%, the mean dose to the contralateral breast is reduced by 23% and the V_{5Gy} of the total lung is reduced by 40% in the Arc-MBRT plan.

TABLE 4.4: Comparison of the dosimetric quantities of the Arc-MBRT, Static-MBRT and VMAT plans for case 2 (left WBI). The best value of each quantity is highlighted in bold.

	Arc-MBRT	Static-MBRT	VMAT
HI (%)	8.5	8.8	**8.4**
CI	**0.50**	0.49	0.49
Heart D_{mean} (Gy)	**2.5**	**2.5**	3.7
Contr. breast D_{mean} (Gy)	**2.0**	2.1	2.6
Ips. lung V_{17Gy} (%)	6.4	6.8	**6.0**
Total lung V_{5Gy} (%)	**19.2**	20.6	39.6
Spinal canal $D_{2\%}$ (Gy)	4.1	**3.3**	5.0
Normal tissue $V_{10\%}$ (%)	**10.9**	11.6	16.5
Estimated delivery time (min)	**4.4**	8.9	5.3
Electron dose contribution (%)	16	15	–

Cases 3&4: Left and right WBI+LNI

The DVH comparison of the Arc-MBRT, Static-MBRT and VMAT plans for cases 3 and 4 (right and left WBI+LNI) are shown in fig. 4.7. In table 4.5, the dosimetric values and delivery times for case 3 (right WBI+LNI) are compared and the dosimetric values and delivery times for case 4 (left WBI+LNI) are compared in table 4.6.

In case 3 (right WBI+LNI), the Arc-MBRT and Static-MBRT achieved similar dosimetric plan quality. Both plans have a similar PTV coverage as the VMAT plan. When comparing the Arc-MBRT plan to the VMAT plan, the

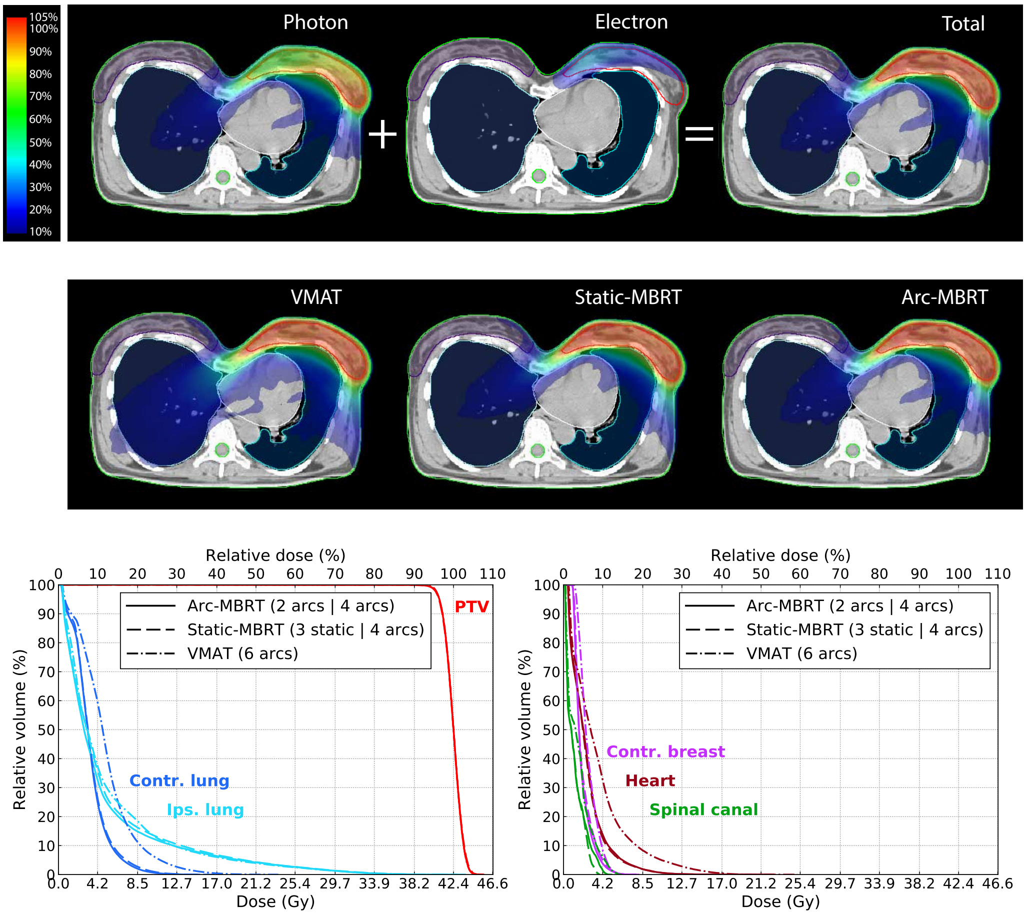

Figure 4.6: Dose color wash comparison (top) on a representative transversal plane between the photon and electron dose contributions of the Arc-MBRT plan, dose color wash comparison (middle) and DVH comparison (bottom) of the Arc-MBRT, Static-MBRT and VMAT plans for case 2 (left WBI).

mean dose to the heart is reduced by 60%. Similarly, the mean dose to the contralateral breast is reduced by 51% and the V_{5Gy} of the total lung is reduced by 24%.

The Arc-MBRT and Static-MBRT plans for case 4 (left WBI+LNI) have similar dosimetric plan quality, except for the lung, which has a lower dose bath in the Static-MBRT plan compared to the Arc-MBRT plan. The VMAT plan has the same PTV coverage as both MBRT plans, but the mean dose to the heart is reduced by 38%, the mean dose to the contralateral breast is reduced by 23% and the V_{5Gy} of the total lung is reduced by 15% in the MBRT plans compared to the VMAT plan.

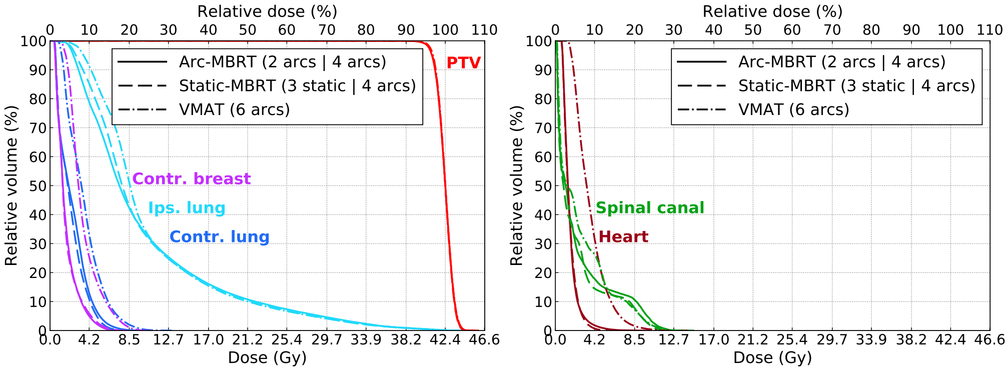

(a) Case 3: Right WBI+LNI

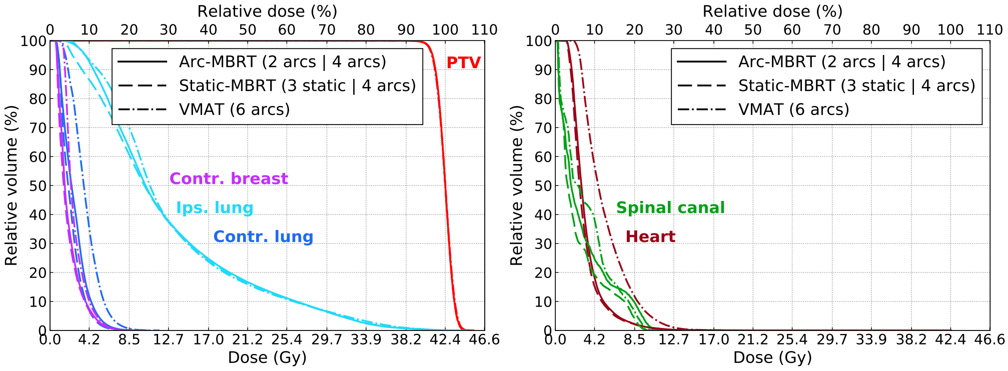

(b) Case 4: Left WBI+LNI

FIGURE 4.7: DVH comparison of the Arc-MBRT, Static-MBRT and VMAT plans for case 3 (a) and case 4 (b).

4.5.3 Dosimetric validation

The Arc-MBRT plans for case 2 (left WBI) and case 3 (right WBI+LNI) case were successfully delivered on a TrueBeam and film measurements were taken for the total plans (one fraction), only the electron arcs of each plan and the

Table 4.5: Comparison of the dosimetric quantities of the Arc-MBRT, Static-MBRT and VMAT plans for case 3 (right WBI+LNI). The best value of each quantity is highlighted in bold.

	Arc-MBRT	Static-MBRT	VMAT
HI (%)	7.9	7.8	**7.7**
CI	**0.50**	**0.50**	**0.50**
Heart D_{mean} (Gy)	**1.5**	**1.5**	3.8
Contr. breast D_{mean} (Gy)	**1.7**	**1.7**	3.5
Ips. lung V_{17Gy} (%)	16.1	15.8	**15.4**
Total lung V_{5Gy} (%)	**43.2**	45.8	56.8
Spinal canal $D_{2\%}$ (Gy)	10.6	**10.1**	10.3
Normal tissue $V_{10\%}$ (%)	22.7	**21.5**	27.9
Estimated delivery time (min)	4.4	10.3	**4.1**
Electron dose contribution (%)	15	25	–

Table 4.6: Comparison of the dosimetric quantities of the Arc-MBRT, Static-MBRT and VMAT plans for case 4 (left WBI+LNI). The best value of each quantity is highlighted in bold.

	Arc-MBRT	Static-MBRT	VMAT
HI (%)	**7.6**	**7.6**	8.0
CI	**0.50**	**0.50**	**0.50**
Heart D_{mean} (Gy)	3.3	**3.1**	5.3
Contr. breast D_{mean} (Gy)	**2.0**	**2.0**	2.6
Ips. lung V_{17Gy} (%)	24.7	24.3	**23.7**
Total lung V_{5Gy} (%)	46.2	**42.4**	54.6
Spinal canal $D_{2\%}$ (Gy)	9.9	**8.9**	9.4
Normal tissue $V_{10\%}$ (%)	29.3	**26.0**	34.3
Estimated delivery time (min)	4.7	9.8	**4.6**
Electron dose contribution (%)	24	29	–

electron arcs of each plan with a collapsed gantry angle to 0°. The results of the comparisons between the measured and calculated dose distributions for all six deliveries are shown in fig. 4.8. The gamma analysis for case 2 (left WBI) resulted in a passing rate of 98.5% for the total dose, 99.5% for the electron dose and 100% for the collapsed dose, respectively. The passing rates of case 3 (right WBI+LNI) were 100% for all three dose distributions.

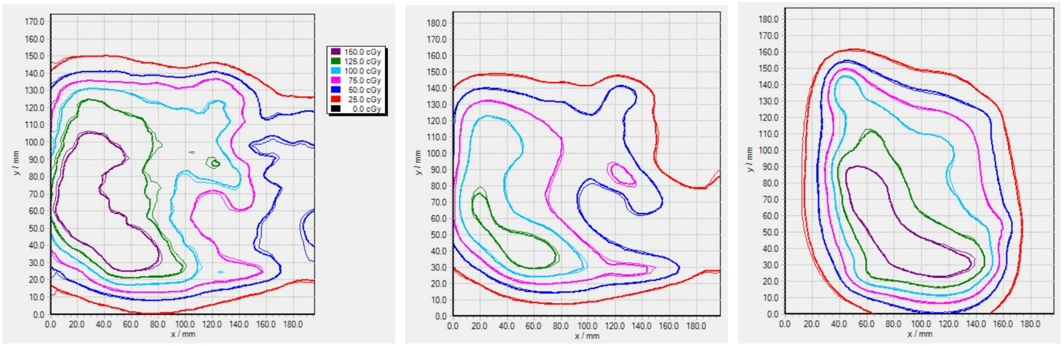

(a) total (b) electron (c) collapsed

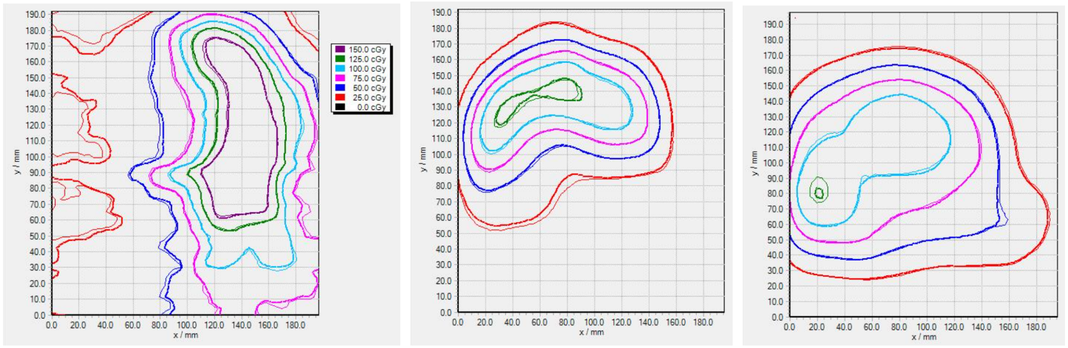

(d) total (e) electron (f) collapsed

Figure 4.8: Measured (thin) and calculated (thick) isodose lines for dose distributions of case 2 (top) and case 3 (bottom). In a) and d) the total Arc-MBRT plans consisting of electron and photon arcs were delivered, in b) and e) the electron arcs were delivered with dynamic gantry and table and in c) and f) the electron arcs were delivered with a collapsed gantry angle.

4.6 Discussion

In this work, a TPP for creating Arc-MBRT plans was successfully developed. The Arc-MBRT plans consist of intensity-modulated electron arcs and static or dynamic photon beams. The intensity-modulated electron arcs are achieved with a pMLC-based sliding-window technique and synchronous dynamic gantry rotation and table translation to keep a shortened SSD. In contrast to Static-MBRT, which contains intensity-modulated electron beams delivered from a static gantry angle, the gantry moves continuously during beam-on for electron arcs. This shortens the delivery time substantially. For the four investigated cases, the delivery times of the Arc-MBRT plans are less than half the time of the Static-MBRT plans. This is similar to the advantage of VMAT over IMRT, which also has reduced delivery time due to the dynamic gantry rotation (Teoh et al., 2011). Additionally, creating a suitable beam setup for Static-MBRT plans is not always straightforward. Multiple beams must be chosen carefully to achieve an acceptable coverage of the PTV by the electrons. The presented TPP improves this, as setting up gantry ranges for electron arcs is more straightforward. The TPP presented here can create Arc-MBRT plans, but plans consisting of electron arcs only can also be created with the same TPP in a similar way.

The dosimetric plan quality of Arc-MBRT plans are generally similar to the Static-MBRT but are superior compared to the photon-only treatments, except for the combination of electron arcs with static conformal photon beams. A possible explanation for this is that the dose of the conformal photon beams is predetermined and only the MU weight of the conformal beams can be changed during intensity modulation optimization. This indicates that the simultaneous optimization of photon and electron intensity modulation is important. For all other setups, the mixed beam plans achieved the same PTV coverage while reducing the dose to the OARs. Most notably, MBRT plans reduced the mean dose to the heart compared to photon-only plans, which is correlated with ischemic heart disease (Darby et al., 2013). Similar results were obtained by Li et al., 2000; Al-Yahya et al., 2005b; Alexander et al., 2011; Renaud, Serban, and Seuntjens, 2017 using different MBRT techniques. This shows the potential dosimetric superiority of MBRT plans over photon-only treatments for breast cases also for MBRT utilizing intensity modulated electron arcs.

When comparing Arc-MBRT plans with different number of electron arcs, it seemed that for the investigated breast cases no more than two electron arcs are necessary to achieve a good dosimetric plan quality and that more electron arcs only increase the delivery time without improving the dosimetric result substantially. This can be explained by the fact that energy modulation does not play a substantial role for this treatment site, as the range of treatment depths is narrow. Rather, the electron dose acts as a base dose in the superficial parts of the PTV, allowing for a lower photon dose to the OARs while maintaining a sharp dose falloff outside the PTV. In the cases including LNI, the lymph nodes are essentially only covered with photons. Because the lymph nodes are not near the patient's skin, a larger portion of normal tissue would be irradiated if the electron beams would contribute more to this area and thus only the superficial parts of the PTV in the breast are covered with electrons.

Arc-MBRT plans were successfully delivered on a TrueBeam and the dosimetric validation shows good agreement between the measured and calculated dose distributions. This shows that the multiple-source beam model and algorithm used for the electron dose calculation are suitable for Arc-MBRT plans and that a TrueBeam can deliver electron arcs accurately. Ma et al., 2019 investigated dosimetric characterizations of electron arcs and achieved good agreements between Monte Carlo dose calculations and measurements as well. However, no intensity-modulated electron arcs were measured.

In the presented TPP for Arc-MBRT, the time for dose calculation can be substantially longer compared to the time required for photon-only VMAT plans. There are several approaches possible to reduce this dose computation time. One approach is to use a coarser dose scoring grid to determine suitable electron energies. The number of electron energies for which beamlet dose has to be calculated on the regular dose scoring grid can thus be reduced. Another approach is to use faster dose calculation algorithms based on a GPU implementation (Franciosini et al., 2023) or on deep learning methods for denoising MC dose distributions (Bai et al., 2021; Neph et al., 2021).

One aspect which was not investigated in this work is the robustness of the treatment plans against setup uncertainties and patient breathing. The assumption that the dose distribution is not perturbed by setup uncertainties does not hold for electrons and the electron dose distribution moves with the patient in the incident beam direction (Thomas, 2006). Additionally, electron beams might be more robust than photon beams due to their larger beam penumbra. Renaud, Serban, and Seuntjens, 2019; Heath et al., 2021 developed a clinical target volume (CTV) based robust optimization approach for Static-MBRT. They showed that robust-optimized plans exhibited less dosimetric impact due to setup uncertainties compared to plans using conventional PTV margins and that the electron dose contribution was higher in the robust-optimized plans. Additionally, it has been shown that also photon-only plans could benefit from CTV-based robust optimization as well (Byrne, Hu, and Archibald-Heeren, 2016). Hypothetically, robust-optimized Arc-MBRT would show the same benefit and will be investigated in future research, but the potential burden on computer memory and calculation time of the many MC beamlets needed for robust optimization needs to be addressed adequately (Mueller et al., 2023).

This work focused on breast cases to show the dosimetric plan quality and efficiency of Arc-MBRT plans. However, there is a potential advantage of MBRT also for other treatment sites with a superficial part such as head-and-neck cancers (Mu et al., 2004; Mueller et al., 2018a), brain tumors (Rosca, 2012; Heath et al., 2021), sarcomas (Renaud, Serban, and Seuntjens, 2017), tumors in the abdomen (Unkelbach et al., 2022) or scalp irradiations (Eldib et al., 2017). Additionally, non-coplanar beam directions for photon and electron beams might offer an additional advantage. Electron beams with dynamic trajectories similar to the dynamic trajectories of photon beams in dynamic mixed beam radiotherapy (Mueller et al., 2018b) might be explored in future research. Although, ensuring collision avoidance for the shortened SSD might be challenging for non-coplanar electron beams.

4.7 Conclusion

A TPP for pMLC-based Arc-MBRT containing intensity-modulated electron beams with dynamic gantry rotation was successfully developed. Created Arc-MBRT plans for four breast cases showed similar dosimetric plan quality to Static-MBRT plans while outperforming photon-only plans. For the investigated breast cases, two electron arcs were enough to achieve a good dosimetric plan quality. On average, the mean heart dose is reduced by 32% in the MBRT plans compared to the photon-only plans. The Arc-MBRT plans reduced the delivery time by half compared to Static-MBRT plans and were similar to VMAT plans, which further facilitates integration of pMLC-based mixed-beam radiotherapy into clinical practice.

4.8 Acknowledgements

This work was supported by grant 200021_185366 of the Swiss National Science Foundation and by Varian, a Siemens Healthineers company. Calculations are performed on UBELIX (http://www.id.unibe.ch/hpc), the high-performance computing cluster at the University of Bern. The data that support the findings of this study are available upon request from the authors.

5

Technical note: A collision prediction tool using Blender

Gian Guyer[1], Silvan Mueller[1], Yanick Wyss[1], Jenny Bertholet[1], Remo Schmid[1], Marco F. M. Stampanoni[2], Peter Manser[1] and Michael K. Fix[1]

[1] Division of Medical Radiation Physics and Department of Radiation Oncology, Inselspital, Bern University Hospital, and University of Bern, Switzerland
[2] Institute for Biomedical Engineering, ETH Zurich and PSI, Villigen, Switzerland

Published in
Journal of Applied Clinical Medical Physics
2023, Vol. 24, No. 11, e14165
DOI: 10.1002/acm2.14165

5.1 Preface

One of the challenges of creating deliverable non-coplanar radiotherapy plans is to predict possible collisions between the gantry and the patient and table during the treatment planning process such that the infeasible beam directions are excluded. Additionally, there is a need to determine the distance between the gantry and the patient and table to assess the collision risk of a given plan. Thus, the objective of this study is to develop a collision prediction tool able to procude maps of collision-free zones and to test treatment plans for collisions.

Contribution: G. Guyer was involved in concieving the idea. G. Guyer and Y. Wyss created the collision prediction tool and wrote the code. G. Guyer created the GUI. G. Guyer performed the measurements for this study. G. Guyer wrote the manuscript and created all figures with critical feedback from all co-authors.

5.2 Abstract

Background: Non-coplanar radiotherapy treatment techniques on C-arm linear accelerators have the potential to reduce dose to organs-at-risk in comparison with coplanar treatment techniques. Accurately predicting possible collisions between gantry, table and patient during treatment planning is needed to ensure patient safety.
Purpose: We offer a freely available collision prediction tool using Blender, a free and open-source 3D computer graphics software toolset.
Methods: A geometric model of a C-arm linear accelerator including a library of patient models is created inside Blender. Based on the model, collision predictions can be used both to calculate collision-free zones and to check treatment plans for collisions. The tool is validated for two setups, once with and once without a full body phantom with the same table position. For this, each gantry-table angle combination with a 2° resolution is manually checked for collision interlocks at a TrueBeam system and compared to simulated collision predictions. For the collision check of a treatment plan, the tool outputs the minimal distance between the gantry, table and patient model and a video of the movement of the gantry and table, which is demonstrated for one use case.
Results: A graphical user interface allows user-friendly input of the table and patient specification for the collision prediction tool. The validation resulted in a true positive rate of 100%, which is the rate between the number of correctly predicted collision gantry-table combinations and the number of all measured

collision gantry-table combinations, and a true negative rate of 89%, which is the ratio between the number of correctly predicted collision-free combinations and the number of all measured collision-free combinations.
Conclusions: A collision prediction tool is successfully created and able to produce maps of collision-free zones and to test treatment plans for collisions including visualization of the gantry and table movement.

5.3 Introduction

Modern C-arm linear accelerators (linacs) equipped with a multileaf collimator (MLC) support state-of-the-art treatment techniques such as intensity modulated radiotherapy (IMRT) and volumetric modulated arc therapy (VMAT) (Bortfeld, 2006; Teoh et al., 2011). In recent years, non-coplanar treatment techniques on C-arm linacs enabled through table rotations were developed (Smyth et al., 2019b; Manser et al., 2019). However, patient safety in terms of collision avoidance remains a concern. There are measures to prevent direct collisions, for example on a TrueBeam system (Varian, a Siemens Healthineers Company, Germany) these include machine motion models, live view monitoring, touch guards and a laserguard (Varian Medical Systems, 2012). With these measures, the treatment delivery is ideally interrupted before a direct collision. However, potential subsequent replanning can cause delays in the treatment for several days in the worst case and a partially delivered plan is problematic for the therapeutic process. Thus, it is of great importance to include the information about collision-free zones already in the treatment planning using a collision prediction tool to ensure deliverability of the treatment plan.

Several collision prediction tools for C-arm linear accelerators have been developed in the past (Humm et al., 1995; Nioutsikou, Bedford, and Webb, 2003; Dong et al., 2014; Padilla, Pearson, and Pelizzari, 2015; Yu et al., 2015; Cardan, Popple, and Fiveash, 2017; Suriyakumar et al., 2017; Mann et al., 2019; Islam et al., 2020; Hueso-Gonález et al., 2020; Wang et al., 2021; Northway et al., 2022). These collision prediction tools consist of a geometric model for the C-arm linear accelerator and most of these tools also include a model for the patient (Nioutsikou, Bedford, and Webb, 2003; Dong et al., 2014; Padilla, Pearson, and Pelizzari, 2015; Yu et al., 2015; Cardan, Popple, and Fiveash, 2017; Suriyakumar et al., 2017; Mann et al., 2019; Islam et al., 2020; Hueso-Gonález et al., 2020; Wang et al., 2021; Northway et al., 2022). The geometric models of the C-arm linac and table consist either of simple geometric shapes such as cuboids and cylinders (Humm et al., 1995; Nioutsikou, Bedford, and Webb, 2003; Padilla, Pearson, and Pelizzari, 2015; Islam et al., 2020; Wang et al., 2021), 3D meshes taken from measurements (Cardan, Popple, and Fiveash, 2017; Suriyakumar et al., 2017; Northway et al., 2022) or detailed vendor-provided machine data (Dong et al., 2014; Yu et al., 2015; Mann et al., 2019; Hueso-Gonález et al., 2020). However, to our knowledge the laserguard is not incorporated in any of the published models.

In this work, we offer an implementation of a freely available collision prediction tool for a TrueBeam system using Blender. Blender is a free and open-source computer graphics software (Blender Online Community, 2018), offering a modelling tool to create objects, a built-in collision detection system between objects, a application programming interface (API) for easy automatization, and multiple render engines for visualization of treatment plans. Nonetheless, Blender has to our knowledge never been used for a collision prediction tool in the field of radiotherapy.

5.4 Methods

5.4.1 Blender model

A model of a TrueBeam system was created in Blender. For this, measurements on a machine were taken with a tape measure and the machine was recreated using the integrated modelling tools inside Blender. A model for the gantry, the collimator, the table base and the table top was created. Additionally, the sensitive area of the laserguard of the TrueBeam was modelled using information from the TrueBeam manual as well as from measurements. The laserguard detects collisions using an infrared laser scanning device on a plane between the collimator and the patient. The sensitive area of the laserguard is V-shaped with a notch in the middle (Varian Medical Systems, 2012). Because collision interlocks between the gantry and the table stop the treatment a few centimeters before the actual collision, additional enveloping structures around the table top with 2 cm extra and around the table base with 5 cm extra were created. The extra distances were determined by measuring the smallest distance between the gantry and the table after triggering a collision interlock. Additionally, a carbon fiber head plate (Civco Medical Solutions, Kalona, USA) used for fixation of thermoplastic head masks was modelled.

For the patient model, a patient library was generated based on average human proportions. For this, the proportions of a human base-mesh was transformed using MakeHuman, a free and open-source 3D character modelling software (*MakeHuman* 2020). The proportions were fitted to the 25th and 75th percentile of measurements of US adult males and females taken from Segars et al., 2010. The 25th percentile is denoted the small size and the 75th percentile is denoted the large size for male and female patients, respectively. The patient library consists in total of 8 patient models, with two positions for each size and sex of the patient model: head-first supine with the arms down and head-first supine with the arms up above the head.

5.4.2 Collision-free zones

To calculate the collision-free zones, a python script using the Blender API was written, which simulates all possible gantry-table angle combinations according to a specified resolution based on user input data. Using bounding volume hierarchies (BVHs), the script determines overlap of the 3D meshes of gantry and laserguard with the 3D meshes of the enveloping structures for table and patient model. Optionally, the user inputs safety margins in which case a collision is considered if the minimum distance between the 3D meshes is smaller than this margin. The initial table positions are specified with one of two ways:

- The table positions are specified relative to a reference point on the head plate by measuring the difference between the treatment plan isocenter and the reference point in x, y and z coordinates in the patient coordinate system. This difference is added to the table positions when the reference point is in the isocenter.
- The table positions are specified in absolute table values.

Because the table position varies between fractions, tolerances for pitch, roll and rotation and lateral, vertical and longitudinal table axes can be specified. The table position is shifted or rotated from its initial position plus and minus the specified tolerance in each axis. The tool then checks for collision also for each combination of tolerance shifts and rotations.

A map with the predicted collision-free zones is created as output. To ease the specification of the input data, a graphical user interface (GUI) is created using the scripting application programming interface (API) of a research version of the Eclipse treatment planning system (Varian, a Siemens Healthineers Company, Germany).

5.4.3 Validation

To validate the geometric model, collision predictions for each gantry-table angle combination with a 2° resolution were generated for one initial table position with two different setups:

- Laserguard enabled, no patient model, head plate disabled, no additional margin, zero tolerance.
- Laserguard enabled, small male patient model with arms down, head plate enabled, no additional margin, zero tolerance.

On a TrueBeam, the table was moved to the initial table position and the table and gantry were rotated to each gantry-table angle combination with a 2° resolution once with the table alone and once with an Alderson Radiation Phantom (ART) positioned on the table. Each of the gantry-table angle combination was manually checked for a collision interlock either between the laserguard and the table or the gantry and the table.

The predicted and measured collision interlocks were evaluated for each gantry-table combination using the evaluation metrics shown in table 5.1.

TABLE 5.1: The evaluation metrics between the predicted and measured collision interlocks.

collision measured	collision predicted	
	yes	no
yes	true positive (TP)	false negative (FN)
no	false positive (FP)	true negative (TN)

The number of TP, FN, FP and TN values over all gantry-table combinations were determined and the true positive rate (TPR) and true negative rate (TNR) were calculated using the following equations.

$$TPR = \frac{\#TP}{\#TP + \#FN} * 100\% \tag{5.1}$$

$$TNR = \frac{\#TN}{\#TN + \#FP} * 100\% \tag{5.2}$$

5.4.4 Collision check of treatment plans

As a second application of the collision prediction tool, the fields of a treatment plan can be checked for collisions. The fields are checked for collision by giving the static or dynamic table angle and position, gantry angle and collimator angle as additional input. The tool then checks for collisions for the static position or along the dynamic path of the field using the same method as described above.

For demonstration, a dynamic trajectory radiotherapy (DTRT) path with dynamic gantry rotation, table rotation and collimator rotation was created retrospectively for a head and neck (H&N) case using the method described by Fix et al Fix et al., 2018. Additionally, a second path was created with an increased source-to-target distance (STD) of 110 cm by translating the table 10 cm away from the gantry in the beam direction along the whole path as described by Guyer et al Guyer et al., 2022. The initial table position was set using the relative method with the reference point on the head plate. The large male patient model with the arms down was chosen and an additional margin of 3 cm was set for the patient model. For pitch, roll and rotation axes, a tolerance of 2° was used and for lateral, longitudinal and vertical axes a tolerance of 3 mm was used. The tolerances were determined by retrospectively reviewing the clinically applied treatment plan and taking the largest applied setup table shifts for each axis over all fractions.

5.5 Results

5.5.1 Blender model and GUI

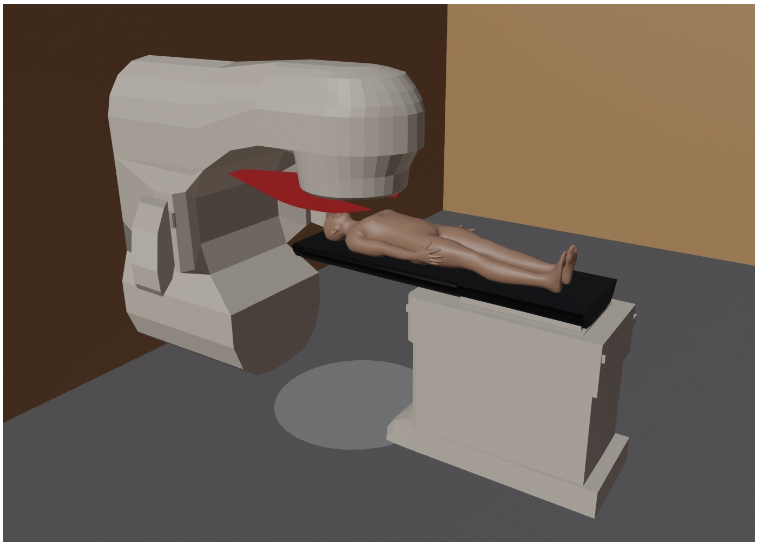

FIGURE 5.1: Screenshot of the Blender model including gantry and table stand in light grey, table top in black, laserguard in red and patient in skin color.

A screenshot of the Blender model is shown in fig. 5.1 and two screenshots of the developed GUI using Eclipse scripting API are shown in fig. 5.2. The

GUI allows the user to disable or enable the head plate and laserguard, to choose a patient model, to set the table positions in absolute values or relative to a head plate, to set additional safety margins and to set tolerances for the table position and rotation. The model and source code are freely available at https://github.com/gianguyer/collisionCheck.

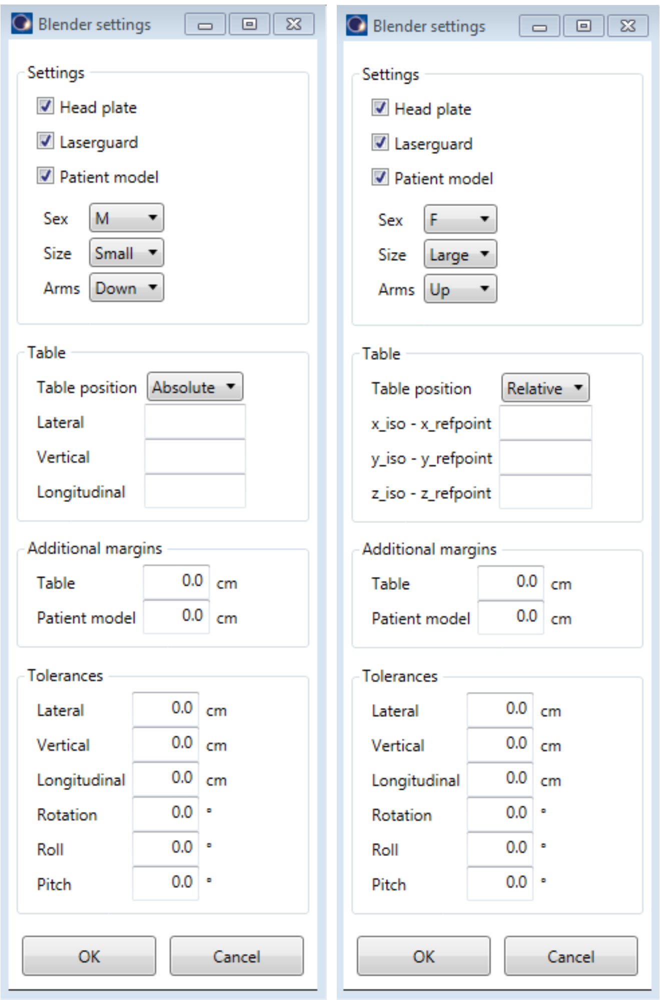

Settings
☑ Head plate
☑ Laserguard
☑ Patient model
Sex M
Size Small
Arms Down

Table
Table position Absolute
Lateral
Vertical
Longitudinal

Additional margins
Table 0.0 cm
Patient model 0.0 cm

Tolerances
Lateral 0.0 cm
Vertical 0.0 cm
Longitudinal 0.0 cm
Rotation 0.0 °
Roll 0.0 °
Pitch 0.0 °

Settings
☑ Head plate
☑ Laserguard
☑ Patient model
Sex F
Size Large
Arms Up

Table
Table position Relative
x_iso - x_refpoint
y_iso - y_refpoint
z_iso - z_refpoint

Additional margins
Table 0.0 cm
Patient model 0.0 cm

Tolerances
Lateral 0.0 cm
Vertical 0.0 cm
Longitudinal 0.0 cm
Rotation 0.0 °
Roll 0.0 °
Pitch 0.0 °

(a) (b)

FIGURE 5.2: Two screenshots of the GUI to specify input for the collision prediction tool. The selected option for specifying the table position is absolute in (a) and relative in (b).

5.5.2 Validation

In figure fig. 5.3, a gantry-table map is shown with an evaluation between the measured and predicted collisions for all gantry-table angle combinations. For the setup without phantom, the TPR is 100.0% and the TNR is 88.8%. For the setup with the ART phantom, the TPR is 99.9% and the TNR is 89.1%.

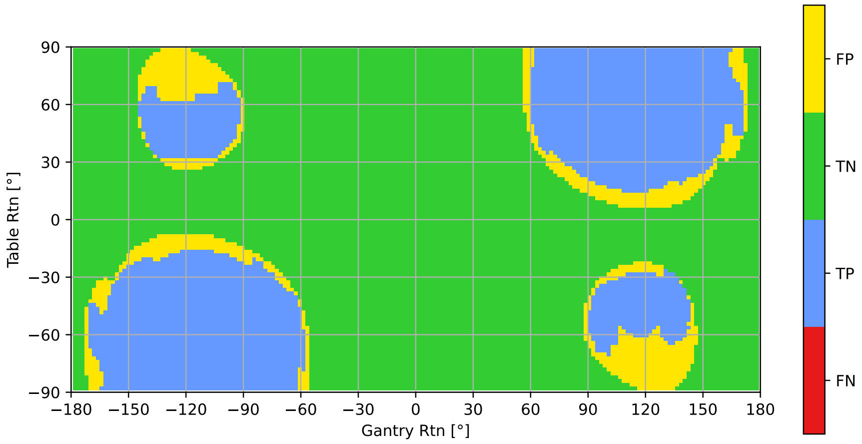

(a) without phantom

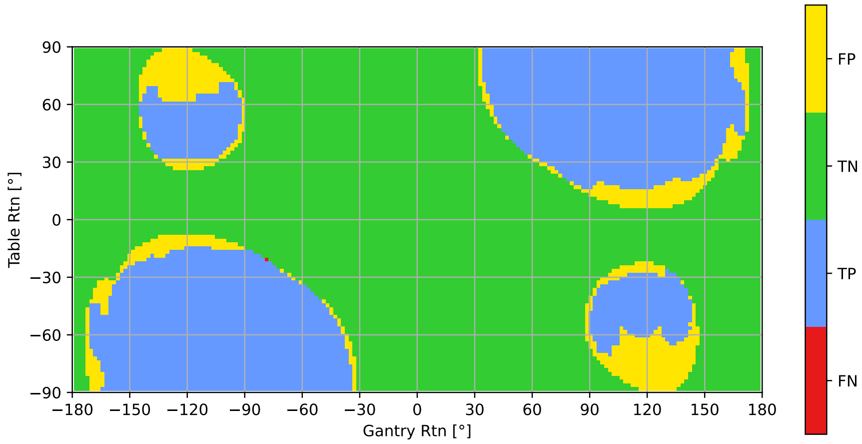

(b) with phantom

FIGURE 5.3: Map of gantry-table combinations resulting in false positive (FP), true negative (TN), true positive (TP) and false negative (FN) values when comparing predicted and measured results for the setup without any phantom on the table (a) and with the ART phantom on the table (b).

5.5.3 Collision check of plans

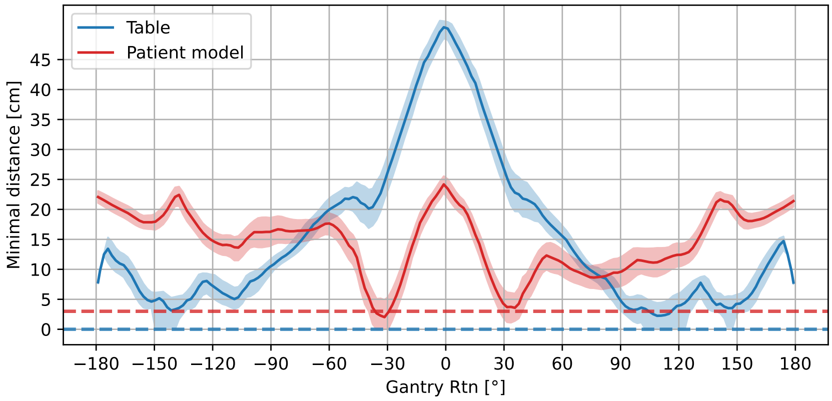

(a) STD = 100 cm

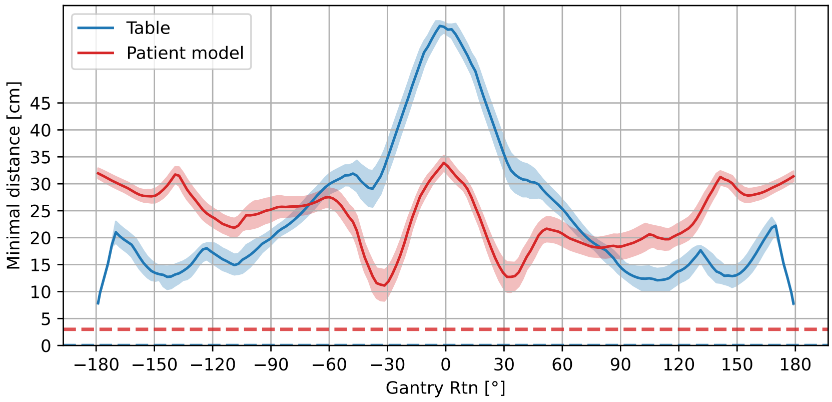

(b) STD = 110 cm

FIGURE 5.4: Minimum predicted distances between the gantry and the table and the patient model for a DTRT path for a H&N case with an STD of 100 cm (a) and an STD of 110 cm (b). The minimum distances over all combinations of axes tolerances are shown in bands. The nominal combination, i.e. the situation with tolerance values of zero, is shown as a solid line. In blue and red dashed horizontal lines, the additional margin between gantry and table and gantry and patient model is indicated, respectively.

A DTRT path with a STD of 100 cm and a DTRT path with an extended STD of 110 cm were checked for collisions. The minimum distances between the gantry and the table and the gantry and the patient model are shown in Figures fig. 5.3(a) and fig. 5.3(b) for STD of 100 and 110 cm, respectively. As can be seen, the tool predicts collisions with the table for the path with an STD of 100 cm for certain combinations of axes tolerances. For the path with STD of 110 cm, the distance between the gantry and table and gantry and patient model is above the specified margins for the whole path and all combinations of tolerances. A video of the gantry and table movement simulation inside Blender is provided in the supplementary material.

5.6 Discussion

Using Blender, a model of a C-arm linac was successfully created. Blender is a free and open-source software, which allows broad access to a powerful computer graphics software toolset. The python API allows for easy automatization of simulations inside Blender. Using the python API, two applications for collision prediction were created. First, calculation of collision-free zones, which allows to avoid unfeasible gantry-table combinations during the treatment plan creation. Second, a plan check feature, which allows for checking a path of a treatment plan for specific table positions. This second feature is especially helpful, if the table position deviates from the expected position at the planning stage or if the plan was not created using the collision-free maps. Additionally, tolerances for the table position can be considered in both applications. The tolerances allow to consider the daily table shifts in the collision prediction. In this work, the laserguard is integrated into the collision prediction tool using a model of the sensitive area of the laserguard, which is an advantage over collision prediction tools which use vendor provided data without any laserguard (Yu et al., 2015; Mann et al., 2019; Hueso-Gonález et al., 2020) or which use a model based on 3D surface scans (Cardan, Popple, and Fiveash, 2017).

In the collision check of plans feature, also videos of the simulation of the gantry and table movement are created, similar to the work of (Suriyakumar et al., 2017; Wang et al., 2021). This has the benefit, that the dynamic rotations and translations of gantry, collimator and table in DTRT plans are visualizable prior to the delivery. Additionally, precarious areas where the table or patient may come close to the gantry are easier identifiable. Furthermore, the simulations can serve as a visual aid in explaining the radiotherapy treatment to patient and staff, also to reduce potential patient anxiety (Morley et al., 2013; Williams et al., 2017; Wang et al., 2022a).

The Blender model was validated for one lateral, vertical and longitudinal table position by comparing predictions of collisions for all gantry-table angle combinations to measurements. For a collision prediction tool, it is important, that the TPR is practically 100%, because otherwise collision might still occur which the tool did not predict. On the other hand, a low TNR indicates that the collision-free space is reduced unnecessarily. In the balance, safety (a high TPR) is more preferred. In the validation, some false negatives did occur for collision interlocks with the laserguard but overall, the model is deemed adequate. The TNR is lower than the TPR due to some false positive areas around the smaller collision zones. This is mainly due to the complex shape of the collimator and the applicator mounting and the fact that the sensitive area of the laserguard has a notch, which is difficult to model correctly.

In this work, the patient is modelled by relying on averaged data of human proportions and predefined patient positionings. Because of this simplification, collision interlocks between the patient and gantry might still occur with the custom positioning of the patient, such as having their arms in a different location, and not a wide enough margin around the patient model is applied. To model the patient more accurately, others have suggested to use a commercial 3D surface scanner (Padilla, Pearson, and Pelizzari, 2015; Cardan, Popple, and Fiveash, 2017; Hueso-Gonález et al., 2020; Islam et al., 2020). With this, the patient's anatomy as well as the custom positioning of each patient can be considered. Furthermore, the patient's surface can be scanned daily and a collision prediction with the daily scan can be performed. Because Blender can import STL files, which is a standard output format of 3D surface scanners, an extension of the Blender collision prediction tool for automatic import and registration of patient surface scans is feasible in the future.

5.7 Conclusion

In this work, a collision prediction tool using Blender is successfully developed. The prediction tool is able to predict collision zones as well as check treatment plans for collisions including laserguard and positioning variations. Additionally, videos of the gantry and table movement of treatment plans can be produced and minimum distances between gantry, table and patient model are visualized. The tool facilitates a smoother clinical workflow with less replannings due to collision interlocks.

5.8 Acknowledgements

This work was supported by grant 200021_185366 of the Swiss National Science Foundation and by Varian, a Siemens Healthineers Company.

6

A direct aperture optimization-based path determination approach for non-isocentric dynamic trajectory radiotherapy

Gian Guyer[1], Jenny Bertholet[1], Silvan Mueller[1], Chengchen Zhu[1], Werner Volken[1], Daniel M. Aebersold[1], Peter Manser[1], Michael K. Fix[1]

[1] Division of Medical Radiation Physics and Department of Radiation Oncology, Inselspital, Bern University Hospital, and University of Bern, 3010 Bern, Switzerland

To be submitted to
Physics in Medicine and Biology

6.1 Preface

In the previous chapters, a treatment planning process was developed for treatment techniques including dynamic table translations. However, the set up of the dynamic table translations is a manual process, and optimizing the table translations could further improve the dosimetric treatment plan quality. In this work, a path determination for dynamic trajectory radiotherapy including dynamic table translations is developed. The collision prediction tool developed in the last chapter is used to ensure the deliverability of the created treatment plans.

Contribution: G. Guyer wrote the code for the path generation. G. Guyer did the treatment planning. G. Guyer did the measurements together with J. Bertholet. G. Guyer did the analysis and created all figures. G. Guyer wrote the manuscript with critical feedback from J. Bertholet.

6.2 Abstract

Objective: Non-isocentric dynamic trajectory radiotherapy (DTRT) involves dynamic table translations in synchrony with intensity modulation and dynamic gantry, table, and/or collimator rotation. This work aims to develop and evaluate a novel dosimetrically motivated path determination technique for non-isocentric DTRT.

Approach: The path determination considers all available beam directions, given on a user-specified grid of gantry angle, table angle, and longitudinal, vertical, and lateral table position. Additionally, the source-to-target distance of all beam directions can be extended by moving the table away from the gantry along the central beam axis to increase the collision-free space. The path determination uses a column generation algorithm to iteratively add beam directions to paths until a user-defined total path length is reached. A subsequent direct aperture optimization of the intensity modulation along the paths creates deliverable plans.

Non-isocentric DTRT plans using the path determination and non-isocentric DTRT plans using a manual path setup were created for a craniospinal and a spinal irradiation case. Furthermore, VMAT, isocentric DTRT, and non-isocentric DTRT plans with an extended source-to-target distance are created for a breast, head and neck, and esophagus case. The plans are compared in terms of the dosimetric treatment plan quality and estimated delivery time.

Main results: For the craniospinal and spinal irradiation case, the non-isocentric DTRT plans using path determination resulted in similar treatment plan quality compared to those with manual path setup.

The non-isocentric DTRT plans maintained target coverage while reducing the mean dose to organs-at-risk on average by 1.7 Gy (breast), 1.0 Gy (head and neck), and 1.6 Gy (esophagus) compared to the VMAT plans and by 0.8 Gy (breast), 0.6 Gy (head and neck), and 0.8 Gy (esophagus) compared to the isocentric DTRT plans.

Significance: A general dosimetrically motivated path determination applicable to non-isocentric DTRT plans was successfully developed, further advancing the treatment planning for non-isocentric DTRT.

6.3 Introduction

Recently, there has been an increasing interest in non-coplanar radiotherapy on C-arm linear accelerators (Smyth et al., 2019b). By exploiting additional degrees of freedom, non-coplanar radiotherapy has been shown to improve organ-at-risk (OAR) sparing over current state-of-the-art treatment techniques like intensity-modulated radiotherapy (IMRT) and volumetric modulated arc therapy (VMAT) for multiple treatment sites (Yang et al., 2011; Smyth et al., 2013; Papp, Bortfeld, and Unkelbach, 2015; Wild et al., 2015; MacDonald et al., 2020; Smyth et al., 2019b; Langhans et al., 2018; Mullins et al., 2020a; Fix et al., 2018; Lyu et al., 2018a; Dong, Liu, and Xing, 2018; Bertholet et al., 2022; Bertholet et al., 2023). There is a variety of non-coplanar radiotherapy techniques. In 4π IMRT, intensity-modulated beams are given from multiple non-coplanar static beam directions (Dong et al., 2013; Rwigema et al., 2015; Yu et al., 2018). In non-coplanar VMAT, multiple VMAT arcs are delivered with different static table angles (Audet et al., 2011; Clark et al., 2012; Wild et al., 2015; Reis et al., 2021). The table is rotated dynamically during beam-on within a technique called dynamic trajectory radiotherapy (DTRT) either without (Smyth et al., 2013; MacDonald and Thomas, 2015; Papp, Bortfeld, and Unkelbach, 2015; Wild et al., 2015; Lyu et al., 2018a; Mullins et al., 2020a) or with simultaneous dynamic collimator rotation (Yang et al., 2011; Fix et al., 2018; Langhans et al., 2018; Dong, Liu, and Xing, 2018; MacDonald et al., 2020). In recent years, DTRT was extended with a non-isocentric approach, in which the table is translated dynamically, possibly in combination with dynamic gantry, collimator, or table rotation (Manser et al., 2020; Guyer et al., 2022; Mullins et al., 2020b). We previously developed a treatment planning process (TPP) for non-isocentric DTRT (Guyer et al., 2022) applied to three use cases. Non-isocentric DTRT reduced delivery time for a craniospinal irradiation (CSI) case compared to IMRT, reduced the risk of collision between the gantry and the patient by extending the source-to-target distance compared to isocentric DTRT, and improved dosimetric plan quality for a bilateral breast case compared to multi-isocentric VMAT.

Two key steps are involved in the treatment planning for DTRT: Determining the dynamic path and the intensity modulation along the path. These two steps are either solved sequentially or simultaneously. Sequential approaches, where path determination is followed by intensity modulation optimization, are relatively simple in that they mimic standard treatment planning approaches. These can be classified into four groups:

- Class solutions: The paths are pre-determined in class solutions, such as in the commercially available HyperArc (Ohira et al., 2018). Class solutions profit from straightforward treatment planning, but the chosen trajectories may only be suited for some patients due to potential collisions and suboptimal beam arrangements. Wilson, Otto, and Gete, 2017 used a generalizable baseball stitch class solution with an adjustable number of partial gantry arcs while Lincoln et al., 2022 created class solutions based on an organ overlap method for brain treatments.

- Manual setup: The paths are set up manually by a planner as, for example, in Guyer et al., 2022, where non-isocentric DTRT plans for CSI consisted of a manual path with a longitudinal table translation along the spinal cord, a gantry rotation around the head, and another longitudinal table translation along the spinal cord. However, this requires planner expertise to set up the paths and the paths may be suboptimal.

- Cost map: In cost map solutions, a scoring method determines a cost for every beam direction, such as the relative overlap between the OAR and the planning target volume (PTV) seen from the beam's eye view (Yang et al., 2011). An improvement of the OAR/PTV scoring method includes a weighting of the OAR overlap metric based on the distance to the source, mimicking a photon beam (Smyth et al., 2013; MacDonald and Thomas, 2015; Fix et al., 2018; MacDonald et al., 2020; Reis et al., 2021). A search algorithm then determines the path with the minimum cost on the map. Guyer et al., 2022 added a post-processing step to extend the source-to-target distance of the paths by moving the table systematically away from the gantry along the beam's central axis, which resulted in reduced risk of collision (Guyer et al., 2023). However, the additional collision-free space owing to the extended source-to-target distance could also be exploited to further improve the dosimetric quality of DTRT plans by enabling otherwise infeasible beam directions, as demonstrated by Yu et al., 2018.

- 4π approaches: In 4π IMRT-inspired solutions, anchor points are determined and connected to dynamic trajectories. The anchor points are selected either using a genetic algorithm (Wild et al., 2015) or by a fluence map optimization and iterative elimination of beam directions (Papp, Bortfeld, and Unkelbach, 2015; Langhans et al., 2018). Wild et al., 2015; Papp, Bortfeld, and Unkelbach, 2015 used a traveling salesman solver to connect the anchor points, while Langhans et al., 2018 used a combination of a cost map and a traveling salesman solving algorithm. Bertholet et al., 2023 developed a variation of the 4pi approach for non-coplanar arc treatment with or without dynamic collimator rotation by iterating between 4pi FMO and beam direction elimination.

More recently, one-step solutions were investigated, simultaneously solving the path and intensity modulation determination. Dong, Liu, and Xing, 2018 developed an iterative approach based on a Monte Carlo tree search, where in each round, a score was given to all available beam directions based on the objective function value, and a beam direction was randomly chosen with a score-weighted probability. Lyu et al., 2018a developed an optimization strategy alternating between intensity modulation optimization based on direct aperture optimization (DAO) and trajectory determination, where the trajectory was determined using a path search algorithm on the fluence map from the intensity modulation optimization. Finally, Mullins et al., 2020a proposed an iterative DAO approach using column generation (CG), in which neighboring beam directions are selected on a progressively smaller grid resolution. However, one-step solutions add more jerky movements to the dynamic trajectories, and in these studies, deliverability of the created plans was not shown.

In this work, a dosimetrically motivated path determination strategy for non-isocentric DTRT is developed, which iteratively adds beam directions to the path through CG. A final DAO on the resulting paths creates deliverable plans. Non-isocentric DTRT plans with optimized paths are created for two CSI cases and compared to non-isocentric DTRT plans with a manual path setup to show the suitability of the path determination strategy. Non-isocentric DTRT plans with an extended source-to-target distance are created and compared to isocentric DTRT and VMAT plans for three cases to investigate the potential of the path determination to utilize the increased collision-free space for dosimetric benefits. Finally, a measurement of one non-isocentric DTRT plan is performed to validate the dosimetric accuracy.

6.4 Methods

6.4.1 Treatment planning process

The TPP for creating non-isocentric DTRT plans with dosimetrically optimized paths is illustrated in fig. 6.1 and described in detail in the following. The developed TPP creates plans to be delivered on a TrueBeam system (Varian, a Siemens Healthineers Company, Germany) equipped with a Millennium 120 multileaf collimator (MLC) (Varian, a Siemens Healthineers Company, Germany).

Map creation

In the first step, a map consisting of beam directions, called map points, defined by the gantry angle, table angle, and table position is set up. The patient's CT and structure set are exported from a research version of Eclipse embedded in the Aria framework v15.6 (Varian, a Siemens Healthineers Company, Germany). The user needs to specify the desired axes $a_1, \dots, a_N$ for the map and their respective range and resolution. The available axes a_i are:

$$
\begin{aligned}
a_i \in \{ \quad & \text{gantry angle, table angle, longitudinal table position,} \\
& \qquad \text{vertical table position, lateral table position} \}
\end{aligned}
$$

In this work, a resolution of 10° is used for the gantry and table angle axes, and a resolution of 8 cm is used for the table position axes. The user-specified axes then define an N-dimensional grid, resulting in the map. The collimator angle is aligned to the axis of minimum inertia of the PTV to reduce potential leaf travel (Bertholet et al., 2023).

Next, map points that can lead to a potential collision are eliminated using a collision prediction tool (Guyer et al., 2023). The collision prediction tool considers the estimated absolute table position, the gantry angle, and a generic patient model to calculate potential collisions between the gantry, including the laser guard, and the table or patient. Optionally, an additional distance Δd can be provided. Each map point is then shifted Δd along the central beam,

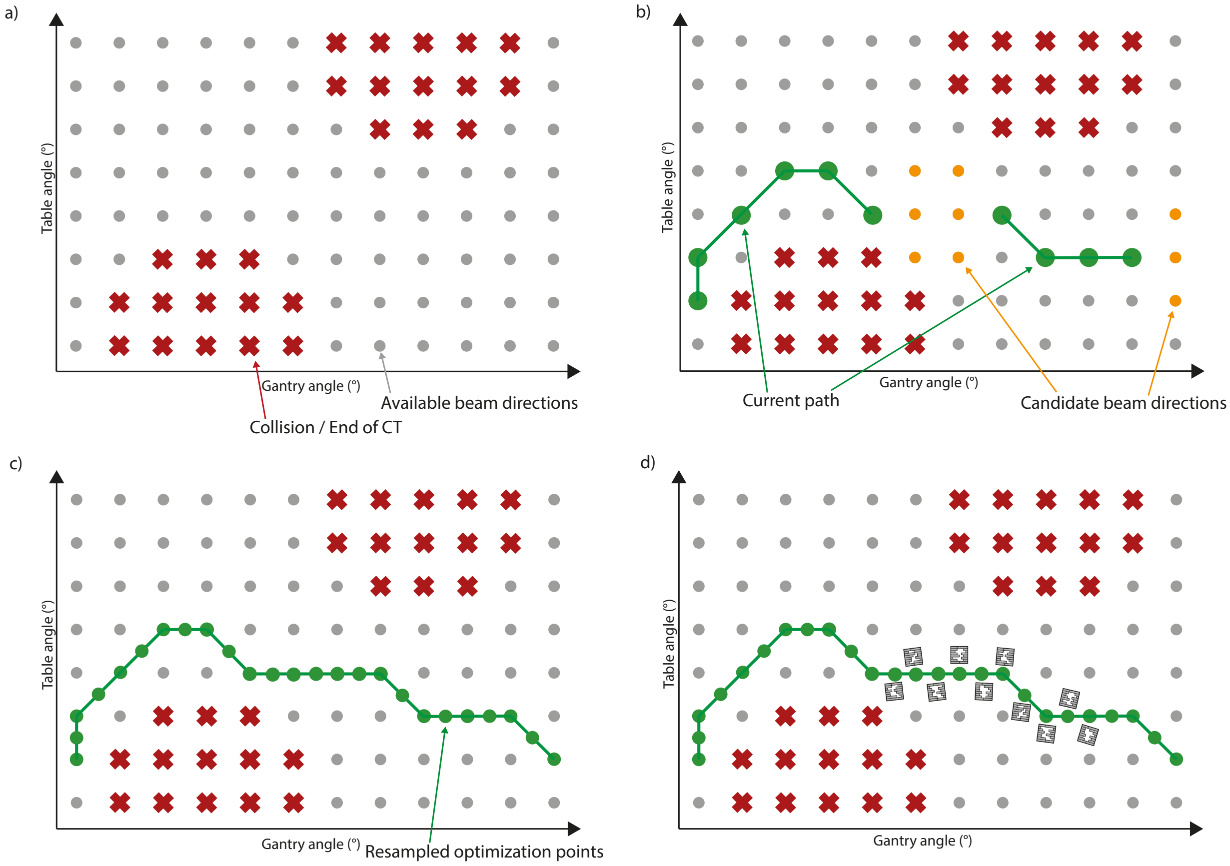

FIGURE 6.1: Ilustation of the treatment planning process with path determination for non-isocentric DTRT. a) Map setup with the exclusion of infeasible beam directions. b) Path determination on the map using column generation. c) Resampling of the control points of the path. d) Final plan creation.

resulting in an extended source-to-target distance. Map points with beams entering through the CT stack's end are also eliminated.

For all remaining map points, a beamlet dose calculation is performed with a beamlet size of 5 x 5 mm^2 and 5 x 10 mm^2 for the inner and outer leaves of a Millennium 120 MLC, respectively. A precalculated phase space at a plane located at the exit of the treatment head and the VMC++ dose calculation algorithm inside the Swiss Monte Carlo Framework (SMCP) (Fix et al., 2007) are used to calculate the beamlet dose distributions. This study uses a CT voxel size of 5 x 5 x 5 mm^3 for this beamlet dose calculation. To reduce the computational burden, a sparse thresholding of 0.1% of the maximum beamlet dose is applied, and voxels with a minimum distance from the target of 1 and 2 cm are merged to 2 x 2 x 2 = 8 (medium) and 4 x 4 x 4 = 64 (large) voxels as described in detail by Mueller et al., 2023.

Path determination

Next, the path is determined based on the remaining map points using a column generation algorithm following the schematic in fig. 6.2. For this, the user specifies the number of paths to be generated, the total maximum path length, a list of optimization objectives, and a maximal change angle.

The path determination consists of a column generation algorithm with two nested loops. The inner loop iterates over all specified paths and adds candidate beam directions for these paths to a pool. The outer loop adds the most promising aperture out of all candidate beam directions in the pool to the respective path. The most promising aperture is selected based on the gradient on the objective function value, described by Mueller et al., 2022.

Regarding the inner loop, there are three ways to identify candidate beam directions: First, all available map points are considered as the starting point for the path. Second, map points are considered at the end of a path to grow the existing path, with an existing path defined as a path containing at least one control point. Third, map points are considered in between existing control points of a path.

Certain restrictions apply when adding candidate beam directions to existing paths (fig. 6.3). Candidate beam directions at the end of the path are only considered as long as the total path length is not reached. If this is true, beam directions are considered if their distance to the end of the path is shorter than the maximal requested path length minus the current total path length. For this, the total path length of all paths is calculated. Due to the different units of axes, a norm factor n_{a_i} is introduced to transform all axes into the same

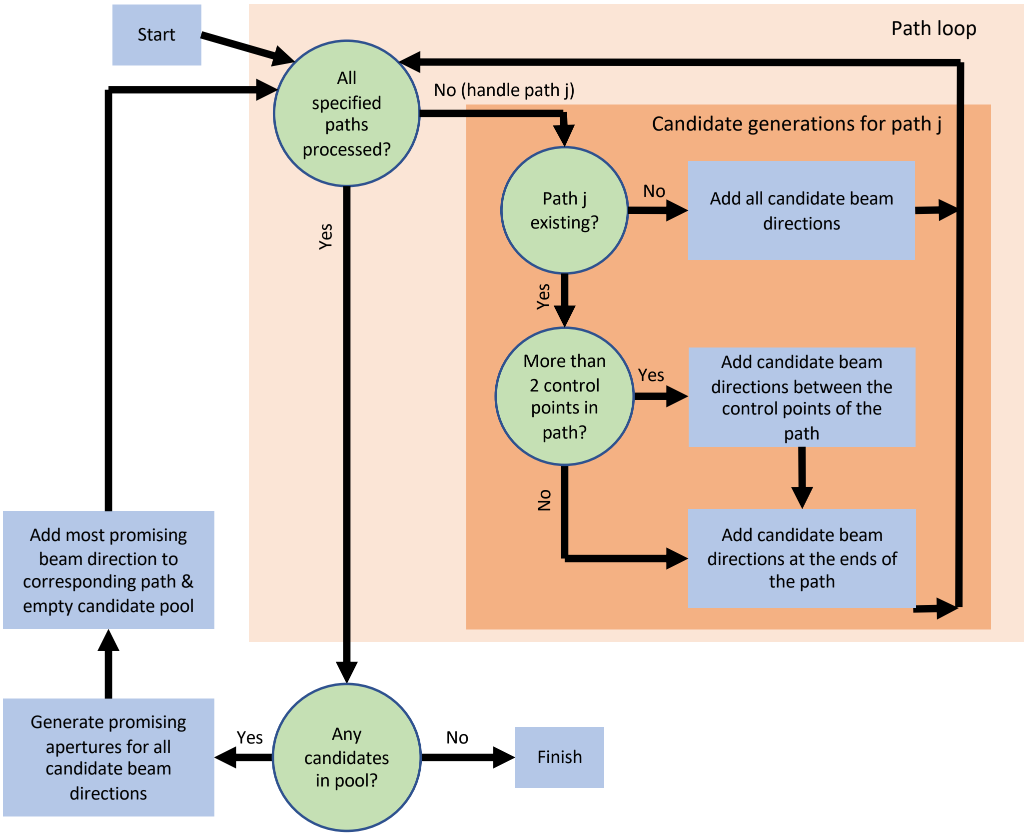

Figure 6.2: Workflow of the path determination. For each specified path, candidate beam directions are added to a pool. The most promising aperture in the pool is added to the respective path in each iteration until the maximal path length is reached and the spaces between control points are filled.

dimension. In this work, the norm factor is 1 for all rotation angles and 1.25 for all translation axes, which is the ratio between the rotational and translational resolution for the map. The length l of a path is then calculated by taking the L_∞ norm along the path:

$$l = \sum_{j=0}^{m-1} \max_{i=1,\ldots,N} \left(n_{a_i} \cdot (c_{a_i}^{j+1} - c_{a_i}^{j}) \right), \tag{6.1}$$

where m is the number of control points in the current path, and $c_{a_i}^{j}$ is the value of the axis a_i of the jth control point. The length of all paths is then summed.

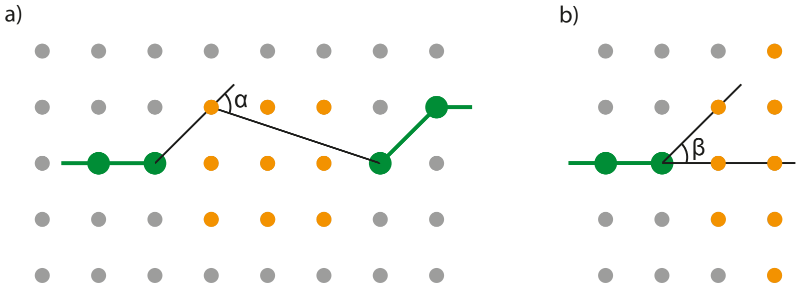

FIGURE 6.3: Ilustration of the angles considered for restricting candidate beam directions. The green points represent the control points of the path, and the orange points represent the candidate beam directions. In a), the angle for candidates between control points of the current path is indicated and in b), the angle for candidates at the end of the path is indicated.

Because the resulting control points of a path do not necessarily have to be adjacent on the map when extending the path, beam directions in between control points of one path are added. Thus, the beam directions added between the control points fill up the gaps. Beam directions are only considered candidates if they do not exceed a maximal change angle of the current path. Let's assume there are two control points c^j and c^{j+1} belonging to the current path and a map point p. Two vectors are then calculated; $v = p - c^j$ and $w = c^{j+1} - p$. Using these two vectors, the change angle is calculated:

$$\alpha = \cos^{-1}\left(\frac{\sum_{i=1,\ldots,N} n_{a_i} \cdot v_{a_i} \cdot w_{a_i}}{\left(\sum_{i=1,\ldots,N} n_{a_i} \cdot v_{a_i} \cdot v_{a_i}\right)^{1/2} \cdot \left(\sum_{i=1,\ldots,N} n_{a_i} \cdot w_{a_i} \cdot w_{a_i}\right)^{1/2}} \right) \tag{6.2}$$

The map points are not considered as candidates if the change angle is larger than the user-defined maximal change angle. The changing angle β at the start of the path is calculated using the following vectors: $v = c^0 - c^1$ and

$w = p - c^0$. Similarly, the change angle at the end of the path is calculated using the following vectors: $v = c^m - c^{m-1}$ and $w = p - c^m$, where m is the number of control points. In this work, the maximal change angle between control points is 90°, while the maximal change angle at the end is 45°. These values were chosen such that the paths retain a level of smoothness while still allowing them to connect two control points of a path without severe restrictions.

The path determination terminates when no more candidate beam directions are available. That is when the total path length is reached, and the paths consist of control points down to the map resolution.

Final plan creation

The resulting paths from the path determination are then used for final plan creation. For this, the paths are resampled to a resolution of 5° for all rotational axes and 4 cm for all translational axes by linear interpolation, resulting in the control points for the path. Then, a second beamlet dose calculation using a finer voxel grid of 2.5 x 2.5 x 2.5 mm^3 is performed for the control points using the same phase space and dose calculation algorithm as in section 6.4.1.

This is followed by an intensity modulation optimization for the resampled paths using a hybrid column generation and simulated annealing DAO (Mueller et al., 2022; Guyer et al., 2022), in which apertures are iteratively added to the control points until each control point has exactly one aperture. Here, the maximal MLC movement between consecutive control points and the maximal number of monitor units (MUs) per control point are restricted such that the delivery is not slowed down due to MLC leaf travel or MU rate. Furthermore, the fluence between consecutive control points is interpolated during the intensity modulation optimization.

After the intensity modulation optimization, a final dose calculation is performed considering an exact MLC model, the MLC's full dynamic delivery, and all dynamic axes. For this, a phase space placed above the secondary collimator jaws is used, and the VMC++ algorithm inside the SMCP is used for the particle transport through the jaws and the MLC and the dose calculation inside the patient. Finally, the MU weights of the apertures are re-optimized using a limited-memory Broyden-Fletcher-Goldfarb-Shanno (L-BFGS) algorithm (Liu and Nocedal, 1989), resulting in the final plan.

TABLE 6.1: Path setups for the CSI and spinal irradiation cases.

Case	DTRT$_{optimized}$	DTRT$_{manual}$
CSI	1 path, 500° total path length on a gantry angle-longitudinal table position map	path consisting of: - longitudinal translation along spine (210° gantry angle) - gantry rotation around skull from 210° to 150° - longitudinal translation along spine (150° gantry angle)
Spinal irradiation	1 path, 500° total path length on a gantry angle-longitudinal table position map	2 paths consisting of: - longitudinal translation along spine (210° gantry angle) - longitudinal translation along spine (150° gantry angle)

TABLE 6.2: Path setups for the breast, H&N, and esophagus cases.

Case	VMAT setup	Isocentric DTRT setup	Non-isocentric DTRT setup
Breast	2 partial arcs with a gantry range from 290° to 179° (500° total)	2 paths, 500° total path length on a gantry angle-table angle map	2 paths with 500° total path length on a gantry angle-table angle map with extended source-to-target distance
Head and neck	2 full arcs (720° total)	2 paths, 720° total path length on a gantry angle-table angle map	2 paths with 720° total path length on a gantry angle-table angle map with extended source-to-target distance
Esophagus	2 full arcs (720° total)	2 paths, 720° total path length on a gantry angle-table angle map	2 paths with 720° total path length on a gantry angle-table angle map with extended source-to-target distance

6.4.2 Investigated cases

Two different use cases are investigated using the developed TPP: First, non-isocentric DTRT plans using optimized paths created by the path determination algorithm (DTRT$_{optimized}$) on a gantry angle-longitudinal table position map are compared to non-isocentric DTRT plans using a manual path setup (DTRT$_{manual}$). The plans are compared in terms of dosimetric plan quality and delivery efficiency for a craniospinal irradiation (CSI) and a spinal irradiation case, both with a prescribed dose of 13 x 1.8 Gy to the median dose to the PTV. Second, the TPP is used to create isocentric DTRT plans and non-isocentric DTRT plans with an extended source-to-target distance of 10 cm for a breast, an esophagus, and a head and neck (H&N) case, which are then compared to VMAT plans. The prescribed dose is 16 x 2.65 Gy (median PTV) for the breast, 25 x 2 Gy (95% of the PTV) for the H&N, and 28 x 1.8 Gy (median PTV) for the esophagus case, respectively. The plan setups are described in detail in table 6.1 and table 6.2. The plans used the same list of objectives for the path determination and the final plan creation. The plans are evaluated based on their final objective function value and dosimetric endpoints. Additionally, the delivery time is estimated by summing the time per control point of all arcs/trajectories of a plan, while the accelerations of the mechanical axes are neglected. The homogeneity index (HI) is calcuated as HI $= (D_{2\%} - D_{98\%})/D_p$, where D_p is the prescribed dose. The conformity index (CI) is calculated using Paddick's formula (Paddick, 2000).

6.4.3 Validation

Deliverability of the five non-isocentric DTRT plans was tested on the TrueBeam system in Developer Mode. Furthermore, the dose of the non-isocentric DTRT plan of the esophagus case was measured using two interleaved radiochromic EBT3 film sheets (Ashland Advanced Materials, Bridgewater, NJ) placed inside a PMMA cube. The same measurement protocol as described in Guyer et al., 2022 was used. In brief, the film sheets were scanned using an Epson XL 10000 flatbed scanner (Seiko Epson Co., Tokyo, Japan) 18h after irradiation, corrected for the lateral response artifact, converted to absolute dose using a triple channel calibration (Micke, Lewis, and Yu, 2011), and rescaled according to the one-scan protocol by using two additional film strips (Lewis et al., 2012). The measured dose distributions were compared to the dose distributions of the non-isocentric DTRT plan recalculated inside the PMMA cube using a gamma evaluation with a 3% (global) / 2 mm criterion and a 10% dose threshold of the maximum dose.

6.5 Results

6.5.1 Craniospinal irradiation

Table 6.3 shows the dosimetric endpoints and estimated delivery time for the $\text{DTRT}_{optimized}$ and DTRT_{manual} plans for the CSI case. In fig. 6.4, the paths are illustrated in 3D, the dose distributions are shown on a sagittal plane, and dose-volume histograms (DVHs) are shown for the two plans. Note that the resulting optimized path is similar to the manual path, with a movement along the spinal cord, a gantry rotation around the skull, and a movement back along the spine. The $\text{DTRT}_{optimized}$ plan resulted in better sparing of the heart, bowel, left lung, and thyroid, while the DTRT_{manual} plan resulted in better sparing of the eyes, larynx, right lung, and kidneys (table 6.3).

In fig. 6.5, the manual and optimized paths are illustrated, the dose distribution is shown on a sagittal plane, and the DVHs of the $\text{DTRT}_{optimized}$ and DTRT_{manual} plans are shown for the spinal irradiation case. Here, the optimized path resulted in a movement along the spine, a gantry rotation in the abdomen region, and a movement back along the spine. Table 6.4 show the plans' dosimetric endpoints and estimated delivery time. The $\text{DTRT}_{optimized}$ plan resulted in improved conformity and improved sparing of the heart, larynx, and thyroid while worsening the sparing of the kidneys, bowel, liver, and lungs compared to the DTRT_{manual} plan.

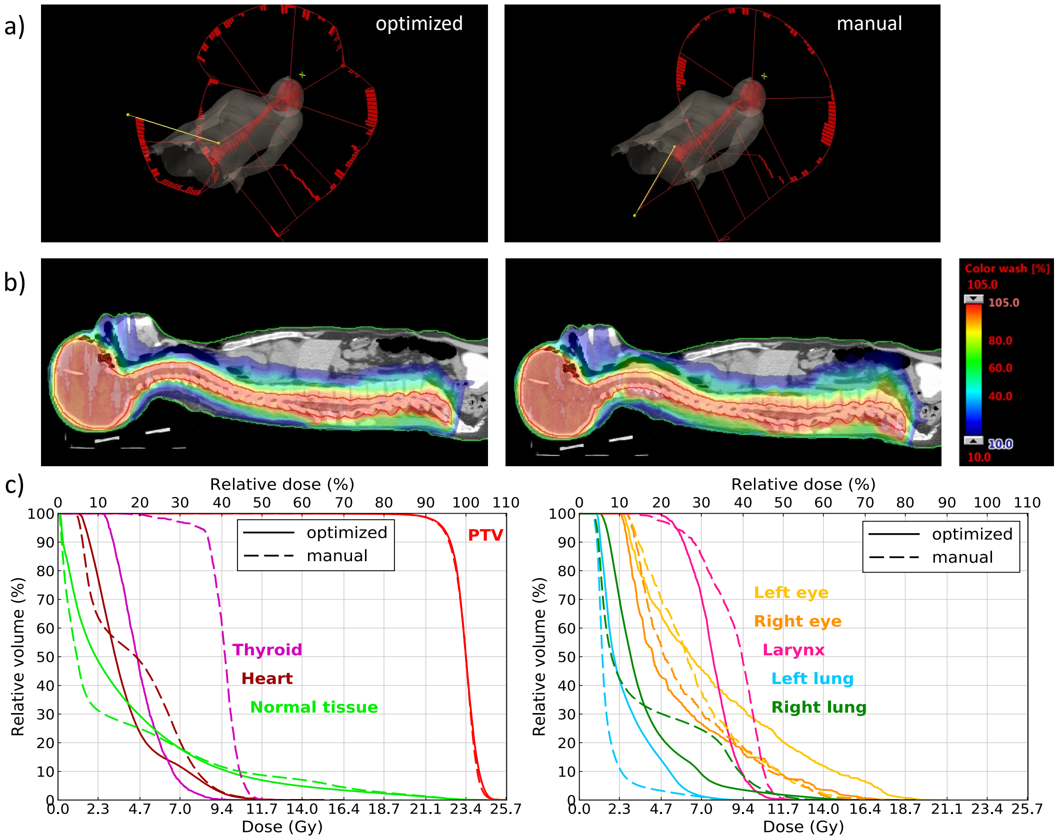

FIGURE 6.4: The optimized path and the manual path of the non-isocentric DTRT plans for the CSI case are illustrated in a). In b), the dose distributions of the non-isocentric DTRT plans are shown in color wash for a sagittal plane and in c), the corresponding DVHs are shown.

TABLE 6.3: Dosimetric endpoints and estimated delivery times of the non-isocentric DTRT plans for the CSI case. The best value in each row is highlighted in bold.

	$\text{DTRT}_{optimized}$	DTRT_{manual}
PTV CI	**0.48**	**0.48**
PTV HI (%)	13.5	**13.3**
Left lens $D_{2\%}$ (Gy)	4.7	**3.8**
Right lens $D_{2\%}$ (Gy)	**4.3**	5.5
Left eye $D_{2\%}$ (Gy)	17.6	**14.4**
Right eye $D_{2\%}$ (Gy)	14.9	**13.8**
Heart D_{mean} (Gy)	**3.9**	4.5
Left kidney D_{mean} (Gy)	2.4	**1.9**
Right kidney D_{mean} (Gy)	2.4	**2.0**
Large bowel D_{mean} (Gy)	**4.9**	5.4
Duodenum D_{mean} (Gy)	**7.7**	8.9
Stomach D_{mean} (Gy)	3.6	**3.4**
Larynx D_{mean} (Gy)	2.6	**1.6**
Liver D_{mean} (Gy)	**3.7**	3.8
Left lung D_{mean} (Gy)	**4.8**	9.5
Right lung D_{mean} (Gy)	5.6	**4.4**
Thyroid D_{mean} (Gy)	**7.9**	10.5
Estimated delivery time (min)	3.2	**2.6**

TABLE 6.4: Dosimetric endpoints and estimated delivery times of the non-isocentric DTRT plans for the spinal irradiation case. The best value in each row is highlighted in bold.

	$\text{DTRT}_{optimized}$	DTRT_{manual}
PTV CI	**0.47**	0.35
PTV HI (%)	20.5	**17.3**
Heart D_{mean} (Gy)	**2.2**	6.0
Left kidney D_{mean} (Gy)	3.4	**1.9**
Right kidney D_{mean} (Gy)	3.1	**1.7**
Large bowel D_{mean} (Gy)	4.8	**3.3**
Duodenum D_{mean} (Gy)	**6.2**	**6.2**
Stomach D_{mean} (Gy)	7.7	**4.9**
Larynx D_{mean} (Gy)	**10.6**	16.5
Liver D_{mean} (Gy)	4.2	**4.0**
Left lung D_{mean} (Gy)	5.1	**3.4**
Right lung D_{mean} (Gy)	5.6	**4.4**
Thyroid D_{mean} (Gy)	**7.9**	10.5
Estimated delivery time (min)	**3.2**	5.8

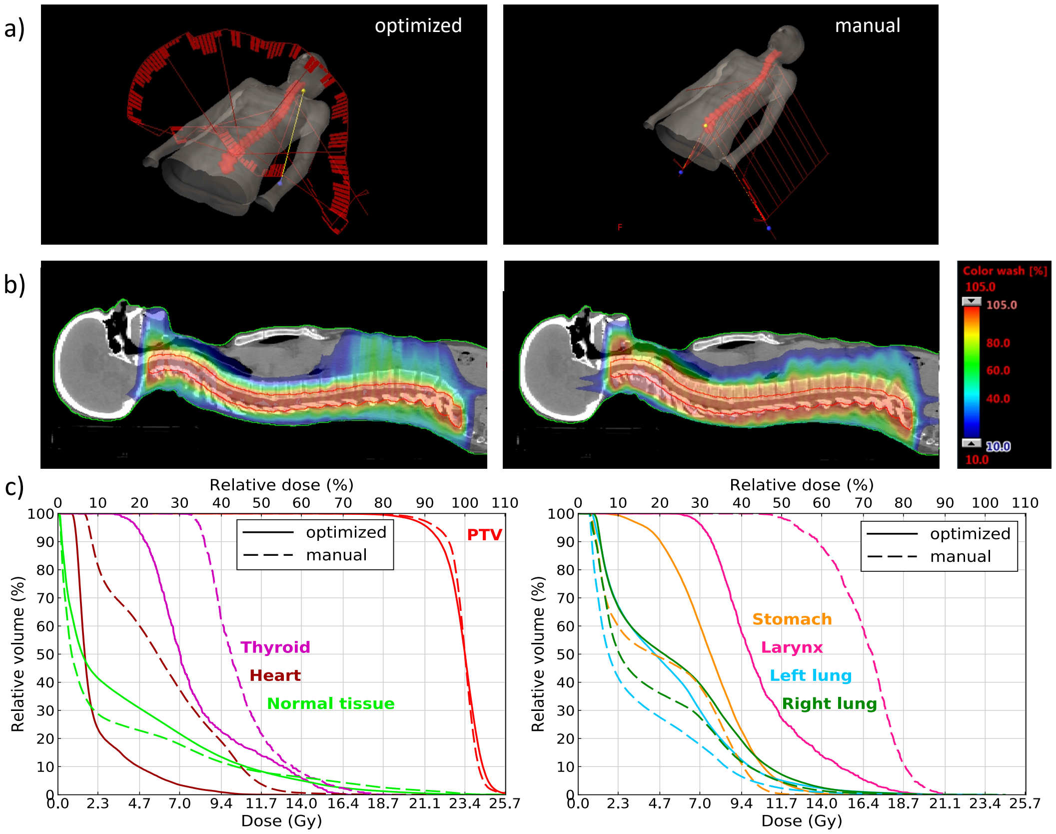

FIGURE 6.5: a) Illustration of the manual and optimized paths of the non-isocentric DTRT plans for the spinal irradiation. b) Dose distributions on a sagittal plane of the non-isocentric DTRT plans in color wash. c) DVHs of the non-isocentric DTRT plans.

6.5.2 Extended source-to-target distance

In fig. 6.6, the objective function values after path generation, intensity modulation optimization, final dose calculation, and MU re-optimization are illustrated for all created plans for the breast, H&N, and esophagus case. The final objective function is the lowest for the non-isocentric DTRT plans for all three cases.

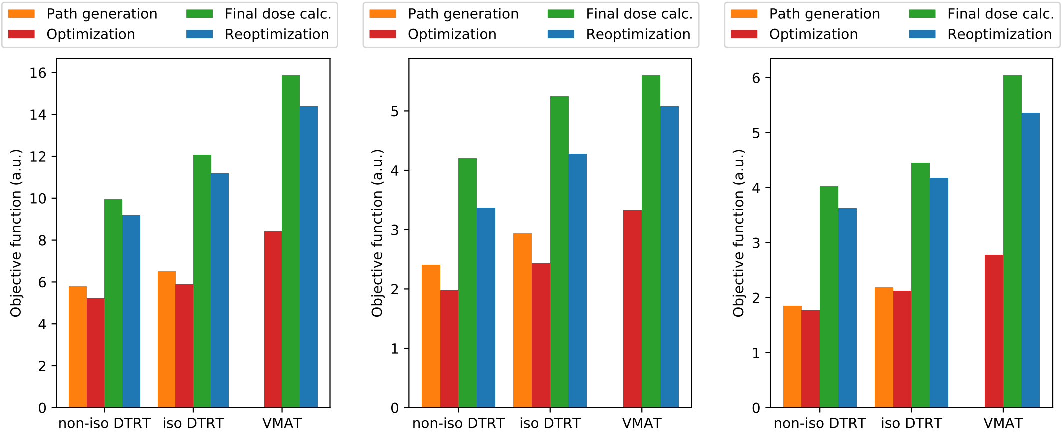

(a) Breast case (b) H&N case (c) Esophagus case

FIGURE 6.6: Objective function values of the non-isocentric DTRT, isocentric DTRT, and VMAT plans for the breast (a), H&N (b), and esophagus case (c).

Breast case

TABLE 6.5: Dosimetric endpoints and estimated delivery times of the VMAT, isocentric DTRT, and non-isocentric DTRT plans for the breast case. The best value in each row is highlighted in bold.

	VMAT	Isocentric DTRT	Non-isocentric DTRT
PTV CI	**0.5**	**0.5**	**0.5**
PTV HI (%)	11.0	10.7	**10.6**
Ips. lung D_{mean} (Gy)	10.6	10.6	**9.9**
Contr. lung D_{mean} (Gy)	4.0	**3.3**	3.5
Lung total V_{5Gy} (%)	45.1	41.4	**38.6**
Heart D_{mean} (Gy)	5.4	4.9	**4.5**
Contr. breast D_{mean} (Gy)	3.0	2.9	**2.7**
Spinal canal $D_{2\%}$ (Gy)	11.9	11.0	**9.8**
Estimated delivery time (min)	**1.9**	2.4	3.1

Figure 6.7 illustrates the paths of the non-isocentric and isocentric DTRT plans for the breast case. As the reduced red regions in the gantry-table maps show, the extended source-to-target distance increases the collision-free space

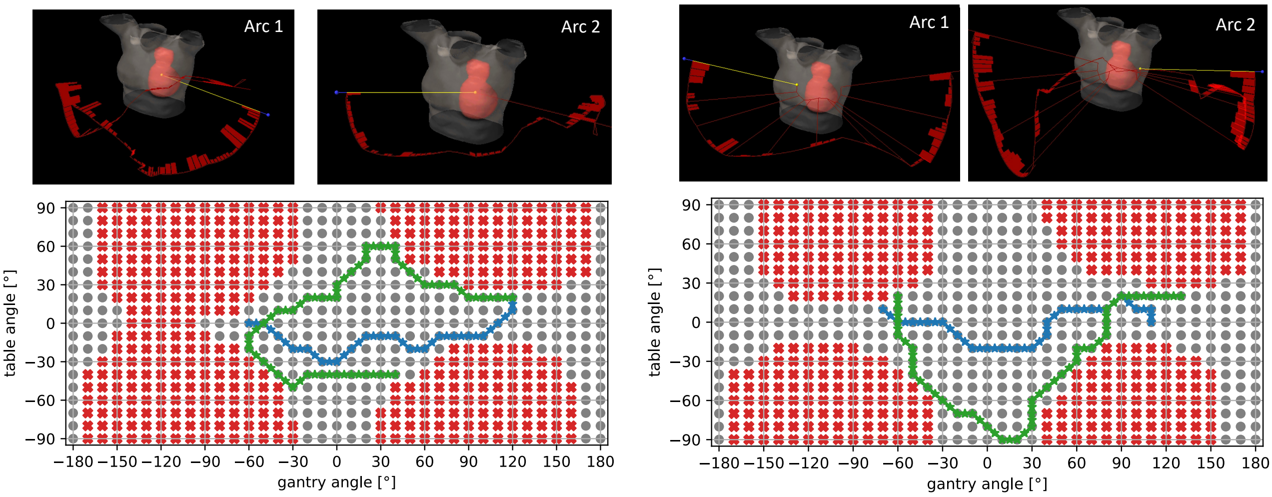

(a) isocentric DTRT (b) non-isocentric DTRT

Figure 6.7: Illustration of the paths of the isocentric DTRT (a) and non-isocentric DTRT (b) plans for the breast case. On top, the paths are illustrated using red bands. On the bottom, the paths are shown on a gantry-table map. All available map points are shown in gray, while the infeasible beam directions are indicated in red. The two paths of the DTRT plans are illustrated in blue and green.

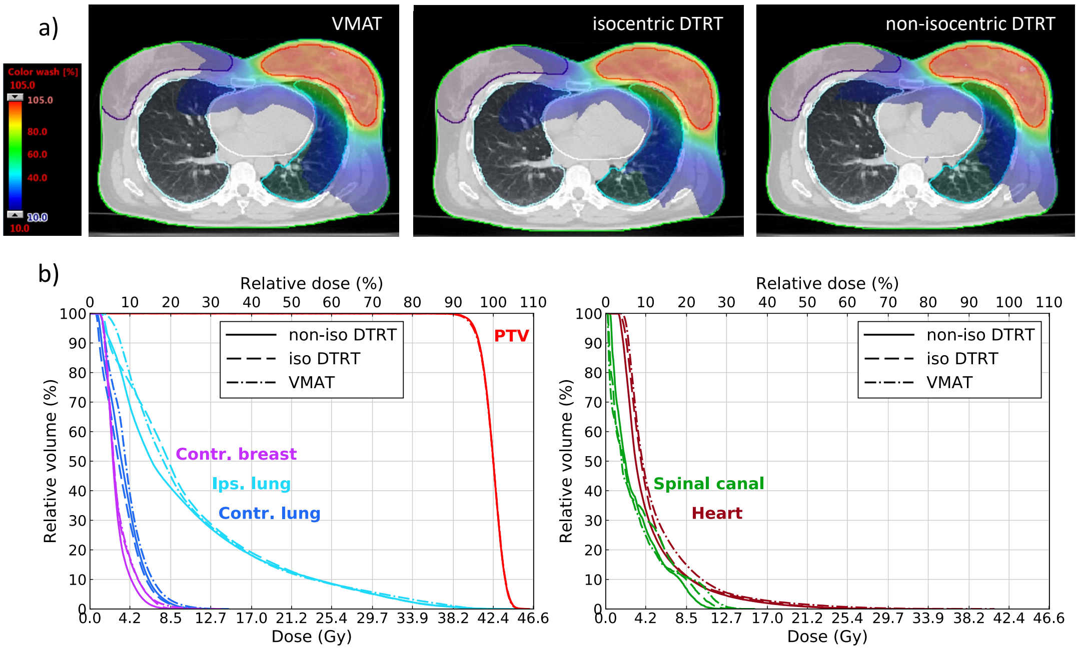

Figure 6.8: Dose distributions in color wash on an axial slice (a) and DVHs (b) of the VMAT, isocentric DTRT, and non-isocentric DTRT plans for the breast case.

compared to the isocentric setup. The path determination of the non-isocentric DTRT plan exploits these extra regions. Table 6.5 shows the dosimetric endpoints and estimated delivery times, and fig. 6.8 shows the dose distributions on an axial slice and DVHs of the VMAT, isocentric DTRT, and non-isocentric DTRT plans.

H&N case

In the isocentric DTRT plan, the first arc carries out a full gantry rotation, while the second arc resembles a half arc. The paths in the non-isocentic DTRT plan consist of highly non-coplanar directions going over the patient's head. Two collision regions (corresponding to collision of the gantry with the corners at the cranial end of the table) are completely avoided in the non-isocentric DTRT. The dosimetric endpoints and estimated delivery times are shown in table 6.6, while the dose distributions of an axial and a coronal slice and the DVHs are shown in fig. 6.10.

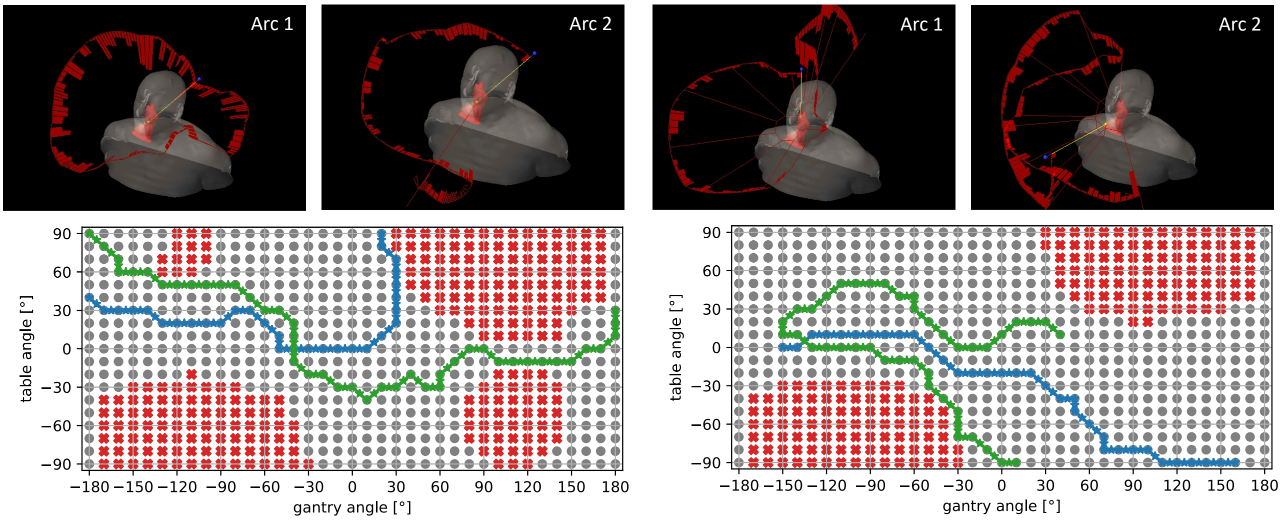

(a) isocentric DTRT

(b) non-isocentric DTRT

FIGURE 6.9: Illustration of the paths of the isocentric DTRT (a) and non-isocentric DTRT (b) plans for the H&N case. On top, the paths are illustrated using red bands. On the bottom, the paths are shown on a gantry-table map. All available map points are shown in gray, while the infeasible beam directions are indicated in red. The two paths of the DTRT plans are illustrated in blue and green.

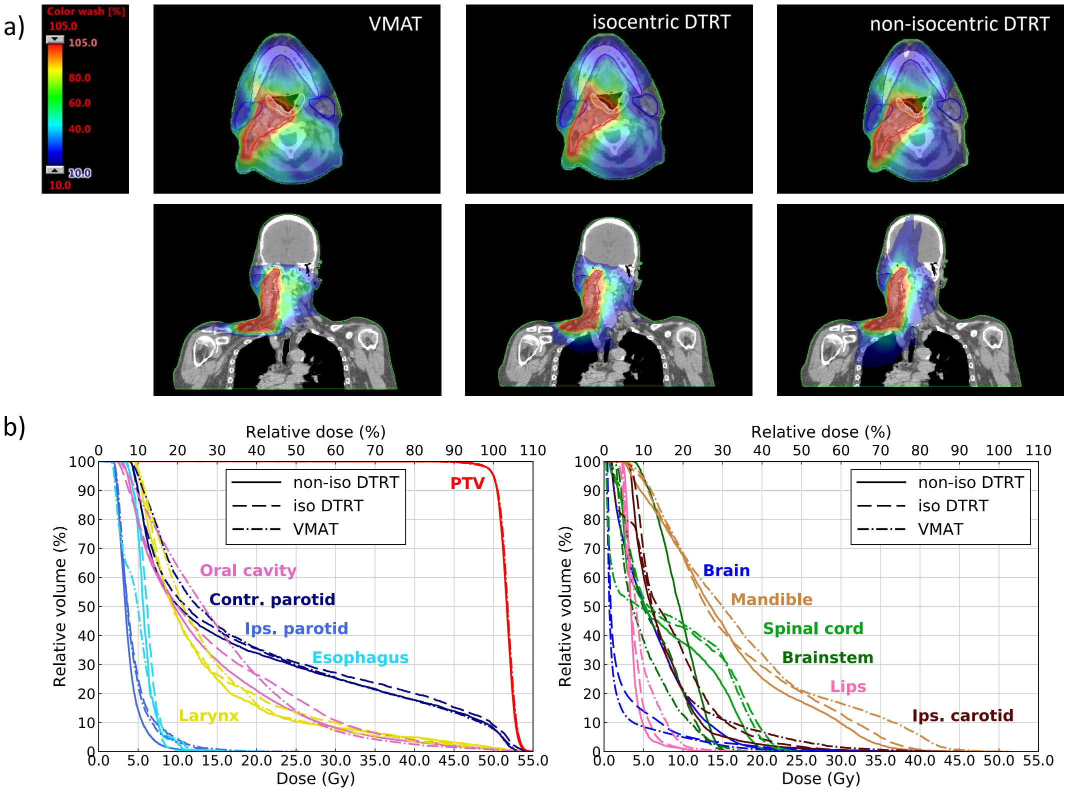

FIGURE 6.10: Dose distributions in color wash on an axial slice (a) and DVHs (b) of the VMAT, isocentric DTRT, and non-isocentric DTRT plans for the head and neck case.

TABLE 6.6: Dosimetric endpoints and estimated delivery times of the VMAT, isocentric DTRT, and non-isocentric DTRT plans for the head and neck case. The best value in each row is highlighted in bold.

	VMAT	Isocentric DTRT	Non-isocentric DTRT
PTV CI	**0.88**	0.84	0.85
PTV HI (%)	9.2	8.9	**8.6**
Spinal cord $D_{2\%}$ (Gy)	21.0	21.8	**19.4**
Brainstem $D_{2\%}$ (Gy)	14.7	**13.7**	14.5
Brain $D_{2\%}$ (Gy)	**15.2**	18.7	18.0
Mandible $D_{2\%}$ (Gy)	42.3	37.7	**35.4**
Oral cavity D_{mean} (Gy)	15.2	14.3	**13.3**
Pharynx D_{mean} (Gy)	33.7	**33.0**	33.2
Larynx D_{mean} (Gy)	13.9	13.7	**13.1**
Ips. parotid D_{mean} (Gy)	19.9	19.7	**18.8**
Contr. parotid D_{mean} (Gy)	4.3	4.4	**3.8**
Ips. carotid D_{mean} (Gy)	7.8	8.8	**7.4**
Lips D_{mean} (Gy)	5.0	3.8	**3.7**
Esophagus D_{mean} (Gy)	**5.0**	6.1	5.9
Estimated delivery time (min)	**2.3**	3.7	3.9

Esophagus case

Figure 6.11 shows the resulting paths of the isocentric and non-isocentric DTRT plans for the esophagus case. The paths are similar for the two plans, but the non-isocentric DTRT plan has more beam directions coming from the left side of the patient. Table 6.7 shows the dosimetric endpoints and estimated delivery times of the esophagus plans, and fig. 6.12 shows the dose distributions on an axial slice and the DVHs of the plans.

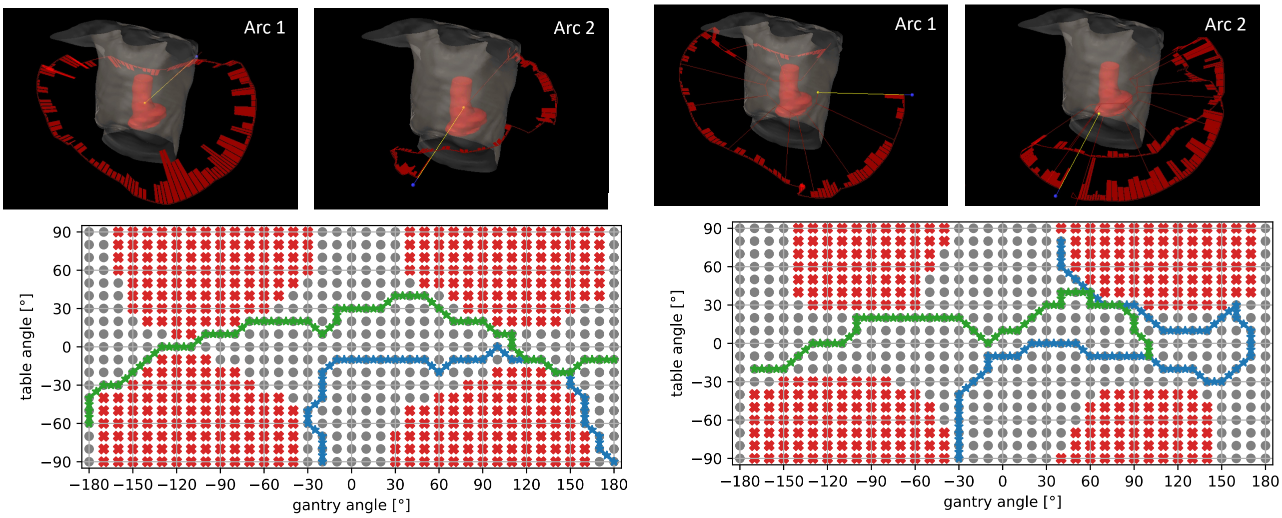

(a) isocentric DTRT (b) non-isocentric DTRT

FIGURE 6.11: Illustration of the paths of the isocentric DTRT (a) and non-isocentric DTRT (b) plans for the esophagus case. On top, the paths are illustrated using red bands. On the bottom, the paths are shown on a gantry-table map. All available map points are shown in gray, while the infeasible beam directions are indicated in red. The two paths of the DTRT plans are illustrated in blue and green.

6.5.3 Validation

All non-isocentric DTRT plans were successfully delivered on a TrueBeam in Developer mode without collision or machine interlocks. For the measured plan, the gamma passing rates between the measured and calculated dose distributions are 97% and 98% for the coronal and sagittal planes, respectively. Figure 6.13 shows the comparison between measured and calculated dose distributions.

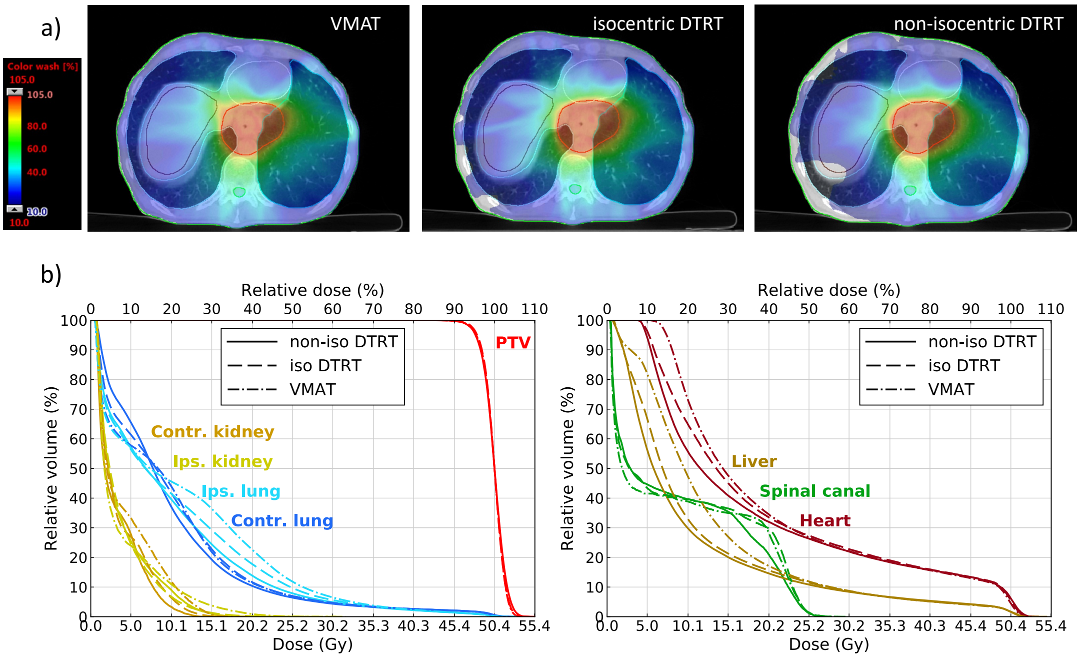

FIGURE 6.12: Dose distributions in color wash on an axial slice (a) and DVHs (b) of the VMAT, isocentric DTRT, and non-isocentric DTRT plans for the esophagus case.

TABLE 6.7: Dosimetric endpoints and estimated delivery times of the VMAT, isocentric DTRT, and non-isocentric DTRT plans for the esophagus case. The best value in each row is highlighted in bold.

	VMAT	Isocentric DTRT	Non-isocentric DTRT
PTV CI	**0.5**	**0.5**	**0.5**
PTV HI (%)	10.3	**10.2**	11.3
Ips. lung D_{mean} (Gy)	11.4	10.5	**9.9**
Contr. lung D_{mean} (Gy)	**9.8**	10.0	9.9
Lung total V_{20Gy} (%)	17.0	14.8	**12.3**
Heart D_{mean} (Gy)	20.4	19.6	**18.6**
Liver D_{mean} (Gy)	13.0	11.4	**10.4**
Ips. kidney D_{mean} (Gy)	3.8	**3.7**	3.8
Contr. kidney D_{mean} (Gy)	4.2	3.6	**3.3**
Spinal canal $D_{2\%}$ (Gy)	24.9	24.9	**24.8**
Bowel $D_{2\%}$ (Gy)	**43.1**	43.4	43.8
Estimated delivery time (min)	**2.2**	3.6	4.1

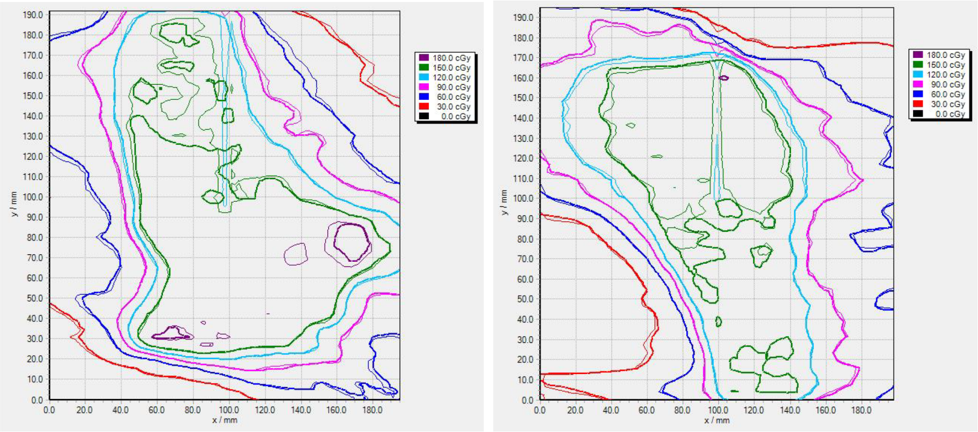

(a) sagittal plane

(b) coronal plane

FIGURE 6.13: Isodose lines of the measured dose (thin lines) and calculated dose (thick lines) of the non-isocentric DTRT plan for the esophagus case on the sagittal plane (a) and coronal plane (b).

6.6 Discussion

This work introduced a dosimetrically motivated path determination strategy based on a column generation approach for non-isocentric DTRT. In the path determination, control points are iteratively added based on their gradient on the objective function considering length restrictions, direction change restrictions, and collision restrictions. The resulting objective function value after path determination of the created plans is similar to the objective function value after intensity modulation optimization along the path. This indicates that the treatment plan quality after path generation is similar to that after final optimization, even though several approximations were made for the path generations, such as using a coarser voxel grid. There is an increase in the objective function value seen after the final dose calculation, primarily due to approximations made for efficiency enhancements of the optimization, as described by Mueller et al., 2023. The developed path determination strategy is applicable for the treatment planning of multiple treatment techniques such as DTRT, DTRT with an extended source-to-target distance, and non-isocentric DTRT for CSI. The path determination can consider any combination of gantry rotation, table rotation, and longitudinal, lateral, and vertical table translations.

Non-isocentric plans using the path determination for CSI and spinal irradiation resulted in similar treatment plan quality compared to plans with a manual path setup. The path determination for the CSI case resulted in a similar path to the manual path setup, with a longitudinal movement along the spinal cord, a gantry rotation around the skull, and a longitudinal movement back along the spinal cord. For the spinal case, the manual path setup consisted of two separate paths irradiating the spinal cord. Here, the path determination resulted in a gantry rotation in the abdomen region instead of the head region, which resulted in a higher low-dose bath in the abdomen region while improving the dose conformity and reducing the dose to the larynx and thyroid substantially compared to the plan with the manual path setup.

Non-isocentric DTRT with an extended source-to-target distance resulted in the lowest objective function value for the three investigated cases. The non-isocentric setup allowed to exploit additional collision-free space, similar to the study of Yu et al., 2018. As a result, non-isocentric DTRT plans reduced the dose to OARs compared to isocentric DTRT and VMAT plans for the breast, H&N, and esophagus cases. In the H&N case, the non-isocentric DTRT plan can use highly non-coplanar beam directions going over the head. This results in less dose to the contralateral side but an increased dose spill to all organs superior and inferior to the target, especially the brain. This may still be desirable because the dose can be spread over a larger region, resulting in an increased low-dose bath while reducing the high-dose bath. However, a critical thing for such highly non-coplanar plans is that organs such as the brain, optical structures, and hippocampus must be contoured to evaluate their dose or even place an objective on the structures for the optimization to meet their dose constraints, as described by Bertholet et al., 2022.

The delivery time of the non-isocentric DTRT plan with the manual path is 20% shorter than the plan with the optimized path for the CSI case, while for the spinal cord, the opposite is true: the delivery time is 80% longer. This is mainly due to the amount of longitudinal table translation in the plan, as the table is allowed to move up to 2 cm / s. Similarly, the non-isocentric DTRT plans for the breast, H&N, and esophagus case resulted in a mean increase in the delivery time of 70% compared to the VMAT plans. Still, the delivery times remain below 5 minutes. If shorter delivery times are desired in the future, a restriction of the table movement during the path determination can be introduced. However, the restriction may impact the treatment plan quality negatively (Loebner et al., 2023b).

One limitation of the developed path generation approach is that the number of paths and total path length must be user-defined. This resembles the treatment planning of VMAT, where a planner decides on the number of arcs and their respective ranges before the intensity modulation optimization. However, choosing suitable values a priori can be difficult, which may increase the time needed for treatment planning, as different settings need to be tested. Still, the choice of the total path length and number of arcs allows the planner to find the appropriate balance between the delivery time and the dosimetric treatment plan quality.

All deliveries of treatment plans were successful, and the dosimetric accuracy of non-isocentric DTRT plans was successfully validated for the esophagus case. This further demonstrates the dose calculation accuracy for non-isocentric DTRT plans, as shown by Manser et al., 2019; Guyer et al., 2022 using the same Monte Carlo dose calculation framework.

Dosimetrically motivated path determination techniques offer an advantage over other two-step approaches, such as OAR/target overlap (Yang et al., 2011; Smyth et al., 2013; MacDonald and Thomas, 2015; Fix et al., 2018; MacDonald et al., 2020; Reis et al., 2021), as it considers the same planning goals as during the intensity modulation optimization, thus eliminating the need of restrictions such as forcing a full gantry rotation to ensure sufficient target coverage. Path determination methods based on 4π IMRT have the disadvantage that the connections between anchor points may not be advantageous beam directions for the dynamic delivery (Wild et al., 2015; Locke and Bush, 2017; Langhans et al., 2018).

Other groups have investigated dosimetrically motivated path determination strategies for DTRT (Dong, Liu, and Xing, 2018; Lyu et al., 2018a; Mullins et al., 2020a), with Mullins et al., 2020a using a column generation approach similar to the one in this study. One limitation of these studies is the lack of a final dose calculation considering the full dynamic movement of all axes. Thus, the dosimetric accuracy of the created plans is difficult to interpret. Furthermore, the deliverability of the created plans was not shown.

One concern of the delivery of non-isocentric DTRT treatment plans is that the multiple simultaneously moving axes may cause nausea and patient discomfort. Furthermore, the direction changes may induce patient movement during the treatment Joehl et al., 2018. One way to counteract this would be to apply smoothing on the path, such that the table axes do not accelerate or decelerate quickly. Another way would be to limit the dynamic movements of certain axes during beam on. Both could be well integrated into the developed TPP.

The developed path-generation method is versatile and may also apply to other treatment techniques. For example, it can be used to create non-coplanar VMAT plans (Audet et al., 2011; Clark et al., 2012; Wild et al., 2015; Reis et al., 2021; Bertholet et al., 2023) by setting the change angle of the path to zero during the path determination. Furthermore, MLC-collimated mixed photon-electron beam radiotherapy with non-coplanar electron and photon arcs/trajectories may further reduce the dose to OARs (Mueller et al., 2017; Mueller et al., 2018b). Thus, the presented TPP may be extended to include electron beams in the future. As the path determination is dosimetrically based, another possibility is to include robust optimization not only for the intensity modulation optimization along the path but also for the path determination, resulting in robust paths.

6.7 Conclusions

A generalizable dosimetrically motivated path determination strategy for non-isocentric DTRT is successfully developed and integrated into a TPP, which can create deliverable plans. The path determination strategy further facilitates standardized treatment planning for non-isocentric DTRT. Non-isocentric DTRT plans resulted in improved dose to OARs for a breast, H&N, and esophagus case compared to isocentric DTRT and VMAT plans. The dosimetric accuracy of one non-isocentric DTRT plan was successfully validated.

6.8 Acknowledgements

This work was supported by grant 200021_185366 of the Swiss National Science Foundation and by Varian, a Siemens Healthineers Company. Calculations were performed on UBELIX (http://www.id.unibe.ch/hpc), the HPC cluster at the University of Bern.

7

Discussion and Outlook

In this thesis, a treatment planning process (TPP) for several external beam radiotherapy (EBRT) treatment techniques on a C-arm linear accelerator (linac) including dynamic table translations was developed. Furthermore, a tool was developed to predict collision interlocks during treatment planning. The TPP was used to create mixed photon-electron radiotherapy (MBRT) plans including electron arcs, which improved the delivery efficiency compared to MBRT plans using static electron beams. Furthermore, non-isocentric dynamic trajectory radiotherapy (DTRT) plans showed several possible use cases, such as improved delivery efficiency for large targets, improved dosimetric treatment plan quality, and reduced collision risk. The following subchapters discuss several points of the developed TPPs and treatment techniques.

7.1 Optimization algorithm

A key component of the TPP of intensity-modulated radiotherapy plans is the optimization of the beam intensities to fulfill the planning goals as well as possible. In chapter 2 and chapter 3, a hybrid direct aperture optimization (H-DAO) based on simulated annealing (SA) and column generation (CG) algorithms is implemented to solve this inverse planning problem. The H-DAO algorithm is capable of optimizing the intensities of photon and electron beams, including dynamic gantry, table and collimator rotations, and dynamic table translations. The H-DAO algorithm is used throughout the thesis to generate intensity-modulated radiotherapy (IMRT), volumetric modulated arc therapy (VMAT), DTRT, non-isocentric DTRT, and MBRT plans.

During the optimization, apertures describing the multileaf collimator (MLC) shape and the monitor unit (MU) weight are iteratively added through the CG algorithm. For dynamic beams, that is, beams with a dynamic gantry, collimator, or table rotation, dynamic table translation, or MLC with a sliding window technique, the beam is divided into control points, and one aperture is added for every control point. Using a step-and-shoot technique, a user-defined number of apertures are added for static beams with a static gantry, collimator, and table. The SA acts on top of the CG algorithm as a leaf refinement step. A branch feature is introduced, which optimizes multiple promising apertures simultaneously and chooses the best aperture based on the lowest objective function value instead of the gradient on the objective function. In general, the optimization algorithm showed good performance, with the objective function value of IMRT and MBRT plans (chapter 2), and VMAT and non-isocentric DTRT plans (chapter 3) being close to the objective function values of their respective benchmark plans.

An essential aspect of intensity modulation optimization algorithms is that the difference between the dose distribution which the optimization algorithm predicts and the delivered dose distribution should be small. That is, the optimization convergence error (OCE) should be minimized, as described by Jeraj, Keall, and Siebers, 2002. Several strategies are employed to reduce the OCE for the H-DAO algorithm. The transmission of photon beams through the multileaf collimator (MLC) is approximated using transmission factors. The continuous delivery during beam on of dynamic beams is approximated by interpolating the fluence between the apertures of consecutive control points. Furthermore, an MU re-optimization of the apertures is performed after a final dose calculation, taking the complete model of the MLC and the continuous movement of all axes into account. As demonstrated in chapter 3, the fluence interpolation and MU re-optimization are vital in reducing the OCE. This is in line with the work from Christiansen, Heath, and Xu, 2018, as they also observed a significant influence of the fluence interpolation on the OCE.

This thesis focused on implementing a TPP that can handle photon and electron beams and the different dynamic axes. The efficiency of the TPP was not a major focus. Still, several methods to improve the efficiency of the TPP as described by Mueller et al., 2023 are implemented. In summary, the statistical uncertainty of the photon and electron beamlet doses used for the intensity modulation optimization is set to 5% and 15%, respectively. Voxels with a beamlet dose less than 0.1% of the maximum beamlet dose are dismissed for the optimization, and a voxel merging of 8 and 64 voxels with distances larger than 1 cm and 2 cm away from the target is performed. Still, in future work, the efficiency of the TPP could be improved further to facilitate the integration of optimization methods with a considerable computational effort such as robust optimization (Renaud, Serban, and Seuntjens, 2017; Heath et al., 2021) and auto-planning (Wortel et al., 2021). The computational effort of the beamlet dose calculation could be reduced further by increasing the statistical uncertainty and using deep learning-based denoising methods (Bai et al., 2021; Neph et al., 2021; Liu et al., 2021). The efficiency of the optimization algorithm could be further improved by implementing a gradient descent with momentum algorithm for the determination of promising apertures (Zhang et al., 2019), by reducing the number of parameters during the optimization using an auto-ecoder (Bice et al., 2021), by approximating the objective function using a Taylor series (MacFarlane et al., 2019), or by employing an interpolation strategy for apertures between specific control points (Wang et al., 2022b). The efficiency of the final Monte Carlo dose calculation could also be improved by a deep learning-based denoising method (Fu et al., 2020; Kontaxis et al., 2020; Bai et al., 2021; Neph et al., 2021; Liu et al., 2021), or by using a GPU-based Monte Carlo dose calculation algorithm (Jia et al., 2011; Li et al., 2022; Franciosini et al., 2023).

7.2 Collimator rotation

Next to dynamic gantry rotation and dynamic table rotation and translation, the developed TPP can also consider dynamic collimator rotation. While the dynamic table rotation and translations enable new beam directions, the beam direction is the same for all collimator rotation angles, but the secondary collimator jaws and the MLC are rotated in the beam's eye view. Thus, dynamic collimator rotation primarily contributes to the connectedness between MLC apertures (Locke and Bush, 2017). This is a secondary effect compared to the availability of beam directions. Still, dynamic collimator rotation has been shown to improve the dosimetric treatment plan quality (Lyu et al., 2018b). Different optimization strategies to determine the dynamic collimator angle were presented in the past, such as minimizing the white space when fitting the MLC conformal to the target (Fix et al., 2018; MacDonald, Thomas, and

Syme, 2018; Battinelli, Fredriksson, and Eriksson, 2021), minimizing organ-at-risk (OAR) and target overlap (Yang et al., 2011), and simultaneous intensity modulation and collimator angle optimization (Lyu et al., 2018b).

In chapter 6, the collimator rotation is determined by aligning the collimator angle to the axis of minimum inertia. This is chosen for two reasons: First, the alignment to the axis of minimum inertia aligns the leaf movement of the MLC perpendicular to the longest part of the target, which reduces potential leaf travel. Second, because the axis of minimum inertia rotates in the beam's eye view synchronously with the gantry and table rotation, the collimator angle does not change drastically from one control point to the next. However, further studies investigating the potential of the dynamic collimator rotation are needed.

Even with dynamic collimator rotation, for large targets, it is possible that the field size in the x-direction is larger than 15 cm to encompass the whole target. This is challenging for the intensity optimization algorithm because, on the Millenium-120 MLC, the leaves of one leaf bank are allowed to be at most 15 cm apart. Thus, it is recommended that a field splitting technique splitting the field size in the x-direction into two halves is used for field sizes larger than 15 cm.

7.3 Potential use cases

Part of the aim of this thesis is to investigate potential use cases for dynamic table translations in EBRT on C-arm linear accelerators (linacs). Several potential use cases were shown throughout the thesis:

- In chapter 3 and chapter 6, a non-isocentric DTRT treatment technique for craniospinal irradiation (CSI) was developed, in which the table is dynamically translated along the longitudinal axis during beam on. The generated non-isocentric DTRT plans for CSI showed similar dosimetric treatment plan quality to a multi-isocentric IMRT plan while improving delivery efficiency.

- In chapter 3, the dosimetric treatment plan quality of a bilateral breast case was improved in a non-isocentric DTRT plan by translating the table dynamically to take advantage of more tangential beam directions compared to a multi-isocentric VMAT plan.

- In chapter 3, the trajectory of an isocentric DTRT plan was changed by moving the table 10 cm away from the gantry along the central beam axis.

  The resulting non-isocentric DTRT plan has a dosimetric treatment plan quality similar to the isocentric DTRT plans. In chapter 5, it was shown that the non-isocentric DTRT plan has an increased distance between the gantry and the patient and table. Hence, the non-isocentric DTRT plan has reduced collision risk compared to the isocentric DTRT plan.

- In chapter 4, it was shown that the delivery time of MBRT plans for four breast cases could be reduced by using electron arcs instead of static electron beams, that is, electron beams with a fixed gantry angle. The source-surface distance of the electron arc was shortened by exploiting dynamic table translations.

- In chapter 6, the additional collision-free space given by moving the table away from the gantry along the central axis was exploited during the path determination step. The resulting non-isocentric DTRT plans improved the dosimetric treatment plan quality compared to the isocentric DTRT plans.

Furthermore, dosimetric plan comparisons between DTRT and MBRT plans and state-of-the-art IMRT and VMAT plans were performed. In chapter 2 and chapter 4, MBRT plans improved dosimetric treatment plan quality compared to photon-only plans for a brain case, a head and neck case, and four breast cases. This further supports the evidence of the dosimetric superiority of pMLC-based MBRT treatments over photon-only treatments for cases including a superficial part. A potential advantage of pMLC-based MBRT was shown in literature for tumors in breast (Míguez et al., 2017), head and neck (Mueller et al., 2018a), brain (Rosca, 2012; Heath et al., 2021), extremities (Renaud, Serban, and Seuntjens, 2017; Heng et al., 2023a), abdomen (Mueller et al., 2018b; Unkelbach et al., 2022), and chest wall (Renaud, Serban, and Seuntjens, 2017). Thus, a broad range of treatment sites could profit from MBRT, with the potential of electron arcs ensuring an efficient delivery.

Similarly, generated DTRT plans were shown to improve dosimetric treatment plan quality over VMAT plans for a brain case (chapter 3), a head and neck case (chapter 6), an esophagus case (chapter 6), and a breast case (chapter 6). Non-coplanar radiotherapy on a C-arm linac has been shown to improve OAR sparing over IMRT and VMAT for multiple treatment sites such as brain (Audet et al., 2011; Clark et al., 2012; MacDonald and Thomas, 2015; Smyth et al., 2016; Wilson, Otto, and Gete, 2017; Yu et al., 2018; Ohira et al., 2018), head and neck (Yang et al., 2011; Wild et al., 2015; Subramanian et al., 2017; Gayen et al., 2020; Pokhrel et al., 2022; Bertholet et al., 2022), liver (Dong et al., 2013; Tran et al., 2017a; Langhans et al., 2018), prostate (Dong et al., 2014; Tran et al., 2017b), lung (Papp, Bortfeld, and Unkelbach, 2015; Fix et al., 2018; Lyu et al., 2018a), breast (Smyth et al., 2013), chest wall (Dong, Liu, and Xing, 2018), esophagus (Dong, Liu, and Xing, 2018; Fix et al., 2018) and treatment of ventricular tachycardia (Reis et al., 2021). Hence, DTRT could improve the dosimetric treatment plan quality for many treatment sites, and non-isocentric DTRT offers reduced collision risk or enables otherwise infeasible beam directions. Furthermore, treatments other than bilateral whole breast irradiation may benefit from more tangential beam directions, such as chest wall treatments or bilateral head and neck treatments, due to their concave target shapes and superficial parts.

In summary, dynamic table translations showed potential benefits in delivery efficiency, dosimetric treatment plan quality, and reduced collision risk for DTRT and MBRT treatment techniques. Here, the focus was on developing the treatment techniques and showing the potential benefit in a few cases. Of course, the limited number of investigated cases only indicates a potential benefit, as cases are diverse, and the same potential may only be observed for some patients. Thus, future work toward clinical implementation should include more comprehensive treatment planning comparisons with larger patient cohorts for treatment techniques including dynamic table translations.

In addition, the focus was on a C-arm linac to implement and investigate dynamic table translations. However, there might also be potential for improving the delivery efficiency on O-ring linacs by translating the table dynamically. For example, the presented CSI treatment technique would also be applicable for O-ring linacs. Additionally, as the field size on the Halcyon system (Varian, a Siemens Healthineers Company, Germany) is smaller than on a C-arm linac (Lim et al., 2019), other treatment sites with large tumors might benefit from the dynamic table translation along the longitudinal axis on the O-ring linac as well.

7.4 Deliverability

An essential aspect of this thesis was to develop treatment plans with dynamic table translations that are accurately deliverable. This includes two aspects: first, the machine must deliver the specified treatment plan accurately, and second, there must be an accurate simulation of the treatment plan to calculate the dose distribution. The deliverability of treatment plans including dynamic table translations was shown in chapter 3, chapter 4, and chapter 6. The plans were delivered without machine interlocks due to any axis being out of tolerance. Yu et al., 2014 tested the mechanical accuracy of dynamic table motion and found the translational accuracy was 0.01 cm and the rotational accuracy was within 0.3°. Similarly, Rodrigues, Yin, and Wu, 2014 found a translational accuracy below 0.1 cm.

A collision prediction tool was developed in chapter 5 to ensure the delivery of the generated treatment plans. The tool can generate maps with collision-free zones and check generated plans for any potential collisions. The validation of the tool showed suitable sensitivity; that is, the collision prediction tool only failed to predict one collision interlock in the validation. All generated treatment plans that used the collision prediction tool to exclude infeasible beam directions were deliverable without collision interlocks. Furthermore, the tool has been used to successfully check for collision-free delivery of DTRT treatment plans in further studies (Bertholet et al., 2022; Loebner et al., 2023a).

Film measurements were performed for several treatment plans including dynamic table translation, to validate the accuracy of the simulated dose distributions. The simulated and measured dose distributions in chapter 3, chapter 4, and chapter 6 are all within tolerance recommended by Miften et al., 2018. This line with the work of Manser et al., 2019, which validated the accuracy of MC-based dose calculation of non-isocentric DTRT, and Smyth et al., 2019a, which validated the accuracy of dose calculation for DTRT plans. Additionally, Wang, Sawkey, and Wu, 2020 validated the accuracy for electron arcs including dynamic table translations; however, only with a collapsed gantry angle.

In this thesis, radiochromic films were used for the validation measurements. Radiochromic films offer a high resolution, 2D dose measurement that works for photon and electron beams, has a minimal energy dependence, is nearly water equivalent, and can be cut to fit in a specific measurement phantom. However, if the presented treatment techniques find their way to clinical implementation, a fast and reliable method for patient-specific quality assurance (PSQA) measurements is needed. While film-based PSQA exists (Popple et al., 2021a), it is not practical as the films need careful handling and do not provide an immediate read-out. Thus, practical and sufficiently sensitive PSQA procedures must be developed to facilitate the implementation of DTRT and MBRT techniques into the clinic. Tai et al., 2023 proposed a PSQA for MBRT based on a 2D diode array and log file analysis. Similarly, Popple et al., 2021b proposed a PSQA with a 2D diode array for non-coplanar VMAT. Of course, such methods would need to be investigated for MBRT and DTRT including dynamic table translations to prove that they are sufficiently sensitive to detect errors in these treatment techniques. There is a push for replacing the measurement-based PSQA with only software-based PSQA (Siochi, Molineu, and Orton, 2013; Basavatia et al., 2021; Cavalli et al., 2023), which would negate the need for the development of new measurement devices for MBRT and DTRT. However, one should be careful to ensure that the software can catch all big errors (such as the ones reported by the New York Times (Bogdanich, 2010)) with 100% certainty.

One concern of the delivery of treatment plans including dynamic table translation is patient comfort, as the accelerating and decelerating of the table may cause nausea. In the study by Yu et al., 2018, patient comfort was assessed for 4π radiation therapy including table rotations and table translations and they reported that the treatments were well tolerated. Míguez et al., 2017 reported in a clinical trial for MBRT, including table translations, no additional inconvenience for the patients. Still, volunteer studies for the assessment of patient comfort in treatment techniques including dynamic table translations are needed in future. If necessary, measures such as reducing the maximal translational table speed or smoothing the dynamic trajectories may be applied.

7.5 Patient setup

One challenge for non-isocentric treatment techniques is that the on-board imaging used for patient setup in image-guided radiotherapy (IGRT) is limited in the field of view. Hence, the corrections applied for the patient setup may only be accurate for a small region around the imaging isocenter, and rotational errors may have a more considerable dosimetric impact (Sagawa et al., 2019; Shen et al., 2023). Especially for large targets such as CSI, how to perform the IGRT for non-isocentric treatment techniques is unclear. One possible solution for this problem is to take X-ray images at multiple locations and then calculate the corrections for the patient positioning using all images simultaneously. Another possible solution offer room-mounted X-ray IGRT systems such as the ExacTrac system (Brain Lab Inc., Germany), as there is the potential for larger fields of view. This would also have the advantage that images can be taken with a non-zero gantry angle. Thus, the correct patient position could also be verified during the treatment delivery. On the same note, surface-guided radiotherapy systems may help ensure the patient's position for non-isocentric and non-coplanar treatment techniques in the future.

As there is a residual patient uncertainty even with IGRT, the robustness of non-isocentric DTRT and MBRT plans to patient setup uncertainties may also be of interest. Thus, the robustness to patient setup uncertainties of non-isocentric treatment techniques may be evaluated using a robustness assessment tool as the one developed by Loebner et al., 2022. One exciting aspect of robustness evaluation for non-isocentric treatment techniques is that for large targets such as in CSI, the dynamic table translation may even increase robustness compared to multi-isocentric treatment planning by negating the possibility of changing the distance between isocenter positions (Myers et al., 2013; Witztum et al., 2014). Another thing to note is that the robustness of the treatment plans using dynamic table rotations and translations may be more critical than treatment plans with a static table because the dynamic table movement may induce patient movements. Joehl et al., 2018 studied the induced uncertainty of the patient's position for table tracking and found a median uncertainty of 0.4-0.8 mm. Also, range uncertainties may impact the robustness of MBRT plans (Heng et al., 2023b). Thus, robust evaluation should be performed for patient setup uncertainties, induced patient motion, and range uncertainties. Furthermore, robust optimization for non-isocentric DTRT and MBRT may further improve the robustness of these treatment techniques.

The patient setup uncertainties also pose a challenge for the collision-free delivery; for example, when the patient or the table is very close to the gantry, and a slight change in the table position can lead to a collision interlock. In the presented collision prediction tool in chapter 5, the patient setup uncertainties can be included in calculating potential collisions of a treatment plan, ensuring that the treatment plan is deliverable for the entire treatment duration. To increase the precision of the collision prediction tool in the future, the tool may be extended to incorporate patient surface scans similar to the work by Padilla, Pearson, and Pelizzari, 2015; Cardan, Popple, and Fiveash, 2017; Hueso-Gonález et al., 2020; Islam et al., 2020. This also allows daily surface scans before treatment which can be integrated into the collision prediction tool to directly indicate potential collision interlocks for the actual patient and table position.

7.6 Future directions

Next to the discussed future work in the previous chapters, multiple other directions for future work are possible. The following gives an outlook of future possible research for non-isocentric treatment techniques.

In this thesis, the photon beams in the created treatment plans always used a flattening filter. However, there is a tendency to do flattening filter-free (FFF)

IMRT and VMAT in clinics (Xiao et al., 2015). As only the intensity modulation optimization changes, the current TPP may easily be extended to create non-isocentric DTRT and MBRT plans with FFF photon beams. The use of FFF photon beams has the potential to further improve the delivery efficiency of non-isocentric DTRT and MBRT plans, especially for high doses per fraction, as FFF beams have a higher maximal dose rate than flattened beams.

While the presented DTRT treatment techniques use non-coplanar photon beams, the electron beams in MBRT are always kept coplanar in this thesis. Including non-coplanar electron beams in MBRT might offer an additional dosimetric advantage, similar to the benefit of non-coplanar beam directions of photon beams. Mixed photon-electron beam radiotherapy including non-coplanar photon and electron beams might thus have an additional dosimetric benefit. Hence, dynamic mixed beam radiotherapy (DYMBER) including dynamic trajectories for electron and photon beams should be investigated in the future. The presented dosimetrically motivated path determination in chapter 6 is extendable such that photon and electron trajectories are optimized simultaneously.

In recent years, adaptive radiotherapy for inter-fractional changes has gained much traction (Bertholet et al., 2020; Glide-Hurst et al., 2021; Liu et al., 2023). Next to robust optimization, adaptive non-isocentric DTRT and adaptive MBRT may also be explored in the future. Adaptive radiotherapy could also help solve the abovementioned difficulties concerning patient setup. Radiotherapy including dynamic trajectories also offers a new dimensionality for adaption, as not only the intensity modulation of the treatment plan can be adapted but the dynamic trajectory itself as well.

Another hot topic of the last years is electron FLASH radiotherapy (e-FLASH) (Vozenin, Bourhis, and Durante, 2022), in which ultra-high dose rates are used to achieve a healthy tissue-sparing effect. One possibility of an e-FLASH treatment uses conventional electron beam energies by converting a C-arm linac to deliver ultra-high dose rates (Rahman et al., 2021; No et al., 2023). However, achieving sufficient target coverage and dose conformity to the target using e-FLASH remains a challenge. One possibility to achieve a FLASH effect while not compromising the conformity of the dose distribution to the target would be to combine e-FLASH with MBRT. Here, dynamic table translations may facilitate a better FLASH effect by shortening the SSD for the photon beams. The shortened SSD facilitates higher dose rates for the photon beams, which could contribute to the overall healthy tissue-sparing effect.

8

Conclusions

In this thesis, multiple treatment techniques for external beam radiotherapy (EBRT) on a C-arm linear accelerator (linac) including dynamic table translations were successfully developed, and several potential use cases of EBRT plans including dynamic table translations were demonstrated. An intensity modulation optimization was developed based on a hybrid simulated annealing and column generation direct aperture optimization (H-DAO). The H-DAO is able to optimize the intensity modulation of photon and electron beams including dynamic gantry, collimator, and table rotations and dynamic table translations. Furthermore, a collision prediction tool was successfully developed.

Non-isocentric dynamic trajectory radiotherapy (DTRT) plans for craniospinal irradiation cases improved delivery efficiency while maintaining the dosimetric treatment plan quality compared to multi-isocentric intensity-modulated radiotherapy (IMRT) plans. Extending the source-to-target distance in DTRT plans could reduce the risk of collision between the gantry and the patient or table. Furthermore, non-isocentric DTRT plans improved the dosimetric treatment plan quality compared to isocentric treatment plans for several treatment sites. In mixed photon-electron beam radiotherapy (MBRT), using electron arcs with dynamic table translations improved delivery efficiency while maintaining the dosimetric treatment plan quality compared to MBRT with static electron beams.

The created treatment plans were shown to be accurately deliverable on a TrueBeam system (Varian, a Siemens Healthineers Company, Germany). The dosimetric accuracy was successfully validated using film measurements for several treatment plans. The developed collision prediction tool was shown to facilitate the delivery of treatment plans without collision interlocks.

In conclusion, this thesis demonstrates the benefits of dynamic table translations in photon and electron beam radiotherapy. Accurately deliverable treatment plans including dynamic table translations are successfully created and validated. With the demonstrated benefits of improved dosimetric treatment plan quality, delivery efficiency, and collision risk, dynamic table translations further facilitate the use of MBRT and DTRT treatment techniques in clinics in the future.

Bibliography

Al-Yahya, Khalid, Frank Verhaegen, and Jan Seuntjens (2007). "Design and dosimetry of a few leaf electron collimator for energy modulated electron therapy". In: *Med. Phys.* 34 (12), pp. 4782–4791. DOI: 10.1118/1.2795827.

Al-Yahya, Khalid et al. (2005a). "Monte Carlo based modulated electron beam treatment planning using a few-leaf electron collimator a feasibility study". In: *Phys. Med. Biol.* 50 (5), p. 847. DOI: 10.1088/0031-9155/50/5/009.

Al-Yahya, Khalid et al. (2005b). "Energy modulated electron therapy using a few leaf electron collimator in combination with IMRT and 3D-CRT: Monte Carlo-based planning and dosimetric evaluation". In: *Med. Phys.* 32 (9), pp. 2976–2986. DOI: 10.1118/1.2011089.

Alahmad, Haitham N. et al. (2020). "A sliding-window approach for improved VMAT dose calculation accuracy". In: *Med. Dosim.* 45 (3), pp. 197–201. DOI: 10.1016/J.MEDDOS.2019.11.001.

Alexander, Andrew, François DeBlois, and Jan Seuntjens (2010). "Toward automatic field selection and planning using Monte Carlo-based direct aperture optimization in modulated electron radiotherapy". In: *Phys. Med. Biol.* 55 (16), pp. 4563–4576. DOI: 10.1088/0031-9155/55/16/S10.

Alexander, Andrew et al. (2011). "Comparison of modulated electron radiotherapy to conventional electron boost irradiation and volumetric modulated photon arc therapy for treatment of tumour bed boost in breast cancer". In: *Radiother. Oncol.* 100 (2), pp. 253–258. DOI: 10.1016/j.radonc.2011.05.081.

Anders, Ahnesjö (1989). "Collapsed cone convolution of radiant energy for photon dose calculation in heterogeneous media". In: *Med. Phys.* 16 (4), pp. 577–592. DOI: 10.1118/1.596360.

Åsell, Mats et al. (1997). "Optimization of 3D conformal electron beam therapy in inhomogeneous media by concomitant fluence and energy modulation". In: *Phys. Med. Biol.* 42 (11), p. 2083. DOI: 10.1088/0031-9155/42/11/006.

Atun, Rifat et al. (2015). "Expanding global access to radiotherapy". In: *Lancet Oncol.* 16 (10), pp. 1153–1186. DOI: 10.1016/S1470-2045(15)00222-3.

Audet, Chantal et al. (2011). “Evaluation of volumetric modulated arc therapy for cranial radiosurgery using multiple noncoplanar arcs”. In: *Med. Phys.* 38 (11), pp. 5863–5872. DOI: `10.1118/1.3641874`.

Bai, Ti et al. (2021). “Deep dose plugin: towards real-time Monte Carlo dose calculation through a deep learning-based denoising algorithm”. In: *Mach. Learn.: Sci. Technol.* 2 (2), p. 025033. DOI: `10.1088/2632-2153/abdbfe`.

Bangert, Mark (2011). “New concepts for beam angle selection in IMRT treatment planning : From heuristics to combinatorial optimization”. In: DOI: `10.11588/heidok.00012272`.

Basavatia, Amar K. et al. (2021). “Comprehensive Patient-Specific Intensity-Modulated Radiation Therapy Quality Assurance Comparing Mobius3D/FX to Conventional Methods of Evaluation.” In: *Cureus* 13 (5), e14910. DOI: `10.7759/cureus.14910`.

Battinelli, Cecilia, Albin Fredriksson, and Kjell Eriksson (2021). “Technical Note: Collimator angle optimization for multiple brain metastases in dynamic conformal arc treatment planning”. In: *Med. Phys.* 48 (9), pp. 5414–5422. DOI: `10.1002/mp.15078`.

Battista, Jerry J., William D. Rider, and Jake Van Dyk (1980). “Computed tomography for radiotherapy planning”. In: *Int. J. Radiat. Oncol. Biol. Phys.* 6 (1), pp. 99–107. DOI: `10.1016/0360-3016(80)90211-4`.

Bedford, James L. (2009). “Treatment planning for volumetric modulated arc therapy”. In: *Med. Phys.* 36 (11), pp. 5128–5138. DOI: `10.1118/1.3240488`.

Bedford, James L. et al. (2012). “Helical Volumetric Modulated Arc Therapy for Treatment of Craniospinal Axis”. In: *Int. J. Rad. Biol. Phys.* 83 (3), pp. 1047–1054. DOI: `10.1016/j.ijrobp.2011.07.039`.

Bedford, James L. et al. (2019). “Treatment planning optimization with beam motion modeling for dynamic arc delivery of SBRT using Cyberknife with multileaf collimation”. In: *Med. Phys.* 46 (12), pp. 5421–5433. DOI: `10.1002/mp.13848`.

Bergman, Alanah M. et al. (2006). “Direct aperture optimization for IMRT using Monte Carlo generated beamlets”. In: *Med. Phys.* 33 (10), pp. 3666–3679. DOI: `10.1118/1.2336509`.

Bertholet, Jenny et al. (2020). “Patterns of practice for adaptive and real-time radiation therapy (POP-ART RT) part II: Offline and online plan adaption for interfractional changes”. In: *Radiother. Oncol.* 153. Physics Special Issue: ESTRO Physics Research Workshops on Science in Development, pp. 88–96. DOI: `10.1016/j.radonc.2020.06.017`.

Bertholet, Jenny et al. (2022). “Organ-at-risk sparing with dynamic trajectory radiotherapy for head and neck cancer: comparison with volumetric arc therapy on a publicly available library of cases”. In: *Radiat. Oncol.* 17 (1), p. 122. DOI: 10.1186/s13014-022-02092-5.

Bertholet, Jenny et al. (2023). “Dosimetrically motivated beam-angle optimization for non-coplanar arc radiotherapy with and without dynamic collimator rotation”. In: *Med. Phys.* n/a.n/a. DOI: 10.1002/mp.16899.

Bice, Noah et al. (2021). “Latent space arc therapy optimization”. In: *Phys. Med. Biol.* 66 (21), p. 215019. DOI: 10.1088/1361-6560/ac1b1c.

Blender Online Community (2018). *Blender - a 3D modelling and rendering package*. URL: http://www.blender.org.

Bogdanich, Walt (2010). “As technology surges, radiation safeguards lag”. In: *New York Times* 23, p. 15.

Bonnett, D. E. (1993). “Current developments in proton therapy: a review”. In: *Phys. Med. Biol.* 38 (10), p. 1371. DOI: 10.1088/0031-9155/38/10/001.

Borras, Josep M. et al. (2015). “The optimal utilization proportion of external beam radiotherapy in European countries: An ESTRO-HERO analysis”. In: *Radiother. Oncol.* 116 (1), pp. 38–44. DOI: 10.1016/j.radonc.2015.04.018.

Bortfeld, Thomas (2006). “IMRT: a review and preview”. In: *Phys. Med. Biol.* 51 (13), R363. DOI: 10.1088/0031-9155/51/13/R21.

Brewster, Linda et al. (1995). “Three dimensional conformal treatment planning with multileaf collimators”. In: *Int. J. Radiat. Oncol. Biol. Phys.* 33 (5), pp. 1081–1089. DOI: 10.1016/0360-3016(95)02061-6.

Brost, Eric E., H. Wan Chan Tseung, and John A. Antolak (2023). “A fast GPU-accelerated Monte Carlo engine for calculation of MLC-collimated electron fields”. In: *Med. Phys.* 50 (1), pp. 600–618. DOI: 10.1002/mp.15938.

Bryant, PJ (1994). *A brief history and review of accelerators*.

Byrne, Mikel, Yunfei Hu, and Ben Archibald-Heeren (2016). “Evaluation of RayStation robust optimisation for superficial target coverage with setup variation in breast IMRT”. In: *Australas. Phys. Eng. Sci. Med.* 39 (3), pp. 705–716. DOI: 10.1007/s13246-016-0466-6.

Bzdusek, Karl et al. (2009). “Development and evaluation of an efficient approach to volumetric arc therapy planning”. In: *Med. Phys.* 36 (6Part1), pp. 2328–2339. DOI: 10.1118/1.3132234.

Cardan, Rex A., Richard A. Popple, and John Fiveash (2017). “A priori patient-specific collision avoidance in radiotherapy using consumer grade depth cameras”. In: *Med. Phys.* 44 (7), pp. 3430–3436. DOI: 10.1002/mp.12313.

Carlsson, Fredrik (2008). “Combining segment generation with direct step-and-shoot optimization in intensity-modulated radiation therapy”. In: *Med. Phys.* 35 (9), pp. 3828–3838. DOI: `10.1118/1.2964096`.

Carlsson, Fredrik and Anders Forsgren (2014). “On column generation approaches for approximate solutions of quadratic programs in intensity-modulated radiation therapy”. In: *Ann. Oper. Res.* 223 (1), pp. 471–481. DOI: `10.1007/s10479-013-1360-1`.

Cassioli, A. and J. Unkelbach (2012). “Aperture shape optimization for IMRT treatment planning”. In: *Phys. Med. Biol.* 58 (2), p. 301. DOI: `10.1088/0031-9155/58/2/301`.

Cavalli, Nina et al. (2023). “Is it still necessary to perform measured based pre-treatment patient-specific QA for SRS HyperArc treatments?” In: *J. Appl. Clin. Med. Phys.* e14156. DOI: `10.1002/acm2.14156`.

Chargari, Cyrus et al. (2019). “Brachytherapy: An overview for clinicians”. In: *CA Cancer J. Clin.* 69 (5), pp. 386–401. DOI: `10.3322/caac.21578`.

Chin, Stephen et al. (2020). “Magnetic resonance-guided radiation therapy: A review”. In: *J. Med. Imaging. Radiat. Oncol.* 64 (1), pp. 163–177. DOI: `10.1111/1754-9485.12968`.

Christiansen, Eric, Emily Heath, and Tong Xu (2018). “Continuous aperture dose calculation and optimization for volumetric modulated arc therapy”. In: *Phys. Med. Biol.* 63 (21). DOI: `10.1088/1361-6560/aae65e`.

Cirillo, Pasquale et al. (2021). *Schweizerischer Krebsbericht 2021 : Stand und Entwicklungen.*

Clark, Grant M. et al. (2012). “Plan quality and treatment planning technique for single isocenter cranial radiosurgery with volumetric modulated arc therapy”. In: *Pract. Radiat. Oncol.* 2 (4), pp. 306–313. DOI: `10.1016/J.PRRO.2011.12.003`.

Convery, D. J. and M. E. Rosenbloom (1992). “The generation of intensity-modulated fields for conformal radiotherapy by dynamic collimation”. In: *Phys. Med. Biol.* 37 (6), p. 1359. DOI: `10.1088/0031-9155/37/6/012`.

Darby, Sarah C. et al. (2013). “Risk of Ischemic Heart Disease in Women after Radiotherapy for Breast Cancer”. In: *N. Engl. J. Med.* 11, pp. 987–98. DOI: `10.1056/NEJMoa1209825`.

Debela, Dejene Tolossa et al. (2021). “New approaches and procedures for cancer treatment: Current perspectives”. In: *SAGE Open Medicine* 9. DOI: `10.1177/20503121211034366`.

Desaulniers, Guy, Jacques Desrosiers, and Marius M. Solomon (2005). *Column Generation*. Springer US, pp. 1–358. ISBN: 0387254854. DOI: 10.1007/B135457/COVER.

Dong, Peng, Hongcheng Liu, and Lei Xing (2018). "Monte Carlo tree search -based non-coplanar trajectory design for station parameter optimized radiation therapy (SPORT)". In: *Phys. Med. Biol.* 63 (13), p. 135014. DOI: 10.1088/1361-6560/AACA17.

Dong, Peng et al. (2013). "4π Non-Coplanar Liver SBRT: A Novel Delivery Technique". In: *Int. J. Radiat. Oncol. Biol. Phys.* 85 (5), pp. 1360–1366. DOI: 10.1016/J.IJROBP.2012.09.028.

Dong, Peng et al. (2014). "Feasibility of prostate robotic radiation therapy on conventional C-arm linacs". In: *Pract. Radiat. Oncol.* 4 (4), pp. 254–260. DOI: 10.1016/J.PRRO.2013.10.009.

du Plessis, F. C. P. et al. (2006). "Characterization of megavoltage electron beams delivered through a photon multi-leaf collimator (pMLC)". In: *Phys. Med. Biol.* 51 (8), pp. 2113–2129. DOI: 10.1088/0031-9155/51/8/011.

Dyk, Jacob Van and Jerry J Battista (1996). "Cobalt-60 : An Old Modality, A Renewed Challenge". In: *Curr. Oncol.* (3), pp. 8–17.

Eldib, Ahmed et al. (2013). "Feasibility of replacing patient specific cutouts with a computer-controlled electron multileaf collimator". In: *Phys. Med. Biol.* 58 (16), p. 5653. DOI: 10.1088/0031-9155/58/16/5653.

Eldib, Ahmed et al. (2017). "Investigating the dosimetric benefits of modulated electron radiation therapy (MERT) for partial scalp patients". In: *Biomed. Phys. Eng. Express* 3 (3), p. 035013. DOI: 10.1088/2057-1976/AA70AB.

Engel, Konrad and Tobias Gauer (2009). "A dose optimization method for electron radiotherapy using randomized aperture beams". In: *Phys. Med. Biol.* 54 (17), p. 5253. DOI: 10.1088/0031-9155/54/17/012.

Ferlay, J. et al. (2020). *Global Cancer Observatory: Cancer Today. Lyon, France: International Agency for Research on Cancer.* URL: https://gco.iarc.fr/today,.

Fix, Michael K. et al. (2007). "An efficient framework for photon Monte Carlo treatment planning". In: *Phys. Med. Biol.* 52 (19), N425. DOI: 10.1088/0031-9155/52/19/N01.

Fix, Michael K. et al. (2013). "Generalized eMC implementation for Monte Carlo dose calculation of electron beams from different machine types". In: *Phys. Med. Biol.* 58, pp. 2841–2859. DOI: 10.1088/0031-9155/58/9/2841.

Fix, Michael K. et al. (2018). “Part 1: Optimization and evaluation of dynamic trajectory radiotherapy”. In: *Med. Phys.* 45 (9), pp. 4201–4212. DOI: 10.1002/mp.13086.

Fix, Michael K. et al. (2023). “Auto-commissioning of a Monte Carlo electron beam model with application to photon MLC shaped electron fields”. In: *Phys. Med. Biol.* DOI: 10.1088/1361-6560/acb755.

Franciosini, G. et al. (2023). “GPU-accelerated Monte Carlo simulation of electron and photon interactions for radiotherapy applications”. In: *Phys. Med. Biol.* 68 (4), p. 044001. DOI: 10.1088/1361-6560/aca1f2.

Freislederer, P. et al. (2020). “Recent advances in Surface Guided Radiation Therapy”. In: *Radiat. Oncol.* 15 (1), p. 187. DOI: 10.1186/s13014-020-01629-w.

Fu, Jiaqi et al. (2020). “Fast Monte Carlo dose calculation based on deep learning”. In: *Proc. - 2020 13th Int. Congr. Image Signal Process. BioMed. Eng. Inform. CISP-BMEI*, pp. 721–726. DOI: 10.1109/CISP-BMEI51763.2020.9263502.

Gaffney, David K. et al. (2001). “Electron arc irradiation of the postmastectomy chest wall with CT treatment planning: 20-Year experience”. In: *Int. J. Radiat. Oncol. Biol. Phys.* 51 (4), pp. 994–1001. DOI: 10.1016/S0360-3016(01)01726-6.

Gauer, T. et al. (2008). “Characterization of an add-on multileaf collimator for electron beam therapy”. In: *Phys. Med. Biol.* 53 (4), p. 1071. DOI: 10.1088/0031-9155/53/4/017.

Gayen, Sanjib et al. (2020). “Dosimetric comparison of coplanar and non-coplanar volumetric-modulated arc therapy in head and neck cancer treated with radiotherapy”. In: *Radiat. Oncol. J.* 38 (2), pp. 138–147. DOI: 10.3857/roj.2020.00143.

Ghaderi, Nima et al. (2022). “A Century of Fractionated Radiotherapy: How Mathematical Oncology Can Break the Rules”. In: *Int. J. Mol. Sci.* 23 (1316). DOI: 10.3390/ijms23031316.

Glide-Hurst, Carri K. et al. (2021). “Adaptive Radiation Therapy (ART) Strategies and Technical Considerations: A State of the ART Review From NRG Oncology”. In: *Int. J. Radiat. Oncol. Biol. Phys.* 109 (4), pp. 1054–1075. DOI: 10.1016/j.ijrobp.2020.10.021.

Guyer, G. et al. (2022). “Enabling non-isocentric dynamic trajectory radiotherapy by integration of dynamic table translations”. In: *Phys. Med. Biol.* 67 (17). DOI: 10.1088/1361-6560/ac840d.

Guyer, Gian et al. (2023). “Technical note: A collision prediction tool using Blender”. In: *J. Appl. Clin. Med. Phys.* 24 (11), e14165. DOI: `10.1002/acm2.14165`.

Hanahan, Douglas and Robert A. Weinberg (2011). *Hallmarks of cancer: The next generation.* DOI: `10.1016/j.cell.2011.02.013`.

Hardemark, B et al. (2003). *Direct Machine Parameter Optimization with RayMachine in Pinnacle.*

Hart, Peter E., Nils J. Nilsson, and Bertram Raphael (1968). “A Formal Basis for the Heuristic Determination of Minimum Cost Paths”. In: *EEE Trans. Syst. Sci. Cybern.* 4 (2), pp. 100–107. DOI: `10.1109/TSSC.1968.300136`.

Healy, B. J. et al. (2017). “Cobalt-60 Machines and Medical Linear Accelerators: Competing Technologies for External Beam Radiotherapy”. In: *Clin. Oncol.* 29 (2), pp. 110–115. DOI: `10.1016/J.CLON.2016.11.002`.

Heath, Emily et al. (2021). “Implementation and experimental validation of a robust hybrid direct aperture optimization approach for mixed-beam radiotherapy”. In: *Med. Phys.* 48 (11), pp. 7299–7312. DOI: `10.1002/mp.15258`.

Heng, Veng Jean et al. (2021). “Ion chamber and film-based quality assurance of mixed electron-photon radiation therapy”. In: *Med. Phys.* 48 (9), pp. 5382–5395. DOI: `10.1002/MP.15081`.

Heng, Veng Jean et al. (2023a). “Robust mixed electron-photon radiation therapy planning for soft tissue sarcoma”. In: *Med. Phys.* 50 (10), pp. 6502–6513. DOI: `10.1002/mp.16709`.

Heng, Veng Jean et al. (2023b). “273 Impact of Range Uncertainties on Robust Mixed Electron-Photon Beam Radiation Therapy”. In: *Radiother. and Oncol.* 186. CARO-COMP Joint Scientific Meeting Interprofessional Collaboration: Better Together September 20-23, 2023, Montréal, Canada, S116–S117. DOI: `10.1016/S0167-8140(23)89365-3`.

Henzen, D. et al. (2014a). “Monte Carlo based beam model using a photon MLC for modulated electron radiotherapy”. In: *Med. Phys.* 41 (2), p. 021714. DOI: `10.1118/1.4861711`.

Henzen, D. et al. (2014b). “Beamlet based direct aperture optimization for MERT using a photon MLC”. In: *Med. Phys.* 41 (12), p. 121711. DOI: `10.1118/1.4901638`.

Hiramoto, Kazuo et al. (2007). “The synchrotron and its related technology for ion beam therapy”. In: *Nuc. Instrum. Methods Phys. Res. B* 261 (1). The Application of Accelerators in Research and Industry, pp. 786–790. DOI: `10.1016/j.nimb.2007.04.287`.

Hiraoka, Masahiro et al. (2020). "The gimbaled-head radiotherapy system: Rise and downfall of a dedicated system for dynamic tumor tracking with real-time monitoring and dynamic WaveArc". In: *Radiother. Oncol.* 153, pp. 311–318. DOI: `10.1016/j.radonc.2020.07.002`.

Ho, Hsiu-Wen et al. (2020). "Dosimetric comparison between RapidArc and HyperArc techniques in salvage stereotactic body radiation therapy for recurrent nasopharyngeal carcinoma". In: *Radiat. Oncol.* 15 (1), p. 164. DOI: `10.1186/s13014-020-01602-7`.

Hodapp, N. (2012). "The ICRU Report 83: prescribing, recording and reporting photon-beam intensity-modulated radiation therapy (IMRT)." In: *Strahlenther. Onkol.* 188 (1). DOI: `10.1007/s00066-011-0015-x`.

Hogstrom, Kenneth R. and Peter R. Almond (2006). "Review of electron beam therapy physics". In: *Phys. Med. Biol.* 51 (13), R455. DOI: `10.1088/0031-9155/51/13/R25`.

Hubenak, Justin R. et al. (2014). "Mechanisms of Injury to Normal Tissue after Radiotherapy: A Review". In: *Plast. Reconstr. Surg.* 133 (1). DOI: `10.1097/01.prs.0000440818.23647.0b`.

Hueso-Gonález, F. et al. (2020). "An open-source platform for interactive collision prevention in photon and particle beam therapy treatment planning". In: *Biomed. Phys. Eng. Express* 6 (5), p. 055013. DOI: `10.1088/2057-1976/aba442`.

Humm, J. L. (1994). "Collision avoidance in computer optimized treatment planning". In: *Med. Phys.* 21 (7), pp. 1053–1064. DOI: `10.1118/1.597397`.

Humm, John L. et al. (1995). "Collision detection and avoidance during treatment planning". In: *Int. J. Rad. Oncol. Biol. Phys.* 33 (5), pp. 1101–1108. DOI: `10.1016/0360-3016(95)00155-7`.

IAEA (2023). *The IAEA Directory of Radiotherapy Centres (DIRAC)*. URL: `https:/dirac.iaea.org/`.

IAEA (2005). *Radiation Oncology Physics*. Non-serial Publications. Vienna: IAEA. ISBN: 92-0-107304-6. URL: `https://www.iaea.org/publications/7086/radiation-oncology-physics`.

Ikawa, Toshiki et al. (2023). "Linear accelerator-based stereotactic radiotherapy for brain metastases, including multiple and large lesions, carries a low incidence of acute toxicities: a retrospective analysis". In: *Radiat. Oncol.* 18 (1), p. 80. DOI: `10.1186/s13014-023-02262-z`.

Islam, Naveed et al. (2020). "A collision prediction framework for noncoplanar radiotherapy planning and delivery". In: *J. Appl. Clin. Med. Phys.* 21 (8), pp. 92–106. DOI: `10.1002/acm2.12920`.

Jansson, Tomas et al. (1998). “Radiotherapy of breast cancer after breast-conserving surgery: an improved technique using mixed electron–photon beams with a multileaf collimator”. In: *Radiother. Oncol.* 46 (1), pp. 83–89. DOI: 10.1016/S0167-8140(97)00176-X.

Jeraj, Robert, Paul J. Keall, and Jeffrey V. Siebers (2002). “The effect of dose calculation accuracy on inverse treatment planning”. In: *Phys. Med. Biol.* 47 (3), pp. 391–407. DOI: 10.1088/0031-9155/47/3/303.

Jia, Xun et al. (2011). “GPU-based fast Monte Carlo simulation for radiotherapy dose calculation”. In: *Phys. Med. Biol.* 56 (22). DOI: 10.1088/0031-9155/56/22/002.

Jin, L. et al. (2008). “Dosimetric verification of modulated electron radiotherapy delivered using a photon multileaf collimator for intact breasts”. In: *Phys. Med. Biol.* 53 (21), p. 6009. DOI: 10.1088/0031-9155/53/21/008.

Jin, Lihui et al. (2014). “Measurement and Monte Carlo simulation for energy- and intensity-modulated electron radiotherapy delivered by a computer-controlled electron multileaf collimator”. In: *J. Appl. Clin. Med. Phys.* 15 (1). DOI: 10.1120/jacmp.v15i1.4506.

Jin, Will H. et al. (2022). “A Review of Boron Neutron Capture Therapy: Its History and Current Challenges”. In: *International Journal of Particle Therapy* 9 (1), pp. 71–82. DOI: 10.14338/IJPT-22-00002.1.

Joehl, Alexander et al. (2018). “Body motion during dynamic couch tracking with healthy volunteers”. In: *Phys. Med. Biol.* 64 (1), p. 015001. DOI: 10.1088/1361-6560/aaf361.

Kallman, P. et al. (1988). “Shaping of arbitrary dose distributions by dynamic multileaf collimation”. In: *Phys. Med. Biol.* 33 (11), p. 1291. DOI: 10.1088/0031-9155/33/11/007.

Kaluarachchi, Maduka M. et al. (2020). “Validation of a Monte Carlo model for multi leaf collimator based electron delivery”. In: *Med. Phys.* 47 (8), pp. 3586–3599. DOI: 10.1002/mp.14194.

Karlsson, Mikael and Björn Zackrisson (1993). “Matching of electron and photon beams with a multi-leaf collimator”. In: *Radiother. Oncol.* 29 (3), pp. 317–326.

Kawrakow, Iwan and Matthias Fippel (2000). “VMC++, a fast MC algorithm for Radiation Treatment planning”. In: *Use Comput. Radiat. Ther. 8th Int. Conf. (Heidelberg, Ger.) ed W Schlegel T Bortfeld (Heidelberg Springer)*, pp. 126–128. DOI: 10.1007/978-3-642-59758-9_46.

Keall, Paul J. et al. (2006). “The management of respiratory motion in radiation oncology report of AAPM Task Group 76”. In: *Med. Phys.* 33 (10), pp. 3874–3900. DOI: `10.1118/1.2349696`.

Khan, F. M. et al. (1977). “Physical Aspects of Electron-Beam Arc Therapy”. In: *Radiology* 124 (2), pp. 497–500. DOI: `10.1148/124.2.497`.

Kim, John J. and Ian F. Tannock (2005). “Repopulation of cancer cells during therapy: an important cause of treatment failure”. In: *Nat. Rev. Cancer* 5 (7), pp. 516–525. DOI: `10.1038/nrc1650`.

Klein, Eric E., Maria Mamalui-Hunter, and Daniel A Low (2008). “Delivery of modulated electron beams with conventional photon multi-leaf collimators”. In: *Phys. Med. Biol.* 54 (2), p. 327. DOI: `10.1088/0031-9155/54/2/010`.

Klein, Eric E. et al. (2008). “Validation of calculations for electrons modulated with conventional photon multileaf collimators”. In: *Phys. Med. Biol.* 53 (5), p. 1183. DOI: `10.1088/0031-9155/53/5/003`.

Klein, Eric E. et al. (2009). “Task Group 142 report: Quality assurance of medical acceleratorsa)”. In: *Med. Phys.* 36 (9Part1), pp. 4197–4212. DOI: `10.1118/1.3190392`.

Kontaxis, C. et al. (2020). “DeepDose: Towards a fast dose calculation engine for radiation therapy using deep learning”. In: *Phys. Med. Biol.* 65 (7), p. 075013. DOI: `10.1088/1361-6560/ab7630`.

Korevaar, Erik W. et al. (2002). “Investigation of the added value of high-energy electrons in intensity-modulated radiotherapy: four clinical cases”. In: *Int. J. Radiat. Oncol. Biol. Phys.* 52 (1), pp. 236–253. DOI: `10.1016/S0360-3016(01)02689-X`.

Langhans, Marco et al. (2018). “Optimizing highly noncoplanar VMAT trajectories: the NoVo method”. In: *Phys. Med. Biol.* 63 (2), p. 025023. DOI: `10.1088/1361-6560/AAA36D`.

Laprie, A. et al. (2015). “Paediatric brain tumours: A review of radiotherapy, state of the art and challenges for the future regarding protontherapy and carbontherapy”. In: *Cancer Radiother.* 19 (8), pp. 775–789. DOI: `10.1016/j.canrad.2015.05.028`.

Leavitt, Dennis D. and J Robert Stewart (1993). “Electron arc therapy of the postmasectomy prosthetic breast”. In: *Int. J. Radiat. Oncol. Biol. Phys.* 28, pp. 297–301. DOI: `10.1016/0360-3016(94)90170-8`.

Leavitt, Dennis D. et al. (1985). “Electron arc therapy: Physical measurement and treatment planning techniques”. In: *Int. J. Radiat. Oncol. Biol. Phys.* 11 (5), pp. 987–999. DOI: `10.1016/0360-3016(85)90122-1`.

Leksell, L. (1951). "The stereotaxic method and radiosurgery of the brain." In: *Acta Chir. Scand.* 102 (4), pp. 316–319.

— (1983). "Stereotactic radiosurgery". In: *J. Neurol. Neurosurg. Psychiatry* 46 (9), pp. 797–803. DOI: 10.1136/jnnp.46.9.797.

Lewis, David and Maria F. Chan (2015). "Correcting lateral response artifacts from flatbed scanners for radiochromic film dosimetry". In: *Med. Phys.* 42 (1), pp. 416–429. DOI: 10.1118/1.4903758.

Lewis, David et al. (2012). "An efficient protocol for radiochromic film dosimetry combining calibration and measurement in a single scan". In: *Med. Phys.* 39 (10), pp. 6339–6350. DOI: 10.1118/1.4754797.

Li, Jonathan G. et al. (2000). "Breast-conserving radiation therapy using combined electron and intensity-modulated radiotherapy technique". In: *Radiother. Oncol.* 56 (1), pp. 65–71. DOI: 10.1016/S0167-8140(00)00189-4.

Li, Ruijiang et al. (2014). "Nonisocentric treatment strategy for breast radiation therapy: A proof of concept study". In: *Int. J. Radiat. Oncol. Biol. Phys.* 88 (4), pp. 920–926. DOI: 10.1016/j.ijrobp.2013.12.029.

Li, Yongbao et al. (2022). "Development of a GPU-superposition Monte Carlo code for fast dose calculation in magnetic fields". In: *Phys. Med. Biol.* 67 (12), p. 125002. DOI: 10.1088/1361-6560/ac7194.

Li, Yongjie, Jonathan Yao, and Dezhong Yao (2003). "Genetic algorithm based deliverable segments optimization for static intensity-modulated radiotherapy". In: *Phys. Med. Biol.* 48 (20), p. 3353. DOI: 10.1088/0031-9155/48/20/007.

Liang, Jieming et al. (2015). "Trajectory Modulated Arc Therapy: A Fully Dynamic Delivery With Synchronized Couch and Gantry Motion Significantly Improves Dosimetric Indices Correlated With Poor Cosmesis in accelerated Partial Breast Irradiation". In: *Int. J. Radiat. Oncol. Biol. Phys.* 92 (5), pp. 1148–1156. DOI: 10.1016/J.IJROBP.2015.04.034.

Lim, Tze Yee et al. (2019). "Characterization of the HalcyonTM multileaf collimator system". In: *J. Appl. Clin. Med. Phys.* 20 (4), pp. 106–114. DOI: 10.1002/acm2.12568.

Lincoln, John David et al. (2022). "Comparison of anatomically informed class solution template trajectories with patient-specific trajectories for stereotactic radiosurgery and radiotherapy". In: *J. Appl. Clin. Med. Phys.* 23 (11), e13765. DOI: 10.1002/acm2.13765.

Lippitz, Bodo et al. (2014). "Stereotactic radiosurgery in the treatment of brain metastases: The current evidence". In: *Cancer Treat. Rev.* 40 (1), pp. 48–59. DOI: 10.1016/j.ctrv.2013.05.002.

Liu, Cong et al. (2021). “NeuralDAO: Incorporating neural network generated dose into direct aperture optimization for end-to-end IMRT planning”. In: *Med. Phys.* 48 (10), pp. 5624–5638. DOI: `10.1002/mp.15155`.

Liu, Dong C. and Jorge Nocedal (1989). “On the limited memory BFGS method for large scale optimization”. In: *Math. Program.* 45.1, pp. 503–528. DOI: `10.1007/BF01589116`.

Liu, Hefei et al. (2023). “Review of cone beam computed tomography based online adaptive radiotherapy: current trend and future direction”. In: *Radiat. Oncol.* 18 (1), p. 144. DOI: `10.1186/s13014-023-02340-2`.

Locke, Christopher Barry and Karl Kenneth Bush (2017). “Trajectory optimization in radiotherapy using sectioning (TORUS)”. In: *Med. Phys.* 44 (7), pp. 3375–3392. DOI: `10.1002/mp.12270`.

Loebner, Hannes A. et al. (2022). “Development of a Monte Carlo based robustness calculation and evaluation tool”. In: *Med. Phys.* 49 (7), pp. 4780–4793. DOI: `10.1002/mp.15683`.

Loebner, Hannes A. et al. (2023a). “Technical note: Feasibility of gating for dynamic trajectory radiotherapy – Mechanical accuracy and dosimetric performance”. In: *Med. Phys.* 50 (10), pp. 6535–6542. DOI: `10.1002/mp.16533`.

Loebner, Hannes A. et al. (2023b). “Impact of the gradient in gantry-table rotation on dynamic trajectory radiotherapy plan quality”. In: *Med. Phys.* 50 (11), pp. 7104–7117. DOI: `10.1002/mp.16749`.

Low, D. A. et al. (1992). “Electron bolus design for radiotherapy treatment planning: Bolus design algorithms”. In: *Med. Phys.* 19 (1), pp. 115–124. DOI: `10.1118/1.596885`.

Low, Daniel A. et al. (1995). “Computer-aided design and fabrication of an electron bolus for treatment of the paraspinal muscles”. In: *Int J Radiat. Oncol. Biol. Phys.* 33 (5). Implementation of Three Dimensional Conformal Radiotherapy, pp. 1127–1138. DOI: `10.1016/0360-3016(95)00257-X`.

Lyu, Qihui et al. (2018a). “A novel optimization framework for VMAT with dynamic gantry couch rotation”. In: *Phys. Med. Biol.* 63 (12). DOI: `10.1088/1361-6560/aac704`.

Lyu, Qihui et al. (2018b). “VMAT optimization with dynamic collimator rotation”. In: *Med. Phys.* 45 (6), pp. 2399–2410. DOI: `10.1002/mp.12915`.

Ma, C. M. et al. (2000). “Energy- and intensity-modulated electron beams for radiotherapy”. In: *Phys. Med. Biol.* 45 (8), pp. 2293–2311. DOI: `10.1088/0031-9155/45/8/316`.

Ma, Chaoqiong et al. (2019). “Electron modulated arc therapy (EMAT) using photon MLC for postmastectomy chest wall treatment I: Monte Carlo-based dosimetric characterizations”. In: *Phys. Med.* 67, pp. 1–8. DOI: 10.1016/j.ejmp.2019.10.018.

MacDonald, R. Lee and Christopher G. Thomas (2015). “Dynamic trajectory-based couch motion for improvement of radiation therapy trajectories in cranial SRT”. In: *Med. Phys.* 42 (5), pp. 2317–2325. DOI: 10.1118/1.4917165.

MacDonald, R. Lee, Christopher G. Thomas, and Alasdair Syme (2018). “Dynamic collimator trajectory algorithm for multiple metastases dynamic conformal arc treatment planning”. In: *Med. Phys.* 45 (1), pp. 5–17. DOI: 10.1002/mp.12648.

MacDonald, R. Lee et al. (2020). “Toward the combined optimization of dynamic axes (CODA) for stereotactic radiotherapy and radiosurgery using fixed couch trajectories”. In: *Med. Phys.* 47 (2), pp. 307–316. DOI: 10.1002/mp.13887.

MacFarlane, Michael et al. (2019). “A fast inverse direct aperture optimization algorithm for intensity-modulated radiation therapy”. In: *Med. Phys.* 46 (3), pp. 1127–1139. DOI: 10.1002/mp.13368.

Mackie, T. R. (2006). “History of tomotherapy”. In: *Phys. Med. Biol.* 51 (13). DOI: 10.1088/0031-9155/51/13/R24.

Magaddino, Vera et al. (2011). “Validation of the Swiss Monte Carlo Plan for a static and dynamic 6 MV photon beam”. In: *Z. Med. Phys.* 21, pp. 124–134. DOI: 10.1016/j.zemedi.2010.10.010.

Maillie, L., L. R. Salgado, and S. Lazarev (2021). “A systematic review of craniospinal irradiation for leptomeningeal disease: past, present, and future”. In: *Clin. Transl. Oncol.* 23 (10), pp. 2109–2119. DOI: 10.1007/S12094-021-02615-8.

MakeHuman (2020). Version 1.2.0. URL: www.makehumancommunity.org.

Mann, Thomas D. et al. (2019). “Development and clinical implementation of eclipse scripting-based automated patient-specific collision avoidance software”. In: *J. Appl. Clin. Med. Phys.* 20 (9), pp. 12–19. DOI: 10.1002/acm2.12673.

Manser, P. et al. (2020). “Advanced Dynamic Trajectory Radiotherapy Using Table Translations and Rotations”. In: *Int. J. Radiat. Oncol. Biol. Phys.* 108 (3), e335.

Manser, Peter et al. (2019). “Dose calculation of dynamic trajectory radiotherapy using Monte Carlo”. In: *Z. Med. Phys.* 29 (1), pp. 31–38. DOI: 10.1016/j.zemedi.2018.03.002.

Masi, Laura et al. (2013). “Impact of plan parameters on the dosimetric accuracy of volumetric modulated arc therapy”. In: *Med. Phys.* 40 (7). DOI: `10.1118/1.4810969`.

Massimino, Maura et al. (2016). “Childhood medulloblastoma”. In: *Crit. Rev. Oncol. Hematol.* 105, pp. 35–51. DOI: `10.1016/j.critrevonc.2016.05.012`.

Masterson-McGary, Mary Ellen (2013). “Robotic Radiosurgery”. In: *Encyclopedia of Radiation Oncology*. Ed. by Luther W. Brady and Theodore E. Yaeger. Berlin, Heidelberg: Springer Berlin Heidelberg, pp. 760–769. ISBN: 978-3-540-85516-3. DOI: `10.1007/978-3-540-85516-3_32`.

McNeely, Lee K. et al. (1988). “Electron arc therapy: Chest wall irradiation of breast cancer patients”. In: *Int. J. Radiat. Oncol. Biol. Phys.* 14 (6), pp. 1287–1294. DOI: `10.1016/0360-3016(88)90408-7`.

Men, Chunhua et al. (2007). “An exact approach to direct aperture optimization in IMRT treatment planning”. In: *Phys. Med. Biol.* 52 (24), pp. 7333–7352. DOI: `10.1088/0031-9155/52/24/009`.

Men, Chunhua et al. (2009). “GPU-based ultrafast IMRT plan optimization”. In: *Phys. Med. Biol.* 54 (21), p. 6565. DOI: `10.1088/0031-9155/54/21/008`.

Micke, Andre, David F. Lewis, and Xiang Yu (2011). “Multichannel film dosimetry with nonuniformity correction”. In: *Med. Phys.* 38 (5), pp. 2523–2534. DOI: `10.1118/1.3576105`.

Miften, M. et al. (2018). “Tolerance limits and methodologies for IMRT measurement-based verification QA: Recommendations of AAPM Task Group No. 218”. In: *Med. Phys.* 45 (4), e53–e83. DOI: `10.1002/MP.12810`.

Míguez, Carlos et al. (2017). “Clinical implementation of combined modulated electron and photon beams with conventional MLC for accelerated partial breast irradiation”. In: *Radiother. Oncol.* 124 (1), pp. 124–129. DOI: `10.1016/J.RADONC.2017.06.011`.

Mihaljevic, Josip et al. (2011). “Monte Carlo simulation of small electron fields collimated by the integrated photon MLC”. In: *Phys. Med. Biol.* 56 (3), p. 829. DOI: `10.1088/0031-9155/56/3/018`.

Mohan, Radhe (2022). “A review of proton therapy – Current status and future directions”. In: *Precis. Radiat. Oncol.* 6 (2), pp. 164–176. DOI: `10.1002/pro6.1149`.

Mohan, Radhe et al. (2000). “The impact of fluctuations in intensity patterns on the number of monitor units and the quality and accuracy of intensity modulated radiotherapy”. In: *Med. Phys.* 27 (6), pp. 1226–1237. DOI: `10.1118/1.599000`.

Morley, Lyndon et al. (2013). “Patient and Staff Assessment of an Audiovisual Education Tool for Head and Neck Radiation Therapy”. In: *J. Canc. Educ.* 28, pp. 474–480. DOI: `10.1007/s13187-013-0489-6`.

Mu, Xiangkui et al. (2004). “Can Photon IMRT be improved by combination with mixed electron and photon techniques?” In: *Acta Oncol.* 43 (8), pp. 727–735. DOI: `10.1080/02841860410002761`.

Mueller, S. et al. (2017). “Simultaneous optimization of photons and electrons for mixed beam radiotherapy”. In: *Phys. Med. Biol.* 62 (14), pp. 5840–5860. DOI: `10.1088/1361-6560/aa70c5`.

Mueller, S. et al. (2018a). “Electron beam collimation with a photon MLC for standard electron treatments”. In: *Phys. Med. Biol.* 63 (2), p. 025017. DOI: `10.1088/1361-6560/aa9fb6`.

Mueller, S. et al. (2018b). “Part 2: Dynamic mixed beam radiotherapy (DYMBER): Photon dynamic trajectories combined with modulated electron beams”. In: *Med. Phys.* 45 (9), pp. 4213–4226. DOI: `10.1002/mp.13085`.

Mueller, S. et al. (2022). “A hybrid column generation and simulated annealing algorithm for direct aperture optimization”. In: *Phys. Med. Biol.* 67 (7), p. 075003. DOI: `10.1088/1361-6560/AC58DB`.

Mueller, S et al. (2023). “Efficiency enhancements of a Monte Carlo beamlet based treatment planning process: implementation and parameter study”. In: *Phys. Med. Biol.* 68 (4), p. 044003. DOI: `10.1088/1361-6560/acb480`.

Mullins, Joel et al. (2020a). “Trajectory-based VMAT for cranial targets with delivery at shortened SAD”. In: *Med. Phys.* 47 (7), pp. 3103–3112. DOI: `10.1002/mp.14151`.

Mullins, Joel et al. (2020b). “Simultaneous trajectory generation and volumetric modulated arc therapy optimization”. In: *Med. Phys.* 47 (7), pp. 3078–3090. DOI: `10.1002/MP.14155`.

Myers, Pamela et al. (2013). “Evaluation of localization errors for craniospinal axis irradiation delivery using volume modulated arc therapy and proposal of a technique to minimize such errors”. In: *Radiother. Oncol.* 108 (1), pp. 107–113. DOI: `10.1016/j.radonc.2013.05.026`.

Neph, Ryan et al. (2021). “DeepMC: a deep learning method for efficient Monte Carlo beamlet dose calculation by predictive denoising in magnetic resonance-guided radiotherapy”. In: *Phys. Med. Biol.* 66 (3), p. 035022. DOI: `10.1088/1361-6560/abca01`.

Neuenschwander, H. and E. J. Born (1992). “A macro Monte Carlo method for electron beam dose calculations”. In: *Phys. Med. Biol.* 37 (1), p. 107. DOI: `10.1088/0031-9155/37/1/007`.

Neuenschwander, H., T. R. Mackie, and P. J. Reckwerdt (1995). “MMC-a high-performance Monte Carlo code for electron beam treatment planning”. In: *Phys. Med. Biol.* 40 (4), pp. 543–574. DOI: `10.1088/0031-9155/40/4/005`.

Nguyen, Dan et al. (2017). “Deterministic direct aperture optimization using multiphase piecewise constant segmentation”. In: *Med. Phys.* 44 (11), pp. 5596–5609. DOI: `10.1002/mp.12529`.

Niemierko, Andrzej (1997). “Reporting and analyzing dose distributions: A concept of equivalent uniform dose”. In: *Med. Phys.* 24 (1), pp. 103–110. DOI: `10.1118/1.598063`.

Nioutsikou, Elena, James L. Bedford, and Steve Webb (2003). “Patient-specific planning for prevention of mechanical collisions during radiotherapy”. In: *Phys. Med. Biol.* 48, pp. 313–321. DOI: `10.1088/0031-9155/48/22/n02`.

No, Hyunsoo Joshua et al. (2023). “Clinical Linear Accelerator-Based Electron FLASH: Pathway for Practical Translation to FLASH Clinical Trials”. In: *Int. J. Radiat. Oncol. Biol. Phys.* 117 (2), pp. 482–492. DOI: `10.1016/j.ijrobp.2023.04.011`.

Nocedal, Jorge and Stephen J. Wright (1999). *Numerical Optimization*. second. New York, NY, USA: Springer. DOI: `10.1007/b98874`.

Northway, Cassidy et al. (2022). “Patient-specific collision zones for 4π trajectory optimized radiation therapy”. In: *Med. Phys.* 49 (3), pp. 1407–1416. DOI: `10.1002/mp.15452`.

Lemoigne, Yves and Alessandra Caner, eds. (2009). *Image Guided Radiotherapy*. Springer Netherlands, pp. 113–125. ISBN: 978-90-481-3097-9. DOI: `10.1007/978-90-481-3097-9_10`.

Ohira, Shingo et al. (2018). “HyperArc VMAT planning for single and multiple brain metastases stereotactic radiosurgery: a new treatment planning approach”. In: *Radiat. Oncol.* 13 (1), p. 13. DOI: `10.1186/s13014-017-0948-z`.

O’Shea, Tuathan P. et al. (2011). “Characterization of an extendable multi-leaf collimator for clinical electron beams”. In: *Phys. Med. Biol.* 56 (23), p. 7621. DOI: `10.1088/0031-9155/56/23/018`.

Otto, Karl (2008). “Volumetric modulated arc therapy: IMRT in a single gantry arc”. In: *Med. Phys.* 35 (1), pp. 310–317. DOI: `10.1118/1.2818738`.

Paddick, Ian (2000). “A simple scoring ratio to index the conformity of radiosurgical treatment plans”. In: *J. Neurosurg.* 93 (Suppl 3), pp. 219–222. DOI: `10.3171/jns.2000.93.supplement`.

Padilla, Laura, Erik A. Pearson, and Charles A. Pelizzari (2015). “Collision prediction software for radiotherapy treatments”. In: *Med. Phys.* 42 (11). DOI: `10.1118/1.4932628`.

Pakela, Julia M. et al. (2020). “Quantum-inspired algorithm for radiotherapy planning optimization”. In: *Med. Phys.* 47 (1), pp. 5–18. DOI: `10.1002/mp.13840`.

Palma, Bianey Atriana et al. (2012). “Combined modulated electron and photon beams planned by a Monte-Carlo-based optimization procedure for accelerated partial breast irradiation”. In: *Phys. Med. Biol.* 57 (5), p. 1191. DOI: `10.1088/0031-9155/57/5/1191`.

Papp, Dávid, Thomas Bortfeld, and Jan Unkelbach (2015). “A modular approach to intensity-modulated arc therapy optimization with noncoplanar trajectories”. In: *Phys. Med. Biol.* 60 (13), pp. 5179–5198. DOI: `10.1088/0031-9155/60/13/5179`.

Park, Ji-Yeon et al. (2017). “Angular under-sampling effect on VMAT dose calculation: An analysis and a solution strategy”. In: *Med. Phys.* 44 (6), pp. 2096–2114. DOI: `10.1002/MP.12250`.

Pawlik, Timothy M. and Khandan Keyomarsi (2004). “Role of cell cycle in mediating sensitivity to radiotherapy”. In: *Int. J. Radiat. Oncol. Biol. Phys.* 59 (4), pp. 928–942. DOI: `10.1016/j.ijrobp.2004.03.005`.

Perkins, George H. et al. (2001). “A custom three-dimensional electron bolus technique for optimization of postmastectomy irradiation”. In: *Int. J. Radiat. Oncol. Biol. Phys.* 51 (4), pp. 1142–1151. DOI: `10.1016/S0360-3016(01)01744-8`.

Podgorsak, Ervin B. et al. (1988). “Dynamic stereotactic radiosurgery”. In: *Int. J. Radiat. Oncol. Biol. Phys.* 14 (1), pp. 115–126. DOI: `10.1016/0360-3016(88)90059-4`.

Pokhrel, Damodar et al. (2022). “HyperArc VMAT stereotactic radiotherapy for locally recurrent previously-irradiated head and neck cancers: Plan quality, treatment delivery accuracy, and efficiency”. In: *J. Appl. Clin. Med. Phys.* 23 (5), e13561. DOI: `10.1002/acm2.13561`.

Popple, Richard A. et al. (2021a). “Transition From Manual to Automated Planning and Delivery of Volumetric Modulated Arc Therapy Stereotactic Radiosurgery: Clinical, Dosimetric, and Quality Assurance Results”. In: *Pract. Radiat. Oncol.* 11 (2), e163–e171. DOI: `10.1016/j.prro.2020.10.013`.

Popple, Richard A. et al. (2021b). “Evaluation of a two-dimensional diode array for patient-specific quality assurance of HyperArc”. In: *J. Appl. Clin. Med. Phys.* 22 (12), pp. 203–210. DOI: `10.1002/acm2.13438`.

Preciado-Walters, Felisa et al. (2006). “Column generation for IMRT cancer therapy optimization with implementable segments”. In: *Ann. Oper. Res.* 148 (1), pp. 65–79. DOI: `10.1007/s10479-006-0080-1`.

Rahman, Mahbubur et al. (2021). “Electron FLASH Delivery at Treatment Room Isocenter for Efficient Reversible Conversion of a Clinical LINAC”. In: *Int. J. Radiat. Oncol. Biol. Phys.* 110 (3), pp. 872–882. DOI: `10.1016/j.ijrobp.2021.01.011`.

Reis, Cristiano Q. M. et al. (2021). “SBRT of ventricular tachycardia using 44π optimized trajectories”. In: *J. Appl. Clin. Med. Phys.* 22 (12), pp. 72–86. DOI: `10.1002/acm2.13454`.

Renaud, Marc-André, Monica Serban, and Jan Seuntjens (2017). “On mixed electron-photon radiation therapy optimization using the column generation approach”. In: *Med. Phys.* 44 (8), pp. 4287–4298. DOI: `10.1002/MP.12338`.

Renaud, Marc-André, Monica Serban, and Jan Seuntjens (2019). “Robust mixed electron-photon radiation therapy optimization”. In: *Med. Phys.* 46 (3), pp. 1384–1396. DOI: `10.1002/mp.13381`.

Rodrigues, Anna, Fang Fang Yin, and Qiuwen Wu (2014). “Dynamic electron arc radiotherapy (DEAR): A feasibility study”. In: *Phys. Med. Biol.* 59 (2), pp. 327–345. DOI: `10.1088/0031-9155/59/2/327`.

Rogers, D. W. O. (2006). “Fifty years of Monte Carlo simulations for medical physics*”. In: *Phys. Med. Biol.* 51 (13), R287. DOI: `10.1088/0031-9155/51/13/R17`.

Romeijn, H. Edwin et al. (2005). “A column generation approach to radiation therapy treatment planning using aperture modulation”. In: *SIAM J. Optim.* 15 (3), pp. 838–862. DOI: `10.1137/040606612`.

Rosca, Florin (2012). “A hybrid electron and photon IMRT planning technique that lowers normal tissue integral patient dose using standard hardware”. In: *Med. Phys.* 39 (6Part1), pp. 2964–2971. DOI: `10.1118/1.4709606`.

Rwigema, Jean-Claude M. et al. (2015). “4π Noncoplanar Stereotactic Body Radiation Therapy for Head-and-Neck Cancer: Potential to Improve Tumor Control and Late Toxicity”. In: *Int. J. Radiat. Oncol. Biol. Phys.* 91 (2), pp. 401–409. DOI: `10.1016/J.IJROBP.2014.09.043`.

Sagawa, Tomohiro et al. (2019). “Dosimetric effect of rotational setup errors in stereotactic radiosurgery with HyperArc for single and multiple brain metastases”. In: *J. Appl. Clin. Med. Phys.* 20 (10), pp. 84–91. DOI: `10.1002/acm2.12716`.

Salguero, Francisco Javier et al. (2010). “Intensity- and energy-modulated electron radiotherapy by means of an xMLC for head and neck shallow tumors”. In: *Phys. Med. Biol.* 55 (5), p. 1413. DOI: `10.1088/0031-9155/55/5/010`.

Schmidhalter, Daniel et al. (2014). “Assessment of patient setup errors in IGRT in combination with a six degrees of freedom couch”. In: *Z. Med. Phys.* 24 (2), pp. 112–122. DOI: `10.1016/j.zemedi.2013.11.002`.

Segars, W. P. et al. (2010). “4D XCAT phantom for multimodality imaging research”. In: *Med. Phys.* 37 (9), pp. 4902–4915. DOI: `10.1118/1.3480985`.

Seravalli, Enrica et al. (2018). “Dosimetric comparison of five different techniques for craniospinal irradiation across 15 European centers: analysis on behalf of the SIOP-E-BTG (radiotherapy working group)”. In: *Acta Oncol.* 57 (9), pp. 1240–1249. DOI: `10.1080/0284186X.2018.1465588`.

Sgouros, George et al. (2020). “Radiopharmaceutical therapy in cancer: clinical advances and challenges”. In: *Nat. Rev. Drug Discov.* 19 (9), pp. 589–608. DOI: `10.1038/s41573-020-0073-9`.

Sharma, P. K. et al. (2011). “Electron Arc Therapy for Bilateral Chest Wall Irradiation: Treatment Planning and Dosimetric Study”. In: *Clin. Oncol.* 23 (3), pp. 216–222. DOI: `10.1016/j.clon.2010.09.005`.

Shen, Zhenjiong et al. (2023). “Optimization of isocenter position for multiple brain metastases single-isocenter stereotactic radiosurgery to minimize dosimetric variations due to rotational uncertainty”. In: *Phys. Med.* 111, p. 102614. DOI: `10.1016/j.ejmp.2023.102614`.

Shepard, D. M. et al. (2002). “Direct aperture optimization: A turnkey solution for step-and-shoot IMRT”. In: *Med. Phys.* 29 (6), pp. 1007–1018. DOI: `10.1118/1.1477415`.

Siochi, Ramon Alfredo C., Andrea Molineu, and Colin G. Orton (2013). “Patient-specific QA for IMRT should be performed using software rather than hardware methods”. In: *Med. Phys.* 40 (7), p. 070601. DOI: `10.1118/1.4794929`.

Smyth, Gregory et al. (2013). “Trajectory optimization for dynamic couch rotation during volumetric modulated arc radiotherapy”. In: *Phys. Med. Biol.* 58 (22), p. 8163. DOI: `10.1088/0031-9155/58/22/8163`.

Smyth, Gregory et al. (2016). “Non-coplanar trajectories to improve organ at risk sparing in volumetric modulated arc therapy for primary brain tumors”. In: *Radiother. Oncol.* 121 (1), pp. 124–131. DOI: `10.1016/j.radonc.2016.07.014`.

Smyth, Gregory et al. (2019a). “Dosimetric accuracy of dynamic couch rotation during volumetric modulated arc therapy (DCR-VMAT) for primary brain tumours”. In: *Phys. Med. Biol.* 64 (8). DOI: `10.1088/1361-6560/ab0a8e`.

Smyth, Gregory et al. (2019b). “Recent developments in non-coplanar radiotherapy”. In: *Br. J. Radiol. Suppl.* 92 (1097). DOI: 10.1259/bjr.20180908.

Steel, G. Gordon, T. J. Mcmillan, and J. H. Peacock (1989). “The 5rs of radiobiology”. In: *Int. J. Radiat. Biol.* 56 (6), pp. 1045–1048. DOI: 10.1080/09553008914552491.

Su, Shiqin, Kathryn Moran, and James L. Robar (2014). “Design and production of 3D printed bolus for electron radiation therapy”. In: *J. Appl. Clin. Med. Phys.* 15 (4), pp. 194–211. DOI: 10.1120/jacmp.v15i4.4831.

Subramanian, Vallinayagam Shanmuga et al. (2017). “Multi-isocentric 4π volumetric-modulated arc therapy approach for head and neck cancer”. In: *J. Appl. Clin. Med. Phys.* 18 (5), pp. 293–300. DOI: 10.1002/acm2.12164.

Suriyakumar, Vinith M. et al. (2017). “Open-source software for collision detection in external beam radiation therapy”. In: *Presented at SPIE Medical Imaging*. URL: www.slicer.org.

Surucu, Murat et al. (2010). “Planning tools for modulated electron radiotherapy”. In: *Med. Phys.* 37 (5), pp. 2215–2224. DOI: 10.1118/1.3395573.

Tai, Yee Man et al. (2023). “Quality assurance for mixed electron–photon beam radiation therapy using treatment log files and MapCHECK”. In: *Med. Phys.* DOI: 10.1002/mp.16759.

Teoh, M. et al. (2011). “Volumetric modulated arc therapy: a review of current literature and clinical use in practice”. In: *Br. J. Radiol.* 84, pp. 967–996. DOI: 10.1259/bjr/22373346.

Thomas, S. J. (2006). “Margins between clinical target volume and planning target volume for electron beam therapy”. In: *Brit. J. Radiol.* 79 (939), pp. 244–247. DOI: 10.1259/bjr/70202978.

Thwaites, David (2013). “Accuracy required and achievable in radiotherapy dosimetry: have modern technology and techniques changed our views?” In: *J. Phys.: Conf. Ser.* 444 (1), p. 012006. DOI: 10.1088/1742-6596/444/1/012006.

Timmerman, Robert D. and Brian D. Kavanagh (2005). “Stereotactic Body Radiation Therapy”. In: *Curr. Probl. Cancer* 29 (3), pp. 120–157. DOI: 10.1016/j.currproblcancer.2005.05.001.

Tran, Angelia et al. (2017a). “Predicting liver SBRT eligibility and plan quality for VMAT and 4π plans”. In: *Radiat. Oncol.* 12 (1), p. 70. DOI: 10.1186/s13014-017-0806-z.

Tran, Angelia et al. (2017b). “Treatment planning comparison of IMPT, VMAT and 4π radiotherapy for prostate cases”. In: *Radiat. Oncol.* 12 (1), p. 10. DOI: 10.1186/s13014-016-0761-0.

Ulmer, W., J. Pyyry, and W. Kaissl (2005). “A 3D photon superposition/convolution algorithm and its foundation on results of Monte Carlo calculations*”. In: *Phys. Med. Biol.* 50 (8), p. 1767. DOI: `10.1088/0031-9155/50/8/010`.

Unkelbach, Jan et al. (2022). “Joint Optimization of Radiotherapy Treatments Involving Multiple Radiation Modalities”. In: *IEEE Trans. Radiat. Plasma Med. Sci.* 6 (3), pp. 294–303. DOI: `10.1109/TRPMS.2021.3092423`.

Varian Medical Systems (2017). *Eclipse Photon and Electron Algorithms 15.5 Reference Guide Document.*

Varian Medical Systems (2012). *TrueBeam Radiotherapy System Built-In Safety Features Brief.* URL: `https://varian.widen.net/view/pdf/s5zwk3cbtl/TrueBeamSafety_ProductBrief_RAD10274_December2012.pdf?u=wefire`.

Vassiliev, Oleg N. et al. (2010). “Validation of a new grid-based Boltzmann equation solver for dose calculation in radiotherapy with photon beams”. In: *Phys. Med. Biol.* 55 (3), p. 581. DOI: `10.1088/0031-9155/55/3/002`.

Vatanen, Tero, Erik Traneus, and Tapani Lahtinen (2009). “Comparison of conventional inserts and an add-on electron MLC for chest wall irradiation of left-sided breast cancer”. In: *Acta Oncol.* 48 (3), pp. 446–451. DOI: `10.1080/02841860802477907`.

Verbakel, Wilko F.A.R. et al. (2009). “Rapid delivery of stereotactic radiotherapy for peripheral lung tumors using volumetric intensity-modulated arcs”. In: *Radiother. Oncol.* 93 (1), pp. 122–124. DOI: `10.1016/j.radonc.2009.05.020`.

Verellen, Dirk, Mark De Ridder, and Guy Storme (2008). “A (short) history of image-guided radiotherapy”. In: *Radiother. Oncol.* 86 (1), pp. 4–13. DOI: `10.1016/j.radonc.2007.11.023`.

Vozenin, Marie-Catherine, Jean Bourhis, and Marco Durante (2022). “Towards clinical translation of FLASH radiotherapy”. In: *Nat. Rev. Clin. Oncol.* 19 (12), pp. 791–803. DOI: `10.1038/s41571-022-00697-z`.

Wang, Liam J et al. (2022a). “Virtual Reality-Based Education for Patients Undergoing Radiation Therapy”. In: *J. Canc. Educ.* 37, pp. 694–700. DOI: `10.1007/s13187-020-01870-7`.

Wang, Xiaorong, Daren Sawkey, and Qiuwen Wu (2020). “Technical Note: A dose calculation framework for dynamic electron arc radiotherapy (DEAR) using VirtuaLinac Monte Carlo simulation tool”. In: *Med. Phys.* 47 (1), pp. 164–170. DOI: `10.1002/mp.13882`.

Wang, Yu-Jen et al. (2021). “CT-Based Collision Prediction Software for External-Beam Radiation Therapy”. In: *Front. Oncol.* 11, p. 617007. DOI: `10.3389/fonc.2021.617007`.

Wang, Yuanbo et al. (2022b). “A practical algorithm for VMAT optimization using column generation techniques”. In: *Med. Phys.* 49 (7), pp. 4335–4352. DOI: `10.1002/mp.15776`.

Webb, S. (1989). “Optimisation of conformal radiotherapy dose distribution by simulated annealing”. In: *Phys. Med. Biol.* 34 (10), p. 1349. DOI: `10.1088/0031-9155/34/10/002`.

Webb, S (1997). *The Physics of Conformal Radiotherapy: Advances in Technology*. Medical science series. Institute of Physics Publishing. ISBN: 9780750303965. DOI: `10.1201/9780367806545`.

Wild, Esther et al. (2015). “Noncoplanar VMAT for nasopharyngeal tumors: Plan quality versus treatment time”. In: *Med. Phys.* 42 (5), pp. 2157–2168. DOI: `10.1118/1.4914863`.

Williams, Katelyn et al. (2017). “Meeting radiation therapy patients informational needs through educational videos augmented by 3D visualisation software”. In: *J. Med. Radiat. Sci.* 64, pp. 35–40. DOI: `10.1002/jmrs.220`.

Wilson, Byron, Karl Otto, and Ermias Gete (2017). “A simple and robust trajectory-based stereotactic radiosurgery treatment”. In: *Med. Phys.* 44 (1), pp. 240–248. DOI: `10.1002/mp.12036`.

Witztum, A. et al. (2014). “Dosimetric Effect of Setup Errors on Multiple Isocenter Volumetric Modulated Arc Radiation Therapy for Craniospinal Axis”. In: *Int. J. Radiat. Oncol. Biol. Phys.* 90 (1), S838–S839. DOI: `10.1016/j.ijrobp.2014.05.2408`.

Wortel, Geert et al. (2021). “Characterization of automatic treatment planning approaches in radiotherapy”. In: *Phys. Imaging Radiat. Oncol* 19, pp. 60–65. DOI: `10.1016/j.phro.2021.07.003`.

Wu, Andrew (1992). “Physics and Dosimetry of the Gamma Knife”. In: *Neurosurg. Clin. N. Am.* 3 (1). Stereotactic Radiosurgery, pp. 35–50. DOI: `10.1016/S1042-3680(18)30681-8`.

Wu, Qiuwen and Radhe Mohan (2000). “Algorithms and functionality of an intensity modulated radiotherapy optimization system”. In: *Med. Phys.* 27 (4), pp. 701–711. DOI: `10.1118/1.598932`.

Xiao, Ying et al. (2015). “Flattening filter-free accelerators: a report from the AAPM Therapy Emerging Technology Assessment Work Group”. In: *J. Appl. Clin. Med. Phys.* 16 (3), pp. 12–29. DOI: `10.1120/jacmp.v16i3.5219`.

Xiong, W. et al. (2004). “Optimization of combined electron and photon beams for breast cancer”. In: *Phys. Med. Biol.* 49 (10), p. 1973. DOI: `10.1088/0031-9155/49/10/010`.

Yang, Jie et al. (2018). "Aperture generation based on threshold segmentation for intensity modulated radiotherapy treatment planning". In: *Med. Phys.* 45 (4), pp. 1758–1770. DOI: `10.1002/mp.12819`.

Yang, Yingli et al. (2011). "Choreographing Couch and Collimator in Volumetric Modulated Arc Therapy". In: *Int. J. Radiat. Oncol. Biol. Phys.* 80 (4), pp. 1238–1247. DOI: `10.1016/J.IJROBP.2010.10.016`.

Yu, Victoria Y. et al. (2014). "Quality control procedures for dynamic treatment delivery techniques involving couch motion". In: *Med. Phys.* 41 (8Part1), p. 081712. DOI: `10.1118/1.4886757`.

Yu, Victoria Y. et al. (2015). "The development and verification of a highly accurate collision prediction model for automated noncoplanar plan delivery". In: *Med. Phys.* 42 (11), pp. 6457–6467. DOI: `10.1118/1.4932631`.

Yu, Victoria Y. et al. (2018). "A Prospective 4π Radiation Therapy Clinical Study in Recurrent High-Grade Glioma Patients". In: *Int. J. Radiat. Oncol. Biol. Phys.* 101 (1), pp. 144–151. DOI: `10.1016/j.ijrobp.2018.01.048`.

Zhang, Liyuan et al. (2019). "Aperture shape generation based on gradient descent with momentum". In: *IEEE Access* 7, pp. 157623–157632. DOI: `10.1109/ACCESS.2019.2949871`.

Zou, Wei et al. (2015). "Potential of 3D printing technologies for fabrication of electron bolus and proton compensators". In: *J. Appl. Clin. Med. Phys.* 16 (3), pp. 90–98. DOI: `10.1120/jacmp.v16i3.4959`.

List of publications

- **Guyer, G.**, Mueller, S., Mackeprang, P.-H., Frei, D., Volken, W., Aebersold, D.M., Loessl, K., and Manser, P., and Fix, M.K. (2023), Delivery time reduction for mixed photon-electron radiotherapy by using photon MLC collimated electron arcs. *Phys Med Biol*, https://doi.org/10.1088/1361-6560/ad021a
- **Guyer, G.**, Mueller, S., Wyss, Y., Bertholet, J., Schmid, R., Stampanoni, M.F.M., Manser, P. and Fix, M.K. (2023), Technical note: A collision prediction tool using Blender. *J Appl Clin Med Phys*, e14165. https://doi.org/10.1002/acm2.14165
- Bertholet, J., Mackeprang, P.-H., Loebner, H.A., Mueller, S., **Guyer, G.**, Frei, D., Volken, W., Elicin, O., Aebersold, D.M., Fix, M.K. and Manser, P. (2023), Comparison of Dynamic Trajectory Radiotherapy and Volumetric Modulated Arc Therapy for Loco-Regionally Advanced Oropharyngeal Cancer. *Int J Radiat Oncol Biol Phys*, 117, 2: e644. https://doi.org/10.1016/j.ijrobp.2023.06.2057
- Loebner, H.A., Frauchiger, D., Mueller, S., **Guyer, G.**, Mackeprang P.-H., Stampanoni M.F.M., Fix, M.K., Manser, P. and Bertholet, J. (2023),Technical note: Feasibility of gating for dynamic trajectory radiotherapy – Mechanical accuracy and dosimetric performance. *Med Phys*, 50: 6535–6542. https://doi.org/10.1002/mp.16533
- Fix, M.K., Frei, D., Mueller, S., **Guyer, G.**, Loebner, H.A., Volken, W. and Manser, P. (2023), Auto-commissioning of a Monte Carlo electron beam model with application to photon MLC shaped electron fields. *Phys Med Biol*, 68: 044004. https://doi.org/10.1088/1361-6560/acb755
- Mueller, S., **Guyer, G.**, Volken, W., Frei, D., Torelli, N., Aebersold, D.M., Manser, P. and Fix, M.K. (2023), Efficiency enhancements of a Monte Carlo beamlet based treatment planning process: implementation and parameter study. *Phys Med Biol*, 68: 044003. https://doi.org/10.1088/1361-6560/acb480

- **Guyer, G.**, Mueller, S., Koechli, C., Frei, D., Volken, W., Bertholet, J., Mackeprang, P.-H., Loebner, H.A., Aebersold, D.M., Manser, P. and Fix, M.K. (2022), Enabling non-isocentric dynamic trajectory radiotherapy by integration of dynamic table translations. *Phys Med Biol*, 67: 175003. https://doi.org/10.1088/1361-6560/ac840d

- Bertholet, J., Mackeprang, P.-H., Mueller, S., **Guyer, G.**, Loebner, H.A., Wyss Y., Frei, D., Volken, W., Elicin, O., Aebersold, D.M., Fix, M.K., and Manser, P. (2022), Organ-at-risk sparing with dynamic trajectory radiotherapy for head and neck cancer: comparison with volumetric arc therapy on a publicly available library of cases. *Radiat Oncol* 17, 122. https://doi.org/10.1186/s13014-022-02092-5

- Henzen, D., Schmidhalter, D., **Guyer, G.**, Stenger-Weisser, A., Ermis, E., Poel, R., Deml, M.C., Fix, M.K., Manser, P., and Aebersold, D.M. and Hemmatazad, H. (2022), Feasibility of postoperative spine stereotactic body radiation therapy in proximity of carbon and titanium hybrid implants using a robotic radiotherapy device. *Radiat Oncol* 17, 94. https://doi.org/10.1186/s13014-022-02058-7

- Loebner, H.A., Volken, W., Mueller, S., Bertholet, J., Mackeprang, P.-H., **Guyer, G.**, Aebersold, D.M., Stampanoni, M.F.M., Manser P. and Fix, M.K. (2022), Development of a Monte Carlo based robustness calculation and evaluation tool. *Med Phys* 49: 4780–4793. https://doi.org/10.1002/mp.15683

- Mueller, S., **Guyer, G.**, Risse, T., Tessarini, S., Aebersold, D.M., Stampanoni, M.F.M., Fix, M.K. and Manser, P. (2022), A hybrid column generation and simulated annealing algorithm for direct aperture optimization. *Phys Med Biol*, 67: 075003. https://doi.org/10.1088/1361-6560/ac58db

- Heath, E., Mueller, S., **Guyer, G.**, Duetschler, A., Elicin, O., Aebersold, D., Fix, M.K. and Manser, P. (2021), Implementation and experimental validation of a robust hybrid direct aperture optimization approach for mixed-beam radiotherapy. *Med Phys*, 48: 7299–7312. https://doi.org/10.1002/mp.15258

- Kueng, R., **Guyer, G.**, Volken, W., Frei, D., Stabel, F., Stampanoni, M.F.M., Manser, P. and Fix, M.K. (2020), Development of an extended Macro Monte Carlo method for efficient and accurate dose calculation in magnetic fields. *Med Phys*, 47: 6519-6530. https://doi.org/10.1002/mp.14542

Declaration of Originality

Last name, first name: Guyer, Gian Mauro Carlo

Matriculation number: 14-932-990

I hereby declare that this thesis represents my original work and that I have used no other sources except as noted by citations.
All data, tables, figures and text citations which have been reproduced from any other source, including the internet, have been explicitly acknowledged as such.
I am aware that in case of non-compliance, the Senate is entitled to withdraw the doctorate degree awarded to me on the basis of the present thesis, in accordance with the "Statut der Universität Bern (Universitätsstatut; UniSt)", Art. 69, of 7 June 2011.

Bern, February 5, 2024

G. Guyer

Gian Mauro Carlo Guyer